



**HAL**  
open science

# Interface Design for Halide Perovskite Solar Cells

Claire Darin Bapaume

► **To cite this version:**

Claire Darin Bapaume. Interface Design for Halide Perovskite Solar Cells. Material chemistry. Institut Polytechnique de Paris, 2023. English. NNT : 2023IPPAX057 . tel-04555562

**HAL Id: tel-04555562**

**<https://theses.hal.science/tel-04555562>**

Submitted on 23 Apr 2024

**HAL** is a multi-disciplinary open access archive for the deposit and dissemination of scientific research documents, whether they are published or not. The documents may come from teaching and research institutions in France or abroad, or from public or private research centers.

L'archive ouverte pluridisciplinaire **HAL**, est destinée au dépôt et à la diffusion de documents scientifiques de niveau recherche, publiés ou non, émanant des établissements d'enseignement et de recherche français ou étrangers, des laboratoires publics ou privés.

# Interface design of halide perovskite solar cell

Thèse de doctorat de l'Institut Polytechnique de Paris  
préparée à l'École polytechnique

École doctorale n°626 Institut Polytechnique de Paris (ED IP Paris)  
Spécialité de doctorat: Physique

Thèse présentée et soutenue à Palaiseau, le 05/07/2023, par

**CLAIRE DARIN BAPAUME**

## Composition du Jury :

Lionel Hirsch Directeur de Recherche, Université de Bordeaux (CNRS)	Rapporteur
Emilie Planes, Maitre de Conférence, Université de Savoie (CNRS)	Rapporteur
Christian Perruchot Maitre de Conférence, Université Paris Cité (CNRS)	Examineur
Yvan Bonnassieux Professeur, Ecole Polytechnique (CNRS)	Examineur Président
Philip Schulz Directeur de Recherche, IPVF (UMR 9006 CNRS-IPVF)	Directeur de thèse
Muriel Bouttemy Ingénieur de Recherche, Institut Lavoisier de Versailles (MUR 8180 CNRS-UVSQ)	Co-encadrante de thèse

## **Remerciements**

Ce manuscrit de thèse présente trois et demi de travail que j'ai pu réaliser à l'Institut Photovoltaïque d'Ile-de-France (IPVF) et l'Institut Lavoisier de Versailles (ILV) et cela n'aurait jamais été possible sans l'appui et le souhait d'un grand nombre de personnes.

Je souhaite tout d'abord remercier mes encadrants Philip Schulz et Muriel Bouttemy pour m'avoir permis d'entrer à l'IPVF et m'avoir fait confiance pour continuer l'aventure sur une thèse. Je leur remercie aussi bien pour l'encadrement que pour les échanges scientifiques et personnelles, de m'avoir aidé et été présent pour tout questionnement quant à la direction à prendre sur ma thèse. Il y a eu des hauts et des bas, des challenges et épreuves, des inattendues, comme le covid par exemple, autour de cette thèse depuis mes premiers pas à l'IPVF jusqu'à la rédaction de cette dernière. Je vous remercie de m'avoir permis de ne pas lâcher et de continuer à m'accrocher à cette thèse.

Je souhaite aussi remercier Lionel Hirsch, Emilie Planes, en tant que rapporteur and rapportrice, Christian Perruchot, et Yvan Bonnassieux, en tant qu'examineur, d'avoir accepté de prendre de leur temps afin de devenir membre de mon comité de thèse.

Je remercie aussi l'IPVF et UMR CNRS, ainsi que l'ILV qui m'ont permis de réaliser mes travaux au sein de leur laboratoire et d'utiliser leur équipements me permettant de mener les travaux au cours de ma thèse sans encombre.

Je remercie Daniel Lincot et Jean-François Guillemoles sans qui je n'aurais sûrement jamais eu cette opportunité à l'IPVF. Je remercie aussi Claire Vialette pour aussi bien les aides administratives que pour nos petites discussions entre deux couloirs.

Je remercie tous les membres de l'IPVF, de l'UMR CNRS et l'ILV pour aussi bien scientifiquement que personnelle. Vous avez été présent aussi pour m'aider, vous m'avez formé en laboratoire comme Nicolas, Armelle, Baptiste, Julie, Frédérique, Marion, Régis et tant d'autre que j'ai sûrement oublié. Pour toute l'équipe de l'ILV, merci énormément. Je vous remercie pour votre accueil, l'ambiance et les discussions au sein du laboratoire. Je suis surtout reconnaissant au cours de cette rédaction de la thèse, comme vous avez pu le constater, j'ai beaucoup stressé et paniqué au cours de cette période et je vous remercie profondément de m'avoir accueilli et aidé un peu à prendre l'air et me détendre. Merci à Solène pour avoir supporter mes jérémiades et pour nos discussions, Mathieu aussi bien pour les manipulations XPS que pour les discussions autour des résultats, Mirella et toute l'équipe.

Institut Polytechnique de Paris

91120 Palaiseau, France



La team MOPGA élargie, la team 4<sup>ème</sup> étage et les autres: je ne vous remercierai jamais assez. Je sais que la dernière partie de ma thèse s'est passée un peu différemment, je souhaite vous remercier énormément pour les moments échangés et partagés pendant ces trois ans ensemble aussi bien Javid, qu'on a commencé le stage ensemble, Alexandre Py, qu'on a commencé notre premier jour de thèse, Maryline, qui est maintenant à Bessy, Pilar, avec nos innombrables discussions, Elisa, notre sportive nationale, Vincent, qui finit sa thèse deux jours après moi, Nitin, Davide, Aleksandre C., Arthur, Shang-ting, Célia, Marie, Van-Son, Amelle et d'autres que j'ai peut-être oublié. Merci pour tous les moments partagés ensemble que cela soit les pauses repas, discussions et échanges ou les sorties hors du laboratoires que j'ai pu participer.

Merci aussi à mon tout premier stage Peng d'avoir accepté de travailler avec moi. J'ai beaucoup appris sur l'encadrement et les nouvelles perspectives de travail en équipe en tant que leader grâce à cela. Merci à Philippe Lang, Asma et Heidi d'ITODYS pour d'avoir accepté de collaborer avec moi suite à un échange au cours de ma première JNPVF. Je remercie aussi Simon Biberger sur les études de nouvelles options pour la pérovskites en poudre et afin que son groupe pour leur accueil dans la petite ville de Bayreuth en Allemagne.

Je sais sûrement oublié pas mal de personnes sur le mot ou j'écris ces mots et je suis désolée mais je ne vous inquiétez et je ne vous oublie pas. Ces remerciements seront sûrement réécrits car pour cette raison.

Je remercie mes amies, surtout Caroline qui m'a récupéré en petite miettes à plusieurs reprises au cours de cette thèse. Je remercie ma famille pour son soutien car sans elle je ne serais pas là aujourd'hui. J'espère que j'ai pu les rendre fière. J'ai encore du mal à me rendre compte de tout ce que j'ai fait jusqu'à présent mais je vous remercie énormément car je pense que ces trois ans et demi de thèse au sein de vous tous mon fait aussi bien grandir scientifiquement et personnelles. Je pense que j'ai eu beaucoup de chance autour de cette thèse avec mes différentes rencontres. Sans vous tous, cette période aurait pu se passer de manière très différentes. Je suis devenue la personne que je suis aujourd'hui grâce à vous et je tenterai tout pour continuer à m'améliorer au cours de ce long voyage pour être la personne que vous serez fière demain.

*Pour une ènième fois, Merci !*

## ***Table of contents***

List of Figures .....	7
List of abbreviations and symbols .....	14
Chapter 1: Context and State of the art.....	17
1.1 Development and context of photovoltaic (PV) technologies.....	19
1.1.1 General context.....	19
1.1.2 Solar cell principle of operation.....	19
1.1.3 The different photovoltaic technologies .....	22
1.2 Perovskite solar cells (PSC).....	23
1.2.1 Development of halide perovskite thin-films as absorber layers in solar cell designs 23	
1.2.2 Properties of mixed cation halide perovskite.....	25
1.2.3 Architectures of perovskite solar cells PSC.....	28
1.2.4 State of the art.....	30
1.2.5 Issues and challenges.....	33
1.2.6 Perovskite solar cell development – A focus on interface optimization .....	37
1.3 Main objectives and structure of this thesis.....	40
1.4 References.....	43
Chapter 2: Methods and Experiments .....	49
2.1 Perovskite cell fabrication process at IPVF .....	51
2.1.1 Glass/FTO substrate.....	51
2.1.2 Electron transport layer .....	52
2.1.3 Perovskite absorber deposition .....	57
2.1.4 Hole transport layer (HTL).....	58
2.1.5 Metal contact.....	60
2.1.6 Alternative surface modifiers and interfaces layers studied .....	61
2.2 Electrical characterization techniques .....	66
2.2.1 Current Density-Voltage (JV) measurement.....	66
2.2.2 External quantum efficiency (EQE) .....	68
2.3 Optical characterization techniques .....	69
2.3.1 Absorption, transmission, reflection .....	69
2.4 Structural characterization techniques.....	70
2.4.1 Scanning electron microscopy .....	70
2.4.2 X-ray diffraction .....	71
2.5 Surface chemical characterization .....	71
2.5.1 X-ray Photoelectron Spectroscopy principle .....	71
2.5.2 X-ray Photoelectron Spectroscopy spectra description .....	75
2.6 Resume.....	81
2.7 References.....	82

Chapter 3: A potential new family of molecular additives for the perovskite solar cell top interface: adamantane and its derivatives .....	84
3.1 Adamantane molecules and its derivatives .....	86
3.2 Incorporation trials in the device .....	87
3.2.1 Morphology characterization .....	87
3.2.2 Integration of adamantane-based surface modifiers into perovskite solar cells and device characterization .....	91
3.2.3 Evidence for molecular adsorption .....	95
3.2.4 Optoelectronic characterization of perovskite films with adamantane surface modification .....	106
3.2.5 Expanded device series for optimization and reproducibility of PSCs with AD-based interlayers .....	110
3.2.6 Aging of perovskite films and devices with adamantane-based interlayer .....	112
3.2.7 Conclusion .....	123
3.2.8 References .....	124
Chapter 4: Development and tests of synthesized amino carboxylic acids: an approach at the bottom interface .....	126
4.1 Aminocarboxylic acid as passivation layer at the perovskite / ETL rear interface .....	128
4.2 Deposition process of the SAMs layers on mesoporous TiO <sub>2</sub> .....	129
4.3 Characterization of the mesoporous TiO <sub>2</sub> layer after SAM grafting .....	131
4.4 Integration of the SAMs interlayer in the device .....	132
4.4.1 Influence of surface preparation of the metal oxide layer on the device properties	132
4.4.2 Integration of the amino and amino-methyl based SAMs (SAM1-4) in the perovskite solar cell structure .....	136
4.4.3 Integration of the amidino-based SAMs (SAM 5-6) in the perovskite solar cell structure	142
4.4.4 Integration of the amidino-based biphenyl SAM (SAM 7) in the perovskite solar cell structure	147
4.5 Discussion .....	150
4.6 References .....	152
4.7 Annexes .....	153
4.7.1 ATR-FITR spectra of the SAM-deposited sample in mesoporous TiO <sub>2</sub> compared to a KBr pellet with SAM molecule incorporated .....	153
Chapter 5: Another alternative: understanding and application of polymethacrylate PMMA in a device .....	155
5.1 Introduction .....	157
5.2 Methods .....	158
5.3 Top interface optimization: PMMA .....	158
5.3.1 Low concentration PMMA .....	158
5.3.2 High concentration PMMA – mesoporous TiO <sub>2</sub> ETL .....	162
5.3.3 Low concentration of PMMA – mesoporous TiO <sub>2</sub> .....	167

5.4	Incorporation of the PMMA:PCBM layer .....	172
5.4.1	Material characterization of half-cells .....	172
5.4.2	Electrical performance .....	173
5.5	Conclusion .....	177
5.6	References.....	178
Chapter 6: Summary and Perspectives .....		180
6.1	Summary of thesis objectives, key results and suggestions for follow-up studies.....	180
6.2	Outlook beyond the design of interfaces.....	184
Chapter 7: Résumé en français .....		186

## ***Table of figures***

Figure 1.1: Schematic of a PN junction in several conditions (a) before contact; (b) after contact in equilibrium; (c) after contact under illumination. Figure Taken from A. Bojar's thesis <sup>4</sup> .....	19
Figure 1.2: Schematic of NIP perovskite solar cell circuit .....	21
Figure 1.3: Schematic energy diagram of semiconductors (a) with a direct bandgap (b) with an indirect bandgap .....	22
Figure 1.4: Compilation of all of the known solar cell and current developments within the fields. Figure taken from Pastuszak J. et al <sup>9</sup> .....	22
Figure 1.5: Metal halide perovskite crystalline structure .....	24
Figure 1.6: Perovskite solar cell architectures commonly used .....	28
Figure 1.7: Literature values for the energy levels with respect to the vacuum level of different materials which act as electron-selective (left), perovskite absorber and hole-selective layers (right) in perovskite solar cells taken from Zardetto et al <sup>29</sup> .....	30
Figure 1.8: Interface-related loss mechanisms in the device after light-induced excitation. Figure redrawn from <sup>71</sup> .....	36
Figure 1.9: Example of a two-terminal perovskite silicon tandem solar cell with advanced optics using light trapping at the rear by Fraunhofer ISE <sup>73</sup> .....	37
Figure 1.10: Self-assembled molecule ideal configuration at the interface ETL/HTL. Taken from Qiao et al <sup>74</sup> .....	38
Figure 1.11 Recap of the work done during the tests. The studies presented in this manuscript are highlighted in the different boxes.....	41
Figure 2.1: Schematic architecture of the NIP configuration architecture Glass/FTO/ETL/Perovskite/HTL/Gold used during this thesis .....	51
Figure 2.2: Spray Pyrolysis process. Figure reproduced from the publication of Messing G. et al, Ceramic Powder Synthesis by Spray Pyrolysis, in 1993 <sup>1</sup> .....	53
Figure 2.3: Atomic Layer Deposition Cycle process. [Example with ZnO: Oxygen red sphere, Zinc-blue sphere, Carbon black sphere, Hydrogen white sphere] Figure taken from the thesis of Fournier Olivier submitted in 2021 "Synthèse par ALD et caractérisation de couches extractrices d'électrons pour application dans les cellules solaires à base de pérovskite" <sup>2</sup> .....	54
Figure 2.4: Triple cation lead halide perovskite (HTL) solution preparation process. ....	57

Figure 2.5: Devices (a) before and (b) after chemical etching and gold deposition. (c) Metallic shadow mask for gold deposition, (d) Schematic of the several etching steps in solar cell fabrication in IPVF .....	61
Figure 2.6: Skeletal formulas of adamantane (AD), 1-adamantanamine (1ADA), 1-adamantanamine hydrochloride (1ADAHCl) .....	62
Figure 2.7: Skeletal formula of PMMA's monomer, methyl methacrylate, and PCBM, (6,6)-Phenyl C61 butyric acid methyl ester .....	63
Figure 2.8: JV curve description with the maximum power point annotation [Example taken from pveducation.org <sup>20</sup> ] .....	68
Figure 2.9: External quantum efficiency of a solar cell with the contribution of the mechanisms applied on the device [Example of pveducation.org <sup>21</sup> with a CIGS sample] .....	69
Figure 2.10: Schema of the level transition (1) X absorption, photoelectric effect and photoelectron emission, (2) de-excitation by X fluorescence and Auger electron emission .....	72
Figure 2.11: Schematic of the XPS analyses principle (a) interaction X-ray beam / sample (angles correspond to geometry collection of the electrons), (b) implementation of this technique to the present research work .....	73
Figure 2.12: Thermo Scientific NEXSA Escalab and 250 Xi spectrometers used for surface characterization .....	74
Figure 2.13: Survey spectra of the perovskite active layer measured on the half-cell Glass/FTO/c-TiO <sub>2</sub> /MA <sub>0.14</sub> , FA <sub>0.86</sub> Cs <sub>0.05</sub> Pb(Br <sub>0.16</sub> , I <sub>0.84</sub> ) <sub>3</sub> . The selected peaks for high energy resolution spectra acquisition are labeled. ....	75
Figure 2.14: HR spectra measured on the samples of Table 2.4 .....	77
Figure 2.15: Impact of the 400 μm X-ray spot of the NEXSA equipment on a P reference sample ..	78
Figure 3.1: Schematic of the working steps through this thesis on NIP configuration perovskite solar cells . Highlight on top interface with Chapter 3 .....	84
Figure 3.2: Adamantane (AD) and its derivatives: 1-adamantanamine (1ADA) and 1-adamantanamine hydrochloride (1ADAHCl) .....	86
Figure 3.3: (A) Photograph of glass/FTO/perovskite samples bathed for several hours in a solvent ((1) in IPA (2) in acetone (3) in acetonitrile (4) in toluene (5) in chlorobenzene). (B-F) Corresponding SEM images of perovskite films exposed to (B) IPA, (C) acetone, (D) acetonitrile, (E) toluene and (F) chlorobenzene (G) non-exposed perovskite film reference. ....	87

Figure 3.4: Cross section of HaP layer (A) Reference sample (B) 1ADAHCl .....	88
Figure 3.5: (A) Perovskite crystal structure and molecular structure of adamantane and its derivatives used in this study. (B) SEM images of the surfaces of glass/FTO/perovskite samples with (1) AD (2) 1ADA (3) 1ADAHCl on top and (4) a control sample, (C) XRD measurements of glass/FTO/c-mTiO <sub>2</sub> /perovskite samples with additives compared to the control sample .....	90
Figure 3.6: (a) JV curves of the best devices after gold deposition and (b) solar cells parameters of HaPSC measured fresh (after the gold deposition) and after 11 weeks comparing the antisolvent method and the spin-coating method using AD and 1ADA as an additive .....	93
Figure 3.7: XPS spectra of high energy resolution Pb 4f <sub>7/2</sub> , I 3d <sub>5/2</sub> , Br 3d, Cs 3d <sub>5/2</sub> , C 1s, N 1s, O 1s and Cl 2p with and without surface modifiers (— Reference, — AD, — 1ADA, — 1ADAHCl) .....	97
Figure 3.8: XPS spectrum C 1s (A) and N 1s (B) peaks fit position of the perovskite reference sample. Experimental data in black and fit curves in colored solid lines.....	98
Figure 3.9: XPS peak fit of Reference and AD conditions with the sample at day 0 .....	102
Figure 3.10: XPS peak fit of 1ADA and 1ADAHCl conditions with the sample at day 0 .....	103
Figure 3.11: (A) Spectrophotometer of AD,1ADA, and 1ADAHCl compared to a reference (B) photovoltage (SPV) and (C) surface work function (WF) of glass/FTO/perovskite samples with and without molecular layer on top measured by Kelvin Probe measurement using a green light (550nm) .....	108
Figure 3.12: TRPL curves of (left) half-cell and (right) full-cell and its insert graph zoom in the region 40-500 ns with a reference, AD, 1ADA and 1ADAHCl at 30 suns .....	109
Figure 3.13: Typical triple cation lead halide perovskite solar cell with glass/FTO/c-TiO <sub>2</sub> /m-TiO <sub>2</sub> /HaP/Spiro-MeOTAD/gold .....	110
Figure 3.14: Solar cell parameters of the devices Glass/FTO/compact TiO <sub>2</sub> /mesoporous TiO <sub>2</sub> /HaP/Additive/Spiro-MeOTAD/Gold with AD, 1ADA and 1ADAHCl treated devices compared to the control samples (A) J-V curves of the best devices for each conditions (B) Solar cell parameters of the various devices depending on the deposited additives .....	111
Figure 3.15: Evolution of the XPS spectrum of C 1s spectrum, its respective normalized values curves through time ( <b>d0</b> , <b>d15</b> , <b>d45</b> , <b>d90</b> ) for Reference, AD, 1ADA and 1ADAHCl .....	113
Figure 3.16: Evolution of the XPS spectrum of N 1s spectrum, its respective normalized values curves through time ( <b>d0</b> , <b>d15</b> , <b>d45</b> , <b>d90</b> ) for Reference, AD, 1ADA and 1ADAHCl .....	114
Figure 3.17: Plotting of the ratio $I_{I+Br}$ at d0 and d15 .....	115

Figure 3.18: Peak ratio evolution through time (d0, d15, d45, d90) for different conditions: control, AD, 1ADA and 1ADAHCl .....	117
Figure 3.19: XPS spectrum Pb 4f <sub>7/2</sub> peak contribution overtime at d0, d15, d45 and d90 under several conditions (AD, 1ADA and 1ADAHCl compared to a reference sample) .....	118
Figure 3.20: XPS spectrum O 1s peak contribution overtime at d0, d15, d45 and d90 under several conditions (AD, 1ADA and 1ADAHCl compared to a reference sample) .....	119
Figure 3.21: Picture of the devices stored under air atmosphere and day/night cycle for 5 weeks (A) coupled with the IV spectrums at d0 (B) and at 5 weeks (C).....	120
Figure 3.22: Power tracking of light illumination for 15 hours under air-atmosphere .....	122
Figure 4.1: Schematic of the working steps through this thesis on NIP configuration perovskite solar cells. Highlight on the bottom interface with Chapter 4 .....	126
Figure 4.2: Possible binding modes of carboxylic acid group on TiO <sub>2</sub> nanoparticles: (i) Electrostatic attraction, (ii, iii) H-bonding, (iv) monodentate (ester-like linkage), (v) bidentate bridging, and (vi) bidentate chelating. Taken from Qu et al <sup>3</sup> .....	128
Figure 4.3:RMN experimental spectrum of SAM 7 .....	130
Figure 4.4: FTIR-ATR spectra (1) the region of 1000 – 800 cm <sup>-1</sup> and (2) in the region 1800 – 1000 cm <sup>-1</sup> of SAM 7 (a) in KBr pellet and (b) grafted on c-m TiO <sub>2</sub> .....	131
Figure 4.5: Solar cell parameters comparison for the devices fabricated with the m-TiO <sub>2</sub> prepared layers as detailed in Table 4.4. (A) J(V) curves of the champion device for each substrate pretreatment condition, (B) table of the solar cell parameters of the best devices, and (C) compilation of the solar cell parameters of the entire series with cell statistics.....	134
Figure 4.6: (A) J(V) curve with the best cell results of the samples of the series without/with SAMs compared to a classic sample (REVERSE) (B) coupling with its table (C) Solar parameters values of the first series per SAMs (forward/reverse) .....	138
Figure 4.7: Solar cell parameters of the second series of the measurements depending on the molecules deposited on the mesoporous TiO <sub>2</sub> measured at day 0, after one week (day 7), after three weeks (day 21) and after eight weeks (day 56) .....	141
Figure 4.8: Comparison of formadinium (FA <sup>+</sup> ) and 4-amidinobenzoic acid similarity.....	142
Figure 4.9: Solar cell parameters comparison of the optimized series of the ITODYS-IPVF collaboration (A) JV curves and (B) EQE of the best devices (C) Solar cell parameters of all of the devices at day 0 (0d) .....	144

Figure 4.10: Light ageing degradation tests of non-encapsulated devices under 1 sun for 100 hours .....	146
Figure 4.11: Devices with the newly introduced SAM 7 (A) EQE and calculated $J_{sc}$ and (B) JV of the best devices in each condition (C) Solar cell parameters of all of the devices at day 0 and after two weeks (day 12) .....	149
Figure 4.12: FTIR-ATR spectra (left) in the region $1800 - 1000 \text{ cm}^{-1}$ and (right) the region of $1000 - 800 \text{ cm}^{-1}$ of (a) SAM 1 in KBr pellet, (b) SAM 1 and (c) SAM 2 grafted on m $\text{TiO}_2$ .....	153
Figure 4.13: FTIR-ATR spectra (left) in the region $1800 - 1000 \text{ cm}^{-1}$ and (right) the region of $1000 - 800 \text{ cm}^{-1}$ of (a) SAM 3 in KBr pellet, (b) SAM 3 grafted on c-m $\text{TiO}_2$ .....	153
Figure 4.14: FTIR-ATR spectra (left) in the region $1800 - 1000 \text{ cm}^{-1}$ and (right) the region of $1000 - 800 \text{ cm}^{-1}$ of (a) SAM 4 in KBr pellet, (b) SAM 4 grafted on c-m $\text{TiO}_2$ .....	154
Figure 4.15: FTIR-ATR spectra (left) in the region $1800 - 1000 \text{ cm}^{-1}$ and (right) the region of $1000 - 800 \text{ cm}^{-1}$ of (a) SAM 5 in KBr pellet, (b) SAM 4 grafted on c-m $\text{TiO}_2$ .....	154
Figure 5.1: Schematic of the working steps through this thesis on NIP configuration perovskite solar cells. Highlight on the bottom and top interface with Chapter 5 .....	155
Figure 5.2: Chemical structure of (left) poly methyl methacrylate (PMMA) and (right) [6,6]-phenyl-C61-butyric acid methyl ester (PCBM) .....	157
Figure 5.3: Structural and optical characterization of initial sample runs: (a) XRD of glass/FTO/ $\text{TiO}_2$ /Perovskite/PMMA; (b) XRD and (c) Transmission of glass/FTO/ $\text{SnO}_2$ /Perovskite/PMMA samples in three conditions: ● Control, ● PMMA 0.5 mg/mL and ● PMMA 1.0 mg/mL .....	160
Figure 5.4: Solar cell parameters of glass/FTO/ $\text{SnO}_2$ /HaP/PMMA/Spiro-MeOTAD/Gold in three conditions: (a) Control samples, (b) PMMA 0.5 mg/mL and (c) PMMA 1.0 mg/mL. (d) EQE of the best cell in this corresponding batch .....	162
Figure 5.5: Samples of glass/FTO/ $\text{TiO}_2$ /HaP/PMMA/Spiro-MeOTAD with varied PMMA solution concentrations (5, 10, 15, 20 mg/mL) compared to the reference sample: (a) Photograph of the devices before the gold deposition; (b) UV-Vis optical transmittance and absorption of the samples glass/FTO/ $\text{TiO}_2$ /HaP/PMMA; (c) Photoluminescence of glass/FTO/ $\text{TiO}_2$ /HaP/PMMA .....	164
Figure 5.6: Photoelectrical performance of devices glass/FTO/c-m $\text{TiO}_2$ /HaP/PMMA/Spiro-MeOTAD/Gold. (a) JV curve and (b) QE measurements with five conditions: 5 mg/mL, 10 mg/mL, 15 mg/mL and 20 mg/mL of PMMA compared to reference samples .....	165

Figure 5.7: Schematics of the carrier dynamics model in perovskite solar cells (a) without and (b) with a PMMA layer. Taken from the publication of Wang et al. <sup>12</sup> .....	166
Figure 5.8: Photoelectrical measurements of glass/FTO/c-m TiO <sub>2</sub> /HaP/PMMA/Spiro-MeOTAD devices at low concentrations of PMMA (1.5 mg/mL, 3 mg/mL and 5 mg/mL compared to the reference device): (a) JV curves and (b) QE of the best devices in each condition .....	168
Figure 5.9: Distribution of the solar cell parameters for control and different PMMA passivated cell concentrations. (a) Voc. (b) Jsc. (c) FF. (d) PCE .....	169
Figure 5.10: Aging test results of champion cells at each condition: Normalized power in maximum power point (P <sub>MPP</sub> ) tracking .....	170
Figure 5.11: Sample of glass/FTO/c-m TiO <sub>2</sub> /HaP/PMMA: (a) Normalized PL measurements for various conditions of PMMA; (b) TRPL measurements on perovskite layer with and without PMMA interlayer passivation. The laser intensity is $8 \times 10^{17}$ photon/(cm <sup>2</sup> ·s). The inset table displays the average carrier lifetime of each measured sample from different groups calculated from the ExponentialDecay function fitting. The inset figure zooms on the curves between 80 ns to 200 ns to show the decay rate after the injection.....	171
Figure 5.12: Sample of glass/FTO/c-m TiO <sub>2</sub> /PMMA:PCBM/HaP with several ratios of PMMA:PCBM (1:1, 1:3 and 1:5): (a) Normalized photoluminescence measurements (b) the X-ray diffraction ...	173
Figure 5.13: Sample of glass/FTO/c-m TiO <sub>2</sub> /PMMA:PCBM/HaP/Spiro-MeOTAD with several ratios of PMMA:PCBM (1:1, 1:3 and 1:5): (a) JV curves (b) EQE spectra .....	174
Figure 5.14: (a) Aging test results of champion cells for each condition: (top) Tracking of the normalized Voc; (bottom) Tracking of the normalized efficiency. (b) TRPL measurements on perovskite layer with and without PMMA:PCBM interlayer passivation. The inset table displays the average carrier lifetime of each measured sample for the samples with different PMMA:PCBM ratios from a fit by a single exponential decay function .....	176
Figure 6.1: JV curve of glass/FTO/ETL/HaP/modifiers/Spiro-MeOTAD (a) ETL comparison of references devices without Adamantane-based interlayer with c-m TiO <sub>2</sub> and SnO <sub>2</sub> (b) Comparison of the devices with 1ADAHCl and the reference devices .....	181
Figure 6.2: Absorption spectrum of the perovskite layer (red) "precursor" sample made for the classic HaP IPVF's recipe (black) "powder" made from the ball-milling fabrication process .....	185
Figure 7.1: (a) Structure cristalline de la pérovskite aux halogénures métalliques (b) Photographie d'une cellule pérovskite .....	186

Figure 7.2 : Récapitulatif de mes travaux au cours de mon doctorat .....	187
Figure 7.3 : Adamantane (AD) et ces dérivés: 1-adamantanamine (1ADA) and 1-adamantanamine hydrochloride (1ADAHCl).....	188
Figure 7.4 :Cellule pérovskite de verre/FTO/c-m TiO <sub>2</sub> /HaP/Spiro-MeOTAD/Or stocké sous air ambient (a) Photographie des cellules après 5 semaines (b) courbe JV avant le stockage des échantillons (c) JV après 5 semaines.....	189
Figure 7.5 : Cellule pérovskite avec une ETL de TiO <sub>2</sub> vs SnO <sub>2</sub> (verre/FTO/c-m TiO <sub>2</sub> /HaP/X/Spiro-MeOTAD/Or) (a) Cellule de reference (b) traité à l'1ADAHCl (=X) .....	190
Figure 7.6 : Comparaison des similarités entre (a) formadinium (FA <sup>+</sup> ) et (b) 4-amidinobenzoic acid (c) Courbes JV et (d) EQE des meilleurs cellules pour la série finale avec SAM 3, 4, 5 et 7 .....	191
Figure 7.7 : Mesures photoelectriques de cellules verre/FTO/c-m TiO <sub>2</sub> /HaP/PMMA/Spiro-MeOTAD traité par PMMA (1.5 mg/mL, 3 mg/mL and 5 mg/mL comparé à la cellule de reference): (a) Courbe JV et (b) EQE .....	192
Figure 7.8 : (a) Courbe JV de cellule verre/FTO/c-m TiO <sub>2</sub> /PMMA:PCBM/HaP/Spiro-MeOTAD/Or avec différents ratio PMMA :PCBM (b) Mesure TRPL de couches pérovskite avec ces couches de PMMA:PCBM en interface (insert table avec les temps de vie des charges dans chaque condition) .....	192

## ***List of abbreviations and symbols***

### **List of abbreviations**

ALD	Atomic Layer Deposition
AS	Antisolvent
CDB	Chemical Bath Deposition
CIGS	Copper indium gallium selenide
DSSC	Dye-sensitive solar cell
ETL	Electron transport layer
FTIR	Fourier transform infrared spectroscopy
HaP	Halide perovskite
HaPSC	Halide perovskite solar cell
HTL	Hole transport layer
ILV	Institut Lavoisier de Versailles
IPVF	Institut photovoltaïque d'île-de-france
ITODYS	Interfaces Traitements Organisation et DYnamique des Systèmes
IV	Current-Voltage
JV	Current density-voltage
KP	Kelvin probe
NMR	Proton nuclear magnetic resonance
PCE	Power conversion efficiency
PL	Photoluminescence
PV	Photovoltaic
SC	Spin-coated
SEM	Scanning emission microscope
SnO <sub>2</sub>	Tin oxide
SPV	Surface photovoltage
c-TiO <sub>2</sub>	Compact titanium dioxide
m-TiO <sub>2</sub>	Mesoporous titanium dioxide
c-m TiO <sub>2</sub>	Compact and mesoporous dioxide

TRPL	Time-resolved photoluminescence
UV	Ultraviolet
WF	Work function
XRD	X-ray diffraction
XPS	X-ray photoelectron spectroscopy
ZnO	Zinc oxide

### List of chemicals

1ADAHCl	1-adamantanamine hydrochloride
1ADA	1-adamantanamine
AD	Adamantane
FA	Formammidinium
FK209	Tris(2-(1H-pyrazol-1-yl)-4-tert-butylpyridine)cobalt(III) tri[bis(tri fluoromethane)sulfonamide]
FTO	Fluor doped tin oxide
IPA	Propan-2-ol
ITO	Indium-tin oxide
Li-TFSI	Lithium bis(tri fluoromethanesulfonyl)imide
MA	Methylammonium
PCBM	6,6-phenyl-C61-butyric acid methyl ester
PMMA	Poly(methyl methacrylate)
PTAA	Poly(triaryl amine)
Spiro-MeOTAD	2,2',7,7'-tetrakis[N,N-di(4-methoxyphenyl)amino]-9,9'- spirobiuorene
TAA	Titanium(IV) diisopropoxide bis(acetylacetonate)
tbp	Tert-butyl pyridine

### List of symbols

$\lambda$	Wavelength
E	Energy
$E_c, E_v$	Energy position of the conduction band and the valence band

$E_F$	Energy Fermi
$E_g$	Band gap
EQE	External quantum efficiency
FF	Fill Factor
I	Current
J	Current density
$J_{sc}$	Short circuit current density
PCE	Power conversion efficiency
$R_s$	Series resistance
$R_{sh}$	Shunt resistance
t	Tolerance factor
T	temperature
V	Voltage
Voc	Open-circuit voltage
Wf	Work function

## Chapter 1: Context and State of the art

---

*The subject of this thesis is the interface design of the perovskite solar cell. However, one question we can have is how the photovoltaic device works and how come we came to use this technology. In this chapter, we will briefly explain the functioning of the perovskite solar, as well as its outstanding properties praised for a decade. Furthermore, we will discuss the concerns around this material and the issues around this subject. In the end, I will project several projects I work on to solve some problems.*

## *Table of contents*

1.1	Development and context of photovoltaic (PV) technologies .....	19
1.1.1	General context.....	19
1.1.2	Solar cell principle of operation .....	19
1.1.3	The different photovoltaic technologies .....	22
1.2	Perovskite solar cells (PSC).....	23
1.2.1	Development of halide perovskite thin-films as absorber layers in solar cell designs 23	
1.2.2	Properties of mixed cation halide perovskite .....	25
1.2.3	Architectures of perovskite solar cells PSC.....	28
1.2.4	State of the art .....	30
1.2.5	Issues and challenges.....	33
1.2.6	Perovskite solar cell development – A focus on interface optimization .....	37
1.3	Main objectives and structure of this thesis .....	40
1.4	References.....	43

## 1.1 Development and context of photovoltaic (PV) technologies

### 1.1.1 General context

The planet reaches a total of 8 billion living people. This rapid population growth and the industrial improvement of countries lead to an increase in demand for energy by 19% from 2009 to 2019<sup>1</sup>. However, energy sources such as fossil fuels have started becoming unavailable and incompatible with our current state of living. This is why we observe solid economic and industrial growth toward renewable energy sources to meet these demands, with renewables satisfying 12.6% of the total final energy consumption in 2020<sup>1</sup>.

Solar energy is one of the most abundant sources available, and harnessing this power has been a core strategy for a sustainable transition of our energy economy. In this regard, photovoltaic devices, i.e., solar cells that directly convert sunlight into electricity, have risen to the most prominent application and now have the highest growth rates of all technologies for electricity generation<sup>2</sup>.

### 1.1.2 Solar cell principle of operation

The working principle of a solar cell is based on the photoelectric effect. Under illumination, electron-hole pairs are generated, and with the presence of an electrical field from the PN junction, the holes and the electrons travel in opposite ways.<sup>3</sup> Then, thanks to the device's architecture, the photogenerated charge carriers (holes and electrons) are separated to finally be collected at the device's electrical contact, leading to the generation of electrical current. To simplify our explanation of the basics of solar cells, we use the example of a conventional solar cell with a PN junction, with an example on Figure 1.1.

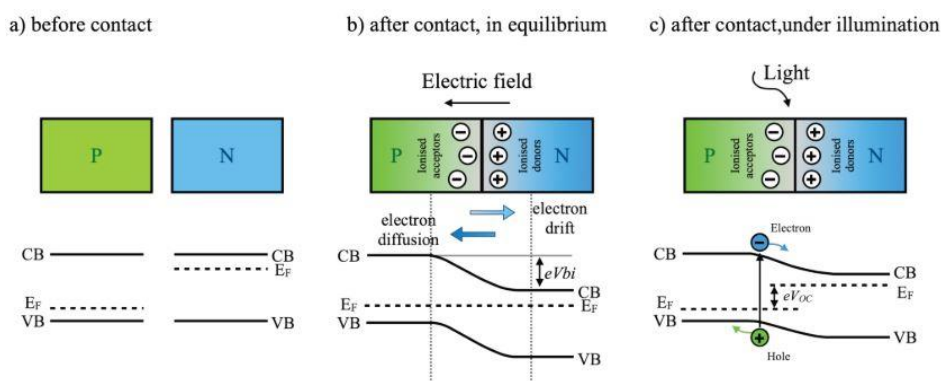
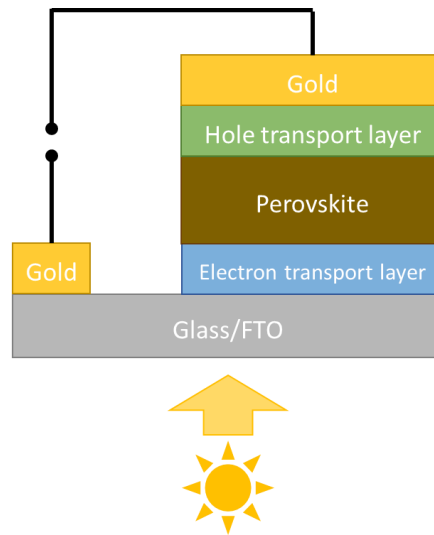


Figure 1.1: Schematic of a PN junction in several conditions (a) before contact; (b) after contact in equilibrium; (c) after contact under illumination. Figure Taken from A. Bojar's thesis<sup>4</sup>

The p-type material corresponds in our configuration to a hole transport layer (HTL), and the n-type material corresponds to an electron transport layer (ETL). Each semiconductor contains a bandgap, representing the minimum energy difference between the maximum energy level of the valence band (VB) and the minimum energy level of the conduction band (CB) with the own Fermi level depending on the doping of the material. The PN junction work as an interface by a p-type semiconductor with holes as majority carriers and a n-type semiconductor with electrons as majority carriers. The formation of the junction induces the diffusion of the carriers due to the gradient in their concentration at junction. At the thermal equilibrium, the electrons from the n-type material diffuse to the p-type material, leaving minority carriers of holes at the interface, and the holes diffuse from the p-type material to the n-type. This region existing at this interface is called depletion region. We observed the electric field's presence, as depicted in Figure 1.1.(b). The Fermi level of the semiconductors are aligned, indicated the internal potential produced. With no external inputs of light or applied voltage, an equilibrium is obtained between the carrier generation, recombination, diffusion and drift in the presence of the electric field.

In our case, we call our junction PIN, as we add an intrinsic layer between the n-type and p-type layer. For PIN junction solar cells, the intrinsic layer is used as a absorption layer to enhance the absorption of the solar cell. The ETL and HTL are presented to create the electric field. When an absorbed photon creates an electron-hole pair, the electron move toward the n-type layer and the hole to the p-type layer, as in Figure 1.1.(c). A quasi-Fermi level (QFL) splitting is observed, indicating a direct measurement of the open-circuit voltage ( $V_{oc}$ ) under illumination<sup>5</sup>.

Finally, the carriers are collected by the electrical contact situated at the top and back of the device. These contacts link to the external cell terminals to collect the photo-induced current as sketched in Figure 1.2(a).



*Figure 1.2: Schematic of NIP perovskite solar cell circuit*

The choice of the solar cell architecture is primordial for the device's efficiency and longevity. In particular, the choice of the material used as an absorber will govern the band alignment at the interfaces, the absorption domain of the sunlight, and confer the inherent stability of this layer and many other aspects important because they impose the deposition method of the other layers constitutive of the cell (interface roughness, temperature range stability ...). In direct bandgap, the maximum energy level of VB and the minimum energy level of CB occur at the same momentum. Therefore, the electron can excite or relax through the absorption or emission of photons, and there is no influence of the phonon in these processes. As the electron does not need to be given momentum, the electron energy produced through the electron-hole pair is equivalent to the bandgap energy ( $E_g$ ). Conversely, in an indirect bandgap, VB's maximum and CB's minimum energy levels are misaligned with different momentum<sup>6</sup>. The electron energy change after the transition. For momentum and energy conservation, phonons are used to the conservation process.<sup>7,8</sup>The type of transition is inert to the used material and cannot be changed. Depending on the need, one material is favored over another. A material with a direct transition is usually privileged to negligible the influence of the absorbed photon on the momentum.

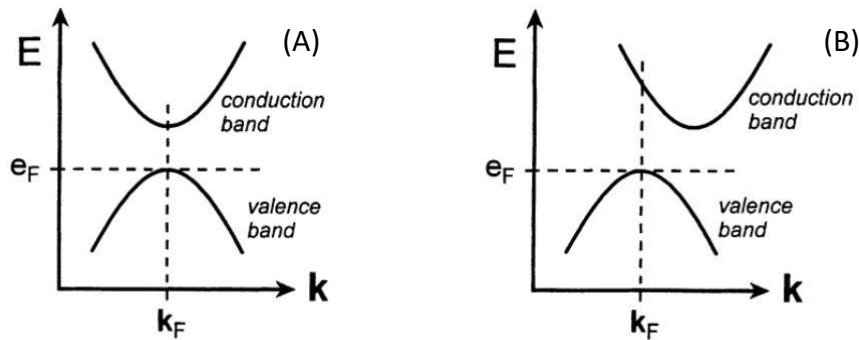


Figure 1.3: Schematic energy diagram of semiconductors (a) with a direct bandgap (b) with an indirect bandgap

### 1.1.3 The different photovoltaic technologies

A wide range of semiconductors is available for photovoltaic applications. The semiconductors are usually composed of silicon or a combination of two or three elements like the groups III-V (like GaAs or InSb), group II-VI or even group I-III-VI<sub>2</sub> (like CIGS: Copper Indium Gallium Sulfur/Selenium). Photovoltaic technologies can be separated in several generations indicated in Figure 1.4

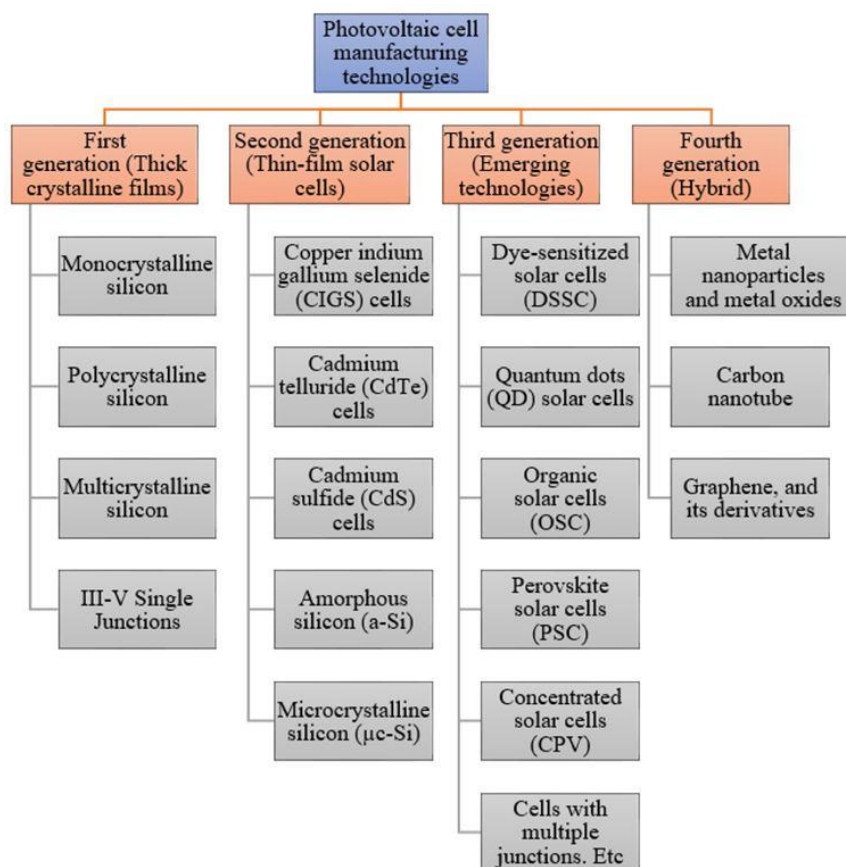


Figure 1.4: Compilation of all of the known solar cell and current developments within the fields.

Figure taken from Pastuszak J. et al<sup>9</sup>

The first generation wafer-based solar cells that use single-junction, monocrystalline and polycrystalline silicon (c-Si). This technology represented 95% of the total production in 2021 and has proven its high robustness and reliability to high temperatures and humidity, which is advantageous for commercial use even in locations often under harsh weather conditions<sup>10</sup>. However, this technology exhibits a limit in the maximum attainable power conversion efficiency and is not adaptable to mechanically flexible applications.

The second generation is thin film based solar cell regrouping devices with amorphous silicon, cadmium telluride (CdTe), gallium arsenic (GaAs), and CIGS absorber. The advantage of thin film based device compared to c-Si is a higher absorption coefficient due to their direct bandgap transition leading to a thinner thickness, from a few nanometers to tens of micrometers.<sup>9,11</sup> This technology can be well-adapted for application in modules and flexible devices. The cost of this technology is still high but these technologies are robust. GaAs devices, for example, present a record efficiency at 30%<sup>12</sup>, and a higher resistance than c-Si under harsh extrinsic conditions, making them good candidates for spatial applications, a domain in which efficiency is a priority to the cost<sup>13</sup>. The third generation regroups new emerging technologies focusing on low-cost materials and processing routes, such as nanocrystal-based devices, polymer-based cells, dye-sensitized solar cells (DSSC), and perovskite solar cells (PSC). Perovskite solar cells are one of the promising technology, for which we will explain why and what are the present challenges we need to overcome in the context of this thesis work. In particular, this technology has gained interest due to its lower and easier deposition process, compatibility with upscaling and industrialization, and a competitive power conversion efficiency reaching 25.7%<sup>12,14</sup> in 2022. Finally, a fourth generation emerged, represented by solar cells technologies using graphene and its derivatives, carbon nanotubes, or metal nanoparticles. This generation, known as hybrid inorganic, combines the low cost and flexibility of polymer thin films<sup>9</sup>.

## 1.2 Perovskite solar cells (PSC)

### 1.2.1 Development of halide perovskite thin films as absorber layers in solar cell designs

The perovskite crystallographic structure was initially associated exclusively with several oxides like  $\text{CaTiO}_3$  and  $\text{SrTiO}_3$ , leading to an  $\text{ABO}_3$  structure (A: +II, B: +IV). This material was discovered by

Institut Polytechnique de Paris

91120 Palaiseau, France



Gustav Rose in 1839 and further researched by a mineralogist, Le Perovski, who named it "Perovskite". The considerable interest in this structure is the choice of elements A and B, leading to a wide range of possible properties: superconductivity, magneto resistance, ionic conductivity and dielectric properties<sup>15</sup>.

An alternative structure of the perovskite crystal structure existed, leading to the formation of a semiconductor by replacing the metallic center B with lead or tin. This alternative was first introduced with methylammonium lead halide perovskite (MAPI) in 2009<sup>16</sup>, composed of  $\text{CH}_3\text{NH}_3\text{PbI}_3$ . This synthetic perovskite is a semiconductor capable of absorbing light, and layer thickness of less than  $1\ \mu\text{m}$  is needed to yield the same performance levels as established c-Si technologies.. Since then, the alternative family of semiconductor has been introduced in heterojunction architecture in NIP and PIN configuration. Therefore, for photovoltaic applications, we turn towards using halide-based perovskites as a novel absorber material. More generally, the crystalline structure of a perovskite material is a cubic structure  $\text{ABX}_3$ . In the case of halide perovskites, the element A is a monovalent cation, methylammonium ( $\text{MA}^+$ ,  $\text{CH}_3\text{NH}_3^+$ ), formamidinium ( $\text{FA}^+$ ,  $\text{CH}(\text{NH}_2)^+$ ) and/or cesium  $\text{Cs}^+$ . B is a divalent cation a metal site, usually  $\text{Pb}^{2+}$  or  $\text{Sn}^{2+}$ . Finally, the element X is a halide, i.e. iodide ( $\text{I}^-$ ), bromide ( $\text{Br}^-$ ) and chloride ( $\text{Cl}^-$ ). The metal halide perovskite (MHP) structure is presented in Figure 1.5. Notably, with the crystallographic A-site occupied with an organic cation (except for the case of pure alkali halide perovskites), these materials are true hybrid organice/inorganic compounds. An exchange and mixture of the various ions leads to a broad tunability of the halide perovskite materials properties.

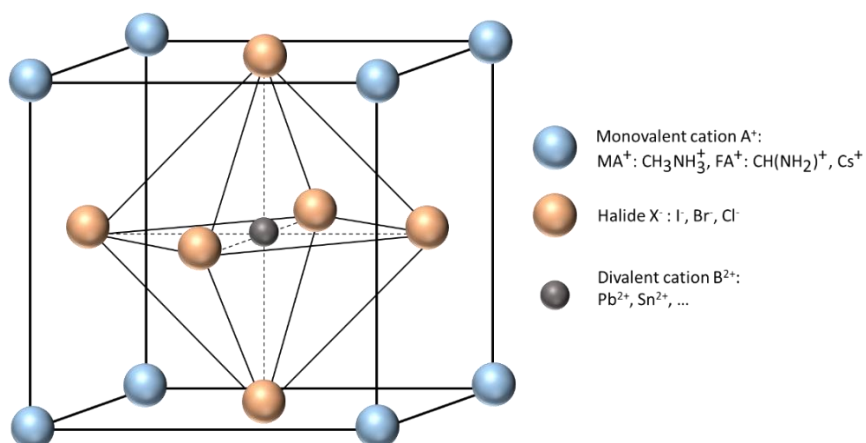


*Figure 1.5: Metal halide perovskite crystalline structure*

Using these properties, this mineral could be an introduction in solar cells as the perovskite can act as an efficient light absorber while still maintaining good transport properties of charge carriers.

PINAs said above, the first use of these perovskite absorbers in solar cells was established in 2009 by Miyasaka et al. in dye-sensitive solar cell (DSSC) architecture associated with titanium oxide (TiO<sub>2</sub>) with a power conversion efficiency (PCE) at 3.5%.<sup>16</sup> Then, Park et al. reach a higher power conversion efficiency of up to 6.5% in 2011<sup>17</sup> with MAPI quantum dots as a nanomaterial crystal. The use of the perovskite continued to evolve with the incorporation in a mesoporous device architecture as Snaith and Lee et al. from Oxford University implemented a hole transport layer (HTL) of 2,2',7,7'-Tetrakis[N,N-di(4-methoxyphenyl)amino]-9,9'-spirobifluorene (sprio-MeTOAD) and achieved a PCE of 10.9% in 2012.<sup>18</sup> Then, in just a few years, perovskite solar cells became the most rapidly evolving emerging PV technology and reached a new height of performance within just a decade. Currently, the best power conversion efficiency in the laboratory reached 25.7% in 2022 by UNIST<sup>14</sup> with a FAPbI<sub>3</sub>:0.38MDACl<sub>2</sub> (methylenediamine dihydrochloride).

## 1.2.2 Properties of mixed cation halide perovskite

### 1.2.2.1 Crystallinity

In recent formulation developed, the triple cation halide perovskite is named a hybrid compound: in the crystalline structure, the A site corresponds to a mix of organic methylammonium and formamidinium molecules and an inorganic cesium element. As the element/molecule size is relatively small, the crystal structure does not change depending on the chosen element/molecule. The B site corresponds to the metallic center of lead in our case. The ionic radius is fixed at  $1.19 \times 10^{-10}$  m. The X site is linked to a mix of halide with iodine and bromine. Depending on the ionic radius, the crystal structure of the perovskite can be affected. To predict the futur structure, we can calculate the Goldschmidt tolerance factor.

The Goldschmidt tolerance factor is a simple calculation that can determine the total crystal organization consistency of the ABX<sub>3</sub> perovskite. It corresponds theoretically to:  $t = \frac{R_A + R_X}{\sqrt{2}(R_B + R_X)}$ ; with R<sub>A</sub>, the radius of the element or molecule on the A-site, R<sub>B</sub>, the radius of the element on the B-site, and R<sub>X</sub>, the radius of the element on the X-site.

Chemical group	Ionic radius (m)
Cl <sup>-</sup>	1.81E-10
Br <sup>-</sup>	1.96E-10
I <sup>-</sup>	2.20E-10
Cs <sup>+</sup>	1.67E-10
Pb <sup>2+</sup>	1.19E-10
MA <sup>+</sup>	2.17E-10
FA <sup>+</sup>	2.53E-10

$$t = \frac{R_A + R_X}{\sqrt{2}(R_B + R_X)}$$

APbX <sub>3</sub>	Cs <sup>+</sup>	MA <sup>+</sup>	FA <sup>+</sup>
Cl <sup>-</sup>	0.820	0.938	1.023
Br <sup>-</sup>	0.815	0.927	1.008
I <sup>-</sup>	0.807	0.912	0.987

Table 1.1: (left) Ionic radius of the possible used elements in the lead halide perovskite and (right) Goldschmidt tolerance factor for some lead halide crystalline structure with the equation

This factor primarily governs the organization of the perovskite crystalline structure with MA<sup>+</sup> and FA<sup>+</sup>.<sup>19</sup> If the tolerance factor range from  $0.8 < t < 1.1$ , the crystalline structure arrangement is cubic. The elements A and B are not the same size, but depending on the combination, these elements' ratios can reach an ideal value of 1.

The perovskite structure is also influenced by the temperature fabrication coming from its enthalpy calculation<sup>19</sup>. ' 'Let's take the classic example of MAPI. An orthorhombic structure is formed and stable at low temperatures ( $T < 165$  K), adopting a Pnma space group. With an increase of the temperature ( $165 \text{ K} < T < 327 \text{ K}$ ), MAPI goes through its first-order phase transition from orthorhombic to tetragonal space group I4/mcm. The cation is no longer stable in the orthorhombic phase and moves from its initial position. At a higher temperature ( $T > 327 \text{ K}$ ), MAPI undergoes its second-order phase transition from tetragonal to cubic space group  $Pm\bar{3}m$ . The tetragonal phase becomes more isotropic with  $\frac{c}{2a}$  closer to 1 and the molecular disorder increase as well up to this transition.

The crystal structure of perovskite also influences the material's and device's performance and properties. For the device, it is mandatory to form a cubic perovskite layer with FA<sup>+</sup>. In the tetragonal phase, these perovskite crystal structure loses their hallmark properties, such as their high absorption coefficient in the UV-Vis range. For FA<sup>+</sup>, in a tetragonal structure, the perovskite switches to a yellow non-absorbant layer, leading to a non-functional solar cell.

### 1.2.2.2 Energy band gap

As mentioned before, the energy band gap is the minimum energy needed to excite and produce an electron-hole pair between the valence and conduction bands. As perovskite is used in a device, one of the governing models is the Shockley-Queisser limit<sup>20</sup>. This principle states that a single-junction solar cell is limited to a power conversion efficiency of 33% for a maximum band gap of 1.34 eV<sup>20</sup>. Thanks to its tunable composition, the perovskite band gap can range from 1.15 eV to 3.06 eV<sup>21</sup>. The perovskite is hence a good candidate as a versatile absorber material, for instance in multijunction devices that require adapted band gaps. In our case of the triple cation halide perovskite solar cells  $\text{Cs}_{0.05}(\text{FA}_{0.83}, \text{MA}_{0.17})_{0.95}\text{Pb}(\text{Br}_{0.17}, \text{I}_{0.83})_3$ , the band gap is at 1.55 eV.

Contrary to the silicon solar cell, the material's band gap is direct, meaning the valence band's highest point and the conduction band's lowest point are aligned with each other. As a consequence, for the same efficiency, the perovskite thin film thickness is around 300 nm to 900 nm while the silicon thickness is 1000 times more due to silicon's low absorption coefficient.

### 1.2.2.3 Carrier transport

The diffusion length of charge carriers is linked to the carrier lifetime, which photoluminescence measurements can determine. The diffusion length ( $L_D$ ) indicates the travel distance of free carriers before possible recombination, while the carrier's lifetime ( $\tau$ ) is the time between generation and recombination of carriers. Those two parameters are linked through this equation:  $L_D = \sqrt{D\tau}$  with  $D$ , the diffusion coefficient, which is itself linked to the carrier mobility ( $\mu$ ):  $D = \mu \frac{kT}{e}$  with  $k$ , the Boltzmann constant,  $T$ , the temperature (K) and  $e$ , the elementary charge. The photogenerated carriers travel through the material to reach the charge transport layer, where they are extracted. This indicates that having a long diffusion length to travel through the absorber is generally desired as we reduce the possibility of recombination in the absorber.

The electrons and holes diffusion lengths are one of the assets of the high efficiency of perovskite solar cells. These diffusion lengths can exceed 100 nm to 1  $\mu\text{m}$  for some chlorine-doped mixed halide as indicated by Stranks et al.<sup>22-24</sup>. This is an improvement compared to the organic solar cells with a diffusion length usually ten times lower.

The charge mobility ( $\mu$  in  $\text{cm}^2/\text{Vs}$ ) describes the carrier movement in a material in a given direction under an electrical field. The charge mobility average is around 10  $\text{cm}^2/\text{V}$  to a few tens of  $\text{cm}^2/\text{Vs}$  either with electron or hole charge mobility. The higher the charge mobility, the longer the carrier can travel in the semiconductor.

Institut Polytechnique de Paris

91120 Palaiseau, France



### 1.2.3 Architectures of perovskite solar cells PSC

The evolution of the perovskite solar cell was made possible thanks to incremental progress of the device architecture design. The most prevalent type of devices can be roughly divided into three categories of structures: mesostructured NIP, planar NIP, and planar PIN. The name originates from the nature and organization of the stacked layers that constitute the cell, from the bottom to the top. The perovskite layer is typically an intrinsic layer and is sandwiched between an electron transport layer, ETL, N for n-type, and a hole transport layer, HTL, P for p-type. The following figures are the three commonly used architectures for the perovskite solar cell in Figure 1.6.

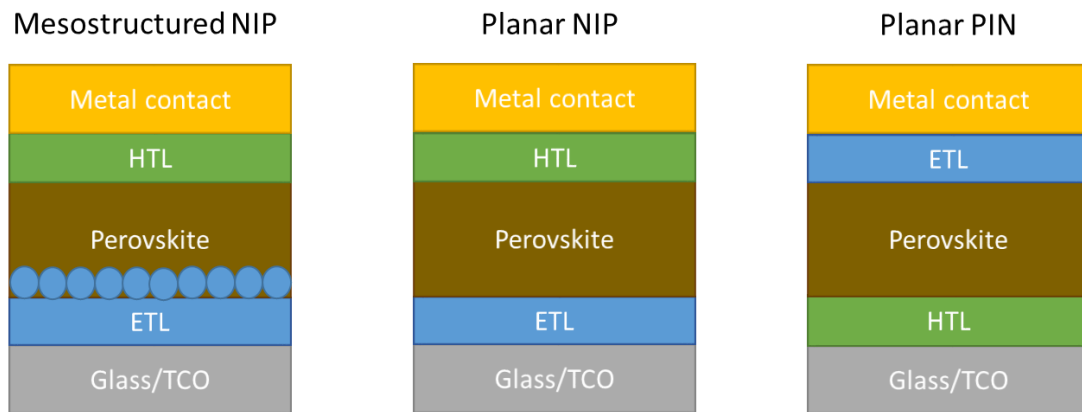


*Figure 1.6: Perovskite solar cell architectures commonly used*

The mesostructures NIP architecture consists of a stack Glass/TCO/ETL/meso-ETL/Perovskite/HTL/Metallic contact. The mesoporous method was used to increase the surface efficacy of the ETL ( $\text{TiO}_2$ ,  $\text{Al}_2\text{O}_3$ , ...). The ETL has to act as a blocking for the holes. Furthermore, it needs to have a compatible LUMO level with the conduction level of the perovskite layer.<sup>22</sup> This ETL meets these criteria as it presents high thermal stability and can be produced at low cost, while its energy level positions are well suited for electron extraction and hole blocking, as presented in Figure 1.7. The mesostructured architecture is completed with the deposition of the perovskite layer and of the HTL layer on top. The HTL is usually a molecule that can act as a blocking layer for the electrons. Consequently, it should fill several requirements: high hole mobility, good solubility in organic solvents, and a compatible HOMO level with the valence level of the perovskite layer. The usual HTLs used are spiro-MeOTAD, poly(triarylamine) (PTAA) and copper thiocyanate (CuSCN) as a new addition. The device is finalized with a metallic contact as gold (Au) or silver (Ag) on top. Snath and Lee et al.<sup>18</sup> first used the mesoporous NIP configuration. Effectively as a development out of

the classical DSSC design, Lee et al. used MAPI in this architecture with a mesoporous  $\text{TiO}_2$  as ETL and spiro-MEOTAD as an HTL, which led to an efficiency of 10.9% in 2012.<sup>18</sup>

One of the issues with the mesostructured configurations is the lack of compatibility with developing large-scale solar cells. Most techniques like spin-coating or spray-pyrolysis are more efficient on a laboratory scale than on an industrial scale. Furthermore, much development is going toward the tandem perovskite solar cell: Perovskite/Si or Perovskite/CIGS. For tandem solar cells, the surface roughness should be limited to reduce the possible formation of pinholes or crack. Therefore, optimization has gone preferentially to the development of the planar architecture.

The planar architecture is possible in both NIP and PIN configurations. In NIP configuration, the sample stack is Glass/TCO/ETL/Perovskite/HTL/Metallic contact. The PIN configuration is also called “inverted” because the order of the ETL and HTL in the layer stack is effectively inverted from bottom to top of the perovskite layer. The configuration favors techniques like atomic layer deposition or blade coating to move toward the industrialization of the devices.  $\text{SnO}_2$  or  $\text{ZnO}$  became attractive candidates for ETLs in NIP configuration thanks to their charge carrier mobilities several orders higher than titanium dioxide ( $\text{TiO}_2$ ).<sup>25</sup> However, particularly in the case of  $\text{ZnO}$ , potential chemical reactions with the halide perovskites can lead to the etching of the  $\text{ZnO}$  and degradation of the layer. The perovskite layer is sandwiched with an HTL, either PTAA or spiro-MeOTAD. In PIN configuration, the deposited HTL could be  $\text{NiO}$  or PTAA. The perovskite is deposited the same way. In this stacking sequence,  $\text{TiO}_2$  from the spray-pyrolysis process is no more compatible as ETL due to its high-temperature deposition ( $400^\circ\text{C}$ )<sup>26</sup> in contrast with the perovskite supporting a maximum temperature  $150^\circ\text{C}$ .<sup>27,28</sup> The deposition goes toward spin-coating deposition, ALD or co-evaporation deposition of [6,6]-phenyl-C61-butyric acid methyl ester (PCBM), fullerene ( $\text{C}_{60}$ ), bathocuproine (BCP) or aluminium-doped zinc oxide ( $\text{ZnO:Al}$ ). The device is completed with a metal contact of silver or gold.

The layer chosen depends on the band alignment compatibility between the CB and VB of the perovskite and the CB and VB or HOMO and LUMO levels of the charge transport layers as indicated in Figure 1.7.

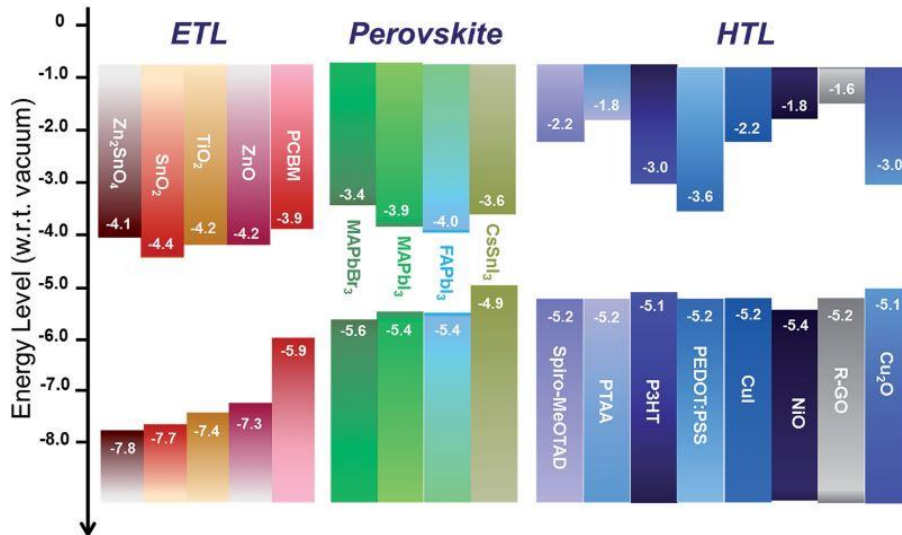


Figure 1.7: Literature values for the energy levels with respect to the vacuum level of different materials which act as electron-selective (left), perovskite absorber and hole-selective layers (right) in perovskite solar cells taken from Zardetto *et al*<sup>29</sup>

## 1.2.4 State of the art

The architecture of the solar cells are presented with several charge transport layers. The cells also change with the evolution of technology and its requirements. Here, I present the state of the art of the usually employed HTL and ETL to showcase the diversity of the cells with a focus on NIP technologies. The charge transport layers are a crucial part of the perovskite solar cell to produce the built-in potential in the device and to extract the carriers<sup>30</sup>. The energy level alignment is needed to ensure a sufficient open-circuit voltage and an efficient carrier extraction. We also need to consider durable materials and chemically compatible materials to ensure the long-term stability of the device.

### 1.2.4.1 Hole transport layer (HTL)

The hole transport layer is used to collect holes and as a blocking layer for the electrons. The most commonly used HTL is the (spiro-MeOTAD) for the NIP configuration and the poly(3,4-ethylenedioxythiophene):poly(styrene sulfonate) (PEDOT:PSS) for the PIN configuration. These two HTLs present a good energy band alignment and carrier mobility, which explains their fair implementation in perovskite solar cells<sup>18,31–36</sup>. The spiro-MeOTAD is a small molecule used in DSSC and incorporated into perovskite solar cells. As its carrier mobility is lower than the perovskite by

three orders of magnitude, the spiro-MeOTAD thickness should be smaller to reduce losses due to high series resistance. One way to improve the conductivity and the physical properties of the spiro-MeOTAD is the doping of the material. The HTL is then doped with molecules: FK209 (tris[2-(1H-pyrazol-1-yl)-4-tert-butylpyridine]cobalt(III) tris(bis(tri-fluoromethylsulfonyl)imide)] (Co), lithium bistrifluoromethanesulfonimide (LiTFSI), 4-tertbutylpyridine (tBP). Thus, the spiro-MeOTAD's Fermi level shifts toward the HOMO, which is favorable for the band gap alignment. One interesting mechanism of the spiro-MeOTAD is the oxidation. This phenomenon is due LiTFSI causing the HTL to be oxidized by the oxygen or by an intermediate oxidation of the perovskite leading to possibly a spiro-MeOTAD<sup>+</sup>TFSI<sup>-</sup> molecule. This molecule is weakly bounded within each other due to its high delocalized charge on TFSI<sup>-</sup>, improving the conductivity<sup>37</sup> and the performance of the perovskite solar cell. Thus, oxidation of the spiro-MeOTAD for a few days under limited exposure to ambient air is beneficial to increase the performance. However, this eventually leads to issues concerning the long-term stability of the device under longer exposure. In longer exposure, the product spiro-MeOTAD<sup>+</sup> continues to be formed, linked to a constant degradation of the spiro-MeOTAD.<sup>37</sup> As the ratio spiro<sup>+</sup>/spiro (%mol) increase, the device performance decrease. In addition, these two HTLs are organic molecules sensitive to moisture and humidity. In high humidity conditions, due to the presence of cracks, the water can penetrate and degrade the perovskite layer.

This leads us to searching for alternatives for the HTLs. The polymer poly[bis(4-phenyl)(2,4,6-trimethylphenyl)amine] (PTAA) is another solution as a NIP, which was first reported by Heo et al.<sup>38</sup> and Noh et al.<sup>39</sup>. PTAA is similar to the spiro-MeOTAD for its thermally stable amorphous morphology, its solubility in a wide range of organic solvents and its good band alignment with the perovskite. Similarly, PTAA can be doped to ensure its electronic properties with LiTFSI and tBP. Consequently, the Fermi level in the PTAA film moves toward the HOMO with increasing doping concentration. The PTAA can be used either in NIP and PIN configuration and is mostly optimized for thickness with minimized resistive. It does not need to be oxidized for a few days at low air exposure compared to spiro-MeOTAD as it is already optimized. Under moisture, Yang et al<sup>40</sup> shows that PTAA slowed down the degradation of the MAPI, as contrary to the spiro-MeOTAD deposited layer, there were pinholes and gaps but no cracking in the PTAA layer. This indicates a better moisture stability comparing the spiro-MeOTAD. This could be linked to the hygroscopicity of LiTFSI, which is usually incorporated in a higher concentration in spiro-MeOTAD. However, exposed to high temperatures in air at 85°C, samples degraded faster with PTAA than spiro-MeOTAD.

As some groups want to focus on full inorganic perovskite solar cell, another alternative exists for the PIN or NIP configuration. The DSSC field introduced copper thiocyanate (CuSCN) and copper iodide (CuI) as solid hole-conducting materials. This alternative CuI was first introduced by Christians et al.<sup>41</sup> with a PCE of 6% with CuI in mesoporous NIP configuration. Then, it was adapted for planar PIN configuration by et al. Another lab also worked with CuSCN, for the first time in mesoporous NIP configuration, with a PCE of 4.85%<sup>42</sup>. CuSCN showcases higher stability than the spiro-MeOTAD-based perovskite solar cell, which is not sensitive to humidity but with a PCE limited at 12.4%<sup>43</sup>. In addition, Pb present in the mesoporous TiO<sub>2</sub> is retrieved in the CuSCN after the coating, indicating Pb dissolution.<sup>43</sup> Through this dissolution, short-circuit can be present due to interdiffusion. CuSCN and CuI working as HTL interact through their anion SCN<sup>-</sup> and I<sup>-</sup>. These anions can replace or exchange with halide from the perovskite and potentially form new perovskite crystals. Nickel oxide (NiO<sub>x</sub>) is also another alternative HTL for inorganic HTL. NiO<sub>x</sub> presents high chemical stability and a deep valence band. This material can be brought in nanoparticles or formed through sputtering, ALD, or in a controlled-temperature oven<sup>44,45</sup>. This layer has been used before in CdS thin film solar cell.

#### **1.2.4.2 Electron Transport Layer (ETL)**

The electron transport layer is a n-type material for extracting the electrons at the back contact of the device thereby completing the electrical circuit in the device. The material differs depending on the configuration. In NIP configuration, the most-applied material is TiO<sub>2</sub>. This material is used thanks to its high thermal stability, low cost and good band alignment energy. The material, as explained above, has a low electron mobility (0.1 to 10 cm<sup>2</sup>/(V.s)) in comparison to the perovskite layer, which could limit the electron transport and increase the probability of charge recombination<sup>25</sup>. To improve the ETL efficacy, an hybrid configuration combining a mesoporous and a compact TiO<sub>2</sub> layer. The mesoporous layer is placed on top The compact electrode role is to protect the back contact. The mesoporous layer is in contact with the perovskite solution, which also fills the pores and increases, effectively increasing the ETL/HaP interface area. This ETL configuration works well and constitutes the mesoporous NIP structure. However, due to its high-temperature process, and instability under UV light, the adaptability of such TiO<sub>2</sub> layers for the large-scale device and commercialization remains limited. Another alternative is tin oxide (SnO<sub>2</sub>). This

layer has properties similar to  $\text{TiO}_2$ , and its electron mobility is higher by 2 orders of magnitude (up to  $240 \text{ cm}^2/(\text{V.s})$ )<sup>25</sup>. This layer can be used in the planar NIP configuration as well.

In PIN configuration, the ETL deposition process must be compatible with the perovskite layer, especially with respect to low temperature ( $< 150 \text{ }^\circ\text{C}$ ) deposition and compatibility with organic solvents. Fullerene as [6,6]-phenyl- $\text{C}_{61}$ -butyric acid methyl ester (PCBM) or  $\text{C}_{60}$  can be used. Present in several publications<sup>46–48</sup>, PCBM and  $\text{C}_{60}$  are n-type materials that can be used as an ETL. The ETL layer can additionally play the role of charge trap passivation at the surface and the grains boundaries, reducing the hysteresis in the device j-V characteristics. Furthermore, it can work as a protective layer for moisture and help the device to improve its long-term stability<sup>48</sup>.

Again, other metal oxides can be used as ETL, such as for instance zinc oxide ( $\text{ZnO}$ )<sup>49–52</sup>. This can be used with PCBM as an interlayer to mitigate chemical reactivity of the  $\text{ZnO}$  film with the perovskites as discussed above or it can be used on its own doped with aluminium.<sup>28</sup> This is thanks to PCBM's properties that make it a good hole-blocking layer: suitable band energy alignment, low cost, and good transparency. Several fabrication methods are available, from a solution process method for lab-scale samples to atomic layer deposition from industrial-scale samples.

As shown in this section, a wide range of charge transport layers is available depending on the desired architecture of the perovskite solar cell and the cumulatively beneficial properties of the HTL and ETL layers. Our focus is on the initial NIP configurations: glass/FTO/compact-mesoporous  $\text{TiO}_2$ /HaP/Spiro-MeOTAD/Gold and glass/FTO/ $\text{SnO}_2$ /HaP/Spiro-MeOTAD/Gold. As explained above, issues arise with the use of this configuration: degradation, surface defects, and charge recombination. To this end, interface design is a key point in order to remedy these weaknesses and improve the device's performance and stability. The next paragraphs will present in more details the main concerns that the perovskite solar cell technology faces, and will introduce the critical role of the perovskite/ETL and perovskite/HTL interfaces. These contextual elements will introduce the current research project, its aims, and the strategy proposed, which rely on interfaces engineering.

### 1.2.5 Issues and challenges

The perovskite solar cells present a variety of architecture and options for their composition and are one of the emerging technologies in the last decade. Thanks to the rapid evolution of this technology, a power conversion efficiency of 25.9% was obtained for the single-junction cell,

Institut Polytechnique de Paris

91120 Palaiseau, France



challenging the performance of silicon heterostructure cells at 26.8% and the silicon single crystal at 26.1%. However, to this date, these devices exhibit several shortcomings and limitations for industrialization.

### 1.2.5.1 Upscaling

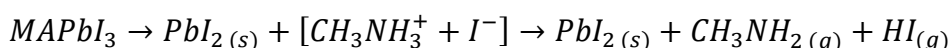
The current record was obtained on a millimeter scale. However, as the size of the device increase, the performance decreased and failing between 18% of efficiencies. This decrease in efficiency is due to multiple factors: increase of the series resistance, lower shunt resistance, and non-uniformity of the material on large areas<sup>53</sup>. To effectively mitigate these performance losses, technologies need to be transferred to large-scale deposition methods that are compatible with large-scale, i.e. going from spin-coating deposition<sup>33,54</sup> to atomic layer deposition<sup>29</sup>, electrodeposition, slot-die coating<sup>55</sup> or blade coating<sup>56</sup>. Furthermore, the materials should be taken in account. Low temperatures method process are mandatory for the perovskite fabrication. These changes can help to improve the technologies toward the tandem solar cells, flexible solar or integrated perovskite solar cells.

### 1.2.5.2 Stability

The other main task is to improve their stability to move toward the device's industrialization. Perovskite is known for its record performance but also for its materials instability. More and more publications showcases devices maintaining the electrical performances after 1000 hours of sun illumination and controlled high humidity<sup>57-60</sup> with no encapsulation. However, to reach this level, we need to take into account that the perovskite solar cell is sensitive to extrinsic factors (temperature, humidity, light exposure) and intrinsic factors (defect and interface).

#### 1.2.5.2.1 Extrinsic factors

The temperature factor has been explained in **1.2.2.1 Crystallinity**. For MAPI, the temperature changes the crystal structure from cubic to tetragonal. However, it does not damage its photoactive properties within the temperature range -15°C to 65°C, thanks to its tolerance factor 0.912. Nevertheless, temperature sensitivity becomes more prevalent at high temperatures, leading to the decomposition of the MAPI into  $PbI_2$ , MAI and HI<sup>15,61</sup>.



The temperature affects the crystal structure of the FA-based and Cs-based perovskite. Depending on the crystal formed, the perovskite changes its structure from a cubic photoactive black phase to a tetragonal yellow phase<sup>61</sup>. Mixing the cations to a triple cation composition is possible a yield

excellent results for high-performance devices.<sup>19</sup> A mixed with Cs and FA helps to reach an ideal pseudo tolerance factor, and coupling MA increases the cristal stability to temperature.

Humidity<sup>61</sup> is another factor to consider concerning the perovskite layer's extrinsic instability. First, it mostly comes from the corrosion of the perovskite layer in the presence of oxygen. As known, the layer is composed of lead which can be oxidized to form lead oxide. For instance, this process has been observed in films of triple cation mixed iodide-bromide lead perovskites exposed to ambient atmosphere illumination.<sup>62</sup> This phenomenon justifies the fabrication of the lead halide perovskite solar cells under a nitrogen atmosphere to avoid humidity and oxygen contamination. Water can lead to the formation of monohydrate and dihydrate perovskites as the molecules can form strong hydrogens bonds with the cations.<sup>63</sup> It weakens the bond between the cation and the  $\text{PbI}_6$  octahedron, which favors the deprotonation of the cation and the effect of extrinsic factors such as temperature. In the end, the degradation of the perovskite layer is accelerated.

A solar cell needs to be operational for more than 20 years for commercialization. However, direct light exposure also affects the PSC degradation as indicated in the previous paragraph. Furthermore, the extra energy from the supra-bandgap illumination can induce the breaking of bonds in the perovskite structure and generate halogen-vacancy/halogen interstitial pairs that allow the halogen to migrate in the perovskite solar cells.<sup>64</sup> While devices have become increasingly resilient to this effect due to compositional stabilization efforts,<sup>65</sup> with several publications stating that no photocurrent changes on the perovskite device after hundreds of hours of operation,<sup>66,67</sup> modifications still occur on the perovskite structure, such as halide segregation, ion migration or compositional degradation. One publication states that the compositional structure changes occur in the mixed lead halide perovskite solar with  $\text{Br}^-$  and  $\text{I}^-$  ions rich phase occurring under light exposure.<sup>68</sup> These changes could be irreversible depending on the stack of the layers. Domanski et al.<sup>69</sup> expose significant changes in the compositional distribution after several hours of illumination, which resulted in a performance drop of up to 15% of the initial efficiency after 100 hours, which was due to a redistribution of the A-site cation; a mechanism that has been suppressed by the choice selection of interlayers, for example by Christians et al.<sup>66</sup>

### 1.2.5.2.2 Intrinsic factors

Perovskite solar cells are furthermore subject to intrinsic factors, such as ion migration, electro-migration, and interfacial reactions,<sup>34</sup> that affect their stability and, thus, their composition and performance over time. The effect of ion migration mainly manifests for the halide anions but can also affect the A-site cation. The following types of defects are predominantly related to this with the presence of several types of defects: Schottky defects, Frenkel defects, and impurities<sup>70</sup>. Schottky defects come on the vacancies or stoichiometric 'vacancies' pairs, which provide a spot for ion migration. Frenkel defects are lattice vacancies mixed with their corresponding interstitial ions in the crystal lattice.

The interface is one of the main factors of perovskite solar cell degradation but also one of the main contributors to the operation of the device<sup>30,71</sup>. Since the device stack is composed of layers with different chemical elements, molecules, and crystal structure, even in the case of perfectly flat surfaces, it is impossible to perfectly line up the approximately  $10^{14}$  bonds/cm<sup>2</sup> that would be forming at an ideal interface. This inadvertently leads to the creation of interfacial defects, which can be energetically located deep in the gap of the material, causing an increase of non-radiative recombination in the interface region.

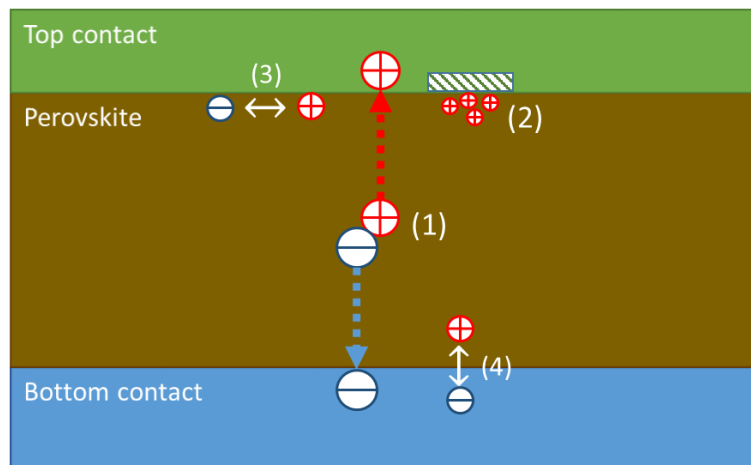


*Figure 1.8: Interface-related loss mechanisms in the device after light-induced excitation. Figure redrawn from<sup>71</sup>*

Thus, the relevant losses in the working principle of a simplified perovskite solar cell can be summarized in four steps depicted in Figure 1.8.: (1) First, the photogenerated charge carriers diffuse in the absorber toward their respective charge transport layer (1). With the present quality of the absorber layer this process occurs with only negligible losses that would be attributed to bulk

recombination. (2) Once the carriers reach the interface, they can encounter an energetic barrier as would be the case for non-ideal band alignment, e.g., an offset between CBs, or VBs, between absorber and transport layer, for electron and hole extraction, respectively. (3) Aside from non-ideal band alignment, the presence of interfacial defects can lead to non-radiative recombination of the photogenerated carriers, as discussed above. (4) Finally, back recombination can occur at the interface of carriers that were already extracted to the charge transport layer, with carriers still residing in the absorber layer if the carriers are not transferred away from the interface fast enough. The interface quality is hence a key point for the carrier dynamic and serves as a charge-selective layer in an ideal device. Our goal is to reduce non-radiative recombination and thereby improve the device by reducing the energy loss at the interface.

### 1.2.6 Perovskite solar cell development – A focus on interface optimization

The interfaces have been widely studied, leading to improving the devices' performances and stabilities.<sup>72</sup> The architecture of solar devices becomes increasingly complex, multiplying the stacked layers and thus interfaces role, emphasizing the need to master them as in Figure 1.9.

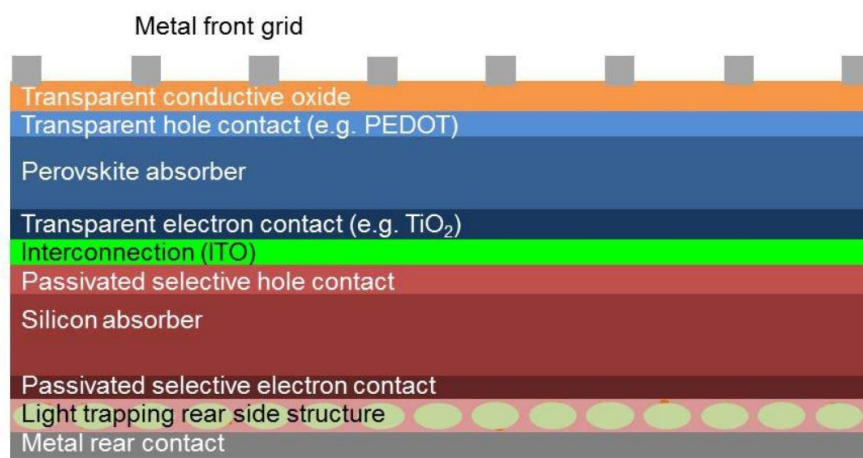


*Figure 1.9: Example of a two-terminal perovskite silicon tandem solar cell with advanced optics using light trapping at the rear by Fraunhofer ISE<sup>73</sup>*

As laid out above, the interface usually suffers from structural mismatch, non-ideal energy level alignment, and interface defects. Incorporation of HTL and ETL for perovskite technology is nowadays unavoidable. Thanks to the research conducted on the charge transport layer and the perovskite layer itself, significant improvements of the stability and of the efficiency of the perovskite solar cells have been realized. Further progress on this end can be achieved by

Institut Polytechnique de Paris

91120 Palaiseau, France

incorporating additional and adapted interfacial layers. The role of these interfacial layers consists in helping the adjustment of the energy band alignment and acting as a blocking layer for the opposite type of carriers (holes or electrons), i.e. charge selectivity, or as protective layer against humidity to enhance stability.

At the ETL/HaP interface, the ETL, as a metal oxide, exhibits surface defects and dangling bonds as a main cause of undesired charge recombination. The surface passivation helps to decrease the surface defects, to improve the carrier transport from the HaP to the ETL, and develop a more compatible surface between the perovskite layer and the ETL. One primary way for the interface passivation is the use of self-assembled monolayers (SAMs). This route consists of functionalizing organic molecules anchoring on the surfaces by adsorption, which organize themselves on the surface, as in Figure 1.10.

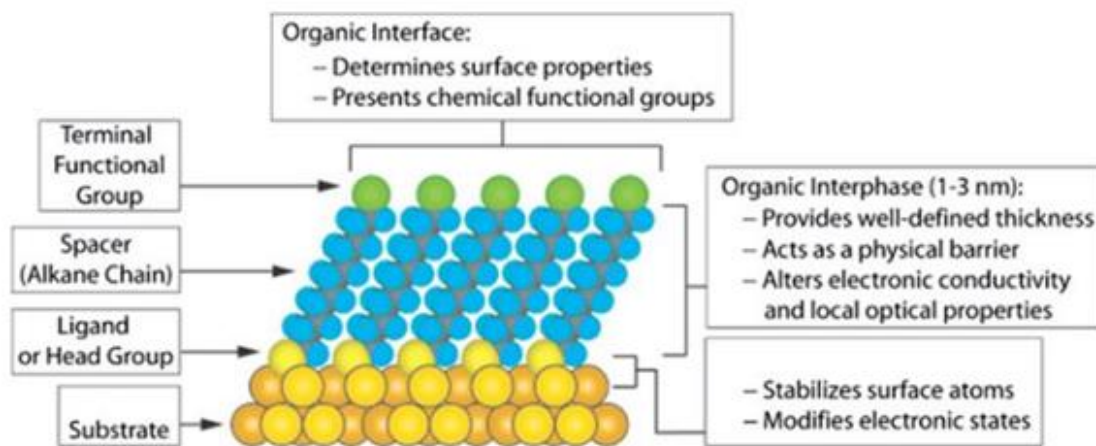


Figure 1.10: Self-assembled molecule ideal configuration at the interface ETL/HaP. Taken from Qiao et al<sup>74</sup>

The functionalized molecule comprises three parts<sup>75</sup>: a head group, a functional group and a spacer. First, the head group anchors to the metal oxide through adsorption. The anchored group is usually a carboxylic, phosphonic, hydroxyl or sulfonic acid group. In addition to attaching the molecule to the surface these groups also passivate specific defect sites, such as oxygen vacancies, in the metal oxide and coordinate the surface. Then, the functional group interacted chemically with the perovskite layer, directly influencing the surface, interface, and properties. The functional group can interact and bond with the vacancy sites in the perovskite layer. The tunability of the surface change

depends on the group and modifies the work function as well as the surface polarity. Usually, the functional group contains amine-based moieties and ammonium salts to match the perovskite's chemical properties by interacting with the cation vacancies. Finally, the tail links the two groups in the organic molecule. The spacer can be an alkyl or aryl chain. Depending on the length and configuration, it can play on the molecule polarity, fabrication process, and charge transport<sup>76</sup>. The molecules do not need to form perfect SAM to have a beneficial impact on the device. The molecule characteristics are the same properties to anchor on the metal oxide or the perovskite layer<sup>55</sup>, to be a doped layer or thin enough<sup>77</sup> to ensure the carrier charge transport. The only change is if the molecules keep a surface orientation or not.

In the ideal case, at the HaP/HTL interface, the perovskite layer would then be passivated through the chemical interaction with the surface vacancies and protected by the molecules from the ingress of other extrinsic species, such as moisture or oxygen. As mentioned in the previous section, the perovskite layer is sensitive to intrinsic and extrinsic factors. Protecting the top surface of the perovskite thus leads to an additional improvement of the device stability. The molecules interacting with the perovskite are similar to the functional group from the self-assembled monolayer, with the same chemical interactions. The passivation can be done with several types of molecules using PCBM and its derivatives, Lewis base<sup>78</sup> molecules such as thiophene or pyridine, or organic materials with hydrophobic properties to protect the perovskite layer.

### 1.3 Main objectives and structure of this thesis

The main objective of this dissertation concerns the interface design between the HaP and the adjacent transport layers by developing innovative interface passivation strategies. As described above, many ways exist to passivate the perovskite layer and enhance the interface formation. For instance, in some collaborative work, I investigated the use of phosphonic acid SAMs at the ETL/HaP interface to improve the charge transport between the ALD-deposited TiO<sub>2</sub> or ZnO and the perovskite, focusing on the deposition method of the SAMs, which was an introduction to the issue of interface optimization.<sup>76</sup>

For my thesis work presented here, one of the key goals was to improve the stability of the HaP layer fabricated in IPVF by protecting it against humidity while at the same time reducing charge recombination at the HaP surface and consequently improving the overall performances of the perovskite solar cell.

These different strategies considered are presented in Figure 1.11, which recapitulates the key research activities pursued during this thesis. Several trials and possibilities have been tested during this thesis to reach this objective, and I will present in this manuscript the most promising results with the following interlayers: adamantane and its derivatives as molecular interlayer at the HaP/HTL interface (*Chapter 3*), aminocarboxylic acids SAM to improve the ETL/HaP interface (out of a collaboration with the team from Prof. Philippe Lang at ITODYS; *Chapter 4*), and PMMA:PCBM interlayer at both perovskite/CTL interfaces(*Chapter 5*).

Thus, the first research axis of this dissertation is focused on the protection of the perovskite layer from humidity through surface passivation. Indeed, in the device, a critical point is the the perovskite instability toward humidity and moisture through the incorporation of oxygen and water. From the literature<sup>79</sup>, we identified the bulky, mostly inert, and hydrophobic organic molecule adamantane as a promising candidate for such an interlayer. Specific derivatives of adamantane contain an amino site which would be well suited to occupy A-site cation vacancies at the perovskite surface. The aim was to use this additive layer at the HaP/HTL interface with the detailed study being presented in *Chapter 3*.

Then, I had the opportunity to further explore the insertion of SAMs at the ETL/HaP interface, which was established through a collaboration with ITODYS (Interfaces Traitements Organisation et DYnamique des Systèmes), a laboratory in Paris, France, and more especially a collaboration with Institut Polytechnique de Paris

91120 Palaiseau, France



the " Organisation Moléculaire Nano2D" ( OMNa2D) team as one of their field of expertise is in organic electronics and in particular the control of interfaces by SAM grafting on metal oxides. This collaboration aimed to graft SAMs of amino carboxylic acids on the ETL layer (TiO<sub>2</sub>) and evaluate the impact of this adaptation on the efficiency of PSC devices in NIP configuration device on the open-circuit voltage and the current density. (see, *Chapter 4*).

Finally, interface passivation by PMMA and PCBM<sup>36,77</sup> was reviewed. The novelty of the present approach resides in a double passivation of the perovskite layer: (1) PMMA deposition at HaP/HTL interface and (2) PMMA:PCBM deposition at ETL/HaP interface, operating as an internal encapsulation of the perovskite layer. This work was done in the frame of a M2 internship that I supervised (Peng BAI student) and is presented in *Chapter V*.

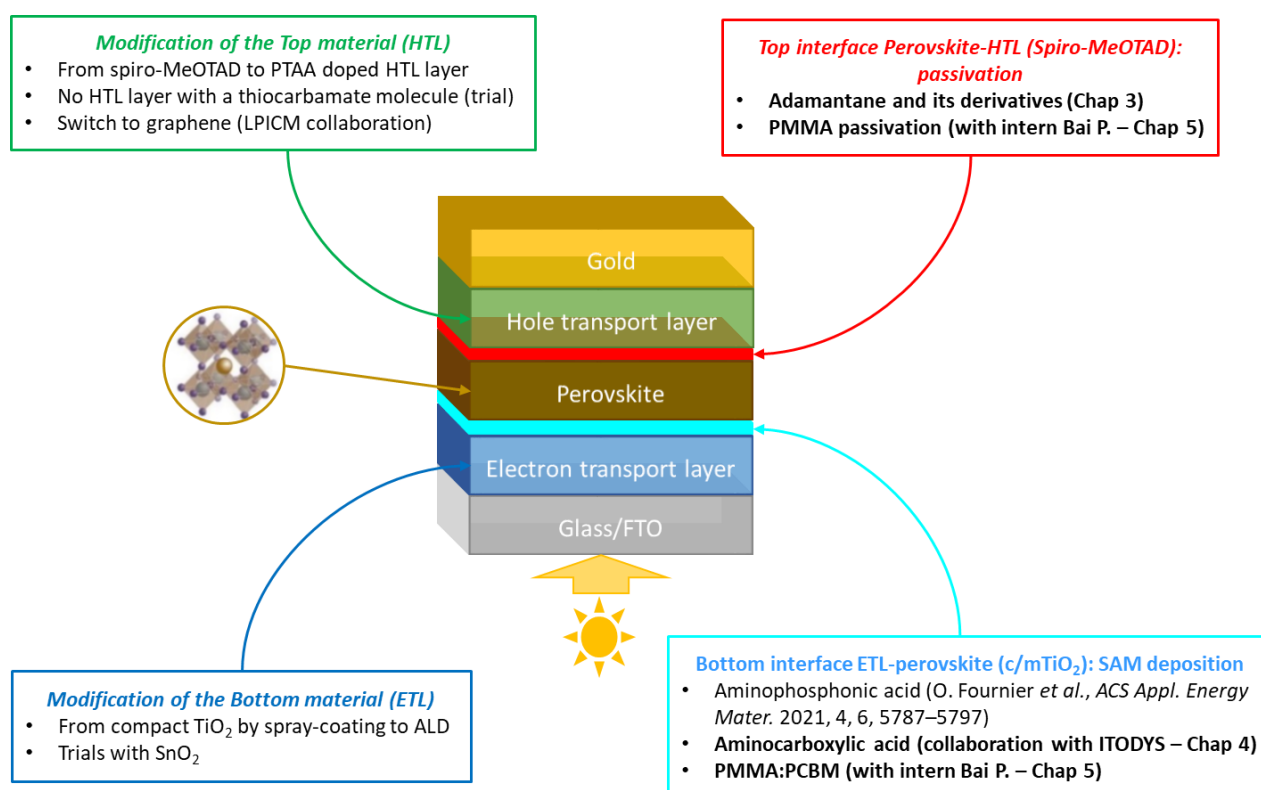


*Figure 1.11 Recap of the work done during the tests. The studies presented in this manuscript are highlighted in the different boxes.*

The different steps of the device fabrication are fully described in *Chapter 2*, which presents the deposition procedure for each constitutive layer of the baseline cell and the additional steps for the deposition of the interlayers considered in this work. Furthermore, surface modifications after the interlayer deposition on the perovskite layer have been accurately studied by combining optical, structural and chemical characterizations and the subsequent device properties variations by means of conventional optical characterizations. These methods are described in *Chapter II*.

To conclude (Chapter 6), a discussion about the capabilities and limits of the interface engineering strategies studied in this PhD work will be presented and an opening on several perspectives will be proposed, such as improvement on the perovskite active layer itself by considering single-powder perovskite materials (collaboration with Bayreuth University (Germany)).

## 1.4 References

1. REN21. Renewable energy data in perspective. 7.-15. (2022).
2. Victoria, M. *et al.* Solar photovoltaics is ready to power a sustainable future. *Joule* **5**, 1041–1056 (2021).
3. Marques Lameirinhas, R. A., Torres, J. P. N. & de Melo Cunha, J. P. A Photovoltaic Technology Review: History, Fundamentals and Applications. *Energies* **15**, 1823 (2022).
4. Bojar, A. Heterojunctions and silicon / perovskite tandem solar cells. (2022).
5. Jain, N. *et al.* Light induced quasi-Fermi level splitting in molecular semiconductor alloys. *Mater. Adv.* **3**, 5344–5349 (2022).
6. Würfel, P. *Physics of Solar Cells*. (Wiley, 2005). doi:10.1002/9783527618545.
7. Univeristy of Cambridge. Direct and Indirect Band Gap Semiconductors. 2007 1.
8. Direct and Indirect band gaps - Engineering Physics.
9. Pastuszak, J. & Węgierek, P. Photovoltaic Cell Generations and Current Research Directions for Their Development. *Materials (Basel)*. **15**, (2022).
10. Fraunhofer Institute for Solar Energy Systems, ISE & PSE Projects GmbH. Photovoltaics Report. (2012).
11. Kirk, A. P. Solar Photovoltaic Cells: Photons to Electricity. Solar Photovoltaic Cells: Photons to Electricity (2014). doi:10.1016/C2014-0-03052-3.
12. NREL. Best Research-Cell Efficiencies: Rev. 19-01-2022. *Best Research-Cell Efficiency Chart | Photovoltaic Research | NREL* <https://www.nrel.gov/pv/cell-efficiency.html> (2022).
13. Verduci, R. *et al.* Solar Energy in Space Applications: Review and Technology Perspectives. *Adv. Energy Mater.* **12**, (2022).
14. Min, H. *et al.* Perovskite solar cells with atomically coherent interlayers on SnO<sub>2</sub> electrodes. *Nature* **598**, 444–450 (2021).
15. Jacobsson, T. J. Temperature effects in lead halide perovskites. *Characterization Techniques for Perovskite Solar Cell Materials* (Elsevier Inc., 2019). doi:10.1016/B978-0-12-814727-6.00008-6.
16. Kojima, A., Teshima, K., Shirai, Y. & Miyasaka, T. Organometal halide perovskites as visible-light sensitizers for photovoltaic cells. *J. Am. Chem. Soc.* **131**, 6050–6051 (2009).
17. Im, J. H., Lee, C. R., Lee, J. W., Park, S. W. & Park, N. G. 6.5% Efficient Perovskite Quantum-Dot-Sensitized Solar Cell. *Nanoscale* **3**, 4088–4093 (2011).

18. Lee, M. M., Teuscher, J., Miyasaka, T., Murakami, T. N. & Snaith, H. J. Efficient Hybrid Solar Cells Based on Meso-Superstructured Organometal Halide Perovskites. *Science (80-. )*. **338**, 643–647 (2012).
19. Organic-Inorganic Halide Perovskite Photovoltaics. Organic-Inorganic Halide Perovskite Photovoltaics (Springer International Publishing, 2016). doi:10.1007/978-3-319-35114-8.
20. Guillemoles, J. F., Kirchartz, T., Cahen, D. & Rau, U. Guide for the perplexed to the Shockley–Queisser model for solar cells. *Nat. Photonics* **13**, 501–505 (2019).
21. Saliba, M., Correa-Baena, J. P., Grätzel, M., Hagfeldt, A. & Abate, A. Perovskite Solar Cells: From the Atomic Level to Film Quality and Device Performance. *Angew. Chemie - Int. Ed.* **57**, 2554–2569 (2018).
22. Yan, Y., Yin, W. J., Shi, T., Meng, W. & Feng, C. Organic-Inorganic Halide Perovskite Photovoltaics. Organic-Inorganic Halide Perovskite Photovoltaics: From Fundamentals to Device Architectures (Springer International Publishing, 2016). doi:10.1007/978-3-319-35114-8.
23. Stranks, S. D. *et al.* Electron-hole diffusion lengths exceeding 1 micrometer in an organometal trihalide perovskite absorber. *Science (80-. )*. **342**, 341–344 (2013).
24. Herz, L. M. Charge-Carrier Mobilities in Metal Halide Perovskites: Fundamental Mechanisms and Limits. *ACS Energy Lett.* **2**, 1539–1548 (2017).
25. Yu, M. *et al.* The influence of the electron transport layer on charge dynamics and trap-state properties in planar perovskite solar cells. *RSC Adv.* **10**, 12347–12353 (2020).
26. Li, Z. *et al.* Bifacial Passivation of Organic Hole Transport Interlayer for NiO<sub>x</sub>-Based p-i-n Perovskite Solar Cells. *Adv. Sci.* **6**, (2019).
27. Akhtar, J., Aamir, M. & Sher, M. Organometal lead halide perovskite. *Perovskite Photovoltaics Basic to Adv. Concepts Implement.* 25–42 (2018) doi:10.1016/B978-0-12-812915-9.00002-2.
28. Raniaga, R. D. *et al.* Strong performance enhancement in lead-halide perovskite solar cells through rapid, atmospheric deposition of n-type buffer layer oxides. *Nano Energy* **75**, (2020).
29. Zardetto, V. *et al.* Atomic layer deposition for perovskite solar cells: Research status, opportunities and challenges. *Sustain. Energy Fuels* **1**, 30–55 (2017).
30. Fan, R. *et al.* The Progress of Interface Design in Perovskite-Based Solar Cells. *Adv. Energy Mater.* **6**, 1600460 (2016).

31. Kegelmann, L. *et al.* It Takes Two to Tango - Double-Layer Selective Contacts in Perovskite Solar Cells for Improved Device Performance and Reduced Hysteresis. *ACS Appl. Mater. Interfaces* **9**, 17245–17255 (2017).
32. Xu, W. *et al.* Minimizing Voltage Loss in Efficient All-Inorganic CsPbI<sub>2</sub>Br Perovskite Solar Cells through Energy Level Alignment. *ACS Energy Lett.* **4**, 2491–2499 (2019).
33. Saliba, M. *et al.* How to Make over 20% Efficient Perovskite Solar Cells in Regular (n-i-p) and Inverted (p-i-n) Architectures. *Chem. Mater.* **30**, 4193–4201 (2018).
34. Wathage, S. C., Song, Z., Phillips, A. B. & Heben, M. J. *Evolution of perovskite solar cells. Perovskite Photovoltaics: Basic to Advanced Concepts and Implementation* (Elsevier Inc., 2018). doi:10.1016/B978-0-12-812915-9.00003-4.
35. Li, W. *et al.* Boost the performance of inverted perovskite solar cells with PEDOT:PSS/Graphene quantum dots composite hole transporting layer. *Org. Electron.* **78**, 105575 (2019).
36. Guerrero, A. *et al.* Interfacial degradation of planar lead halide perovskite solar cells. *ACS Nano* **10**, 218–224 (2016).
37. Rombach, F. M., Haque, S. A. & Macdonald, T. J. Lessons learned from spiro-OMeTAD and PTAA in perovskite solar cells. *Energy Environ. Sci.* **14**, 5161–5190 (2021).
38. Heo, J. H. *et al.* Efficient inorganic-organic hybrid heterojunction solar cells containing perovskite compound and polymeric hole conductors. *Nat. Photonics* **7**, 486–491 (2013).
39. Hong Noh, J., Hyuk Im, S., Hyuck Heo, J., Mandal, T. N. & Il Seok, S. Chemical Management for Colorful, Efficient, and Stable Inorganic– Organic Hybrid Nanostructured Solar Cells. (2013) doi:10.1021/nl400349b.
40. Yang, J., Siempelkamp, B. D., Liu, D. & Kelly, T. L. Investigation of CH<sub>3</sub>NH<sub>3</sub>PbI<sub>3</sub> Degradation Rates and Mechanisms in Controlled Humidity Environments Using in Situ Techniques. *ACS Nano* **9**, 1955–1963 (2015).
41. Christians, J. A., Fung, R. C. M. & Kamat, P. V. An Inorganic Hole Conductor for Organo-Lead Halide Perovskite Solar Cells. Improved Hole Conductivity with Copper Iodide. *J. Am. Chem. Soc.* **136**, 758–764 (2014).
42. Ito, S. *et al.* Carbon-Double-Bond-Free Printed Solar Cells from TiO<sub>2</sub>/CH<sub>3</sub>NH<sub>3</sub>PbI<sub>3</sub>/CuSCN/Au: Structural Control and Photoaging Effects. *ChemPhysChem* **15**, 1194–1200 (2014).

43. Qin, P. *et al.* Inorganic hole conductor-based lead halide perovskite solar cells with 12.4% conversion efficiency. *Nat. Commun.* **5**, 1–6 (2014).
44. Xu, L. *et al.* Inverted perovskite solar cells employing doped NiO hole transport layers: A review. *Nano Energy* **63**, 103860 (2019).
45. Boyd, C. C. *et al.* Overcoming Redox Reactions at Perovskite-Nickel Oxide Interfaces to Boost Voltages in Perovskite Solar Cells. *Joule* **4**, 1759–1775 (2020).
46. Hu, L. *et al.* Unravelling the role of C60 derivatives as additives into active layer for achieving high-efficiency planar perovskite solar cells. *Carbon N. Y.* **167**, 160–168 (2020).
47. Liu, Z. *et al.* Open-Circuit Voltages Exceeding 1.26 v in Planar Methylammonium Lead Iodide Perovskite Solar Cells. *ACS Energy Lett.* **4**, 110–117 (2019).
48. Castro, E., Murillo, J., Fernandez-Delgado, O. & Echegoyen, L. Progress in fullerene-based hybrid perovskite solar cells. *J. Mater. Chem. C* **6**, 2635–2651 (2018).
49. You, J., Meng, L., Hong, Z., Li, G. & Yang, Y. Inverted Planar Structure of Perovskite Solar Cells. in *Organic-Inorganic Halide Perovskite Photovoltaics* 307–324 (Springer International Publishing, 2016). doi:10.1007/978-3-319-35114-8\_12.
50. Liang, Z., Zhang, Q., Jiang, L. & Cao, G. ZnO cathode buffer layers for inverted polymer solar cells. *Energy Environ. Sci.* **8**, 3442–3476 (2015).
51. Baltakesmez, A., Biber, M. & Tüzemen, S. Inverted planar perovskite solar cells based on Al doped ZnO substrate. *J. Radiat. Res. Appl. Sci.* **11**, 124–129 (2018).
52. Jia, X. *et al.* Power Conversion Efficiency and Device Stability Improvement of Inverted Perovskite Solar Cells by Using a ZnO:PFN Composite Cathode Buffer Layer. *ACS Appl. Mater. Interfaces* **8**, 18410–18417 (2016).
53. Isikgor, F. H. *et al.* Scaling-up perovskite solar cells on hydrophobic surfaces. *Nano Energy* **81**, (2021).
54. Saliba, M. *et al.* Cesium-containing triple cation perovskite solar cells: Improved stability, reproducibility and high efficiency. *Energy Environ. Sci.* **9**, 1989–1997 (2016).
55. Hsiao, K. C. *et al.* Enhancing Efficiency and Stability of Hot Casting p-i-n Perovskite Solar Cell via Dipolar Ion Passivation. *ACS Appl. Energy Mater.* **2**, 4821–4832 (2019).
56. Zeng, L. *et al.* s2D-3D heterostructure enables scalable coating of efficient low-bandgap Sn-Pb mixed perovskite solar cells. *Nano Energy* **66**, 104099 (2019).

57. Li, X. *et al.* Perovskite solar cells employing an eco-friendly and low-cost inorganic hole transport layer for enhanced photovoltaic performance and operational stability. *J. Mater. Chem. A* **7**, 7065–7073 (2019).
58. Navazani, S., Yaghoobi Nia, N., Zendeheel, M., Shokuhfar, A. & Di Carlo, A. Fabrication of high efficiency, low-temperature planar perovskite solar cells via scalable double-step crystal engineering deposition method fully out of glove box. *Sol. Energy* **206**, 181–187 (2020).
59. Chen, P. *et al.* In Situ Growth of 2D Perovskite Capping Layer for Stable and Efficient Perovskite Solar Cells. *Adv. Funct. Mater.* **28**, 1–10 (2018).
60. Wang, S. Y. *et al.* Defect Passivation by Amide-Based Hole-Transporting Interfacial Layer Enhanced Perovskite Grain Growth for Efficient p-i-n Perovskite Solar Cells. *ACS Appl. Mater. Interfaces* **11**, 40050–40061 (2019).
61. Boyd, C. C., Cheacharoen, R., Leijtens, T. & McGehee, M. D. Understanding Degradation Mechanisms and Improving Stability of Perovskite Photovoltaics. (2019) doi:10.1021/acs.chemrev.8b00336.
62. Cacovich, S. *et al.* Light-Induced Passivation in Triple Cation Mixed Halide Perovskites: Interplay between Transport Properties and Surface Chemistry. *ACS Appl. Mater. Interfaces* **12**, 34784–34794 (2020).
63. Berhe, T. A. *et al.* Organometal halide perovskite solar cells: Degradation and stability. *Energy Environ. Sci.* **9**, 323–356 (2016).
64. Rahman, M. Z. & Edvinsson, T. X-ray diffraction and Raman spectroscopy for lead halide perovskites. *Characterization Techniques for Perovskite Solar Cell Materials* (Elsevier Inc., 2019). doi:10.1016/B978-0-12-814727-6.00002-5.
65. Abdi-Jalebi, M. *et al.* Maximizing and stabilizing luminescence from halide perovskites with potassium passivation. *Nature* **555**, 497–501 (2018).
66. Christians, J. A. *et al.* Tailored interfaces of unencapsulated perovskite solar cells for >1,000 hour operational stability. *Nat. Energy* **3**, 68–74 (2018).
67. Chen, P. *et al.* In Situ Growth of 2D Perovskite Capping Layer for Stable and Efficient Perovskite Solar Cells. *Adv. Funct. Mater.* **28**, (2018).
68. Mahesh, S. *et al.* Revealing the origin of voltage loss in mixed-halide perovskite solar cells. *Energy Environ. Sci.* **13**, 258–267 (2020).

69. Domanski, K. *et al.* Migration of cations induces reversible performance losses over day/night cycling in perovskite solar cells. *Energy Environ. Sci.* **10**, 604–613 (2017).
70. Yuan, Y., Wang, Q. & Huang, J. Ion Migration in Hybrid Perovskite Solar Cells. in *Organic-Inorganic Halide Perovskite Photovoltaics* 137–162 (Springer International Publishing, 2016). doi:10.1007/978-3-319-35114-8\_6.
71. Schulz, P. Interface Design for Metal Halide Perovskite Solar Cells. *ACS Energy Lett.* **3**, 1287–1293 (2018).
72. Schulz, P., Cahen, D. & Kahn, A. Halide Perovskites: Is It All about the Interfaces? *Chem. Rev.* **119**, 3349–3417 (2019).
73. Fraunhofer Institute for Solar Energy Systems. PersiST – Perovskite-Silicon Tandem Solar Cells.
74. Qiao, R. & Zuo, L. Self-assembly monolayers boosting organic-inorganic halide perovskite solar cell performance. *J. Mater. Res.* **33**, 387–400 (2018).
75. Niu, T., Xue, Q. & Yip, H. L. Molecularly Engineered Interfaces in Metal Halide Perovskite Solar Cells. *J. Phys. Chem. Lett.* **12**, 4882–4901 (2021).
76. Fournier, O. *et al.* Chemical Passivation with Phosphonic Acid Derivatives of ZnO Deposited by Atomic Layer Deposition and Its Influence on the Halide Perovskite Interface. *ACS Appl. Energy Mater.* **4**, 5787–5797 (2021).
77. Peng, J. *et al.* Interface passivation using ultrathin polymer-fullerene films for high-efficiency perovskite solar cells with negligible hysteresis. *Energy Environ. Sci.* **10**, 1792–1800 (2017).
78. Westbrook, R. J. E. *et al.* Lewis Base Passivation Mediates Charge Transfer at Perovskite Heterojunctions. *J. Am. Chem. Soc.* **143**, 12230–12243 (2021).
79. Tavakoli, M. M. *et al.* Adamantanes Enhance the Photovoltaic Performance and Operational Stability of Perovskite Solar Cells by Effective Mitigation of Interfacial Defect States. *Adv. Energy Mater.* **8**, 1–7 (2018).

## Chapter 2: Methods and Experiments

---

*In this part, I discuss the methods and experiments used in this thesis. In the first part, we describe the fabrication process of the perovskite solar cell from the glass coated with the transparent conductive oxide to the top metallic contact. I usually prepared a batch of devices corresponding to 16 devices of  $2 \times 2 \text{ cm}^2$  and their matching samples for characterizations. We also described several surface modifiers and interfaces explored in this thesis. The fabrication process is coupled with an explanation of the deposition method for each layer. In the second part, the characterization methods employed are presented, indicating an involvement from the morphologic description of the samples to device characterization.*

## Table of Contents

2.1	Perovskite cell fabrication process at IPVF .....	51
2.1.1	Glass/FTO substrate .....	51
2.1.2	Electron transport layer .....	52
2.1.3	Perovskite absorber deposition .....	57
2.1.4	Hole transport layer (HTL).....	58
2.1.5	Metal contact.....	60
2.1.6	Alternative surface modifiers and interfaces layers studied .....	61
2.2	Electrical characterization techniques .....	66
2.2.1	Current Density-Voltage (JV) measurement.....	66
2.2.2	External quantum efficiency (EQE) .....	68
2.3	Optical characterization techniques .....	69
2.3.1	Absorption, transmission, reflection .....	69
2.4	Structural characterization techniques.....	70
2.4.1	Scanning electron microscopy .....	70
2.4.2	X-ray diffraction .....	71
2.5	Surface chemical characterization .....	71
2.5.1	X-ray Photoelectron Spectroscopy principle .....	71
2.5.2	X-ray Photoelectron Spectroscopy spectra description .....	75
2.6	Resume .....	81
2.7	References.....	82

## 2.1 Perovskite cell fabrication process at IPVF

The devices are made in IPVF clean room according to the baseline processes developed internally. Thanks to the know-how of IPVF on the perovskite fabrication process, the project started and is based on IPVF baseline HaPSC with glass/FTO/c-TiO<sub>2</sub>/m-TiO<sub>2</sub>/triple cation HaP/ Spiro-MeOTAD/Gold (see in Figure 2.1). The several steps required to obtain perovskite solar cells will be described in more detail later and several layers have been developed during my thesis. The overall architecture of the devices is kept constant and consists in a stack of:

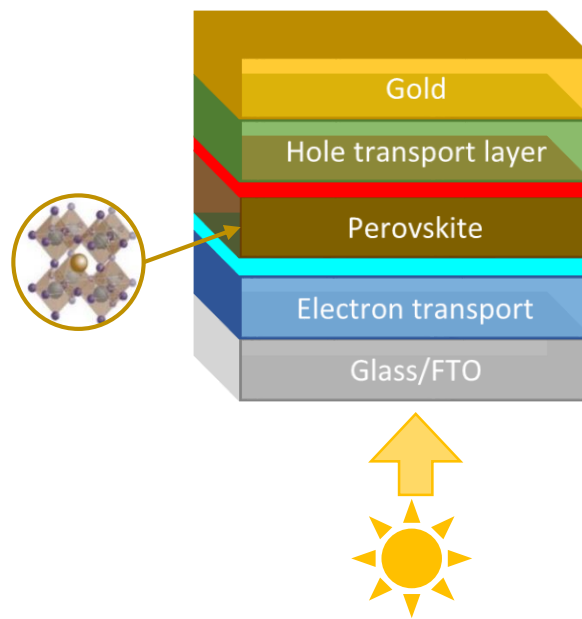


*Figure 2.1: Schematic architecture of the NIP configuration architecture  
Glass/FTO/ETL/Perovskite/HTL/Gold used during this thesis*

My research work is focused on the improvement of these IPVF NIP solar cell reference architecture through innovative interface passivation. To do so, different ETL and HTL configuration are considered. On one hand alternative interlayers consisting of adamantane compounds and PMMA (HTL/perovskite, Chapters I and III); amino carboxylic acids self-assembled monolayer or PMMA-PCBM (ETL/perovskite, Chapters II and III) will be evaluated. First results concerning a new film formation process of the active perovskite layer starting from powders will also be presented (Chapter IV) and their potentiality discussed.

### 2.1.1 Glass/FTO substrate

The fluorine-doped tin oxide (FTO) deposited on glass is furnished by SOLEMS, a company localized in Palaiseau. The samples are cut from 30 x 30 cm<sup>2</sup> size of FTO/glass sheets to a 2 x 2 cm<sup>2</sup> serving as Institut Polytechnique de Paris

91120 Palaiseau, France

substrates for the following depositions steps. The glass thickness is 3 mm covered with a layer of FTO of 500 nm presenting a resistance of 10 ohms. The glass sheets are etched chemically, using zinc powder and a diluted hydrochloric acid solution, or physically, by laser scribing. The glass/FTO sheets are cleaned under an ultrasonic bath in 4 steps: 1) 20 min at 60°C in RBS 30°, a laboratory detergent, 2) 15 minutes in deionized water, 3) 15 minutes in acetone, 4) 15 minutes in isopropanol (IPA). Cleaning under heat helps to remove grease stains from the glass sheet. The heater is turned off after the first step as there is no need to keep it up to 60°C. The glass sheet is rinsed between each step with the future solvent to avoid mixing in the solvent. Furthermore, the cleaning solvent, kept in a glass bottle, is conserved for six usages before trash and refill with a fresh solvent solution. The samples are extracted one by one, rinsed under cold IPA, then dried with a nitrogen gas flux. It is rinsed again to avoid leftover stains on the glass surface due to the fast drying of the slightly hot IPA. To finish, before any deposition on top of the cleaned glass/FTO, the samples are placed under UV ozone for 15 min.

## 2.1.2 Electron transport layer

### 2.1.2.1 Titanium dioxide $TiO_2$

The electron transport layer (ETL) used for the baseline IPVF process consists of a titanium dioxide layer deposited on Glass/FTO in two steps to form a compact layer of 15 nm covered by a mesoporous layer of 100 nm corresponding to the following stack: Glass/FTO/c-TiO<sub>2</sub>/m-TiO<sub>2</sub>.

#### a) Compact TiO<sub>2</sub> – Spray pyrolysis method

Initially, this step was done by the spray pyrolysis method. Spray pyrolysis is an aerosol technique that atomizes a solution into thin droplets through a gun which decomposes at relatively high temperatures to produce solid particles. The droplets are heated fast on top of the hot plate and go from the evaporation of the solvent to the agglomeration of the nanoparticles and then to the formation of solid particles. The experimental procedure is the following. After the cleaning of the glass/FTO substrate, this later is placed on a hot plate. The hot plate is heated up to 500°C and stabilized at 450°C. For 10 mL of solution, the spray solution is made of 0.6 mL of titanium diisopropoxide bis(acetylacetonate) (TAA), 0.4 mL of acetyl acetone, and 9 mL of ethanol or isopropanol. We needed a total of 40 mL to 50 mL of the solution to complete all of the spray runs.

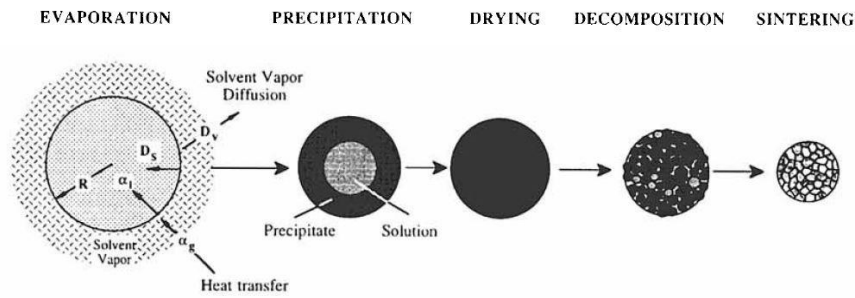


Figure 2.2: Spray Pyrolysis process. Figure reproduced from the publication of Messing G. et al, *Ceramic Powder Synthesis by Spray Pyrolysis, in 1993*<sup>1</sup>

After being drop-cast on top of the substrate, the solid particles form a compact layer of titanium dioxide ( $c\text{-TiO}_2$ ), constituting the first part of the ETL. Several cycles of deposition are done until 20 runs with the direction of the spray deposition being changed every 5 runs to maximize the uniformity of the layer. After the last run, the samples are left for 15 minutes at  $450^\circ\text{C}$ . Finally, the samples are left cooled down on the hot plate to the ambient temperature. The  $c\text{-TiO}_2$  samples can be stored for future use. The spray pyrolysis method has pros and cons. For the pros, this deposition method is cheap and fast to produce as the needed equipment is a hot plate and an air gun linked to an  $\text{O}_2$  source. It is easily applicable to large areas and the requirement for a clean and low-humidity environment is not needed. For the cons, this technique is done manually and thus operator dependent leading to reproducibility issues between series. The performance of the layer formed is quite poor if this later is not uniform and/or too thick.

#### b) Compact $\text{TiO}_2$ – Atomic Layer Deposition method

More recently, the deposition by Atomic Layer Deposition (ALD) is implemented to replace spray pyrolysis based on Olivier Fournier's work during his thesis<sup>2</sup> and his collaborative work with the ALD team of IPVF. The atomic layer deposition is a versatile technique of deposition that can produce a variety of high-quality and conformal thin films of inorganic materials like oxide or sulfides<sup>3</sup>. The ALD working principle follows cycling of self-limiting surface deposition. Glass/FTO sheets are cut on  $13 \times 15 \text{cm}^2$ , laser-scribed, or chemically cleaned before ALD deposition. An advantage of this method is the fact that it is easier to obtain a homogenous layer on big-size glass sheets. In the case of  $\text{TiO}_2$ , the titanium tetra(isopropoxide) as Ti precursor (precursor 1) is introduced in the chamber and reacts on the surface of the glass/FTO substrate with total coverage of the surface. Then, after an  $\text{N}_2$  purge to eliminate residues,  $\text{H}_2\text{O}$  or  $\text{H}_2\text{O}_2$  as oxygen precursors (precursor 2) is introduced in

the deposition chamber and reacts with the previous layer formed during precursor 1 exposition to form the first layer of  $\text{TiO}_2$ . This sequence (cycle) is repeated until the targeted thickness final is reached, presently 15 nm of  $\text{TiO}_2$  layer. With this method, it is possible to control on a nanometer scale, the thickness of the produced layer. Furthermore, this technique guarantees a total coverage of the surface. More details about the ALD parameters can be found in Fournier O. thesis's<sup>2</sup>.

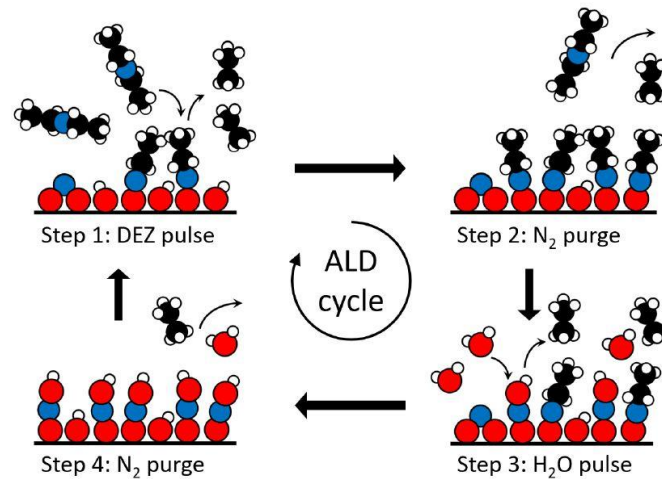


*Figure 2.3: Atomic Layer Deposition Cycle process. [Example with ZnO: Oxygen red sphere, Zinc blue sphere, Carbon black sphere, Hydrogen white sphere] Figure taken from the thesis of Fournier Olivier submitted in 2021 “Synthèse par ALD et caractérisation de couches extractrices d’électrons pour application dans les cellules solaires à base de pérovskite”<sup>2</sup>*

After the c- $\text{TiO}_2$  deposition, the samples are rinsed in an ultrasonic bath for 5 minutes in acetone and 5 minutes of IPA, then dried in a dry nitrogen stream. The c- $\text{TiO}_2$  covered Glass/FTO substrate is cut into smaller pieces for the next steps. For a  $2 \times 2 \text{ cm}^2$  sample size, it is possible to get 42 samples out of a  $13 \times 15 \text{ cm}^2$  ALD c- $\text{TiO}_2$  coated glass sheet. With respect to positive aspects, the ALD deposition leads to uniform, homogeneous layers of controlled thicknesses at a larger scale, both inherent to the chemical process. In addition, the fact that human influence and hence error is limited. However, this technique is expensive, mainly due to the precursor source's prices and the longer time compared to spray pyrolysis for an identical thickness.

### c) Mesoporous $\text{TiO}_2$

After the deposition of the c- $\text{TiO}_2$ , we made sure that the samples are cut to our desirable size ( $2 \times 2 \text{ cm}^2$  for devices). The samples are prepared for the deposition of mesoporous  $\text{TiO}_2$  (m- $\text{TiO}_2$ ). As the electric conductivity is low compared to other metal oxide layers like  $\text{SnO}_2$ , a mesoporous layer is deposited on top of the c- $\text{TiO}_2$  to increase the surface exchange between the perovskite and the

ETL, thus increasing the carrier circulation in the device. 0.5 g to 1.0 g of 30NRD TiO<sub>2</sub> paste is weighted. The obtained weight is multiplied by seven. This proportion corresponds to the ethanol mass needed for the solution preparation. The solution is then secured with parafilm and left under a high stirring for at least overnight to ensure the complete dissolution of the paste. For the deposition of the TiO<sub>2</sub> solution, a hot plate and a spin-coater are used. The hot plate is preheated at 90 °C. One at a time, the samples are placed on the spin-coater and held in place by vacuum. The solution is dropped on the surface in a static position and the spin-coater is accelerated to 4000 rpm with a ramp of 2000 rpm/s, and then held at maximum speed for 30 s. After each deposition, the samples are placed on the hot plate with a closed lid to have a homogenous temperature between the first and last deposited samples. After the last deposition, the hot plate program is launched and proceeds as detailed in Table 2.1 below.

Step	1	2	3	4	5
Ramp Time (min)	5	15	5	5	5
Working temperature (°C)	125	325	375	450	500
Time per step (min)	5	5	5	15	15

*Table 2.1: Mesoporous TiO<sub>2</sub> temperature ramping process*

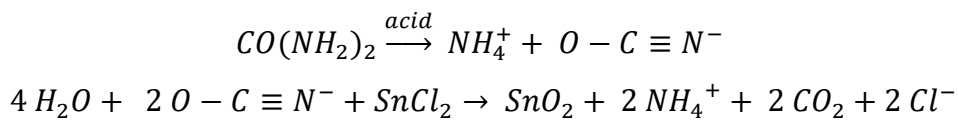
Suppose the sample is going to be used on the same day as the perovskite deposition. In that case, the sample is cooled down to 180°C before entering the glovebox to avoid re-adsorption of water inside the mesoporous layer. Suppose the newly mesoporous deposited samples are going to be stored, before any perovskite deposition. The sample is preheated at 180°C for one hour to eliminate any possible re-adsorbed water in the m-TiO<sub>2</sub> layer. We identify the compact TiO<sub>2</sub>/mesoporous TiO<sub>2</sub> as c-m TiO<sub>2</sub>.

### 2.1.2.2 Tin oxide SnO<sub>2</sub>

#### a) Chemical bath deposition

Another configuration studied is Glass/FTO/SnO<sub>2</sub>. Tin oxide is deposited through chemical bath deposition (CBD)<sup>4</sup>. First, a stock solution is prepared: we mixed in a glass bottle, in this order, 7.5 g of urea, 600 mL deionized water, 150 µL of thioglycolic acid, 7.5 mL of hydrochloric acid and 1.625 g of monohydrated tin chloride. Between each addition of the next component, the solution is agitated to avoid any formation of clusters in the solution. The bottle is placed for three days in a

fridge at 4°C. A hot bath is preheated to 70°C and samples are pre-cut to the right size for the deposition (10 x 5 cm<sup>2</sup>) and etched. The samples are put in a glass container face to the top. The deposition is made twice to ensure full coverage. Out of the 600 mL of the stock solution, 300 mL is diluted in deionized water for a 5:1 ratio of water/stock. The diluted solution is poured into the container with the samples. The remaining stock solution is stored in the fridge. The glass container is placed in the hot bath. Of note, the bath temperature drops slightly with the introduction of the colder substrate. Then, once the bath temperature reaches 70°C again, we leave the samples to sit in the bath for one hour. During the chemical batch, two reactions take place:



First, the urea is decomposed in the acid solution into ammoniac and cyanate. Then, the cyanate and SnCl<sub>2</sub> form SnO<sub>2</sub>. The deposition is uniform on the glass/FTO.

Two chemical bath depositions are done that way. After each CBD, the glass/FTO substrates are cleaned one by one with clean deionized water. Ultimately, the samples are dried and annealed at 180°C for one hour. The samples are cut to the right size for the next deposition steps (2 x 2 cm<sup>2</sup> for the device). Passivation of the SnO<sub>2</sub> layer is done using 10 mM of potassium hydroxide (KOH) just before the perovskite deposition. K<sup>+</sup> cations are beneficial as they can migrate in the layer and passivate the defects<sup>5</sup>.

#### b) Spin-coating deposition

The tin oxide layer can be also deposited by spin-coating using a colloidal solution. The colloidal solution of SnO<sub>2</sub> is a commercial solution with a dispersion of 10% SnO<sub>2</sub> nanoparticles from Thermo Fischer. A diluted solution is made from the colloidal solution in deionized water at 1:3 (colloidal solution / Water) and is spin-coated on the glass/FTO substrates at 3000 rpm, 1500 rpm/s, for 30 seconds. After each deposition, the samples are placed on the hot plate preheated at 100°C. After placing the last deposited samples on the preheated hot plate, the temperature is raised and the samples are annealed at 180°C for one hour.

Note that working in perovskite solar cell field requires to be pro-active and numerous optimizations are performed to maintain a competitive level. Thus, along my thesis, new deposition methods and

materials have been deployed in the IPVF platform to enhance performances and increase the reproducibility of the elaboration methods.

Several ETLs were at your disposition to incorporate and produce solar cell devices through the years of the thesis. Depending on the availability of the ETL, the perovskite solar cell device configuration have thus evolved as will be laid out in the individual results chapters.

### 2.1.3 Perovskite absorber deposition

The usual perovskite used and made during this thesis work is the triple cation lead mixed halide perovskite which will be abbreviated as HaP throughout the manuscript. All of this preparation is made in a glovebox under  $N_2$  atmosphere to avoid any contact with humidity and air. Following the mix from Saliba et al.<sup>4</sup>, the perovskite formula from  $ABX_3$  leads to a stoichiometry of  $Cs_{0.05}(MA_{0.17}, FA_{0.83})_{0.95}Pb(Br_{0.17}, I_{0.83})_3$ . The mixed recipe solution is prepared following these weights: 0.2 M  $MABr_{(g)}$ , 0.2 M  $PbBr_{2(g)}$ , 1.1 M  $PbI_{2(g)}$ , and 1.0 M  $FAI_{(g)}$  in 1 mL of solvent mix DMF/DMSO (4:1). The solution is stirred for two hours to assure the total dissolution of the precursors' powders. For each series of devices, 1 mL of mixed recipe solution is made and completed with 42  $\mu$ L of CsI.

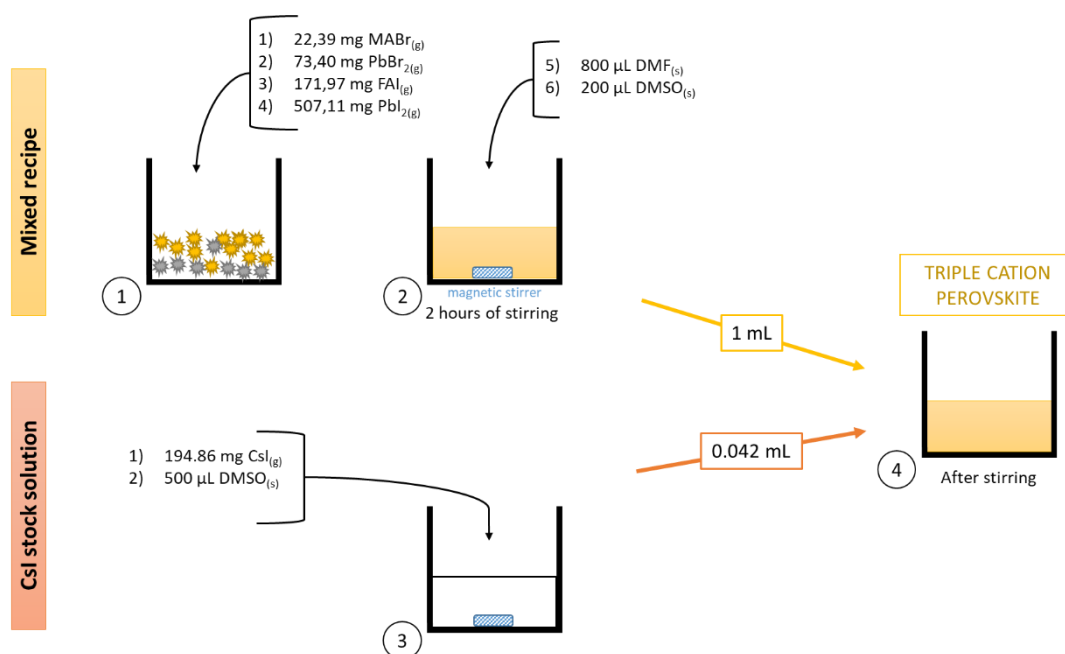


Figure 2.4: Triple cation lead halide perovskite (HaP) solution preparation process.

An excess of 0.1 M  $PbI_2$  is introduced in the solution. It has been demonstrated that this excess helps reaching higher performances of the perovskite solar device by passivating the defects coming from the migration of the  $PbI_2$  via the grain boundaries<sup>6,7</sup>. The solution is prepared and stirred for two

hours at least before the perovskite deposition, to ensure that all the precursors, such as the  $\text{PbI}_2$  powder grains, are well dissolved. As indicated in Figure 2.4, the cesium iodide stock solution is added and mixed in just before the perovskite deposition step. The  $\text{CsI}$  stock solution can be kept for 14 days at ambient temperature under a nitrogen atmosphere. Adding cesium in the mixed recipe improves the performance and reproducibility of the devices fabricated as it helps increase the stability of the perovskite layer due to reducing the yellow phase impurities<sup>8</sup>. From a qualitative point of view, the yellow color and clear aspect of the final solution indicate the precursors' full dissolution. Finally, the perovskite solution is deposited on top of the ETL through spin-coating, a sol-gel method. The sample is placed on the spin-coating and the deposition process occurs in two steps of spins:

- Step 1: 2000 rpm, 1000 rpm/s, 12 seconds
- Step 2: 6000 rpm, 2000 rpm/s, 32 seconds

First, 35  $\mu\text{L}$  of solution is deposited under dynamic 2 seconds after the start of the step 1. We deposited the solution perpendicular to the sample at the center. At the step 2 of the spin program, we washed the perovskite layer with 100  $\mu\text{L}$  of chlorobenzene 12 seconds before the end of the spin. This will chase out the solvent present in the perovskite layer and start the crystallization of the perovskite layer. In the end, the sample is take out of the spin and place on a hot plate at  $100^\circ\text{C}$  for 30 min to finalize the crystallization of the perovskite layer.

### 2.1.4 Hole transport layer (HTL)

Two HTLs were evaluated through this PhD in NIP configuration. HTL's role is to assist in the selective extraction and transport of hole carriers produced by the perovskite toward the top contact of gold. The more common compounds implemented in solar devices are Spiro-MeOTAD (2,2',7,7'-tetrakis[N,N-di(4-methoxyphenyl)amino]-9,9'-spirobifluorene) and PTAA (poly(triarylamine)).

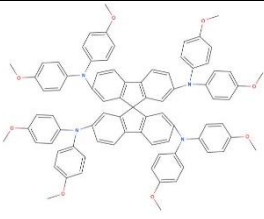
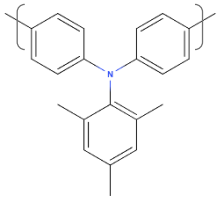
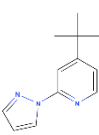
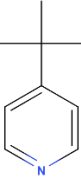
HTL		Additives		
				
Spiro-MeOTAD	PTAA	FK209	LiTFSI	TbP

Table 2.2: Main molecules used in the hole transport layer deposition

#### 2.1.4.1 Spiro MeOTAD

The organic semiconductor Spiro-MeOTAD was the most commonly used charge transport layer since introduced by Grätzel et al. in 1998 for the use in dye-sensitized solar cells<sup>9</sup>. As depicted in Table 2.2, this component is one of the most prevalent materials used for HTL formation in perovskite solar cells, deposited on top of the perovskite layer in an NIP configuration. The supplementary additives dope this layer: (lithium bistrifluoromethanesulfonimide (LiTFSI), 4-tert-butylpyridine (tbP), and tris[2-(1H-pyrazol-1-yl)-4-tert-butylpyridine]cobalt(III) tris(bis(trifluoromethylsulfonyl)imide)] (FK209). These additives are p-dopants and help to obtain a higher conductivity of the spiro-MeOTAD to spiro-MeOTAD<sup>+</sup><sup>10</sup>. The spiro-MeOTAD can hypothetically promote oxidation to improve the device's performance but the speed of this oxidation is slow and required the introduction of the aforementioned additives. However, the spiro-MeOTAD presents limitations as the compound is sensitive to temperature and moisture. In particular, its pristine structure is vulnerable to crystallization due to thermal stress at temperatures higher than 100°C leading to troubling the contacts at the interface<sup>10</sup>. These predicaments affect the contact at the interface. Furthermore, the doped spiro-MeOTAD<sup>+</sup> presents a rapid degradation starting at 85°C as the presence of dopants, sure tBP, evaporates from the layer as well with its oxidation. This leads concomitantly to the degradation of the perovskite with the presence of pinholes in the devices. Moisture is also detrimental for the perovskite layer with the formation of  $\text{PbI}_2(\text{g})$  degradation product.

The spiro-MeOTAD solution is made of 110 mg/mL in 1000  $\mu\text{L}$  of chlorobenzene. The dopants are prepared separately with a stock solution of LiTFSI (520 mg/mL in acetonitrile) and a stock solution of FK209 (400 mg/mL in acetonitrile). The stock solution can be kept for 14 days under  $\text{N}_2$  atmosphere. During the annealing of the perovskite sample, the dopants are add-up to the spiro-MeOTAD solution. For 110 mg of powder, we need 17  $\mu\text{L}$  of FK209 stock solution, 25  $\mu\text{L}$  of LiTFSI stock solution, and 45  $\mu\text{L}$  of tbP commercial solution. The final vial is agitated and deposited under dynamic through spin-coating (3000 rpm / 1500 rpm.s<sup>-1</sup> / 30 s). The final layer color is green on top of the perovskite layer.

#### 2.1.4.2 PTAA

The poly[bis(4-phenyl)(2,4,6-trimethylphenyl)amine (PTAA) is a semiconductor polymer classified as a polytriphenylamine<sup>10</sup>. Thanks to the presence of the benzene ring in its structure, the polymer can

Institut Polytechnique de Paris  
91120 Palaiseau, France



transfer carrier through the layer and guide the hole carrier toward the top contact. This molecule was proposed as an alternative HTL and hence replacement for spiro-MeOTAD<sup>11</sup>, making smooth and stable layers even at 300°C<sup>10</sup> for the pristine structure. Note that this behavior does not change much when the PTAA is p-doped. As mentioned previously, even if the spiro-MeOTAD presents good performance, this layer suffers from poor stability to the presence of humidity, making this compound less compatible than PTAA for long-term device utilization. The PTAA is made of 10 mg/mL in 1000 µL of toluene. For 10 mg of PTAA, we add 3.75 µL of tbP and 2.4 µL from the stock solution of LiTFSI. The final vial is agitated and we deposited the same way as the spiro-MeOTAD layer. The device's final color is brown after deposition.

### 2.1.5 Metal contact

The device is completed with a top metal contact, which is usually made of gold, deposited by vacuum thermal evaporation. Before the gold deposition, the samples are chemically etched on the border to reach the glass/FTO layer and establish the contact (-) using acetonitrile and DMF solvent (Figure 2.5 (a) to (b)). The samples are then placed in a metal evaporator PLASSYS - MEB550SL. With the shadow masks available at IPVF, we can place up to 16 samples in one deposition, defining a sample batch as presented in Figure 2.5 (c). The contact (+) is marked with the 4 x 4 mm<sup>2</sup> square on the center of the device. The device is completed with copper tape to help us connect the device during the JV and EQE measurement.

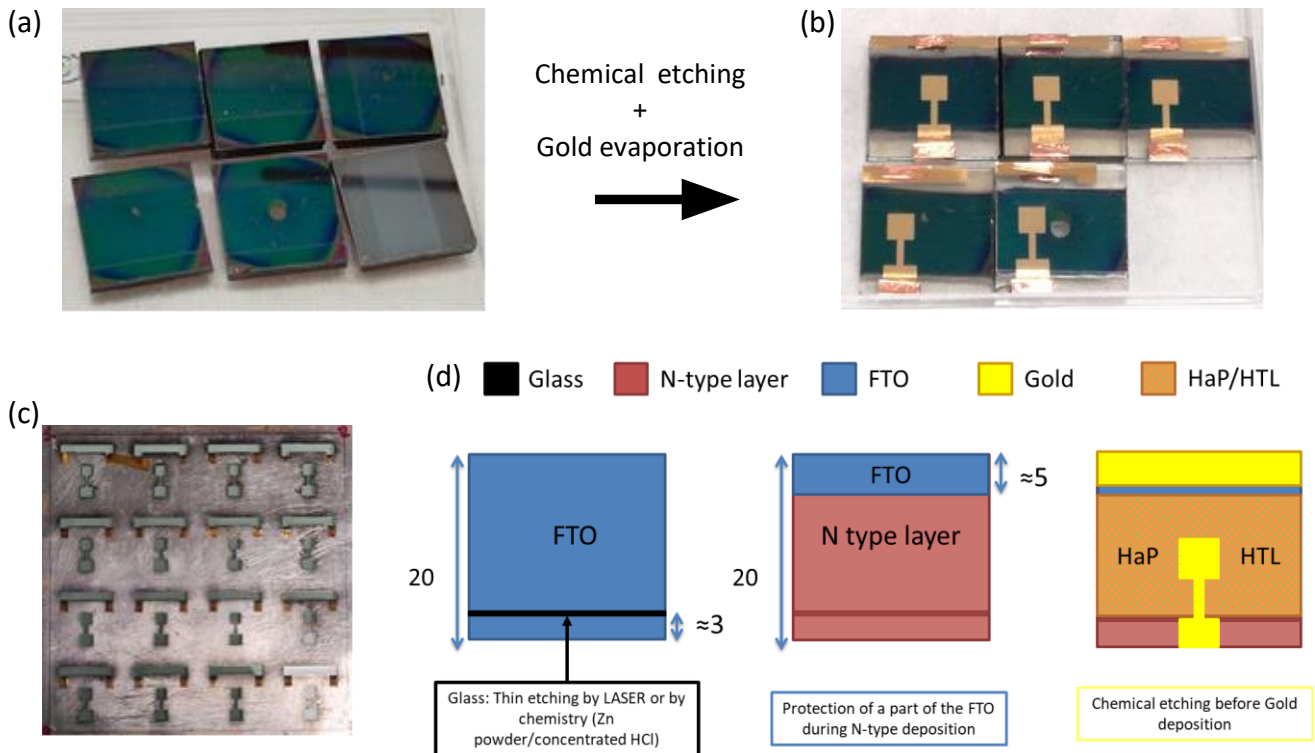


Figure 2.5: Devices (a) before and (b) after chemical etching and gold deposition. (c) Metallic shadow mask for gold deposition, (d) Schematic of the several etching steps in solar cell fabrication in IPVF

## 2.1.6 Alternative surface modifiers and interfaces layers studied

In this work, the focus is made on the optimization of the perovskite/charge transport layer interfaces in the perovskite solar cell, considering different families of compounds introduced as interlayers (protection, passivation properties) or as replacement of active and transport layers (interface quality, stability and band alignment):

- HTL/perovskite interlayer: adamantane and its derivatives, PMMA
- ETL/perovskite interlayer: self-assembled monolayers (collaboration with ITODYS), PMMA-PCBM

### 2.1.6.1 Adamantane and its derivatives

Adamantane (AD) is a colorless and crystalline chemical compound. This is a small hydrophobic and compact hydrocarbon molecule composed of three imbricated cyclohexane rings. Due to its structure, the molecule is then poorly soluble in water as no polar ligands are present but highly soluble in an organic solvent compatible with the glovebox's deposition process. AD exhibits no anchoring group that could lead to defect passivation of the perovskite absorber. For that reason, Institut Polytechnique de Paris

91120 Palaiseau, France

two adamantane derivatives are introduced: 1-adamantanamine (1ADA) and 1-adamantanamine hydrochloride (1ADAHCl), presented also in Figure 2.6. These derivatives incorporate an amino site (-NH<sub>2</sub>) as well as doping with HCl for the 1ADAHCl. Defects can come from the vacancy of the A-site of the perovskite crystal, corresponding to the amino group MA<sup>+</sup>, FA<sup>+</sup> or Cs<sup>+</sup>. The derivatives can interact more efficiently with the perovskite crystal structure by filling these defects with the amine group. Adding these groups will help to reduce the charge recombination on the surface of the absorber by stabilizing the crystalline structure.

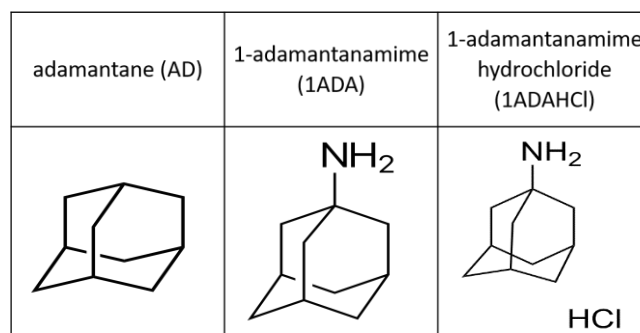


Figure 2.6: Skeletal formulas of adamantane (AD), 1-adamantanamine (1ADA), 1-adamantanamine hydrochloride (1ADAHCl)

Deposited on top of the perovskite layer, the coating aims to produce a hydrophobic layer on top of the perovskite absorber. Since the perovskite layer is sensitive to humidity and water<sup>12</sup>, adding these molecules should improve the protection of the absorber from these induced degradations. As inspiration from the publication of Tavakoli et al.<sup>13</sup>, 1.5 mg of powder is dissolved in 1 mL of chlorobenzene in the case of AD, and a mix of chlorobenzene/isopropanol (2:1) for the derivatives. 100  $\mu$ L of the solution is spin-coated at 4000 rpm/s for 24 s. All the samples are then annealed for 15 min at 110°C. For a hydrocarbon, AD melting point is quite high, at 270°C, which is an indicator of its thermal stability, as well as 1ADA and 1ADAHCl whose respective melting points are at 208°C and 308°C.

### 2.1.6.2 PMMA and PCBM

PMMA (poly(methyl methacrylate)) and PCBM ((6,6)-Phenyl C61 butyric acid methyl ester) well-known polymers are used as interface layers in the device. The ones that we used are commercial products. PCBM is a derivative of the fullerene C<sub>60</sub> highly used in organic solar cell technologies (Figure 2.7A)<sup>14,15</sup>. Deposited at the interface HaP/ETL, this molecule is an electron acceptor and helps with the diffusion of electron carriers in the device. With a low valence band, this material is

a blocking layer for the hole carriers. In the case of PMMA, it is a polymer produced through radical polymerization. The monomer methyl methacrylate is presented in Figure 2.7B.

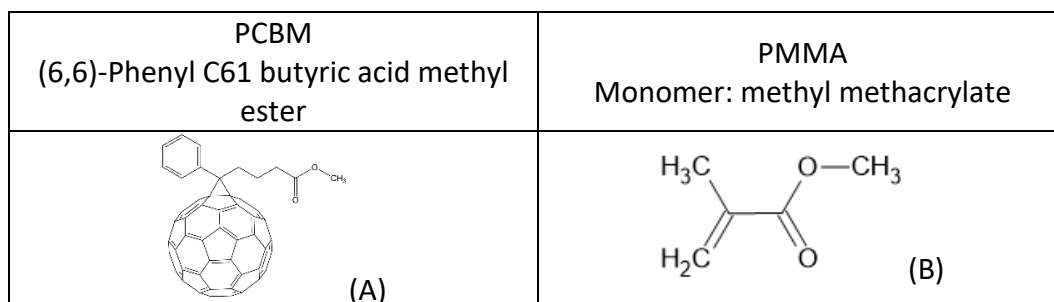


Figure 2.7: Skeletal formula of PMMA's monomer, methyl methacrylate, and PCBM, (6,6)-Phenyl C61 butyric acid methyl ester

PMMA can passivate the perovskite surface by forming a complex with the under-coordinated lead atoms  $Pb^{2+}$ <sup>16</sup> and fill the gap on the ETL layer, reducing the faulty contact on the surface and the non-radiative recombination. In this work, both precursors PMMA and PCBM are bought commercially as powders. The PMMA is used at the top and the bottom interface hoping to form bilayer passivation. 0 to 20 mg/mL of PMMA in chlorobenzene is spin-coated on top of the perovskite layer at 4000 rpm, 1000 rpm/s to deposit the possible passivate layer. On the bottom interface, PMMA is mixed with PCBM<sup>17,18</sup> to increase the hole-blocking effect and increase the electron transport exchange. Several ratios are tried for 1:1 to 1:5 with 1 mg/mL of PMMA to X mg/mL of PCBM. The solution is deposited by spin-coating on the ETL at 3000 rpm, 1500 rpm/s, and then by perovskite absorber deposition. Further details about the process variations are described in the corresponding sections of Chapter 5.

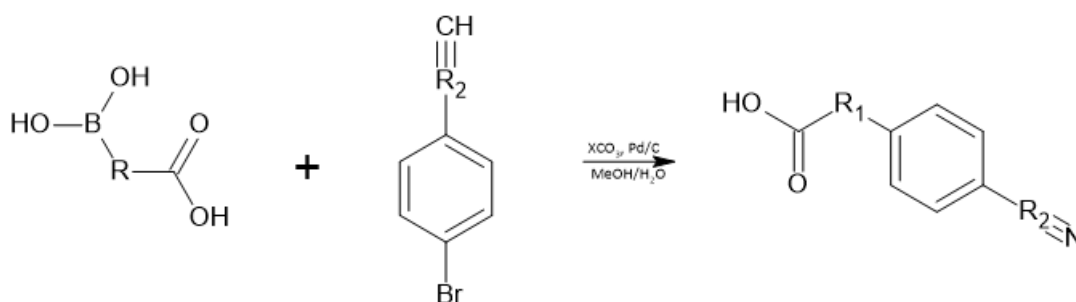
### 2.1.6.3 Aminocarboxylic acids molecules self-assembled monolayer

The molecules for the SAM formation (hereafter abbreviated as SAM  $N$ , with  $N = 1 - 7$ ) have been synthesized and prepared in the ITODYS laboratory and are summarized in table 4.1.<sup>19</sup> The one exception is SAM 1 being the only commercially acquired molecule. The SAM 2 molecule is a derivate from the protonation of the SAM 1 molecule through acid treatment. The synthetis will explain for the SAM 7. The process is similar for all the different SAMs. First, they made through a nucleophilic substitution to obtain the first precursors of cyanophenyl carboxylic acid (SAM 5 and SAM 6) or cyanobiphenyl carboxylic acid (SAM 3, 4, 7).

The first synthesis step is the fabrication of the cyanocarboxylic acid. Depending on the target SAMs, the precursors are changed, but the reaction pathway stays the same. The choice of the precursors depended on the wanted SAM. The choice is on several criteria as mentioned before: a compatible

a) Step 1 : Synthesis of a cyanocarboxylic acid

A mixture of 4-carboxybenzeneboronic acid (24 mmol), 4-bromobenzonitrile (24 mmol), sodium carbonate (48 mmol) and palladium on carbon (1.20 g) are mixed in 100 mL of methanol/water (1:1). The solution is heated up at 77°C overnight. After filtration, the solution is partially evaporated and concentrated on acid by adding some chlorhydric acid (HCl 1N) to reach a pH of 4.0 to 4.5, which triggers the precipitation of the product. The precipitate is then filtered and washed with water to obtain the de-protonated acid. The synthesis products were verified via  $H^1$  NMR to determine if the right product was obtained. This cyanocarboxylic acid type is used afterward as the precursor of the SAMs. The synthesis is similar for all of the SAM with an adjustment of the precursor for the wanted SAM.

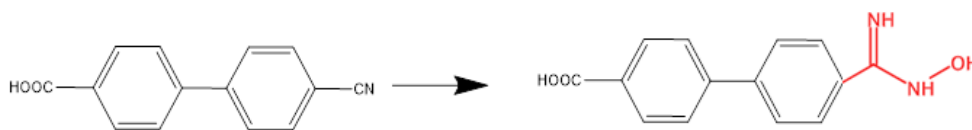


*Reaction 2.1: Catalytic nucleophilic substitution with boronic acid as a nucleophile ( $R_1$ =none, Phenyl or  $CH_2$  /  $R_2$ =none or  $CH_2$ )<sup>19</sup>*

b) Step 2 : Synthesis of the amidoxime molecule from the cyano molecule

For the first step of preparing SAM 7, we mix 4'-Cyano-[1,1-biphenyl]-4-carboxylic acid (4 mmol) in 30 mL of ethanol. Next, we add  $NH_2OH$ , HCl (8.56 mmol) mixed in 3 mL of water and 6 mL of water concentrated with  $K_2CO_3$  (6.48 mmol), and 2 mg of 8-hydroxyquinoline. This solution was put in a reflux montage and left from 4h to a whole night under mechanical agitation. The solvent is eliminated under vacuum using a Rotavap. 30 mL of water is added, and the pH is adjusted to 3.2 using HCl (2M). After filtration and cleaning with water, a white-green solid is obtained. The remaining solution can be filtered twice again using an ethyl acetate as an extractant to collect more

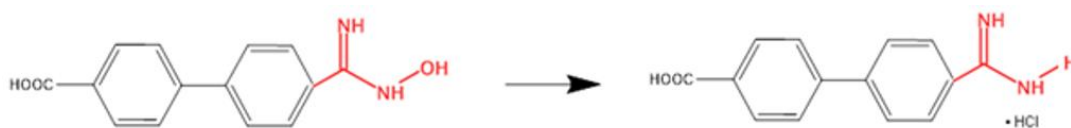
precipitate. All the powders are dried, filtered and condensed under vacuum to obtain a final green powder (4'-amidoxime [1,1'-biphényl] -4-carboxylic acid), as in Reaction 2.2.



*Reaction 2.2: Chemical synthesis reaction from the cyano molecule to the functionalized amidoxime molecule. Example of the SAM 7*

c) Step 3 : Synthesis of 4'- amidino -[1,1'-biphényl]-4-carboxylic acid hydroiodide

For the second synthesis step, 15mg of the new-made powder is mixed with 5mL of acetic acid anhydride and dissolved in 40 mL of icy acetic acid. To accelerate the reaction, 10% of Pd/C is added under a catalytic quantity. Then, launch in a Parr agitator under 50 psi of H<sub>2</sub>, the system is placed under ambient temperature for 23.5 hours. A salt is obtained after filtration, i.e., washing in ethanol and concentration in vacuum. The product is then dissolved in ethanol anhydride containing 5M of HCl, filtered, and washed under EtOH anhydride to get the chlorhydrate salt, as in Reaction 2.3.



*Reaction 2.3: Chemical synthesis reaction from the amidoxime molecule to the SAM 7 after the incorporation of chlorhydrate salt*

The work for the full PSC device fabrication featuring the molecular SAMs as interlayers between the ETL and the perovskite absorber has been executed within a dedicated weekly schedule (Table 4.2). Glass/FTO/c-TiO<sub>2</sub> samples are cut and prepared for the deposition of mesoporous TiO<sub>2</sub> following the conventional IPVF elaboration procedure (see Chapter 2 § 2.1.1). After the annealing, the samples are placed in small boxes and sent to ITODYS in a transport tube under N<sub>2</sub> atmosphere to minimize exposure to ambient atmosphere and contamination.

At ITODYS, the samples (Glass/FTO/c-m TiO<sub>2</sub>) are annealed at 450 °C for one hour and then washed under sulfuric acid. This treatment produces a more accessible site, a metal salt of TiSO<sub>4</sub>, for the SAMs to anchor and form metal carboxylate groups on the surface. Following this step, the molecules are deposited on the Glass/FTO/c-m TiO<sub>2</sub> stack by chemical bath deposition under a solvent of methanol or DMF. The molecules are synthesized, as described above, and characterized through Infrared and Raman spectroscopy. With these methods, it is possible to make sure of the

Institut Polytechnique de Paris

91120 Palaiseau, France

molecular structure of the grafted SAMs before the finalization of the cell in IPVF Lab. Results are presented in Chapter 4. The samples are placed back in a transport tube and transfer to IPVF.

This finalization step consists in the deposition of the lead halide perovskite layer, the spiro-MeOTAD and the gold contact. Finally, the fresh devices are measured by current-voltage measurement and external quantum efficiency to give a rapid idea of the evolution of the performance with respect to the reference sample. The reference sample undergoes the conditions as the SAM-deposited samples, but with no SAMs. The time of the deposition process is referred in Table 2.3.

	Day 1- Monday	Day 2-Tuesday	Day 3- Wednesday	Day 4- Thursday	Day 5-Friday
Localization of the samples	IPVF	IPVF to ITODYS	ITODYS	ITODYS to IPVF	IPVF
Actions taken	<ul style="list-style-type: none"> <li>• Cleaning of the samples</li> <li>• Compact TiO<sub>2</sub> deposition</li> </ul>	<ul style="list-style-type: none"> <li>• Mesoporous TiO<sub>2</sub> deposition</li> <li>• Preparation of the samples in a glovebox</li> <li>• Samples sent to ITODYS (afternoon)</li> </ul>	Grafting of the molecules for 24h	<ul style="list-style-type: none"> <li>• Taking back the samples</li> <li>• Perovskite + Spiro-OMeTAD</li> </ul>	<ul style="list-style-type: none"> <li>• Gold deposition</li> <li>• JV measurement</li> </ul>

Table 2.3: Weekly schedule for the deposition process of the SAM-perovskite solar device

## 2.2 Electrical characterization techniques

### 2.2.1 Current Density-Voltage (JV) measurement

The solar cell behavior in an electrical circuit can be associated with a diode. When the solar cell is illuminated with photons with an energy higher or equal to the bandgap energy of the active layer, namely the perovskite layer here, the corresponding energy absorbed by the perovskite consequently leads to the excitation of an electron from the valence band to the conduction band, leaving a hole in the valence band. The generated carriers are transported to the interfaces or recombined depending on the drift-diffusion, carrier mobility, charge extraction and interface properties.

The current-voltage measurement is an optoelectrical measurement to determine the electric parameters of the photovoltaic device and obtain its power conversion efficiency (PCE): the short-circuit current density ( $J_{sc}$ ), the open-circuit Voltage ( $V_{oc}$ ), and the Fill factor (FF).

$$PCE (\%) = \frac{P_{mpp}}{P_{inc}} = \frac{V_{mpp} \times J_{mpp}}{P_{inc}} = \frac{V_{oc} \times J_{sc} \times FF}{P_{inc}}$$

- $P_{mpp}$ ,  $V_{mpp}$ , and  $J_{mpp}$  are the power, voltage, and current density taken at the maximum power point. The maximum power point corresponds to the maximum power  $P_{mpp}$  that can be provided by the cell.
- $P_{inc}$  is the power of the incident energy of the lamp set at 1 sun.

Theoretically, the JV curve cumulated the curve of a solar cell diode in the dark with the light-generated current and shifted the JV curve down. When operating in the dark, it is possible to retrieve the device's series and shunt resistance.

$$I = I_L - I_0 \left[ e^{\left(\frac{qV}{nkT}\right)} - 1 \right] - I_S = I_L - I_0 \left[ e^{\left(\frac{q(V+IR_S)}{nkT}\right)} - 1 \right] - \frac{V + IR_S}{R_{SH}}$$

With:

- $R_S$  is the resistance series of the solar cell. Its value depends on the layers of the stack;
- $R_{SH}$  is the shunt resistance of the solar cell. Its value depends on the defects of the structure;
- $V$  is the voltage of the cell terminal;
- $I$ ,  $I_0$ , and  $I_L$  correspond to the current of the cell, the dark saturation current, and the light-generated current;
- $n$ ,  $k$ ,  $q$ , and  $T$  correspond to the ideality factor, the Boltzmann constant, the elementary charge, and the temperature (K).

The systems used at IPVF are the Oriel 6 and Oriel 8 sun simulator Sol3A and class AAA from Newport Corporation. The Oriel 6 sun simulator has a 6 x 6 inches lamp alimented with a Xenon source and 8 x 8 inches for the Oriel 8. The sun simulators are linked to a data analysis software to exploit the current density and the voltage measured. The bias range of the voltage is between -0.2V to 1.2V with a sweep rate of 20 mV/s. A forward scan (FW) and reverse scan (RV) are made the measure the hysteresis parameter of the cells. The sample is measured in a superstrate configuration, with the cell illuminated through the glass substrate, as presented on Figure 2.1. During the aging under light,

the sample's maximum power point (MPP) is tracked in time from a few minutes to a month's timescale. This is made using an ARKEOS illuminator specifically dedicated to aging experiments that proceed in ambient air and under constant illumination.

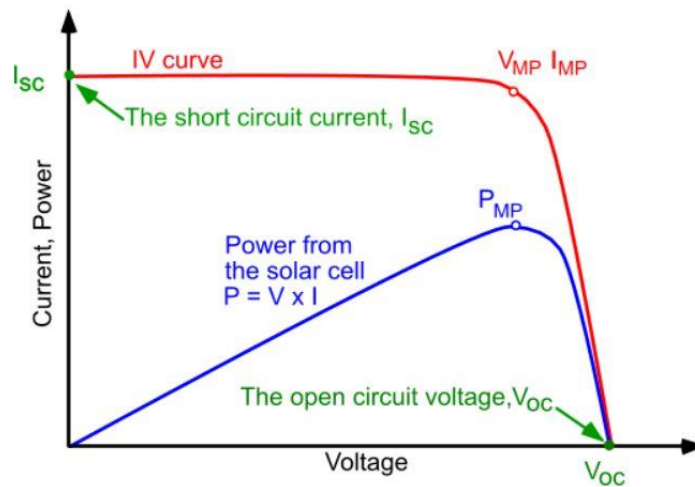


Figure 2.8: *JV curve description with the maximum power point annotation [Example taken from pveducation.org<sup>20</sup>]*

### 2.2.2 External quantum efficiency (EQE)

Quantum efficiency (QE) is the ratio of the quantity of carrier collected by the solar cell for a number of photons ( $d\phi$ ) of a given energy incident ( $d\lambda$ ) arriving on the solar cell. For example, if all of the photons at a given energy are absorbed and the minority carrier generated is collected, the QE at this energy is 100%. The QE of photons with an energy below the bandgap is equal to zero. For an ideal solar cell, the QE curve looks like a square Figure 2.9, which is not the case for most solar cells. The deviation from ideal behavior mostly comes from the recombination effects in the device. Generally, a phenomenon damaging the collection probability also affects the quantum efficiency. The external quantum efficiency (EQE) is the number of electrons provided to the external circuit per photon incident on the device. In the external configuration, the reflection and the transmission effects lead to additional contributions to the curve measured. An example is presented in Figure 2.9.

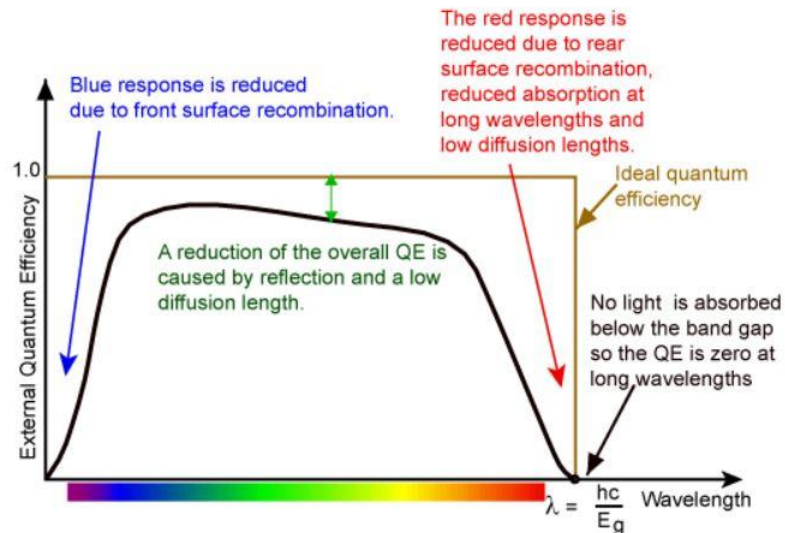


Figure 2.9: External quantum efficiency of a solar cell with the contribution of the mechanisms applied on the device [Example of pveducation.org <sup>21</sup>with a CIGS sample]

$$\text{EQE} = \frac{\text{number of carrier collected by the cell}}{\text{number of incident photon on the device}}$$

As for JV measurements, the device is measured in a superstrate configuration with the light sent through the glass substrate. All interfaces are influencing the collected information. In the low energy range, the EQE is influenced by bottom surface recombination, low absorption from the low energy of the photon as well as the diffusion length; in the mid energy region, by the reflection and the diffusion length of the carriers from the bulk; and in the high energy range by top surface recombination as well as the reduced absorption at long wavelengths. Thanks to interface engineering and optimization of the constitutive layers of the stack, the EQE spectral response can be modulated.

Experiments are realized with an Oriel IQE200 coupled with a Keithley 2400 for the source measurement of a 300W xenon lamp, ranging from 300 nm to 820 nm.

## 2.3 Optical characterization techniques

### 2.3.1 Absorption, transmission, reflection

These values are measured using a UV-visible spectrophotometer. The spectrophotometer (Agilent Cary 5000 spectrophotometer) is composed of two detectors: a R928 PMT for the UV-Visible and a Cooled PbS for the IR. It also contains a light source of tungsten halogen sufficient for our working range between 300 nm to 820 nm. The samples are substrate side toward the beam light. Depending

on the position of the reflective mirror with the sample surface, the instrument measures the absorption, transmission, or reflection.

$$A(\%) = 100 - T - R$$

The value is material dependent. Furthermore, we can also determine the optical bandgap of absorbers and semiconductors using the tauc plot method or the tangent method to extract the data from the absorption curve.

### **2.3.1.1 Photoluminescence**

Photoluminescence (PL) is operated by placing the sample under a laser beam with an energy higher than the one of the bandgap (535 nm), leading to the generation of an electron-hole pair and the excitation of the electron to the conduction band. Due to the beam's high energy, the electron's relaxation is coupled with heat losses and radiative recombination close to the bandgap. The system measures the PL of the semiconductor emitted through fluorescence. Depending on the defects present in the material, the PL signal also changes. If the defects energies are near the bandgap, they are observed in the form of radiative recombination. This will lead to an accumulation of signals and an increase in the PL. However, if the defects energies are far from the bandgap, there are counted as non-radiative recombination. Therefore, the higher the concentration of these defects, the lower the PL signal would be. In our case, time-resolved (TRPL) measurements enable short lifetime characterization and decay tracking.

## **2.4 Structural characterization techniques**

### **2.4.1 Scanning electron microscopy**

Scanning electron microscopy (SEM) with a Zeiss Merlin VP compact 35 field emission gun microscope characterizes the surface morphology of samples. The sample is irradiated by a focused electron beam whose energy is sufficient to generate ejection of electrons, either from core levels and associated de-excitation mechanism radiative and non-radiative (for example, fluorescence and Auger respectively). In particular, secondary electrons are detected, and by scanning the beam on the surface, an image is generated that is representative of the surface composition (atomic number contrast) and morphology (peak and valley contrast). The measurements can be done on the top of the samples or by cross-section. In the present case, the perovskite layer is deposited on top of 3 mm glass/FTO, usually causing charging effects that can be counterbalanced by the deposition of a few nanometer layers of carbon with a primary vacuum metallizer tool. In the present case,

Institut Polytechnique de Paris

91120 Palaiseau, France



operating conditions are a 1.5 mm working distance and a low voltage of 1kV to prevent the perovskite layer's degradation as much as possible.

### **2.4.2 X-ray diffraction**

X-ray diffraction (XRD) is a technique used to primarily characterize material properties such as crystal structure or crystal size determination. The working principle relies on Bragg diffraction to determine the lattice spacing in the crystalline solid. When the X-ray beam impinges on the material, the X-ray beam is reflected in specific directions depending on the beam's wavelength and the crystal lattice's dimensions and orientation. Through elastic scattering in the crystal lattice, the atomic plans emit scattering waves that interfere constructively on specific angles to form the diffraction. With the perovskite layer, we can identify its crystal structure as well as the evolution of the material after aging. X-ray diffraction analyses are realized with a PANALYTICAL Empyrean equipment with a Bragg/Brentano measurement to do  $\theta$ - $2\theta$  angle to determine the crystalline structure of the perovskite layer and to see if there is any modification of the bulk crystallinity with the passivation.

## **2.5 Surface chemical characterization**

### **2.5.1 X-ray Photoelectron Spectroscopy principle**

X-ray Photoelectron Spectroscopy (XPS), also called PhotoEmission Spectroscopy (PES) 23 analyses were performed to complete the analytical pathway and get insights on the surface chemistry before and after interlayer deposition. In Chapter 3 “A potential new family of additives for the perovskite solar cell top interface: adamantane and its derivatives”, this surface analysis technique was used to validate the deposition process and evaluate the surface protection capabilities of the different interlayers (ageing study), in Chapter 4 “Development and tests of synthesized amino carboxylic acids: an approach to the bottom interface” it was employed to attest for the grafting of the molecules. XPS is particularly interesting here as it brings key information about surfaces and interface chemistry, making it an ideal toolkit for this thesis research work dealing with interface optimization. Implementing this technique (and related ones) has become practically systematic to qualify photovoltaic materials and device studies and has proven unavoidable for perovskite technologies. It can address many topics, including elaboration of new active layers and interlayers, stability issues or ageing mechanism understanding<sup>22</sup>.

The experiments were done at ILV (Institut Lavoisier de Versailles), at the CEFS2 (Centre d'Etude et de Formation en Spectroscopies électroniques de Surfaces) connected with the EPI team (Electrochimie et Physico-chimie au Interfaces), and at ITODYS (Interfaces Traitements Organisation et DYnamique des Systèmes, Paris).

This technique is based on X-ray/material interaction to characterize the electronic structure. Photons bombard the sample with an energy  $\hbar\omega$  sufficient to induce the ionization and emission of core level or valence electrons. This can only happen if the energy of the photons exceeds a threshold for the photoelectric effect. The three steps of the photoemission process are schematized in Figure 2.10.

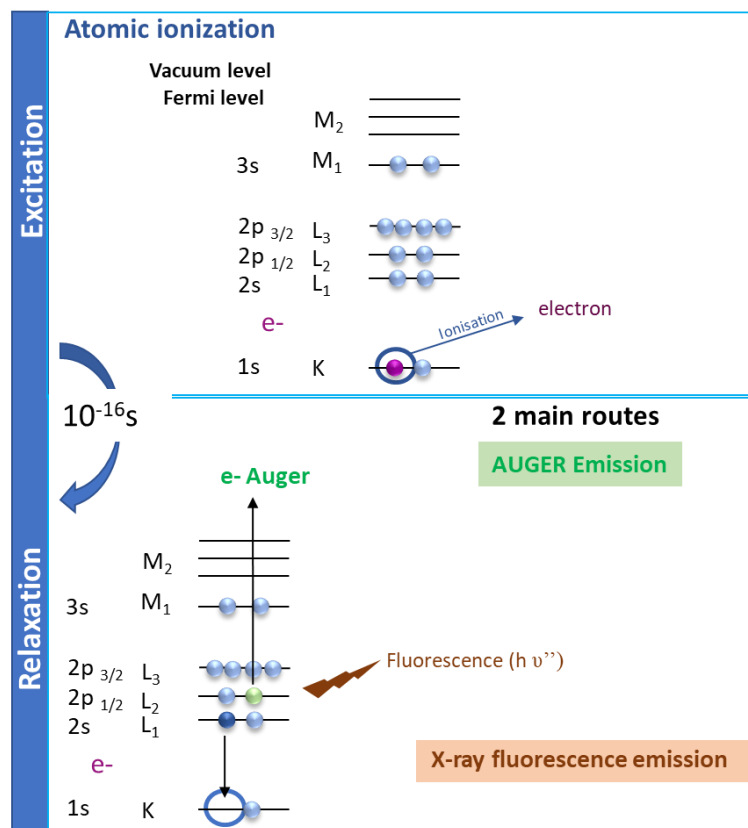


Figure 2.10: Schema of the level transition (1) X absorption, photoelectric effect and photoelectron emission, (2) de-excitation by X fluorescence and Auger electron emission

The kinetic energy of the emitted photoelectrons is measured by the detector, leading to the equation:

$$E_C = \hbar\omega - E_B - \phi_{sp}$$

- $E_C$  corresponds to the kinetic energy of the emitted photoelectron;

- $E_B$ , the binding energy of the atomic orbital from which the electron originates or the difference between the initial and the final states after the electron leaves the atom (scaled to the Fermi level)
- $\Phi_{sp}$ , the spectrophotometer work function.

Analyses are realized under UHV conditions ( $3.10^{-7}$  mbar) to maximize the electron collection and preserve the surface state. A schematic view of the spectrometer is presented Figure 2.11. The photons are emitted from an Al k- $\alpha$  X-ray monochromatized source with an energy of 1486.6 eV. Electrons emitted in the solid angle of the hemispherical analyzer are collected and filtered in energy. This analysis technique is inherently surface sensitive as the depth probed is limited by the escape depth of photoelectrons which is usually in the range of 5-15 nm depending on the sample characteristics which govern the inelastic mean free path of the photoelectrons in the material. Photoelectrons with sufficient energy (and emitted in the solid angle of the analyzer) will be ejected and measured to contribute either to the signal of characteristic photopeaks or to the background and loss features.

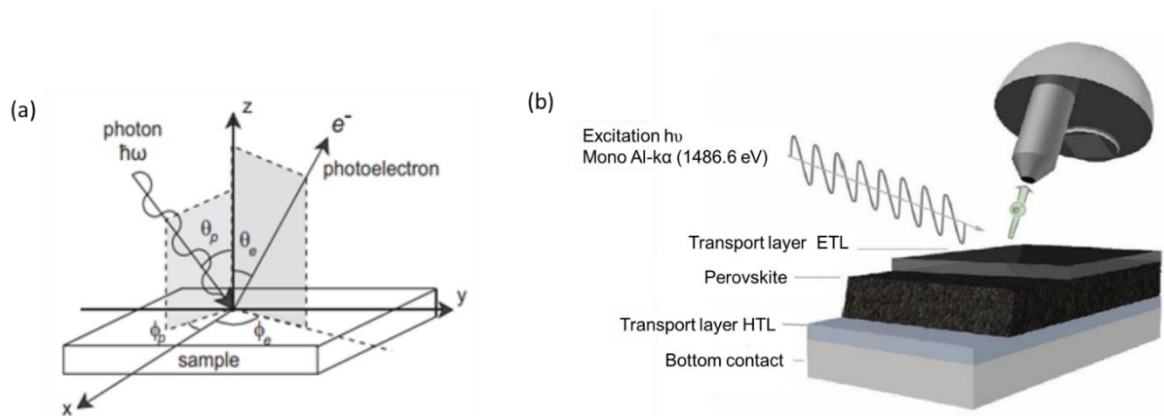


*Figure 2.11: Schematic of the XPS analysis principle (a) interaction X-ray beam / sample (angles correspond to geometry collection of the electrons), (b) implementation of this technique to the present research work*

This method is, at first sight, non-destructive on most surfaces but sometimes requires caution, such as in the case of perovskite materials prone to degradation toward UHV and X-rays irradiation namely<sup>22</sup>. We benefit here from the metrological and methodological expertise developed in the frame of the IPVF-ILV partnership<sup>23</sup> to determine the good practices to obtain reliable information and identify possible artefacts, preventing them from proposing hazardous interpretations.

Finally, if necessary, the use of an ion gun enables to profile the in-depth composition by sequential sputtering or just the cleaning of the sample. But here also, caution has to be taken as the bombardment is also source of analysis artefacts<sup>23</sup>. ILV -CEFS2 set up are equipped with  $\text{Ar}^+$  and  $\text{Ar}_n^+$  sources and a flood gun, employed for insulating samples to overcome charging effects, but preventing them from discussing photopeaks energy position.

XPS surface analyses were carried out using at ILV Lab a Thermo Scientific K-Alpha+, NEXSA spectrometer and a Thermo Scientific Escalab 250 Xi spectrometer equipped with a monochromatic Al-K $\alpha$  X-Ray source (1486.6 eV). The spectrometer at ITODYS lab is also an Escalab 250 Xi,



*Figure 2.12: Thermo Scientific NEXSA Escalab and 250 Xi spectrometers used for surface characterization*

Calibration of the spectrometers was done using Cu and Au samples following the ASTM-E-902-94 standard procedure.

Storage and transfer conditions are of great importance to preserve the initial information<sup>22</sup>. Sample preparation and analyses were synchronized to minimize film fabrication and characterization delay. The samples were stored under glove box atmosphere in dark conditions (packed in plastic boxes covered with aluminum foils) using dedicated transfer tubes sealed inside the glovebox. The maximum delay before introduction inside the XPS spectrometer was 2-3 hours. Introduction inside the analysis chamber was operated as soon as the optimal  $3 \cdot 10^{-7}$  mbar pressure was reached in the load lock.

## 2.5.2 X-ray Photoelectron Spectroscopy spectra description

Both survey spectra, presenting the overall composition along the entire energy scale, and high energy resolution spectral regions (hereafter named HR spectra) of the main elements were acquired.

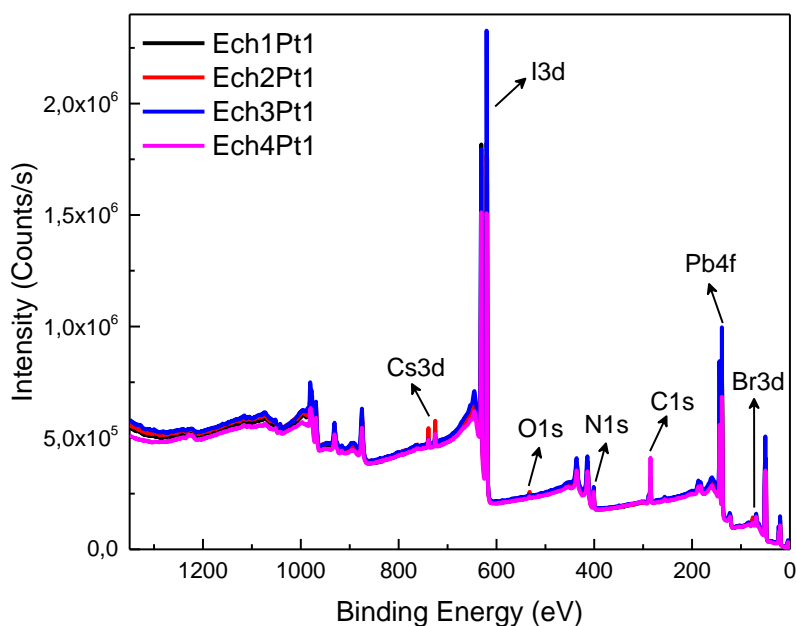


*Figure 2.13: Survey spectra of the perovskite active layer measured on the half-cell Glass/FTO/c-TiO<sub>2</sub>/MA<sub>0.14</sub>, FA<sub>0.86</sub> Cs<sub>0.05</sub>Pb(Br<sub>0.16</sub>, I<sub>0.84</sub>)<sub>3</sub>. The selected peaks for high energy resolution spectra acquisition are labeled.*

The survey spectra bring the overall composition of major and minor elements but the peaks' resolution does not permit to inform about the chemical environments precisely. Nevertheless, this type of analysis is fast (<10 min) and used to verify the surface composition homogeneity by proceeding to a mapping (3-4 points randomly dispersed). This is also the starting point to attest that the perovskite composition is conformal to the expected composition of the baseline, meaning there was no modification due to the deposition process, the storage or the transfer steps. This verification is realized for each batch by conserving 1 sample as a reference without HTL or ETL layer. Table 2.4 shows the results obtained for four reference samples (2.5 x 2.5 cm<sup>2</sup>) from 4 different batches on which five random analysis points were realized. XPS results highlight the good

reproducibility of the perovskite layer deposition process with a composition in agreement with the targeted one. Note that the current deposition process (described in section 2.1.3) systematically measures iodine surface enrichment with the surface-sensitive XPS technique.

Atomic %	Batch 1	Batch 2	Batch 3	Average	S.D
Br	4.8	4.2	4.6	<b>4.5</b>	<b>0.3</b>
O	1.5	4.0	1.4	<b>2.3</b>	<b>1.5</b>
C	36.4	39.4	35,0	<b>36.9</b>	<b>2.2</b>
Cs	0.4	1.3	0.4	<b>0.7</b>	<b>0.5</b>
I	30.7	27.9	31.8	<b>30.1</b>	<b>2.0</b>
N	16.3	13.9	16.4	<b>15.5</b>	<b>1.4</b>
Pb	9.9	9.2	10.4	<b>9.8</b>	<b>0.6</b>

	Ratio theo	Batch 1	Batch 2	Batch 3	Average	S.D
I / (I+ Br)	<b>0.84</b>	0.87	0.87	0.87	<b>0.87</b>	<b>0,00</b>
Pb / (I+ Br)	<b>0.33</b>	0.28	0.29	0.29	<b>0.29</b>	<b>0.01</b>
Cs / Pb	<b>0.05</b>	0.04	0.14	0.04	<b>0.07</b>	<b>0.06</b>
Cs / (I + Br)	<b>0.02</b>	0.01	0.04	0.01	<b>0.02</b>	<b>0.02</b>
N / Pb	<b>1.77</b>	1.65	1.51	1.57	<b>1.58</b>	<b>0.07</b>
N / (I + Br)	<b>0.62</b>	0.46	0.43	0.45	<b>0.45</b>	<b>0.02</b>

Table 2.4: XPS composition obtained from survey spectra of the perovskite layer realized on 4 reference samples ( $2.5 \times 2.5 \text{ cm}^2$ ) from 3 batches in 5 point analyses randomly dispersed at the surface of the half-cell Glass/FTO/c-TiO<sub>2</sub>/MA<sub>0.14</sub>, FA<sub>0.86</sub> Cs<sub>0.05</sub>Pb(Br<sub>0.16</sub>, I<sub>0.84</sub>)<sub>3</sub>. (a) Atomic composition from Br 3d, O 1s, C 1s, Cs 3d<sub>5/2</sub>, I3d<sub>5/2</sub>, N1s and Pb4f<sub>7/2</sub> photopeaks, (b) corresponding ratios.

This homogeneity is also evidenced by the superimposition of the HR spectra in Figure 2.14. One would note the very low O content at 532.5 eV, attributing to adventitious carbonaceous contamination.

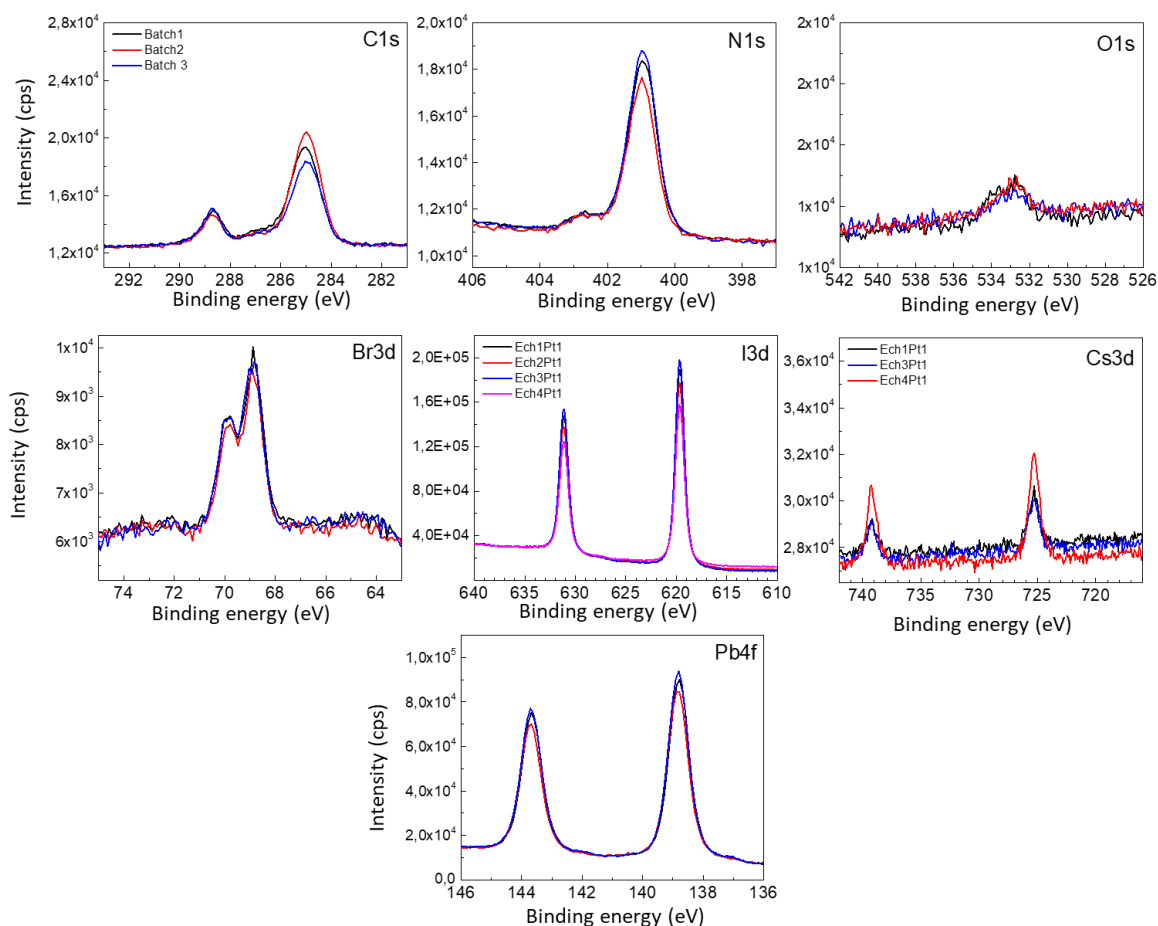
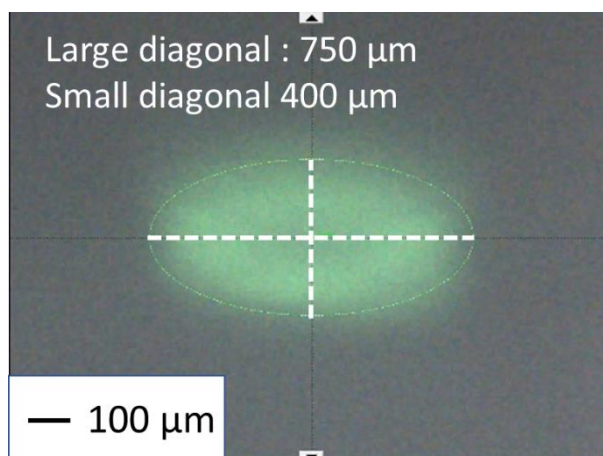


Figure 2.14: HR spectra measured on the samples of Table 2.4

Acquisition parameters for survey spectra and high energy resolution spectral windows are CAE (Constant analyzer Energy) 100 eV, step 1 eV dwell time 100 ms and CAE 20 eV, step size 0.1 eV, dwell time 100 ms respectively. For surface analysis, the exposure to X-ray was optimized and limited to 1 hour per spot measurement as well as the analyses sequence starting with more sensitive elements, i.e. prone to migration or evaporation (survey start - I3d - Pb4f - N1s - C1s- Cs1s - Br3d 5min - O1s - Survey end). The stability of the perovskite layer was verified by comparing two survey spectra on the same spot, at the beginning and the end of the acquisition sequence.

Figure 2.16 shows the X-ray beam's impact on a phosphorus samples (used for spot size calibration) on the NEXSA spectrometer. The dimensions of the elliptic spot are 750 x 400  $\mu\text{m}$ . The spot size of the Escalab 250 Xi is a little bit higher. For information, with the Al source of 72 W (12 kV, 60 mA) and the spot size of "400 $\mu\text{m}$ ", the corresponding X-ray dose is estimated at  $5 \cdot 10^{11}$  photons/s/ $\text{mm}^2$  and thus almost  $2 \cdot 10^8$  photons/ $\mu\text{m}^2$  for 1h.



*Figure 2.15: Impact of the 400  $\mu\text{m}$  X-ray spot of the NEXSA equipment on a P reference sample*

Thermo Fisher Scientific Thermo Scientific™ Avantage data system was used for data treatment and peak fitting (detailed later) of HR spectra. A Shirley background subtraction was applied and spectra were modeled using a convolution of Lorentzian/Gaussian (L/G) contributions representative of the chemical environments and a Powell fitting algorithm. Avantage directly proceeds to the correction of the transmission factor and of the energy compensation, i.e. the inelastic mean free path term (here according to the TPP-2M model). The sensitivity factors used are the sensitivity factors from the constructor library (SF ALTHERMO1). The main adjustment parameters of the contributions are the energy position, the width, the L/G %, the distance between two contributions, and their area ratio (for exemple for a spin orbit doublet). The energy position, and thus chemical environment or oxidation degree attribution, is verified from the literature. A peak shift indicates either a change in the chemistry (new environment, change in the atomic network, ...) or a charging effect. For example, the more an element is near an electronegative environment, the more the bonding energy increase which causes a shift of the elemental peak. A summary table of the main fitting parameters is presented in Table 2.5.

Scan	Reference	Name	Peak BE	Peak Ratio	FWHM fit param (eV)	L/G Mix (%) Product
<b>I 3d</b>	A	I 3d5	620 ± 0.5		0.98 (0.5:1.5)	25.00
<b>Br 3d</b>	D	Br 3d5	68.8 ± 0.5		0.94 (0.5:1.5)	25.00
	E	Br 3d3	D + 1.04	D*0.67	D*1	25.00
<b>Pb 4f</b>	B	Pb4f7	139 ± 0.5		0.75 (0.5 : 3.5)	81.79
<b>Cs 3d</b>	C	Cs3d5	725 ± 0.5		1.08 (0.5 : 3.5)	85.00
<b>N 1s</b>	F	N1s FA	401 ± 0.5		0.97 (0.5 : 1.5)	55.59
	G	N1s MA	F + 1.5 (± 0.2)		1.15 (0.5 : 1.5)	F*1
<b>C 1s</b>	H	C1s C-C	285 ± 0.5		1.27 (1.1 : 1.35)	55.00
	I	C1s C-O	H+1.00 (±0.1)		1.35 (1.1 : 1.35)	55.00
	J	C1s C=O	H+2.60 (±0.1)		I*1	55.00
	K	C1s RCOOH	H+5.00 (±0.05)		I*1	55.00
	L	C1s FA	288.7 ± 0.2		0.95	55.00
	M	C1s MA	L – 1.5 (± 0.2)			55.00
<b>O 1s</b>	N	O1s Cont	533 ± 0.5		2.96 (0.5 : 3.5)	68.46
<b>Cl 2p</b>	O	Cl2p3	198.6 ± 0.5		1.50 (0.7 : 1.5)	75.00
	P	Cl2p1	O+1.60 (±0.1)	O*0.5	O*1	75.00

*Table 2.5: Main fitting parameters adopted for our XPS peak data treatment*

An XPS Survey, I 3d, Pb 4f, N 1s, C 1s, Cl 2p, Cs 3d, Br 3d, O 1s, and an XPS survey in the end from acquisition from 13 min 43 s to 20 min 45 s for 1ADAHCl sample (fresh and aged in N<sub>2</sub> conditions) and from 20 min 45 s to 24 min 26 s (aged in the air). The two XPS surveys are acquired to check the fixed positions on the peak. A shift of the perovskite on the last XPS survey indicated a degradation of the perovskite layer during the analysis. Thanks to this analysis, the chemical structure of the perovskite on the surface can be quantified. Furthermore, as a surface modifier layer is deposited on top of the perovskite, the absorber signal is attenuated and masked given that the depth probing is up to 10 nm. The samples are measurement in several times. First, there are “fresh” measurements one day after the perovskite deposition. Then, for the aging test, the samples are

placed in different conditions for several days, followed by an XPS spectrum. This way, the degradation of the perovskite layer is followed by the evolution of the peak contribution from C 1s, N 1s, Pb 4f, and O 1s.

## 2.6 Resume

In this chapter 2, we described the various tolls and experiments done during this thesis to assist us during this through our projects. We start by describing the perovskite solar cell produced in IPVF and the layers we used. At the start of my PhD, my best reference device of record performance was at 11.9 % (9.39 % in forward bias) with the stack glass/FTO/c-m TiO<sub>2</sub>/HaP/Spiro-MeOTAD/Gold. After 3 years and half of modifications, improvements and adjustments, my best reference sample has a record of 19.8% (15.1% in Forward bias) with glass/FTO/SnO<sub>2</sub>/HaP/Spiro-MeOTAD/Gold. Using several characterizations methods, I try to determine the effect of our changes on the devices from surface characterizations to electrical characterizations. This panel of methods helps to have an overall overview of our samples. To improve the devices' stability and performance, my thesis aimed to use alternative surface modifiers to improve the interfaces on the devices. These works are separated into three projects chapters in this thesis: Chapter 3 “A potential new family of additives for the perovskite solar cell top interface: adamantane and its derivatives”, Chapter 4 “Development and tests of synthesized amino carboxylic acids: an approach to the bottom interface” and Chapter 5 “Another alternative: understanding and application of polymethacrylate PMMA in a device”. In the following Chapter 3, this chapter described the work done on the top interface HaP/HTL using adamantane and its derivatives with the objective to protect against humidity in the perovskite layer.

## 2.7 References

1. Messing, G. L., Zhang, S.-C. & Jayanthi, G. V. Ceramic Powder Synthesis by Spray Pyrolysis. *J. Am. Ceram. Soc.* **76**, 2707–2726 (1993).
2. Fournier, O. Synthèse par ALD et caractérisation de couches extractrices d'électrons pour application dans les cellules à base de pérovskite solaires. (2021).
3. Zardetto, V. *et al.* Atomic layer deposition for perovskite solar cells: Research status, opportunities and challenges. *Sustain. Energy Fuels* **1**, 30–55 (2017).
4. Saliba, M. *et al.* How to Make over 20% Efficient Perovskite Solar Cells in Regular (n-i-p) and Inverted (p-i-n) Architectures. *Chem. Mater.* **30**, 4193–4201 (2018).
5. Kim, S. Y. *et al.* Effects of potassium treatment on SnO<sub>2</sub> electron transport layers for improvements of perovskite solar cells. *Sol. Energy* **233**, 353–362 (2022).
6. Meier, T. *et al.* Impact of excess PbI<sub>2</sub> on the structure and the temperature dependent optical properties of methylammonium lead iodide perovskites. *J. Mater. Chem. C* **6**, 7512–7519 (2018).
7. Ma, Z. *et al.* Excess PbI<sub>2</sub> evolution for triple-cation based perovskite solar cells with 21.9% efficiency. *J. Energy Chem.* **66**, 152–160 (2022).
8. Saliba, M. *et al.* Cesium-containing triple cation perovskite solar cells: Improved stability, reproducibility and high efficiency. *Energy Environ. Sci.* **9**, 1989–1997 (2016).
9. Bach, U. *et al.* Solid-state dye-sensitized mesoporous TiO<sub>2</sub> solar cells with high photon-to-electron conversion efficiencies. *Nature* **395**, 583–585 (1998).
10. Rombach, F. M., Haque, S. A. & Macdonald, T. J. Lessons learned from spiro-OMeTAD and PTAA in perovskite solar cells. *Energy Environ. Sci.* **14**, 5161–5190 (2021).
11. Watthage, S. C., Song, Z., Phillips, A. B. & Heben, M. J. *Evolution of perovskite solar cells. Perovskite Photovoltaics: Basic to Advanced Concepts and Implementation* (Elsevier Inc., 2018). doi:10.1016/B978-0-12-812915-9.00003-4.
12. Aftab, A. & Ahmad, M. I. A review of stability and progress in tin halide perovskite solar cell. *Sol. Energy* **216**, 26–47 (2021).
13. Tavakoli, M. M. *et al.* Adamantanes Enhance the Photovoltaic Performance and Operational Stability of Perovskite Solar Cells by Effective Mitigation of Interfacial Defect States. *Adv. Energy Mater.* **8**, 1–7 (2018).

14. Wang, J., Datta, K., Weijtens, C. H. L., Wienk, M. M. & Janssen, R. A. J. Insights into Fullerene Passivation of SnO<sub>2</sub> Electron Transport Layers in Perovskite Solar Cells. *Adv. Funct. Mater.* **29**, (2019).
15. Hu, L. *et al.* Unravelling the role of C<sub>60</sub> derivatives as additives into active layer for achieving high-efficiency planar perovskite solar cells. *Carbon N. Y.* **167**, 160–168 (2020).
16. Peng, J. *et al.* A Universal Double-Side Passivation for High Open-Circuit Voltage in Perovskite Solar Cells: Role of Carbonyl Groups in Poly(methyl methacrylate). *Adv. Energy Mater.* **8**, 1–9 (2018).
17. Turren-Cruz, H., Hagfeldt, A. & Saliba, M. Methylammonium-free, high-performance, and stable perovskite solar cells on a planar architecture. <http://science.sciencemag.org/>.
18. Aydin, E., De Bastiani, M. & De Wolf, S. Defect and Contact Passivation for Perovskite Solar Cells. *Adv. Mater.* **31**, 1–20 (2019).
19. Kouki, H. *et al.* Tailor-Made Amino-Based Self-Assembled Monolayers Grafted on Electron Transport ZnO Layers: Perovskite Solar Cell Performance and Modified Interface Relationship. *ACS Appl. Energy Mater.* **5**, 1635–1645 (2022).
20. PV Education.
21. <https://www.pveducation.org/>. Quantum efficiency of CIGS.
22. Béchu, S., Ralaiarisoa, M., Etcheberry, A. & Schulz, P. Photoemission Spectroscopy Characterization of Halide Perovskites. *Adv. Energy Mater.* **10**, 1–25 (2020).
23. Cacovich, S. *et al.* Light-Induced Passivation in Triple Cation Mixed Halide Perovskites: Interplay between Transport Properties and Surface Chemistry. *ACS Appl. Mater. Interfaces* **12**, 34784–34794 (2020).

## Chapter 3: A potential new family of molecular additives for the perovskite solar cell top interface: adamantane and its derivatives

In Chapter 1, we position ourselves in the current context of the perovskite solar and the work done at the interfaces, exposing our position for the perovskite field. In Chapter 2, I have made an exhaustive list of the methods and experiments used during this thesis. This panel of techniques helps to try to understand what happens for the devices and at their interfaces. This chapter first presents my first project in this thesis using adamantane and its derivatives at the top interface HaP/HTL. In this work, I go from surface characterization at the interface to device characterization using XPS and JV measurements to understand how these molecules affect the devices. In parallel, the devices' performances of the devices stay the same as I don't succeed in improving with *c-m* TiO<sub>2</sub>. In the end, 1ADAHCl showcases the preservation of the perovskite layer in the short-term.

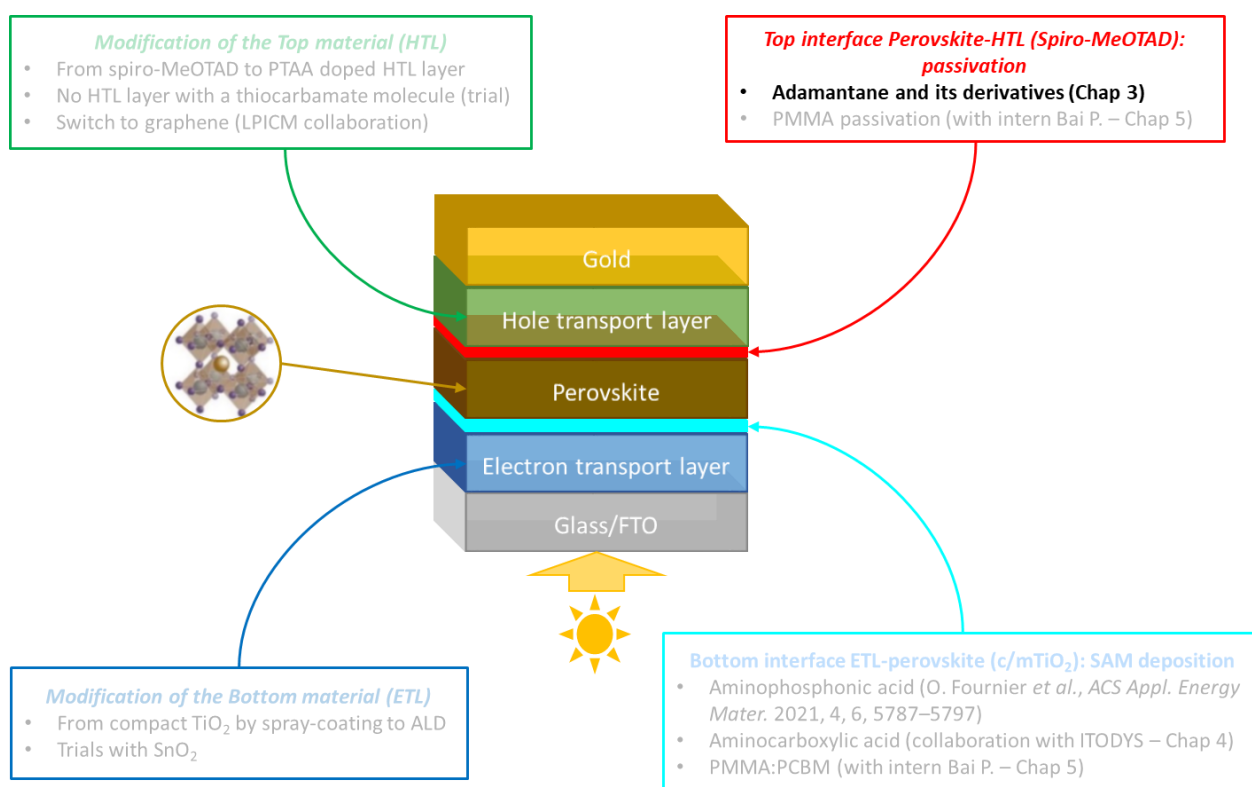


Figure 3.1: Schematic of the working steps through this thesis on NIP configuration perovskite solar cells. Highlight on top interface with Chapter 3

## Table of Contents

3.1	Adamantane molecules and its derivatives .....	86
3.2	Incorporation trials in the device .....	87
3.2.1	Morphology characterization .....	87
3.2.2	Integration of adamantane-based surface modifiers into perovskite solar cells and device characterization .....	91
3.2.3	Evidence for molecular adsorption .....	95
3.2.4	Optoelectronic characterization of perovskite films with adamantane surface modification .....	106
3.2.5	Expanded device series for optimization and reproducibly of PSCs with AD-based interlayers .....	110
3.2.6	Aging of perovskite films and devices with adamantane-based interlayer.....	112
3.2.7	Conclusion .....	123
3.2.8	References.....	124

### 3.1 Adamantane molecules and its derivatives

The interface plays a major role in improving perovskite solar cells stability and performance. Here, we focus on the perovskite surface passivation with adamantane (AD), an organic molecule, and its derivatives, 1-adamantanamine (1ADA) and 1-adamantanamine hydrochloride (1ADAHCl). AD is a diamondoid, a bulky organic molecule constituted of three fused cyclohexane rings (Figure 3.2), and was recently employed to successfully improve PSC device performance and stability by Tavakoli et al<sup>1</sup>. The molecule is thermally stable (melting point 269°C) and hydrophobic thanks to its rigid and strain-free structure. 1ADA and 1ADAHCl exhibit an amino site ( $-NH_3$ ) on one of the tertiary carbons. By passivating the HaP/Hole transport layer (HTL) interface with these molecules, our goal is to further improve the device's performance and stability by reducing charge recombination and protecting the perovskite layer against humidity. Since the components of the HaP used here comprise formamidinium and methylammonium on the A site of the crystal structure, 1ADA and 1ADAHCl compounds can fill surface vacancies at these sites (Figure 3.2). In this study, I investigate the deposition of AD, 1ADA, and 1ADAHCl on a triple cation lead mixed halide perovskite (HaP) film and the impact on the HaP structural and optoelectronic properties.

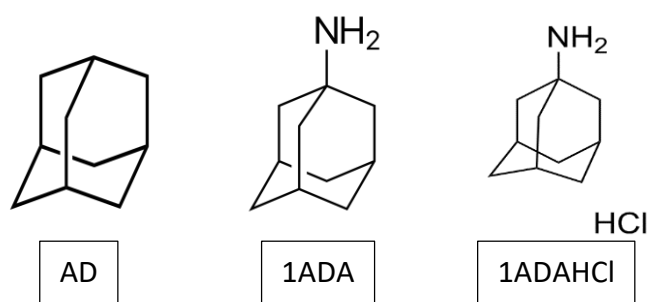


*Figure 3.2: Adamantane (AD) and its derivatives: 1-adamantanamine (1ADA) and 1-adamantanamine hydrochloride (1ADAHCl)*

Furthermore, I provide a detailed surface chemistry analysis by photoemission spectroscopy and track the perovskite film aging through surface modification. Eventually, we introduce the AD-derivatives in PSC devices and monitor the evolution of the performance parameters over time when the devices are exposed to ambient conditions. In this way, we find that AD-based interlayers can be employed in PSCs as an intermediate interface modification that leads to inherently more resilient HaP films and devices. We project that in combination with further interface engineering

on the back side and enhanced encapsulation, our approach can help to extend the lifetime of perovskite photovoltaic technologies further.

## 3.2 Incorporation trials in the device

### 3.2.1 Morphology characterization

Adamantane and its derivatives are used as surface modifiers on the top interface. To dissolve the powder, several mixes of solvents are trialed. Morphology changes like the presence of pinholes and cavities in the layer, can have multiple origins. This phenomenon can be due to applying solvent on the HaP film, which can lead to degradation of the perovskite as shown in the examples in Figure 3.3, where HaP films were exposed to several solvents that are typically used in the spin-coating process to determine the solvent's effect on the absorber.

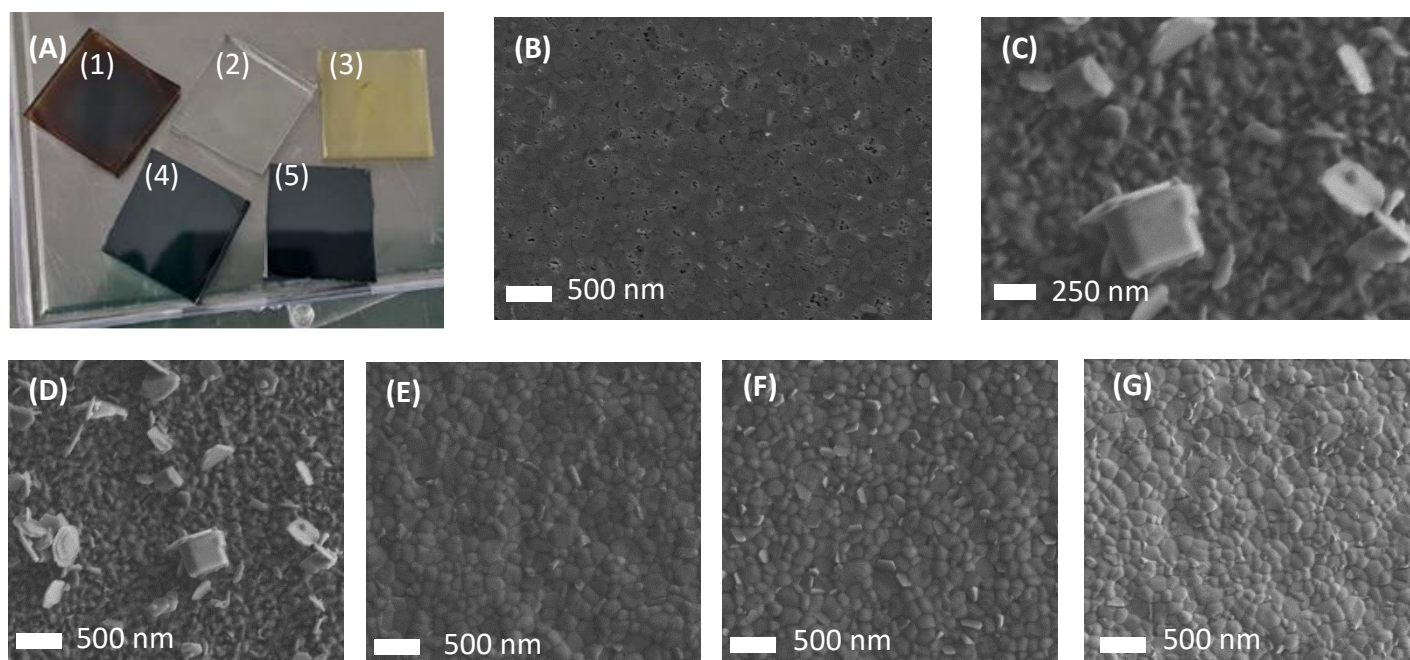


*Figure 3.3: (A) Photograph of glass/FTO/perovskite samples bathed for several hours in a solvent ((1) in IPA (2) in acetone (3) in acetonitrile (4) in toluene (5) in chlorobenzene). (B-F) Corresponding SEM images of perovskite films exposed to (B) IPA, (C) acetone, (D) acetonitrile, (E) toluene and (F) chlorobenzene (G) non-exposed perovskite film reference.*

Aside from the visual changes in the photographs (Figure 3.3A), SEM images (Figure 3.3B to F) reveal the changes on the microstructure. In IPA (B), a start of degradation is noticeable with the presence of pinholes on the absorber. In acetone (C) and acetonitrile (D), the absorber is completely degraded leaving on the surface the FTO layer. In toluene (E) and chlorobenzene (F), the perovskite layer

seems quite stable with no noticeable pinholes. For the deposition of surface modifiers, it will be better to stick if possible to solvents like chlorobenzene or toluene to avoid the degradation of the perovskite layer. IPA can also be used but for a short period to avoid the formation of pinholes. As this sample was exposed for several hours in IPA to reach this state, in the range of time of a spin-coating deposition, the degradation of the HaP is almost not existent. In the end, the adamantane is dissolved in chlorobenzene, which is compatible as chlorobenzene is an organic compound. However, in the case of 1ADA and 1ADAHCl, a solvent with a higher relative polarity is needed to completely dissolve the precursors. The powders are partially dissolved in IPA first until dissolution and partially adjusted with chlorobenzene to reach a mix of IPA/chlorobenzene (1:2).

Starting with the perovskite surface morphology analysis, the SEM top-view images of the HaP film surface with and without AD-based surface modifications reveal a similar size and distribution of grains (Figure 3.3(b) and (c)). All images are taken at a magnification of 50 000 using a working distance of 3 mm. The surface modifier layer is not observed on top of the perovskite layer or cross-section, indicating that any additional surface layer would be very thin (< 5 nm), as in Figure 3.4.

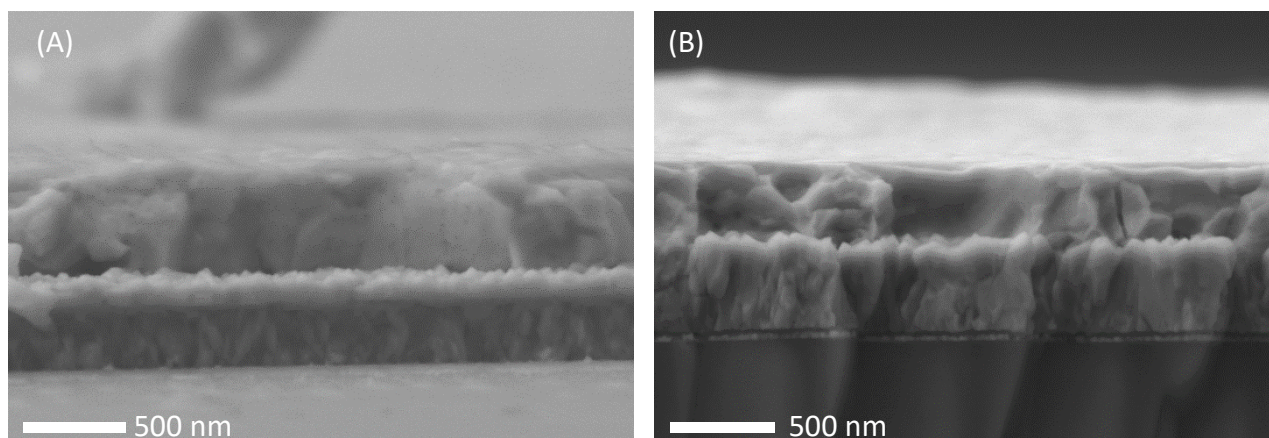


*Figure 3.4: Cross section of HaP layer (A) Reference sample (B) 1ADAHCl-deposited sample*

Since the grain size and boundaries in the perovskite play a role in the movement of charge carriers and have the propensity to aggregate defects leading to recombination, our results indicate that the perovskite film remains mostly unchanged in this regard upon the treatment with the AD derivatives. Further of note, some of the grains light up in brighter colour in the SEM images of the control sample and the samples treated with AD and ADA. This effect is usually attributed to the presence of  $\text{PbI}_2$  grains in accordance with the  $\text{PbI}_2$  excess in the precursor composition <sup>2,3</sup>.

In the next step, I employed X-ray diffraction (XRD) measurements to evaluate further potential structural changes of the perovskite film upon deposition of the AD molecules on top, presented in Figure 3.5.C. The diffraction peaks of the perovskite crystal structure are shown for the reference sample (control samples) where the peaks of the perovskite crystal structure are marked with an (\*). The peak positions of the perovskite do not change as a function of the additive treatment, indicating that the bulk crystal structure is unaffected. Notably, the amount of  $\text{PbI}_2$  in the layers does not vary across the sample series. In summary, SEM and XRD measurements reveal that the additives do not significantly modify the bulk of the perovskite material. We assume that the modifiers are confined to the surface of the perovskite and modify the interface to any subsequent layer. Therefore, we can wonder how the surface of the perovskite layer has changed and has been affected electrically and chemically in the presence of these molecules.

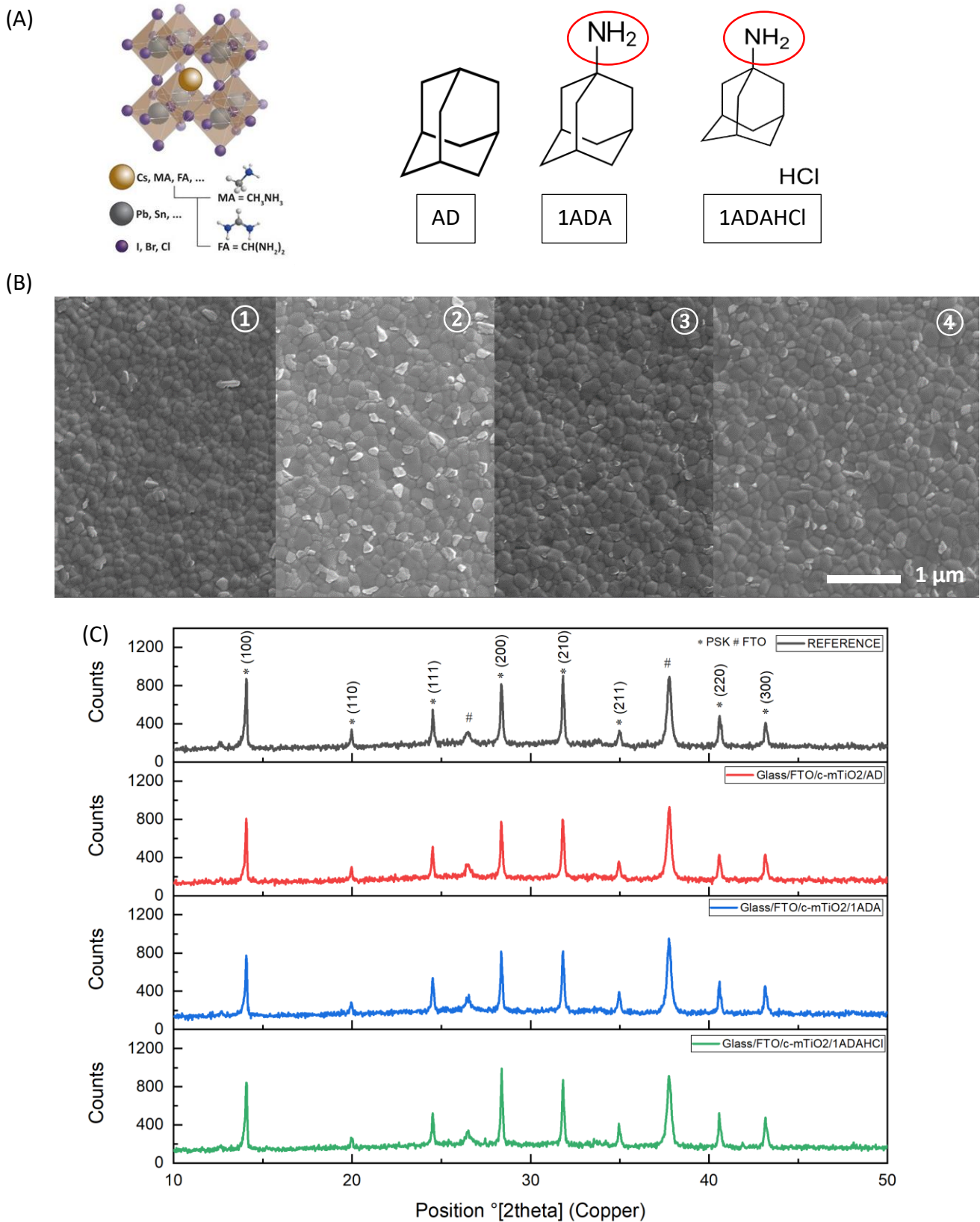


Figure 3.5: (A) Perovskite crystal structure and molecular structure of adamantane and its derivatives used in this study. (B) SEM images of the surfaces of glass/FTO/perovskite samples with (1) AD (2) 1ADA (3) 1ADAHCl on top and (4) a control sample, (C) XRD measurements of Institut Polytechnique de Paris

*glass/FTO/c-mTiO<sub>2</sub>/perovskite samples with additives compared to the control sample*

### **3.2.2 Integration of adamantane-based surface modifiers into perovskite solar cells and device characterization**

Throughout the thesis work, several tests were performed to determine the optimal conditions for applying the molecular surface modifications of the perovskite films in the device. The additives are deposited on top of the perovskite to improve the HTL/HTL interface for its hydrophobic properties as protection against moisture ingress. For the deposition, the same spin-coating method as described for the half-cells was used to apply the additive interlayers in the device. The samples are not taken out from the N<sub>2</sub> atmosphere between the perovskite and the HTL deposition in the glovebox to avoid adding impurities in the materials from outside between depositions. Since this development occurred over the same period as the evolution of the perovskite process fabrication in IPVF, we were also tracking the improvement in the device performances through the years. Of note, over the course of these experimental series and device batches, we find that many extrinsic factors can influence the perovskite solar cell fabrication process, including the lab's environmental conditions, such as the humidity and temperature control. This is further compounded by the fact that precursor starting materials, solvents, and small details of the deposition process can affect film drying and formation processes. Thus, multiple cells and batches have been produced for the various conditions and all device data is presented with the concomitant statistics to evaluate the spread in the reported values.

For the concentration, I aim for a low concentration of around 1.5 mg/mL, as a high concentration produces a thicker layer of hydrophobic additives that could obstruct the transfer of charge carriers from the perovskite to the HTL. Generally speaking, adamantane and its derivatives are electrically insulating hydrocarbons with 1ADA and 1ADAHCl containing an amino site, which does not improve the electrical properties. Thus the adamantane would form a transport-blocking layer on top of the perovskite that carriers would traverse via the tunneling effect. With a thicker layer, the tunneling effect is significantly impeded, and carriers can no longer pass through the molecular interlayer leading to a reduction of current, which we observe as the thickness of the layer increases. Therefore, the preliminary parameter used for the adamantane deposition was 1.5 mg/mL deposited in dynamic spin-casting mode, i.e., dropping the solution on the already spinning sample. The formation of ultra-thin layers via this method was previously confirmed in section 3.2.2 by XPS.

Devices were made in the first preliminary tests to check if the chosen deposition method is coherent and if the additives on top of the perovskite affect the device characteristics. After these initial attempts, the focus shifted to the optimization of the deposition method and further adjustments. First, I established a comparison between two types of deposition methods: antisolvent deposition (AS deposition) and spin-coating deposition (SC deposition), which has been described and used in the results presented before. The principal difference between those two is the point in time when the adamantane-based molecules are incorporated as additives into the perovskite layer. For the antisolvent method as an alternative to the previously studied (sections 3.2.2 and 3.2.3), the additive is mixed into the perovskite antisolvent and is, therefore, likely more interspersed in the final perovskite thin film. As the additives cannot fit in the crystalline structure of the perovskite layer (Goldschmidt tolerance factor:  $t = \frac{R_A + R_x}{\sqrt{2}(R_B + R_x)} = 1.23$  with adamantane radius at 495 pm), the adamantane and its derivatives are possibly present in the grain boundaries of the perovskite layer. For the spin-coating method, an additional layer is deposited on top of the perovskite after the annealing of the perovskite for 30 minutes. Deposited at 4000 rpm on a static deposition, the samples are spin-coated with a solution of surface modifiers and annealed for 15 minutes afterward. With this method, the additives are deposited on the annealed perovskite layer, forming a thin layer on top of the absorber. To compare the two methods, i.e. AS and SC deposition methods, devices are made and characterized using the current density-voltage (JV) curve and EQE.

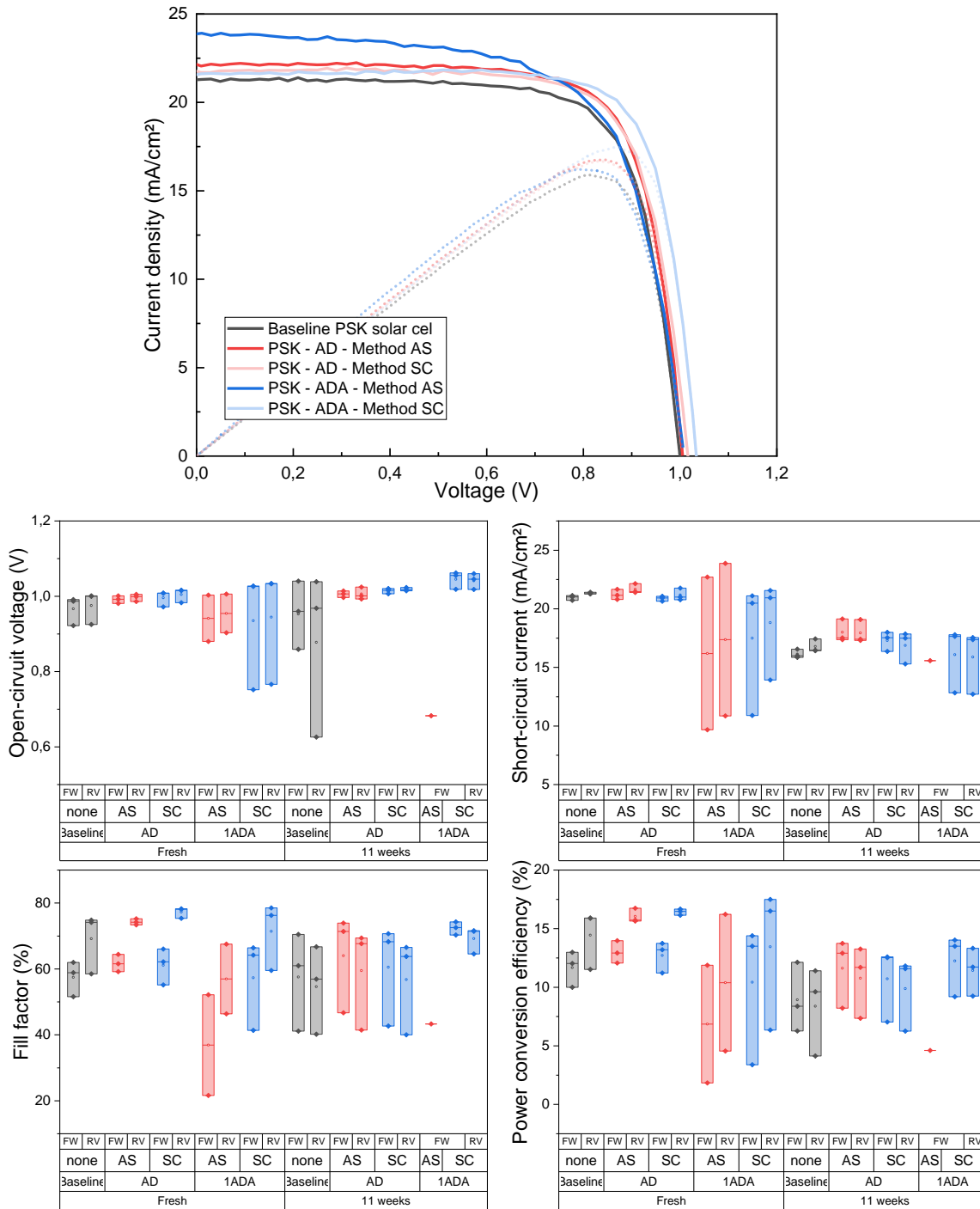


Figure 3.6: (a) JV curves of the best devices after gold deposition and (b) solar cells parameters of HaPSC measured fresh (after the gold deposition) and after 11 weeks comparing the antisolvent method and the spin-coating method using AD and 1ADA as an additive

Conditions	Method	Bias	Voc (V)	Jsc (mA/cm <sup>2</sup> )	FF (%)	Efficiency (%)
Reference	/	Forward	0.99	20.7	58.9	12.0
		Reverse	1.00	21.3	74.8	15.9
AD	AS	Forward	1.00	21.7	64.4	14.0
		Reverse	1.00	22.5	75.2	16.8
	SC	Forward	1.01	21.1	62.2	13.2
		Reverse	1.02	21.8	75.4	16.7
1ADA	AS	Forward	1.00	22.7	52.2	11.9
		Reverse	1.01	23.9	67.5	16.2
	SC	Forward	1.03	21.1	66.4	14.4
		Reverse	1.03	21.6	78.5	17.5

*Table 3.1: JV parameters of the corresponding best devices after gold deposition (fresh)*

When comparing this batch's solar cell parameters data, I used only the AD and 1ADA molecules for these experiments to achieve reasonable statistics. For the sample at day 0, a comparison of the best samples JV curve and table are shown in Figure 3.6 and in Table 3.1. We observe an improvement in device performance compared to the reference device, with an increase in current and open-circuit voltage in the presence of the surface modifiers. From the preceding XRD analysis, we know that the SC deposition of AD and 1ADA molecules did not change the perovskite's crystalline quality and that we do not modify the bulk crystal structure in this method. Hence, we attribute the improvement of the devices to better carrier extraction at the interface to the HTL. Furthermore, the higher Voc improvement is likely linked to an improvement of the contact interface through the passivation of defect states, leading to an overall increase in device efficiency. Interestingly the perovskite film formation could be changed in the AS deposition method, which could yield a difference in absorption and hence the higher currents we observe. When comparing the AS and SC deposition method results, the values are similar in the AD case. However, for 1ADA, the SC method results in higher performances with an increase of up to 1.03 V in  $V_{oc}$  and an efficiency of 17.5 % (FW:14.4%) of efficiency. In summary, the spin-coating deposition after the perovskite annealing resulted in better and more reproducible device characteristics.

The samples were remeasured after 11 weeks of storage under inert conditions in the dark for comparison. For the open-circuit voltage, a slight improvement after 11 weeks is noticeable for the SC method compared to the AS method indicating a further improvement of the contact interface with the presence of additives with respect to the fresh samples. Furthermore, for both AD-deposited and 1ADA-deposited devices, the increase in short-circuit current density with respect to the reference samples remained even after the 11 weeks of storage. Of note, we still measure a

significant hysteresis showing mostly in the fill factor of the devices. While this hysteresis has not been reduced with the additives, an increase of the fill factor in forward bias for AD samples indicates a slight decrease in the device's non-radiative recombination.

By comparing the deposition method, no significant difference in the solar cell parameters can determine which method is better. The two methods produce devices at similar performance levels. We find the SC method to be the better choice for the long term as stable devices last longer with this method upon visual inspection, whereas the samples treated with the AS method showed earlier signs of discoloration. No sample with 1ADA made using the antisolvent method were sustainable after 11 weeks, contrary to the samples made through the spin-coating method. As the objective is to produce long-term stability samples through interface modifications, the spin-coating method has been chosen for the future additive deposition.

As the molecule was identified on the devices on top of the perovskite and first effect of the adamantane and its derivatives has been observed with an improvement of the current density and fill factor, we now turn to optimization methods to produce better devices and to determine the influence of the concentration and the method of deposition on the device performance and the perovskite.

### 3.2.3 Evidence for molecular adsorption

To identify the presence of the additives on the material, I employed XPS measurements to probe the surface of the perovskite layer after deposition. We benefit from the high surface sensitivity of the technique probing almost 10 nm deep of the surface and enabling accurate tracking surface modifications. One of the most challenging issue in the present case is the presence of carbon and nitrogen in the AD-derivative molecules and in the perovskite layer which requires a specific data treatment procedure to extract the contributions of each layer. Superficial carbonaceous contamination has also to be taken into account. The detection of I, Br, Cs and Pb has helped us to evidence that perovskite was or wasn't contributing to the signal collected. The perovskite layer's composition ratio can first be taken from the XPS survey fit to determine a preliminary chemical composition. Fits of all detected peak on the XPS survey is compared to their corresponding XPS peak, helping to think if the data are coherent, as in Table 3.2.

Name	Atomic % of the XPS survey	Atomic % of the XPS peaks
<b>I3d5</b>	32.76	34.28
<b>Pb4f7</b>	9.52	9.00
<b>N1s</b>	21.50	20.29
<b>Cs3d5</b>	0.76	0.74
<b>Br3d</b>	5.78	6.01
<b>C1s</b>	28.17	28.21
<b>O1s</b>	1.52	1.48

*Table 3.2: Surface chemical composition determined on the XPS survey and the XPS peaks from the reference sample*

Oxygen is also important to evaluate the carbon contamination sticking at the samples' surface and to track possible oxidation of the perovskite. In this end, it is essential to first dispose of the reference spectra of the perovskite layer to assess the surface modification after the deposition of the modifiers. The superimposition of the spectra obtained on the reference bare perovskite layer and the 3 surfaces after modifiers deposition is presented in Figure 3.7 to determine their presence on top of the perovskite absorber. The spectra are plotted by raw Intensity =  $f(E_B)$  and superimposed with the same background line via a Y offset shift to level them. From this plot we compare the peak intensity contributions depending on the surface modifiers on top of the perovskite (colored lines), while the reference spectrum, in black, corresponds to the perovskite layer without surface modifier.

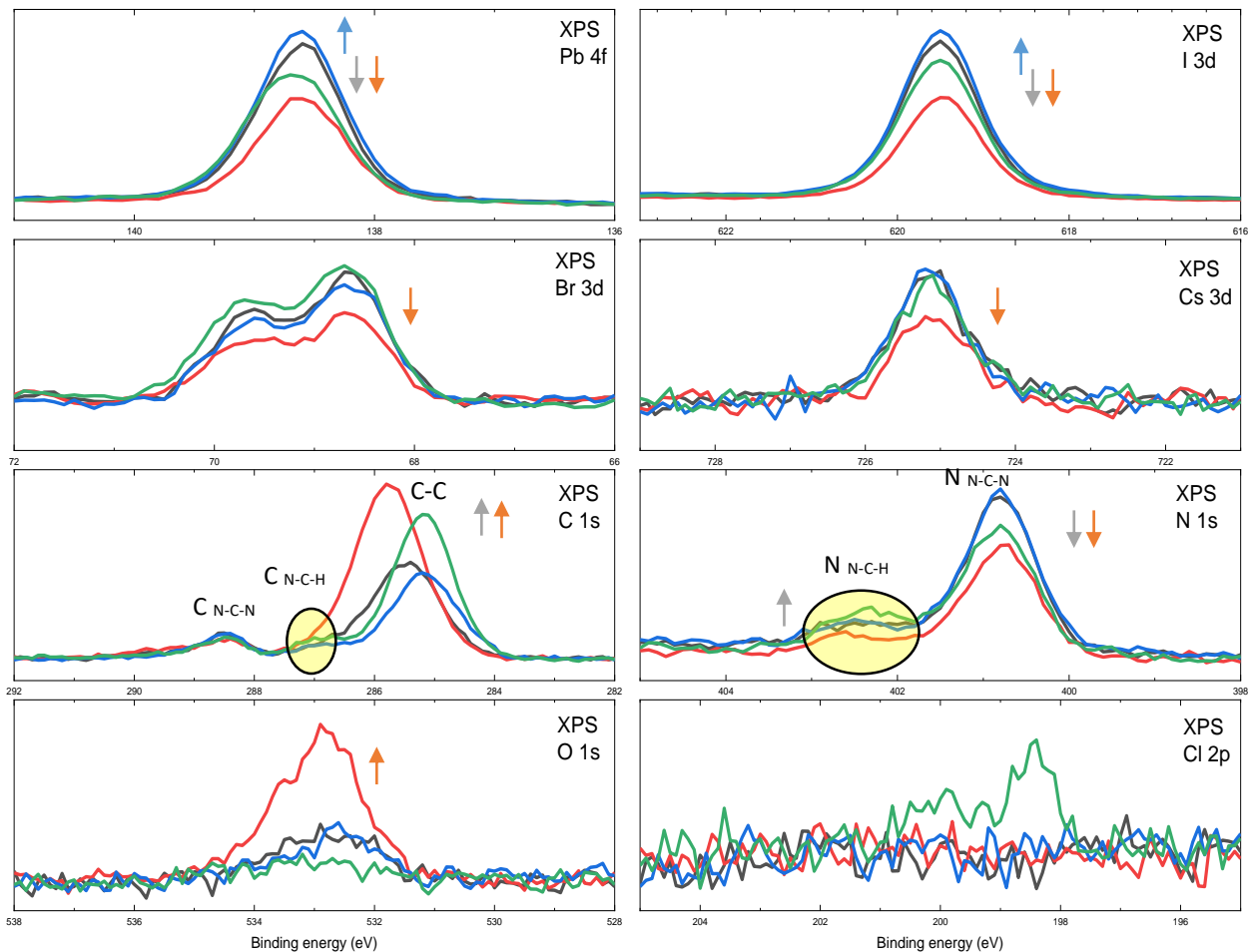


Figure 3.7: XPS spectra of high energy resolution  $Pb\ 4f_{7/2}$ ,  $I\ 3d_{5/2}$ ,  $Br\ 3d$ ,  $Cs\ 3d_{5/2}$ ,  $C\ 1s$ ,  $N\ 1s$ ,  $O\ 1s$  and  $Cl\ 2p$  with and without surface modifiers (— Reference, — AD, — 1ADA, — 1ADAHCl)

Starting with the lead contribution, the peak intensity of the  $Pb\ 4f_{7/2}$  and  $I\ 3d_{5/2}$  core level is reduced in the case of AD and 1ADAHCl and slightly increased for 1ADA. For  $Br\ 3d$  and  $Cs\ 3d_{5/2}$ , an intensity decrease is only clearly visible for the AD treatment. These signals are exclusively linked to the perovskite layer as it is the only component in the layer stack containing these elements. The  $Cl\ 2p$  spectrum marks a special case, as the peak contribution should only be observed for 1ADAHCl, which is effectively observed here. The  $C\ 1s$  and  $N\ 1s$  interpretation is more complicated from a qualitative point of view at first sight. The peak fitting of the perovskite reference's  $C\ 1s$  and  $N\ 1s$  spectra is presented to facilitate the understanding (Figure 3.8). The positions of the  $C\ 1s$  and  $N\ 1s$  peaks contributions have been attributed and determined using reference data from the internal ILV database and literature sources,<sup>4</sup> and implemented in the fitting procedure of our perovskite reference sample. The origin of the contamination layer is sample handling and storage outside of Institut Polytechnique de Paris

an ultrahigh vacuum environment.<sup>5-7</sup> The C 1s photopeak is fitted using 4 contributions for the carbon contamination representative of C-C, C-O, C=O and R-COOH bonds situated respectively at C<sub>C-C</sub>: 285.2 eV, C<sub>C-O</sub>: 286.3 eV, C<sub>C=O</sub>: 287.7 eV and C<sub>C-RCOOH</sub>: 289.5 eV and 2 contributions for the perovskite layer MA<sup>+</sup> (noted C<sub>N-C-H</sub>) at 287.1 eV and FA<sup>+</sup> (noted C<sub>N-C-N</sub>) at 288.7 eV. The carbon contamination C<sub>C-C</sub> whose position is fixed at 285.2 eV  $\pm$  0.2 eV is usually used as a reference for XPS spectra energy scale calibration<sup>5,7,8</sup>. Finally, inversely to Pb 4f<sub>7/2</sub> and I 3d<sub>5/2</sub>, an intensity increase is observed for the C 1s main peak around 285.0 eV, for ADA and ADHCl treated samples, corresponding to the C-C bonds, although no real change is observed for the 1ADA sample. In addition, the perovskite layer contains also carbon in methylammonium (MA<sup>+</sup> = CH<sub>3</sub>NH<sub>3</sub><sup>+</sup>) and formamidinium (FA<sup>+</sup> = CH(NH<sub>2</sub>)<sub>2</sub><sup>+</sup>). Concerning the FA<sup>+</sup> peak, C<sub>N-C-N</sub> contribution follows the same trend as the one observed for Pb 4f<sub>7/2</sub> and I 3d<sub>5/2</sub> which is consistent with an attenuation due to an overlayer, i.e., AD and 1ADHCl modifiers layers in the present case. The derivatives 1ADA and 1ADAHCl contain a C-N bond from the amino site C-NH<sub>2</sub> that is located at the same binding energy position as the perovskite's methylammonium peak contribution C<sub>N-C-H</sub>, i.e. at 287.1 eV for the C 1s peak contribution and at N<sub>N-C-H</sub> at 402.6 eV for the N 1s corresponding peak contribution. No distinct evolution is visible with and without modifiers. A fitting is necessary to separate both contributions from the perovskite and the modifiers. However, if one considers no degradation of the perovskite at t<sub>0</sub>, MA and Fa should follow the same trend.

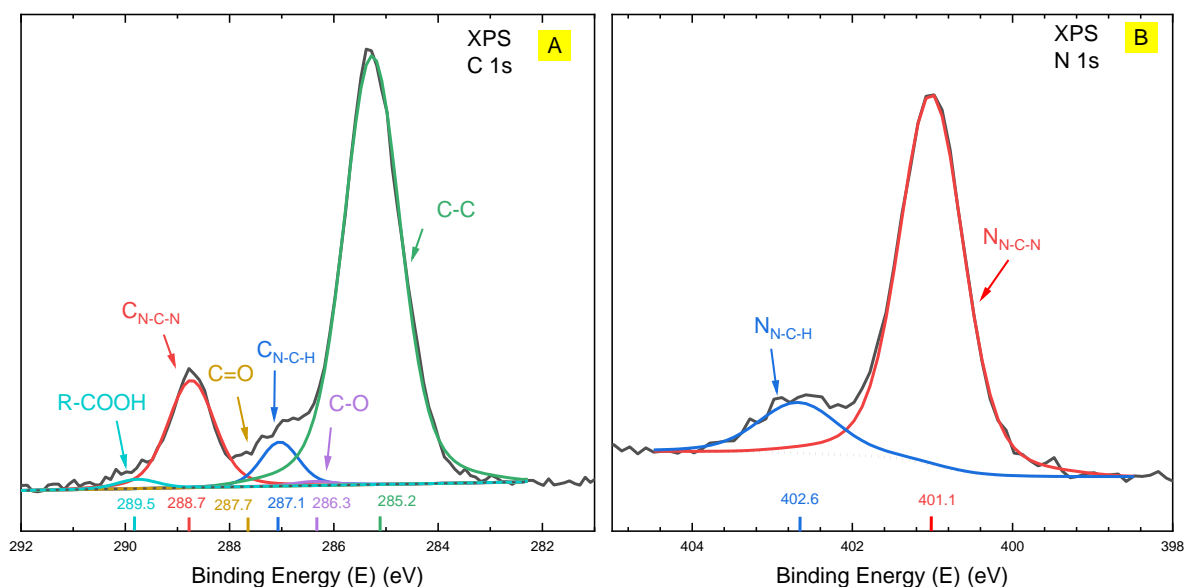


Figure 3.8: XPS spectrum C 1s (A) and N 1s (B) peaks fit position of the perovskite reference sample. Experimental data in black and fit curves in colored solid lines.

In addition, crossing this information with the observations on N 1s and O 1s photopeaks, will permit to assess if this is due to the presence of modifiers or to an increase of the superficial carbon contamination.

The O 1s spectra reveal a small amount of oxygen on the surface in all cases. Since the AD derivatives do not contain any oxygen atoms in their molecular structure, and considering these peaks' high binding energy position, we attribute the O 1s component around 533.0 eV binding energy to surface contamination. In a first approximation, the carbon contamination will be considered equivalent for the reference sample, ADA and 1ADHCl, whose O 1s peaks are similar. Only the 1ADHCl surface presents a higher surface contamination level, in agreement with the small increase of the O 1s peak. This thus does not change the conclusion for AD and 1ADAHCl but the highest C-C intensity for the ADHCl also arise from an increase of carbon contamination.

Finally, the intensities variation of the perovskite elements (I, Cs, Br and Pb) can possibly come from the presence of an additional layer on top of the perovskite that is attenuating the signal from the perovskite, depending in a first approximation on the thickness of the surface modifiers and its composition and the additional fact that the ADHCl sample presents a highest carbon contamination at the surface.

As an initial qualitative summary of these XPS measurements, it is notable that the core level signals of the perovskite and the molecular layer in the case of 1ADA do not follow the same trend as in the case of AD or 1ADAHCl. While the behavior of the peak evolution for the 1ADA-covered perovskite should be similar to the sample covered with 1ADAHCl, as it also contains the same ammonium anchoring group that can improve attachment to the HaP layer, we do not observe the same features. Instead, the 1ADA-treated layer behave similarly to the reference, which suggests an issue with the deposition of the molecule. Either, the molecule was not deposited on the HaP or not uniformly present on the surface. As the X-ray beam spot diameter is covering an elliptic area of 400  $\mu\text{m}$  x 600  $\mu\text{m}$ , it could have it as a non-deposited part.

The surface atomic percentages and key ratios are determined to investigate now the surface chemical composition of the reference sample (perovskite before treatment) and of the films with the molecular layer deposited on top. The overall composition obtained from the survey spectra after background subtraction has been presented above and is refined using the spectral windows of the main photopeaks acquired at higher energy resolution (HR spectra). In addition, photopeaks

modeling is done on HR spectra to determine the different contribution proportions. As explained before, the separation of each contribution is not trivial. The thickness of the surface modifiers is small, and the molecules share similar peak intensity contributions. We are not able to make a clear distinction between the carbon and ammonium contribution coming from the perovskite and coming from the surface modifiers in the fits directly. However, we can potentially infer the attribution by the difference in the intensity ratios. One of the critical steps in the peak fitting is to start fitting a reference peak, usually the fresh sample, and identify the possible numbers of peak components deduced from the molecular structure. This fit was presented at the beginning of the paragraph and optimized by ILV on many HaP samples (baseline IPVF).

The main parameters to fix for the peak fitting are the peak position, the full width at half maximum (FWHM), and the peak area. The peak shape (Lorentzian/Gaussian mix and tail) is adjusted on a reference sample, for each element, and afterward maintained constant for each contribution of the same element during the fitting of the specific photopeak. A Shirley background is also used for HR fitting. Figure 3.9 and Figure 3.10 present the peak fitting of the 4 conditions for the fresh samples, i.e. at day zero (d0) with the spectra of the reference sample, i.e. Glass/FTO/HaP (see Chapter 2.1.3), in the first column and the spectra of the AD, 1ADA and 1ADAHCl-modified samples in columns two to four, respectively.

The peak fitting procedures for the various elements are generally straightforward with the exception of the C 1s spectra, which exhibit a multitude of overlapping peak components as discussed before, but the MA<sup>+</sup> and FA<sup>+</sup> presence can be detected and confirmed by the N 1s spectral signature. Concerning the N 1s spectrum, the main contribution originates from the perovskite layer. As 83% of the A-sites in the perovskite crystal structure are occupied by formamidinium, its peak component at 401.1eV binding energy is the most significant one, as shown in Figure 3.9 and Figure 3.10. The nitrogen from MA<sup>+</sup> and the nitrogen from FA<sup>+</sup> are identified with two different peaks. This is because the two nitrogen species have different electronegativity<sup>6</sup> leading to a chemical shift between the two contributions as demonstrated for the reference sample (see Figure 3.8).

Hence, the distance between the peak positions are fixed for the subsequent measurement in the following way:  $\text{PeakPos}[\text{N}_{\text{N-C-H}}] = \text{PeakPos}[\text{N}_{\text{N-C-N}}] + 1.2 \text{ eV} (\pm 0.2 \text{ eV})$ . The FWHM is ranged between 0.9 to 1.2 eV for the well-defined symmetric peak shapes (1s symmetric shape). The ratio between the Lorentzian and Gaussian contributions in the Pseudo-Voigt profiles is a characteristic of the peak

and the instrument and amounts to 0.56 Lorentzian/Gaussian (L/G) ratio, for N 1s peaks. This value is kept the same for this component for all sample conditions.

This concerns of Pb 4f, I 3d, Cs 3d and Br 3d photopeaks. In the same case, the L/G mix products are determined for each photopeak on the reference sample and fixed for all future additional contributions to this peak . Note that in Figure 3.9 and Figure 3.10 only the Pb 4f<sub>7/2</sub> and I 3d<sub>5/2</sub> are presented since only the peaks used for quantification are presented in this figure.

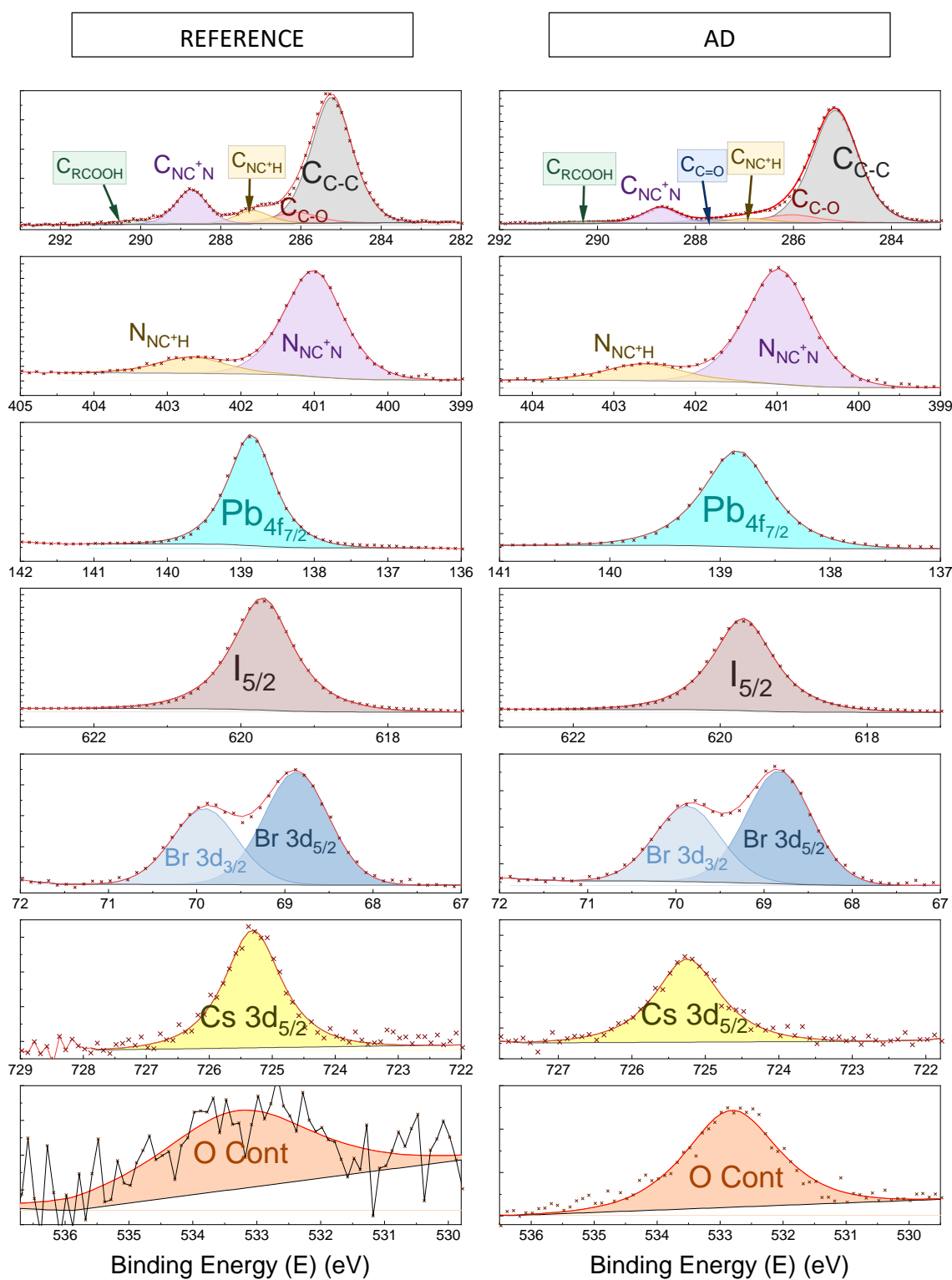


Figure 3.9: XPS peak fit of Reference and AD conditions with the sample at day 0

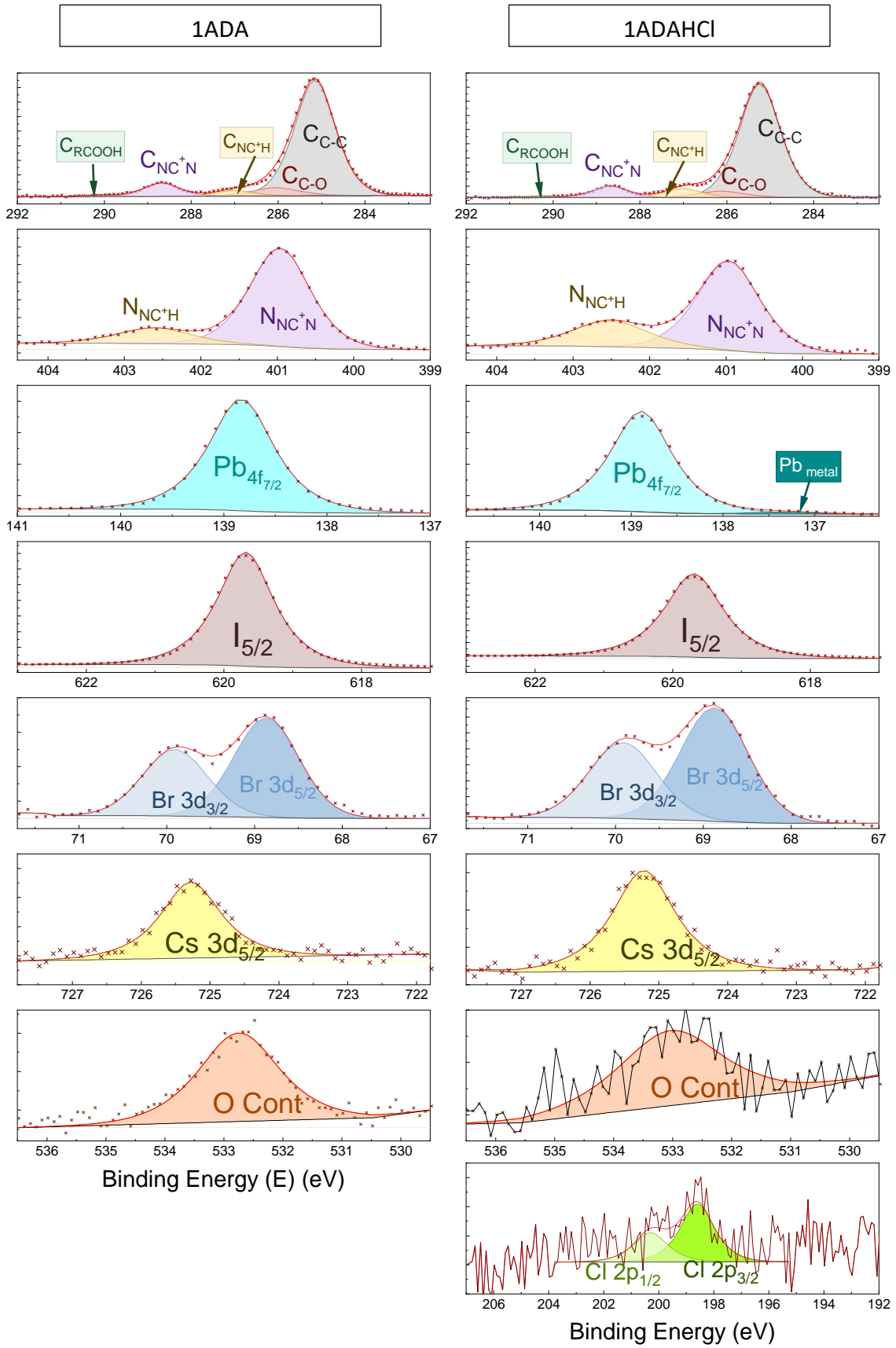


Figure 3.10: XPS peak fit of 1ADA and 1ADAHCl conditions with the sample at day 0

As said before, the energy scale is this calibrated with respect to the C<sub>C-C</sub> contribution, whose position is acquired experimentally at 285.0 eV ± 0.2 eV on the reference sample,<sup>5</sup> and the other carbon contributions position are linked to this peak with specified energy shifts of BE(C<sub>C-C</sub>) + 1.2 eV for C<sub>C-O</sub> (286.1 eV ± 0.1 eV), E(C<sub>C-C</sub>) + 2.7 eV for C<sub>C=O</sub> (287.7 eV ± 0.1 eV) and E(C<sub>C-C</sub>) + 5.1 eV for C<sub>R<sub>COOH</sub></sub> (290.1 eV ± 0.1 eV). Finally, both peaks positions and FWHM (range between 1.1 eV to 1.35 eV depending on the contributions) are fixed at one value for all of these carbon contributions, only intensity changes from a sample to another. The peak positions for the carbon in the HaP layer is validated with our database values that have been established in previous studies at ILV for HaP materials<sup>9</sup>. Furthermore, our deduction of these chemical shifts between the various carbon species in the perovskite corresponds to those made in the N 1s spectrum. The binding energy of C<sub>N-C-H</sub> is 287.2 eV ± 0.1 eV, and the one of C<sub>N-C-N</sub> is 288.7 eV ± 0.1 eV.

On one hand, as explained before, the C<sub>N-C-N</sub> peak is well-defined on the spectrum while on the other hand the C<sub>N-C-H</sub> peak is superimposed by the carbon contamination peak contribution from the C=O and C-O bonds. This can lead to erroneous peak fitting if no restriction on the area is applied and, thus a noncoherent atomic percentage. Therefore, the C<sub>N-C-H</sub> atomic percentage (MA<sup>+</sup>) is fixed with the N<sub>N-C-N</sub> (FA<sup>+</sup>) atomic percentage.

	carbon	nitrogen	% atomic
MA <sup>+</sup>	1	1	%at(N <sub>MA<sup>+</sup></sub> ) = %at(C <sub>MA<sup>+</sup></sub> )
FA <sup>+</sup>	1	2	%at(N <sub>FA<sup>+</sup></sub> ) = 1/2 %at(C <sub>FA<sup>+</sup></sub> )

Table 3.3: Atomic percentage of MA<sup>+</sup> and FA<sup>+</sup> peak contribution

With the known atomic percentage ratio, we can adjust the area and height of the peak to the correct value and adjust the peak fitting. This method is used only for the reference sample, for which no surface modifiers are present on the surface.

The peak fits are then propagated to the scans from the samples with adamantane and its derivatives. As already observed in the qualitative assessment of the spectra, the C 1s peak positions do not change significantly with the application of the surface modifiers. However, the signal from the underlying perovskite layer is attenuated. Therefore, we can now calculate the ratio of the C 1s atomic percentage considering the relation imposed by the stoichiometry and using the N 1s peak where only MA<sup>+</sup> and FA<sup>+</sup> are present :

$$\frac{2\%at(N_{FA^+})}{\%at(N_{MA^+})} = X; \quad \frac{\%at(C_{FA^+})}{\%at(C_{MA^+})} = X$$

The Pb 4f<sub>7/2</sub> and I 3d are distinguishable peaks on the spectrum, respectively at 138.8 eV and at 619.0 eV. The position can identify through the XPS software and literature.<sup>5,10</sup> Having a look at the Pb4f<sub>7/2</sub> peak FWHM ( 138.8 eV), there is no evident enlargement which would reveal an oxidation state. The I 3d does not change depending on the molecule, no affecting the perovskite layer. The Br 3d is also present in the spectrum, coming from the perovskite layer, with a doublet at 68.9 eV for Br 3d<sub>5/2</sub> and BE(Br 3d<sub>5/2</sub>) + 1.04 eV for Br 3d<sub>3/2</sub>. The peak is similar for all of the conditions as well. Finally, we also attempt fit the O 1s and Cl 2p peak contributions (only for 1ADAHCl), which are near the detection limit but are still distinguishable. The presence of Cl validates the modifier deposition. The oxygen comes from carbon contamination as the peak position is around 532.0 eV, attesting that there is no oxygen incorporation.

As a final remark on the peak fit descriptions, we can eventually distinguish a small additional peak centered at 137.6 eV binding energy in the Pb 4f<sub>7/2</sub> core level spectrum of the 1ADAHCl sample. This component is attributed to Pb<sup>0</sup>, a typical degradation product of the perovskite absorber but which can also be induced by illumination during the transfer procedure or X-ray irradiation.<sup>11</sup>

This peak fitting process results in the calculated atomic ratios for each sample with the different surface modifier variants listed in Table 3.4.

RATIO X/(I+Br)	Ratio theory	Ref.	AD	1ADA	1ADAHCl	Ratio X/Pb	Ratio theory	Ref.	AD	1ADA	1ADAHCl
Br	<b>0.17</b>	0.20	0.21	0.20	0.24	Br	<b>0.51</b>	0.57	0.56	0.51	0.68
I	<b>0.83</b>	0.80	0.79	0.80	0.76	I	<b>2.49</b>	2.26	2.17	2.08	2.16
Pb	<b>0.33</b>	0.35	0.37	0.39	0.35	Pb	<b>1.00</b>	1.00	1.00	1.00	1.00
Cs	<b>0.02</b>	0.01	0.01	0.01	0.01	Cs	<b>0.05</b>	0.04	0.04	0.03	0.04
N <sub>tot</sub>	<b>0.58</b>	0.51	0.51	0.48	0.49	N <sub>tot</sub>	<b>1.74</b>	1.44	1.40	1.25	1.39
N <sub>N-C-H</sub>	<b>0.05</b>	0.08	0.08	0.08	0.13	N <sub>N-C-N</sub>	<b>1.58</b>	1.22	1.19	1.04	1.02
C <sub>N-C-H</sub>	<b>0.05</b>	0.10	0.08	0.10	0.16	C <sub>N-C-H</sub>	<b>0.16</b>	0.27	0.21	0.26	0.45
N <sub>N-C-N</sub>	<b>0.53</b>	0.42	0.45	0.43	0.31	N <sub>N-C-H</sub>	<b>0.16</b>	0.22	0.21	0.20	0.37
C <sub>N-C-N</sub>	<b>0.23</b>	0.23	0.21	0.23	0.19	C <sub>N-C+N</sub>	<b>0.79</b>	0.64	0.57	0.59	0.53
						C <sub>C-C</sub>	/	3.15	5.65	5.92	6.27

Table 3.4: Surface layer atomic ratio at d0 compared to the theoretical ratio of a HaP (left) table X/(I+Br) and (right) table X/Pb

The reference ratio of our HaP corresponds well to the theoretical ratio. To allow for a better comparison, the elemental ratios are compared to the total amount of halogens in the perovskite (I+Br) as well as to the amount of Pb. As a slight deviation, we notice that the I/(I+Br) and N/(I+Br)

and more visibly the ratios N/Pb and I/Pb are lower than the theoretical values, which can be linked to either small deviations in the precursor composition during sample fabrication or to partial losses of I and N during transfer to vacuum conditions for the XPS analysis.<sup>12</sup> Another possibility is that it comes from an iodide increase on the surface during to the deposition process. However, the values are still consistent with a perovskite film that has a slight enrichment of  $PbI_2$  at the surface ( $I/Pb > 2$ ).

Cs	I	Br	Pb	FA	MA
0.05	2.71	0.51	1.1	0.85	0.17

Table 3.5: Experimental ratio taking in account the 10% excess of  $PbI_2$

We also observe an increase in the  $C_{C-C}/Pb$  ratio, which is compatible with the peak evolution on the C 1s spectrum in Table 3.4. The values increased from 3.15 for the reference to 5.65 (AD), 5.92 (1ADA) and 6.27 (1ADAHCl). The value for 1ADAHCl is higher as the molecule may anchor better on the surface than AD thanks to its amino group and might benefit from the presence of chloride, which could affect the halide anchoring sites on the perovskite surface. Data of the Tables favor modifiers deposition on 1ADA, which was not evident from previous qualitative assessments.

$N_{N-C-H}$  peak increase is noticeable and  $N_{N-C-N}$  peak decrease is observed for 1ADAHCl in line with the modifier deposition bringing additional amino site C-NH<sub>2</sub> and concomitant perovskite coverage. In parallel, the same changes are observed with the carbon as  $C_{N-C-H}$  peak and  $C_{N-C-N}$  peak these C-N contributions are linked. This is less evident for 1ADA, which confirms a probable lower coverage. The quantitative assessment confirms the deposition of surface modifiers on the surface due to the attenuation of the HaP-related core levels and a concomitant increase in modifier-related carbon, nitrogen, and chloride for 1ADAHCl, and agrees with qualitative information presented earlier. However, the adamantane derivative overlayer remains very thin and would allow for an integration into functional devices.

After working on the chemical surface of the layer, we can wonder how it changes the surface's energies. Defining the valence energy through UPS (UV Photoelectron Spectroscopy) is possible.

### 3.2.4 Optoelectronic characterization of perovskite films with adamantane surface modification

In the next step, I focus on characterizing the optoelectronic properties of the perovskite films to evaluate the changes to the dynamic of charge carriers induced by the deposition of the layer of molecular modifiers and complement the results from the UPS measurements. In this regard, KPFM measurements yield an important reference point for the work function

determination. In addition, we then track the build-up of the surface photovoltage (SPV) by illuminating the samples using a green laser (emission at a wavelength of 550 nm) above the band gap of the perovskites ( $E_g = 1.59$  eV) during the KPFM measurements. The samples are measured in the dark for 5 minutes, then under illumination for 10 minutes and finally for 5 minutes in the dark again. In the dark, the samples already have slightly different values of the work function: Reference at 4.48 eV, AD at 4.56 eV, 1ADA at 4.54 eV and 1ADAHCl at 4.6 eV. These values remain stable over the course of the 5 minutes measurement in the dark. As we turn on the supra-band gap laser illumination, we produce photogenerated carriers in the perovskite, which induced a surface voltage. Here, this dynamic manifests as an increase in the work function is for all samples investigated. The work function of the control sample under these illumination conditions reaches 4.9 eV after 10 minutes of illumination, while the ones for the AD sample, the 1ADA sample, and the 1ADAHCl sample are 4.95 eV, 5.05 eV and 4.93 eV. In this configuration, Glass/FTO/c-m TiO<sub>2</sub>/HaP, the photogenerated electrons could go through the ETL layer to migrate to the metal contact. Furthermore, the hole carriers would then likely accumulate at the top surface of the HaP, reducing the surface charge carrier level at this interface and increasing the work function over time. At the end of the measurement, we leave the samples in the dark for 5 minutes to track changes in the work function as the carriers relax to their equilibrium positions. However, here we note that the work function obtained after the illuminations does not return to its initial value in the dark over the course of five minutes. However, one can discern a progressive reduction of the work function as the light is turned; hence, the process likely requires more time to reach equilibrium in the dark. It is also useful to express this change in work function as a function of illumination to the surface photovoltage via the simple relation:  $SPV = WF_{\text{dark}} - WF_{\text{illum}}$ .

Where  $WF_{\text{dark}}$  is the initial work function at the beginning of the measurement in the dark and  $WF_{\text{illum}}$  is the work function under illumination. This means that an increase in work function under illumination is equal to a negative SPV value.

For all samples, we observe a negative SPV, i.e., the work function of the perovskite increased under illumination. While the trend is the same for all samples, we observe some slight differences linked to the presence of the additives on the surface, while the optical band gap of the perovskite layer does not change depending on their presence, as in Figure 3.11(a). While the 1ADA-modified sample shows a slightly higher SPV than the reference device, the AD and 1ADAHCl-modified surfaces samples show lower SPV. Notably, in all cases, the initial dark state is obtained

during the last 5 minutes of the measurement, as the restitution of the initial surface and hence the decline in the SPV transients happens on a larger time scale. This behavior has been observed for free MHP surfaces and was attributed to carrier trapping with slow release mechanisms, ion migration and surface reactions. From our experiment, the application of the AD-based surface modifiers does not significantly mitigate these processes, which aligns with the hysteresis observed for the full devices.

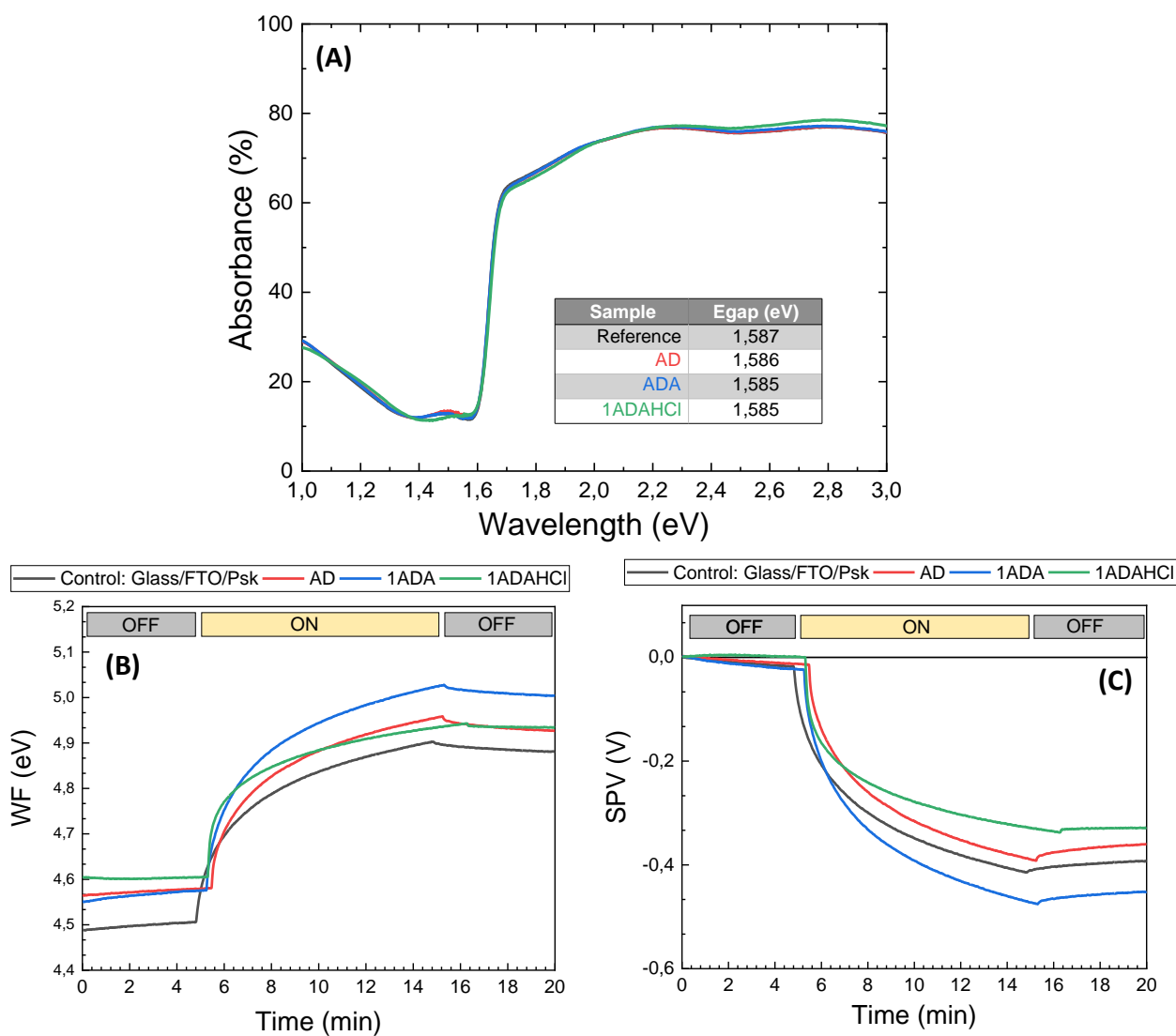


Figure 3.11: (A) Spectrophotometer of AD, 1ADA, and 1ADAHCl compared to a reference (B) photovoltage (SPV) and (C) surface work function (WF) of glass/FTO/perovskite samples with and without molecular layer on top measured by Kelvin Probe measurement using a green light (550nm)

In the next step, we will assess to which extent the presence of the molecular layer on top of the perovskite affects the dynamic of charge carriers. This information is important to elaborate the impact of the interlayers on device performance eventually.

For instance, hysteresis is often reported for this device architecture, which is often attributed to defects present in the perovskite layer and particularly at the interfaces to the adjacent transport layers.<sup>13</sup> To determine if defects are present in the materials and their optoelectronic activity, modulated and time-resolved photoluminescence (TRPL) was used to characterize the pristine surface-modified perovskite layer (half-cell). Due to the departure from the surface sensitive measurements towards these bulk-sensitive optical methods, the same measurements were performed on full cells, which were finalized in the described architecture (Glass/c-mTiO<sub>2</sub>/HaP/X/Spiro-MeOTAD/Au)

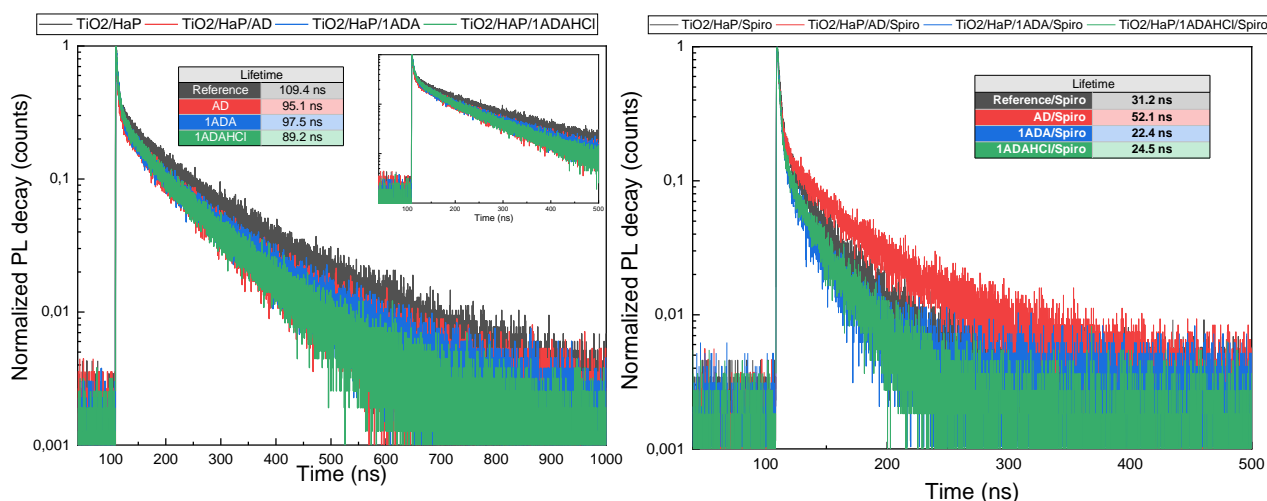


Figure 3.12: TRPL curves of (left) half-cell and (right) full-cell and its insert graph zoom in the region 40-500 ns with a reference, AD, 1ADA and 1ADAHCl at 30 suns

The samples were analyzed to calculate the carrier lifetime evolution in the molecules' presence. For the half-cell, the carrier lifetime of the reference cell is at 109.4 ns, AD at 95.1 ns, 1ADA at 97.5 ns and 1ADAHCl at 89.2 ns. For the full cell, the carrier lifetime reaches 31.2 ns. An increase is observed with AD at 52.1 ns and a drop for 1ADA at 22.4 ns and 1ADAHCl at 24.5 ns. Theoretically, the longer average lifetime in the absorber a carrier can spend in an excited state after electron-hole generation before recombining. It gives carriers more opportunities to transport layers at sides, thus increasing the J<sub>sc</sub> and efficiency of the cell. With the presence of spiro-MeOTAD, a decrease of the carrier lifetime is noticed, as the charge transport layers help the drift of the carrier in the device. Generally, we observe a drop in carrier lifetime of the full cell compared to their half-cell

counterparts. In the half-cell configuration, holes potentially accumulate at the surface the perovskite layer as they can not be extracted, which leads to a higher lifetime. On the other hand, in the full-cell configuration, the spiro-MeOTAD layer results in an efficient extraction of holes and hence quenching of radiative recombination. The difference can tell us if the carrier lifetime comes from the absence of HTL or the effect of the surface modifiers. The increase of the carrier lifetime for the cell with AD can be a good sign for our device and could lead to a rise of the current in the presence of AD.

### 3.2.5 Expanded device series for optimization and reproducibility of PSCs with AD-based interlayers

Following the previous experiments, we selected the deposition method SC for the molecules. I introduce another additive, 1ADAHCl, which the HCl protonated version of 1ADA.



*Figure 3.13: Typical triple cation lead halide perovskite solar cell with glass/FTO/c-TiO<sub>2</sub>/m-TiO<sub>2</sub>/HaP/Spiro-MeOTAD/gold*

The devices were characterized through current-voltage measurement to extract the solar cell parameters and compare the performance of the devices with AD-based interlayer, in the following denoted as AD, 1ADA and 1ADAHCl devices, with the samples without interlayer, in the following denoted as reference. The JV curves of the champion devices and the statistical data are plotted in Figure 3.10. While the PCE of the reference device is at 16.1% in reverse (14.5% in forward), the PSC with AD-based interlayer reach for AD 17.4% (15.4%), for 1ADA 16.8% (15.4%) and for 1ADAHCl 16.3% (14.8%). These slight improvements are related to the increase of the short-circuit current density (J<sub>sc</sub>) and open-circuit voltage (V<sub>oc</sub>) in the presence of these interface layers in the case of AD and 1ADA, which is in line with our previous finding for the initial device runs described in the previous section. Moreover, the result is compatible with our finding that the AD, 1ADA, and 1ADAHCl layers are too thin to be measured by profilometry or SEM but are present on the surface, as evidenced by the preceding XPS analysis. Furthermore, in the case of 1ADA and 1ADAHCl, which

contained an amino group, the interlayer-forming molecule can interact with the lattice of the perovskite layer underneath by filling the A-site cation position corresponding to  $\text{Cs}^+$ ,  $\text{MA}^+$  and  $\text{FA}^+$  vacancies. This would then reduce the surface charge recombination rates and improve  $V_{oc}$  of the device as observed in this batch.

Of note, one of the main issues is the presence of significant hysteresis in the solar device with an average hysteresis index (at the given scan parameters) of 8% for the reference samples. Similar values are obtained with the presence of adamantane and its derivatives (AD: 10%, 1ADA: 9%, 1ADAHCl: 9%) for the samples at day 0 (Figure 3.14(A)). It indicated that the perovskite device still presented some issues in this fabrication process causing a deterioration of the crystalline quality and issues with the charge extraction layer due to ion migration in the perovskite layer<sup>14</sup>. The carrier diffusion changes depending on the applied bias. Forward bias happens when the applied voltage across the device decreases the electric field formed by the NIP junction. It eases carrier diffusion and helps to increase the current diffusion. The reverse bias happens when the applied voltage in the device increases the electric field formed by the NIP junction and decreases the current diffusion. In literature, this hysteresis is often attributed to ion migration of  $\text{MA}^+$ , due to a slightly higher Fermi level of  $\text{TiO}_2$  compared to the perovskite layer leading to “punctual adjustment” of the band gap and an increase of carrier recombination.<sup>15,16</sup>

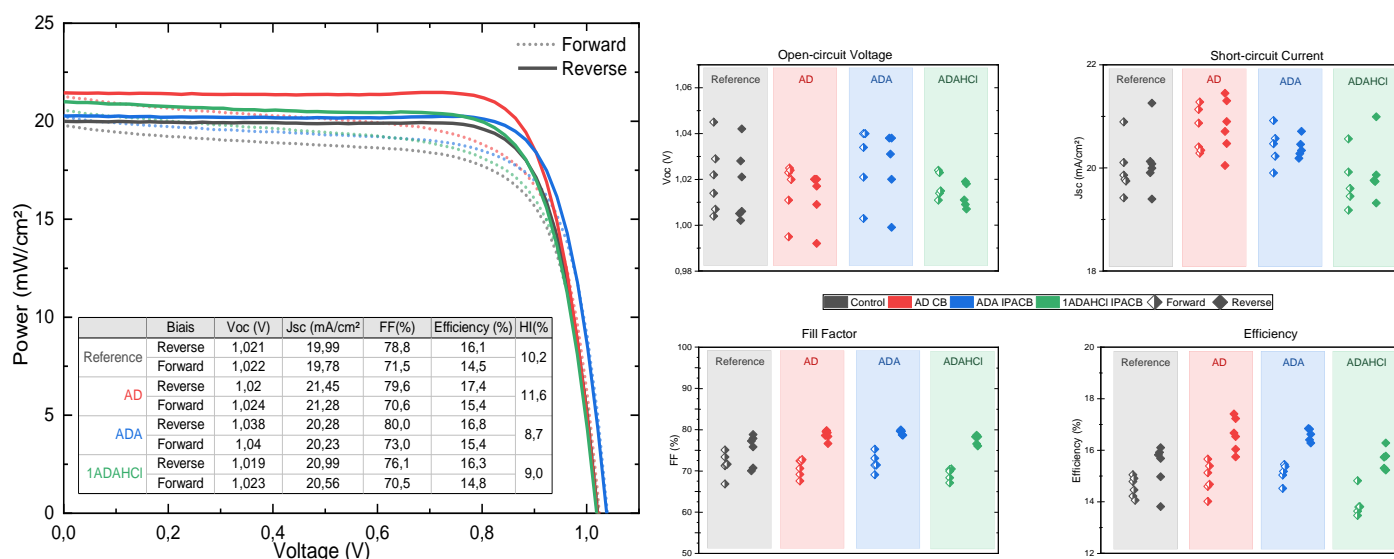


Figure 3.14: Solar cell parameters of the devices Glass/FTO/compact  $\text{TiO}_2$ /mesoporous  $\text{TiO}_2$ /HaP/Additive/Spiro-MeOTAD/Gold with AD, 1ADA and 1ADAHCl treated devices compared to the control samples (A) J-V curves of the best devices for each conditions (B) Solar cell parameters of the various devices depending on the deposited additives

### 3.2.6 Aging of perovskite films and devices with adamantane-based interlayer

In this last section of the chapter, I further evaluate the stability of the perovskite thin films as well as the devices with and without adamantane-based surface modifiers in the case of films and interlayers in the case of devices. Even though the improvement of the device performance remained modest but measurable with the application of the AD-based interlayer, a major stated objective has been to use the bulky molecule as a protection layer and mitigate the incorporation of extrinsic species such as O<sub>2</sub> or H<sub>2</sub>O into the perovskite layer.

#### 3.2.6.1 XPS degradation evaluation

Encouraged by our initial results, we hence probe if the additives would protect the perovskite layer and the device in the long term. The same samples as the one presented in section 3.2.2 were analyzed again during aging sequences. They were fixed on the sample holder, enabling them to conserve their position and change the analysis point for each new measurement not to cumulate X-ray irradiation effect and aging. These 4 samples were aged under a day/night cycle for 90 days under ambient air (45% air humidity) and measured systematically by XPS. The measurements were done one day after the perovskite layer deposition, called “fresh” samples at 0 days, then at 15 days, 45 days and 90 days. We then follow the evolution of the perovskite layer overtime at the hand of the XPS spectra to track the changes to the chemical composition of the surface, which, again, is distinctly identified in the carbon and nitrogen peak contributions. Indeed, the degradation pathway of perovskite in the air mainly implies the organic part degradation, I loss and lead oxidation. Figure 3.15 and Figure 3.16 show the evolution of, respectively, N 1s and C 1s peaks in time. Both raw data and normalized are presented, the normalized one enabling to evaluate the change of carbon contamination during aging.<sup>10</sup> At d15, no major difference in the C 1s spectra with respect to the fresh sample at d0 in the case of all samples.

• *d0* • *d15* • *d45* • *d90*

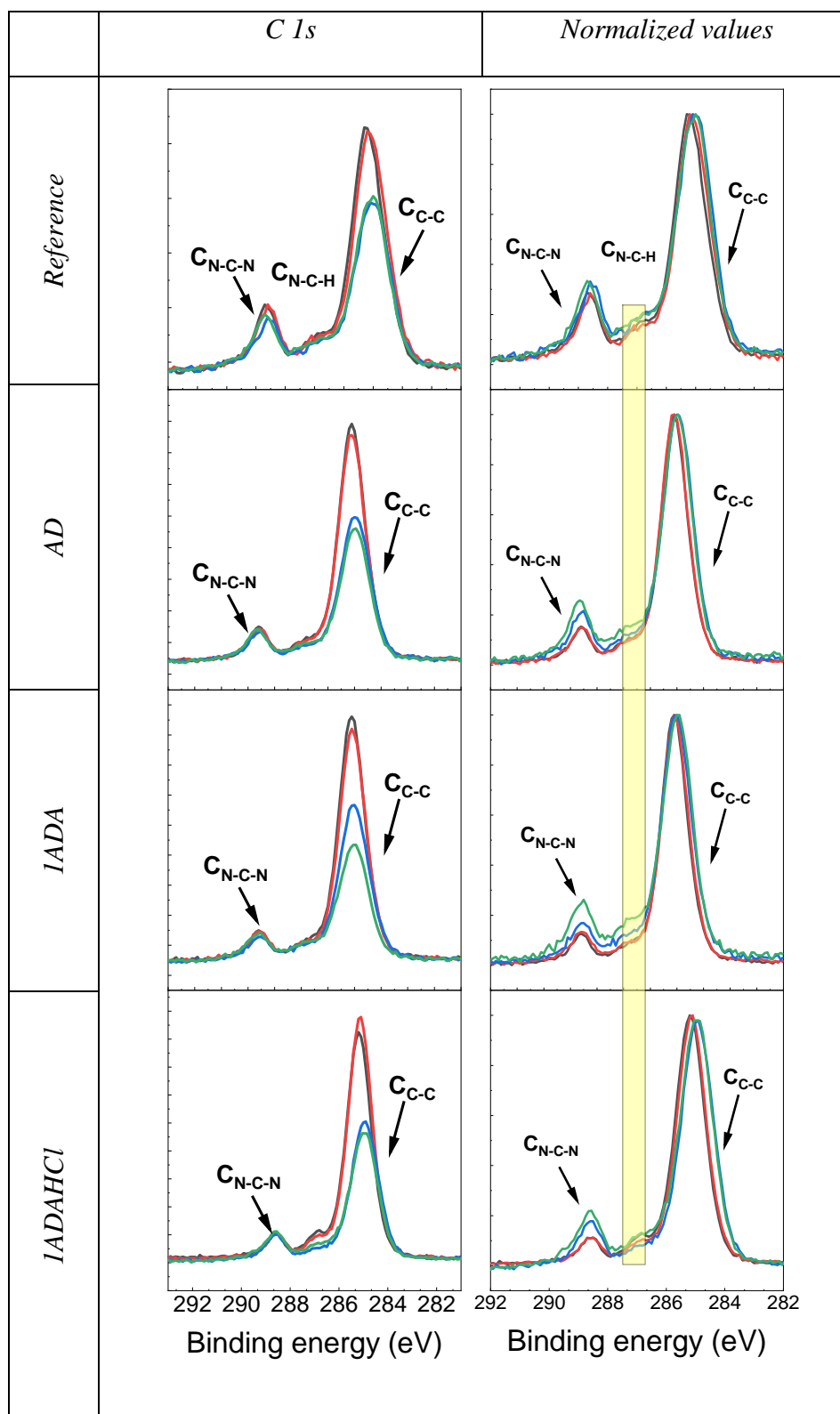


Figure 3.15: Evolution of the XPS spectrum of *C 1s* spectrum, its respective normalized values curves through time (*d0*, *d15*, *d45*, *d90*) for *Reference*, *AD*, *IADA* and *IADAHCl*

• *d0* • *d15* • *d45* • *d90*

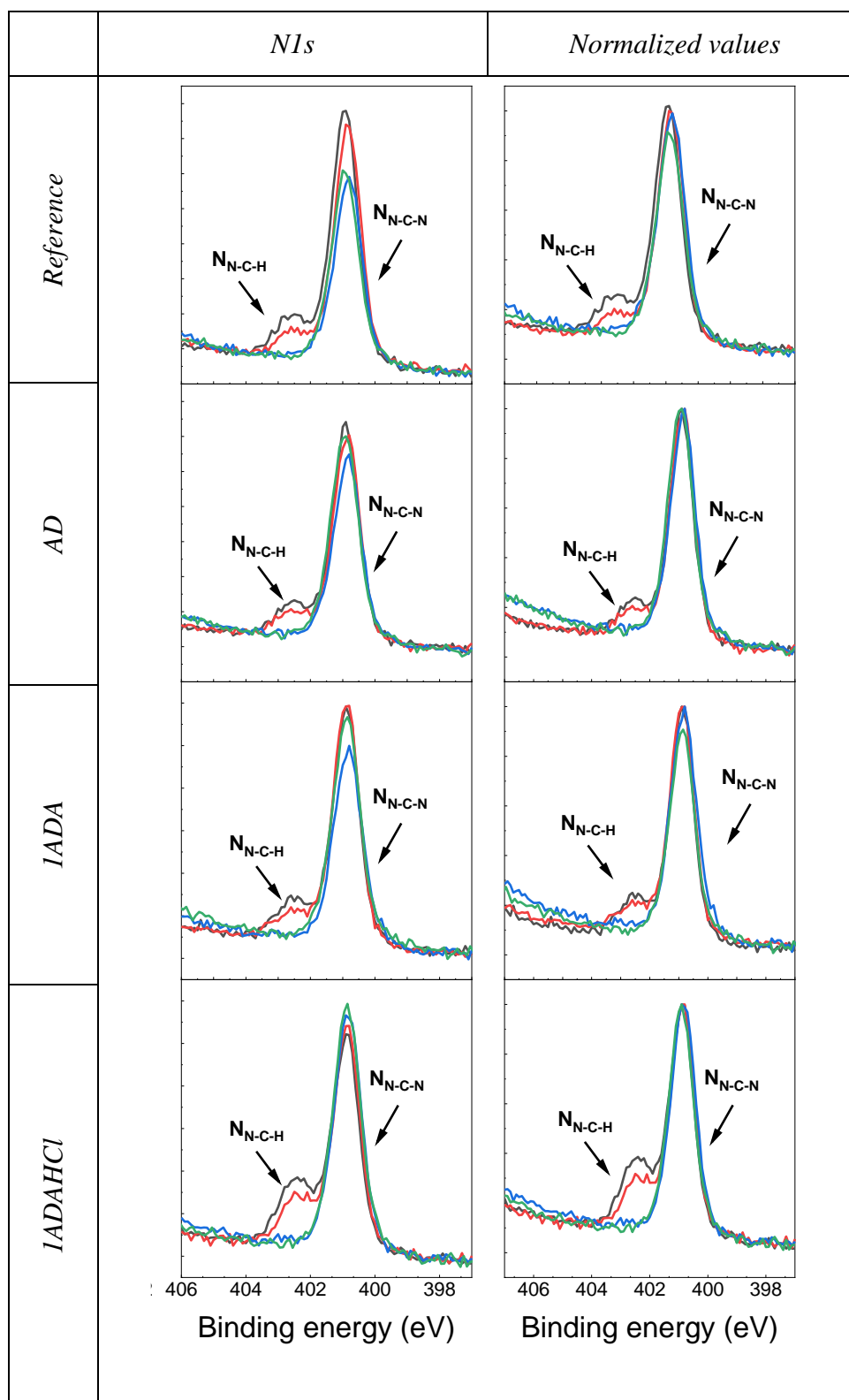


Figure 3.16: Evolution of the XPS spectrum of *N 1s* spectrum, its respective normalized values curves through time (*d0*, *d15*, *d45*, *d90*) for *Reference*, *AD*, *IADA* and *IADAHCl*

For the N 1s spectrum, at d15, a slight reduction of the contribution from  $N_{N-C-H}$  contribution is observed for all samples. It shows a start of degradation from the perovskite sample in the short term. However, this degradation occurs faster for the reference sample than for the other samples with the AD, 1ADA and 1ADAHCl layer on top. The ratio  $\frac{N_{N-C-H+}}{(I+Br)}$  is calculated to quantify this evolution (Figure 3.17). The values extracted from the peak fitting contribution of  $C_{NCH+}$  indicated a reduction of the peak contribution, which is compatible with the observed degradation of the perovskite layer in Table 3.6.

Conditions	Control	AD	1ADA	1ADAHCl
<b>d0</b>	0.08	0.08	0.08	0.13
<b>d15</b>	0.04	0.05	0.05	0.10
<b>d0 – d15</b>	0.03	0.02	0.02	0.02

Table 3.6: Ratio of the peak fit contribution  $N_{NCH+}$  depending on the halogen (I+Br) at d0 and at d15

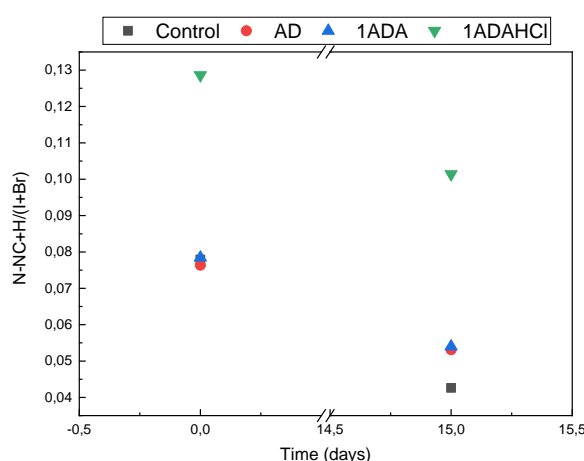


Figure 3.17: Plotting of the ratio  $N_{NCH+}/(I+Br)$  at d0 and d15

From this ratio, plotted in Figure 3.17 and listed in Table 3.6, we confirm that the ammonium-related N 1s peak component is decreasing over the first 15 days. d45 and d90 are not present as the values were under the noise background to be distinguishable. I know that the evolution curve is not mandatory a straight curve, the plot is used to visualize the change. The difference in the ratio between d0 and d15 (last row in Table 3.6) amounts to a significantly higher value for the control sample compared to the samples with the molecular surface modifiers. This suggests a partial protection of the perovskite layer in the presence of surface modifiers.

Then, after 45 days, it is impossible to distinguish the N-C-H peak contribution at 402.6 eV on the N 1s spectrum for all samples, indicating a total loss of the ammonium-containing species ( $MA^+$ , ADA) at the surface (Figure 3.15). Since no peak contribution is obtained on the N 1s spectrum, no N-C-H

peak contributions were considered in the C 1s spectrum. After 90 days, only two distinctive contributions for C 1s spectrum remain observable; C-C bond at 285.0 eV and the N-C-N bond at 288.4 eV. In addition, carbon contamination is further present on the surface but seems to be reduced over time. For the reference sample, we possibly have another layer form on the sample surface, which cause further attenuation of the perovskite peak contribution or potentially a progressive degradation. For AD and its derivatives, the reduction of the nitrogen peak contribution at 400.8 eV ( $\text{FA}^+$ ) is linked to the progressive degradation of the perovskite degradation ( $\text{MA}^+$ ), decreasing the modifiers layer's protective effect. After 90 days, the deposited samples reach values similar to the reference sample and as the C content decreases, this phenomenon shows that the modifier layers progressively disappear. The surface modifiers thus act as a protective layer on top of the perovskite but for a limited hence, delaying the degradation of the perovskite film underneath. Eventually, the molecular layers are desorbed, and hence the degradation of the perovskite film will take its course.

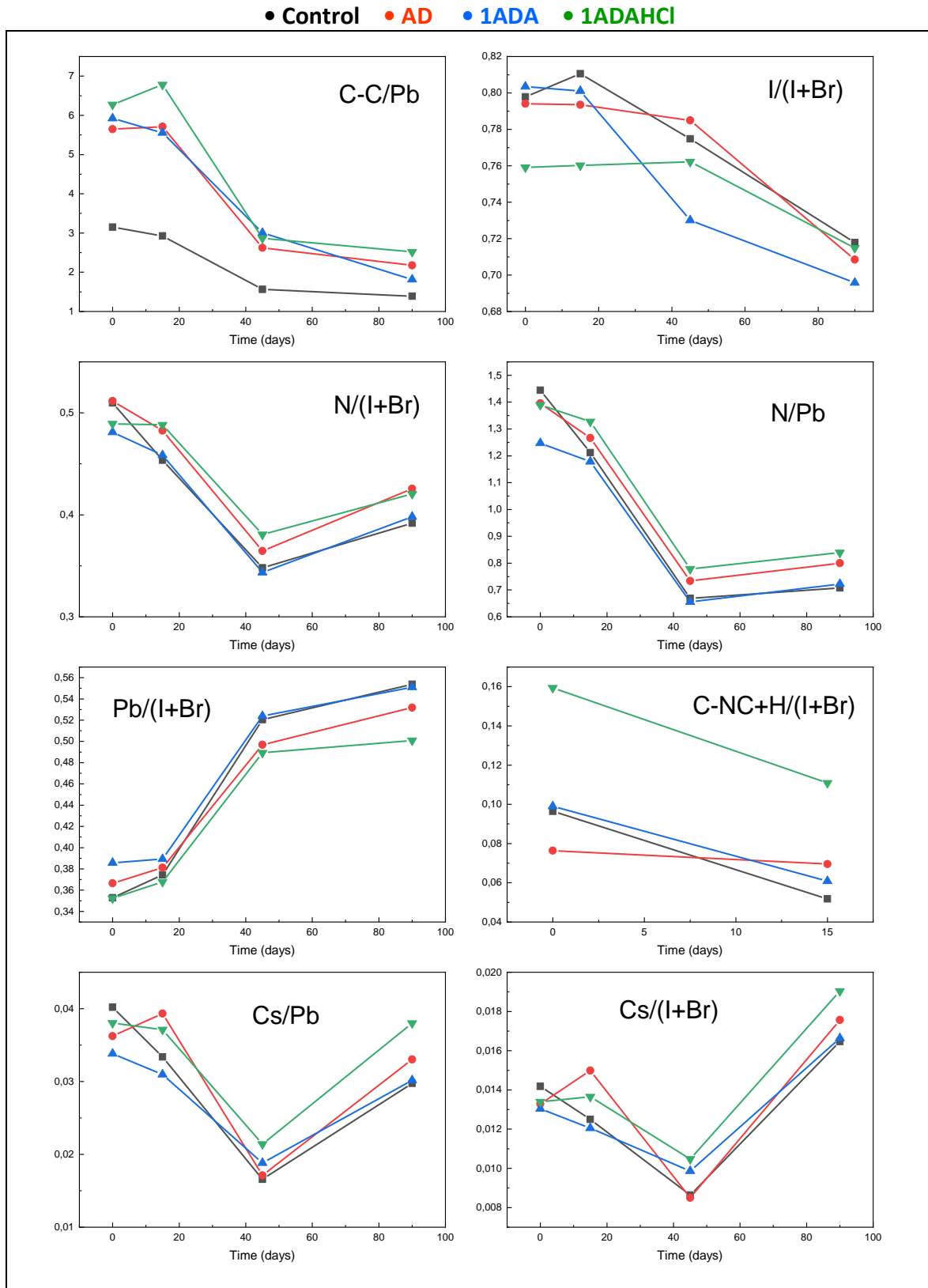


Figure 3.18: Peak ratio evolution through time (d0, d15, d45, d90) for different conditions: control, AD, 1ADA and 1ADAHCl

The nitrogen and cesium peak contributions evolve similarly with a fast degradation after 45 days observed for either ratio, X/Pb or X/(I+Br) in Figure 3.18. As a curious observation, the ratio increases again in the timespan from d45 to d90. This effect could be related to further loss of halides and migration of ions in general. Eventually, this change could be related to the self-healing mechanism that is particularly present in FA-based halide perovskites, which could hence be exacerbated as the films further lose MA<sup>+</sup>.<sup>17</sup> For example, after 90 days, a new contribution is observable for the N 1s spectrum at 398.5 eV. As this contribution is not usually seen for the pristine perovskite nor for the surface modifier, potential degradation pathways of the organic need to be considered. In this end, this contribution could come from pyridinic nitrogen species. In the literature, it has been reported that FA<sup>+</sup> can eventually degrade to triazine<sup>18,19</sup>, which could explain our finding.

Another point is the degradation of the perovskite to metallic lead and lead oxide. After 45 days, the lead area and the FWHM increase are noticed (Figure 3.19). It can be linked to a formation of lead oxide on the top. As the  $Pb_{HAP}^{2+}$  and  $Pb_{PbO_2}^{4+}$  peaks are near each other, their contributions are mixed, making it difficult to distinguish them ( $Pb^{2+}$ :  $\pm 138.8$  eV). A different contribution is also observable at Pb 4f spectrum at  $\pm 137.4$  eV. This could be identified as the peak position contribution of the metallic lead ( $Pb^0$ )<sup>5</sup>.

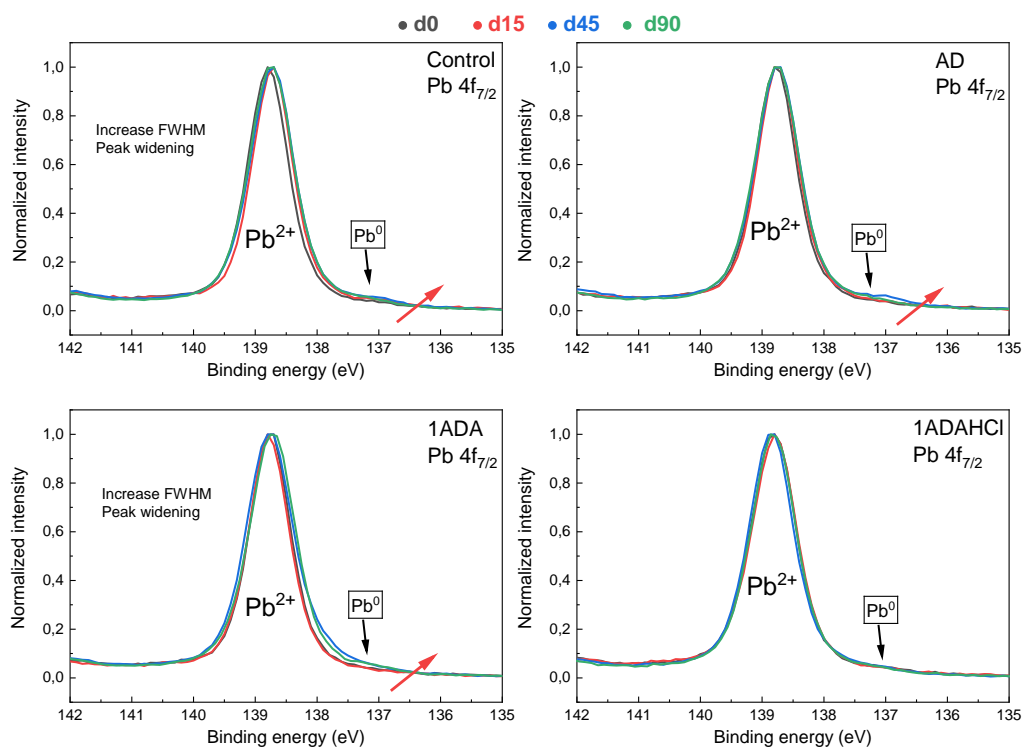


Figure 3.19: XPS spectrum Pb 4f<sub>7/2</sub> peak contribution overtime at d0, d15, d45 and d90 under several conditions (AD, 1ADA and 1ADAHCl compared to a reference sample)

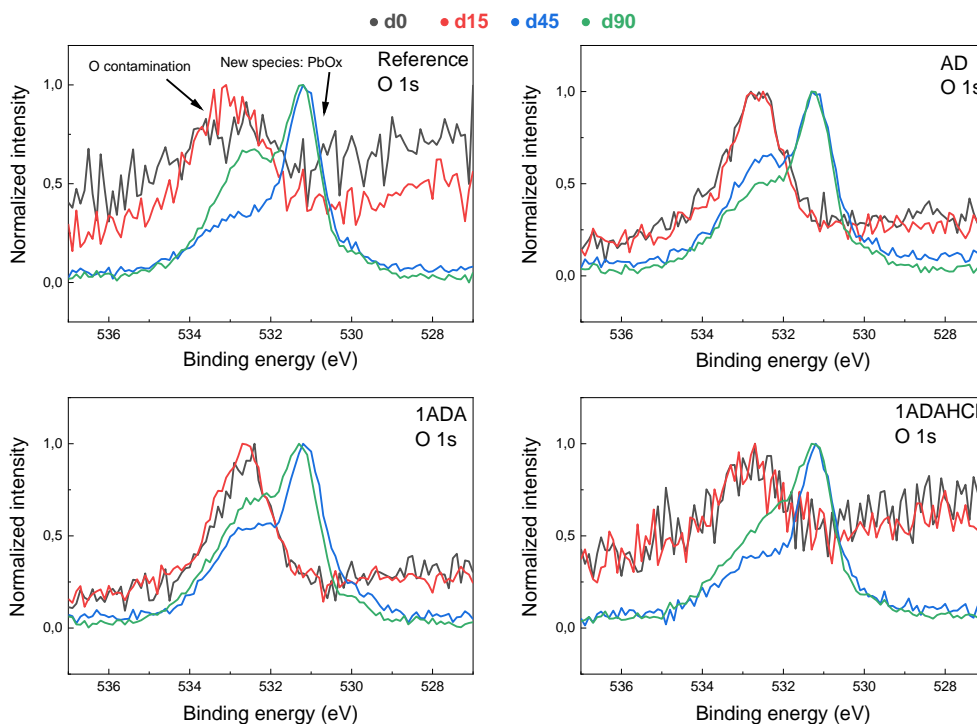


Figure 3.20: XPS spectrum O 1s peak contribution overtime at d0, d15, d45 and d90 under several conditions (AD, 1ADA and 1ADAHCl compared to a reference sample)

At 531 eV on all of the O 1s spectrum (Figure 3.20), we can identify the presence of a new species at d45. This contribution is linked with lead degradation, potentially showing the formation of PbOx in the layer. Metal lead contributions are already presented for the 1ADAHCl at d0 (Pb metal/Pb=0.02), but it does not change after 90 days. After 90 days, all samples contain some Pb<sup>0</sup> resulting from the degradation of the perovskite layer. This degradation possibly comes from the lead halide's degradation mechanism through time leading from the liberation of lead and gas of halide. The degradation is similar to all samples, with a high ratio Pb<sup>0</sup>/Pb<sup>2+</sup> for the reference sample and AD after 90 days. This development tracks with the continuous reduction of iodine content in the material, either confirming the evaporation of diiodide or iodine migration in the bulk. Such an iodine migration process would eventually become detrimental to the layer stability<sup>3,20</sup>.

In the end, the samples are degraded under an air atmosphere for 90 days under a day/night cycle to test the layer stability and the surface modifiers' protection effects. In the short term, the surface modifiers showcase their effect with preserving the N<sub>N-C+</sub> peak contribution. But after 45 days the surface-modified layer reached a ratio similar to the reference sample with a drop of the C<sub>C-C</sub> peak contribution, showing the deposited layer loss. The N loss seems lesser for the 1ADAHCl modifier. Then, after 90 days, the results are compounded by the degradation and ion migration processes in

the perovskite layer itself. The additives may not totally protect the layer (evaporation ?) but can partially preserve the perovskite layer degradation in the short term, which could make for an important intermediate step in device processing. To assess our results in sight of the technological application, we tracked device degradation under illumination.

### 3.2.6.2 Device stability tests with AD-based interlayers

While we were able to distinguish a preservation of the perovskite surface composition with the additive 1ADAHCl in the short term, our final objective is to achieve a long-term protection of the perovskite device to avoid layer degradation and a fast performance reduction. First, the samples are stored in air atmosphere and day/night cycle for five weeks in Figure 3.21. This step was to confirm to preservation effect of the surface modifiers.

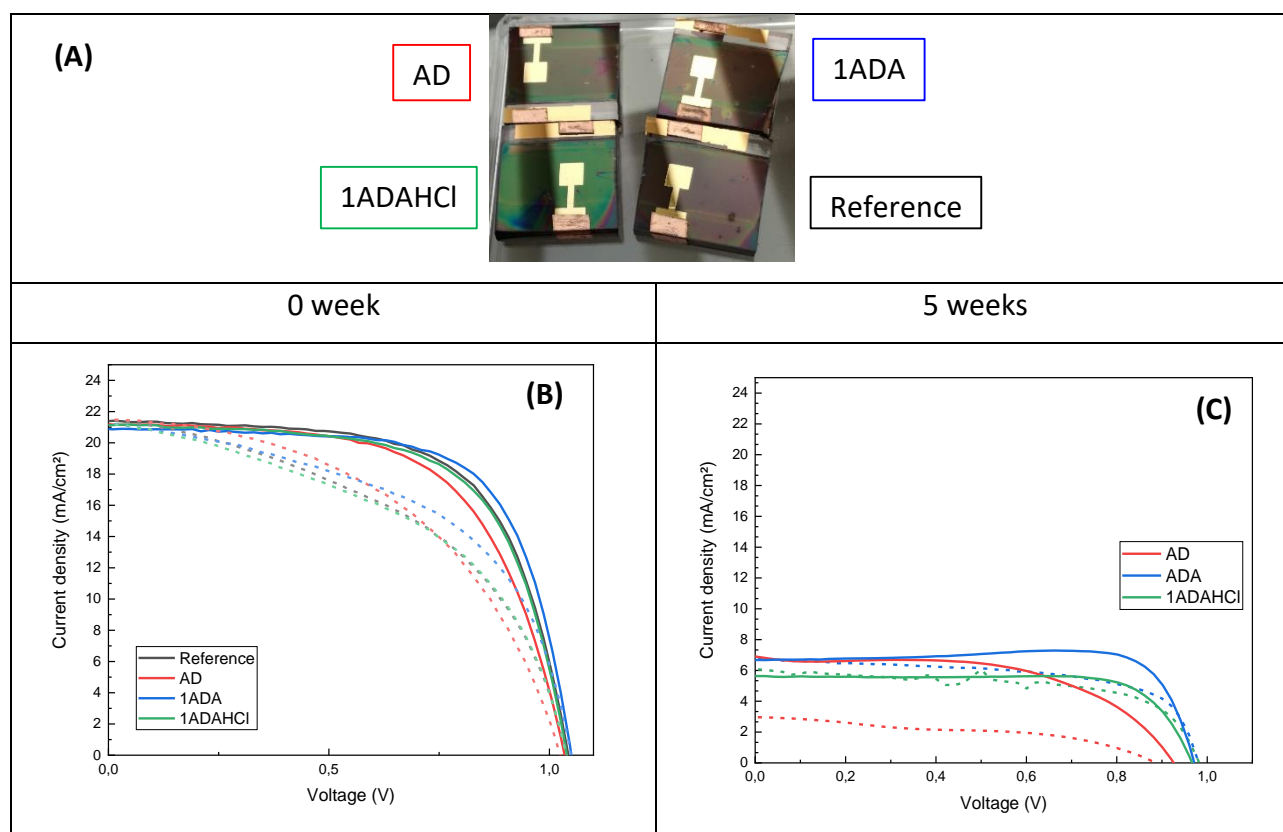
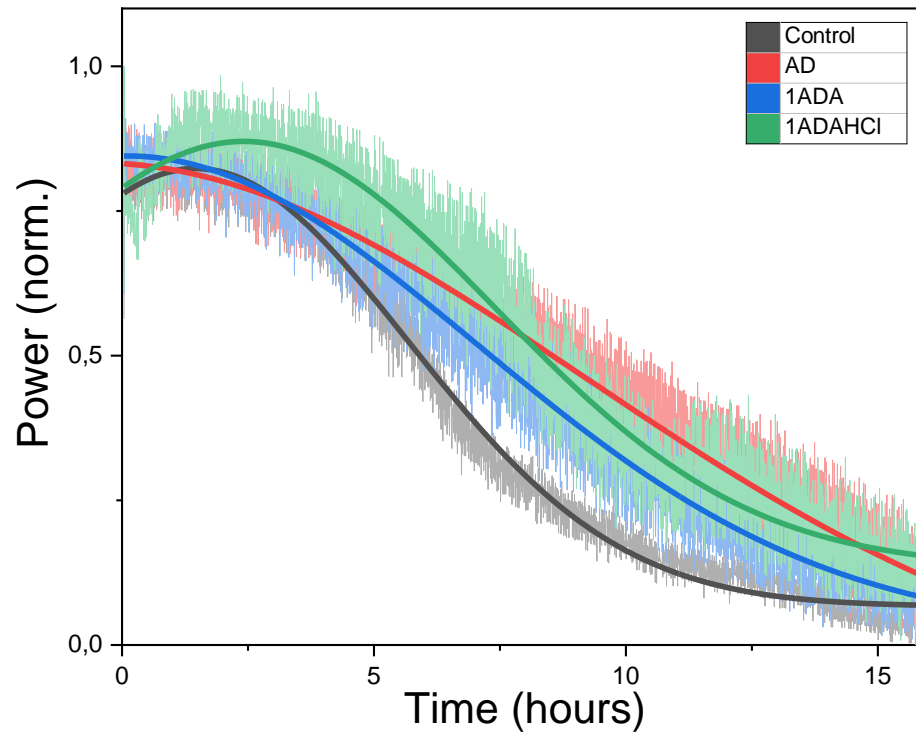


Figure 3.21: Picture of the devices stored under air atmosphere and day/night cycle for 5 weeks (A) coupled with the IV spectrums at d0 (B) and at 5 weeks (C)

In Figure 3.21.A, after 5 weeks, all samples show significant signs of degradation. The reference sample is completely dark brown color. AD and 1ADA samples almost reached this color as well, and 1ADAHCl kept its green color. The degradation is linked to the perovskite layer, and the colour perception depends on the top HTL layer. We use spiro-MeOTAD with cobalt additive, which leads

to a green colour for the final device. It seems that the perovskite layer could be preserved in the presence of 1ADAHCl as it kept its green colour and seemed less degraded than the reference thoroughly degraded sample. The JV measurements before the degradation (Figure 3.13B) show similar device characteristics for all samples indicating a low influence of the additives in the devices similar to our previous detailed analysis of larger data sets which indicated only a very small improvement with the use of the molecular interlayer. However, after 5 weeks, we still retain functioning devices for AD, 1ADA and 1ADAHCl samples, contrary to the reference samples, for which no working sample could be retrieved. Nonetheless, the device performance of the protected devices has still deteriorated significantly which means that the interlayer would not substitute any additional need for encapsulation. However, applying the molecular interlayer obtained a minor effect on device preservation.

To confirm these results, the solar cells have been placed under illumination for several hours in our solar tracking system with no encapsulation. We are able to track the device's power, voltage and current density through time. The results correspond for solar device with AD, 1ADA and 1ADAHCl compared to a reference solar cell (glass/FTO/c- m-TiO<sub>2</sub>/HaP/X/gold). After three hours, the devices with additives present higher efficiencies than the reference sample, especially with 1ADAHCl, indicating a protection of the device performance with the additives. However, the performances are not kept for an extended period as gradually a reduction of the overall performances is observed. The samples with additives still performed better than the reference sample. However, the additives cannot currently be used for long-term stability protection.



*Figure 3.22: Power tracking of light illumination for 15 hours under air-atmosphere*

### 3.2.7 Conclusion

The lead halide perovskite (HaP) solar cell's interface design is the key to developing a stable device with higher power conversion efficiency (PCE) using material engineering and interface passivation. To achieve this goal, this work focused mainly on the hole transport layer / HaP interface, also called the top interface in an NIP configuration using an organic compound called adamantane and its derivatives: 1-adamantanamine and 1-adamantanamine hydrochloride, which exhibit hydrophobic properties. Therefore, we expected a protection against the humidity of the absorber and a long-term improvement of the device stability. Using electrical characterization and XPS analysis, we were able to confirm the presence of additives on the perovskite surface while the bulk of the perovskite layer remained unaffected. This information was used to compare the evolution of the perovskite layer in their presence over time.

While we find some improvement in the initial device parameters for fresh cells, when the molecular interlayer is applied, notably in the open-circuit voltage (Voc) and fill factor (FF) due to a reduction of surface charge recombination, this effect was limited and increased the device efficiency from 16.1% to 17.4%. However, we were able to observe a preservation effect of the surface modifiers to the perovskite surface in the first place and consequently the entire device, which we confirmed by XPS and device tracking under illumination, respectively.

In the end, we proposed the availability of a new family of hydrocarbon molecule, the adamantane and its derivatives. This family exhibit a potential for short-term device preservation, which could aid in the reliability of device fabrication processes.

In this regard, 1ADAHCl give us the most promising results as a good preservation of the perovskite layer on the short term and better perovskite performance in the long-term compared to the reference devices. However, these molecules alone can still not be used to enhance the long-term stability for a final product ultimately. In the end, these molecules could serve as a good base for synthesizing a new generation of surface modifiers for the passivation layer but require further optimization and additional measures to fully protect the perovskite-based device.

### 3.2.8 References

1. Tavakoli, M. M. *et al.* Adamantanes Enhance the Photovoltaic Performance and Operational Stability of Perovskite Solar Cells by Effective Mitigation of Interfacial Defect States. *Adv. Energy Mater.* **8**, 1–7 (2018).
2. Liu, F. *et al.* Is Excess PbI<sub>2</sub> Beneficial for Perovskite Solar Cell Performance? *Adv. Energy Mater.* **6**, 1–9 (2016).
3. Gujar, T. P. *et al.* The role of PbI<sub>2</sub> in CH<sub>3</sub>NH<sub>3</sub>PbI<sub>3</sub> perovskite stability, solar cell parameters and device degradation. *Phys. Chem. Chem. Phys.* **20**, 605–614 (2017).
4. Béchu, S., Ralaiarisoa, M., Etcheberry, A. & Schulz, P. Photoemission Spectroscopy Characterization of Halide Perovskites. *Adv. Energy Mater.* **10**, 1–25 (2020).
5. Briggs, D. X-ray photoelectron spectroscopy (XPS). *Handb. Adhes. Second Ed.* 621–622 (2005) doi:10.1002/0470014229.ch22.
6. Hüfner, S. *Photoelectron Spectroscopy*. (Springer Berlin Heidelberg, 2003). doi:10.1007/978-3-662-09280-4.
7. Thermo Fisher Scientific. Carbon contamination - <https://www.thermofisher.com/fr/fr/home/materials-science/learning-center/periodic-table/non-metal/carbon.html>.
8. Miller, D. J., Biesinger, M. C. & McIntyre, N. S. Interactions of CO<sub>2</sub> and CO at fractional atmosphere pressures with iron and iron oxide surfaces: One possible mechanism for surface contamination? *Surf. Interface Anal.* **33**, 299–305 (2002).
9. Cacovich, S. *et al.* Light-Induced Passivation in Triple Cation Mixed Halide Perovskites: Interplay between Transport Properties and Surface Chemistry. *ACS Appl. Mater. Interfaces* **12**, 34784–34794 (2020).
10. Cacovich, S. *et al.* Light-Induced Passivation in Triple Cation Mixed Halide Perovskites: Interplay between Transport Properties and Surface Chemistry. *ACS Appl. Mater. Interfaces* **12**, 34784–34794 (2020).
11. Zu, F. S. *et al.* Impact of White Light Illumination on the Electronic and Chemical Structures of Mixed Halide and Single Crystal Perovskites. *Adv. Opt. Mater.* **5**, (2017).
12. Steirer, K. X. *et al.* Defect Tolerance in Methylammonium Lead Triiodide Perovskite. *ACS Energy Lett.* **1**, 360–366 (2016).
13. Schulz, P., Cahen, D. & Kahn, A. Halide Perovskites: Is It All about the Interfaces? *Chem. Rev.*

- 119**, 3349–3417 (2019).
14. Habisreutinger, S. N., Noel, N. K. & Snaith, H. J. Hysteresis Index: A Figure without Merit for Quantifying Hysteresis in Perovskite Solar Cells. *ACS Energy Lett.* **3**, 2472–2476 (2018).
  15. Jena, A. K. & Miyasaka, T. Hysteresis Characteristics and Device Stability. in *Organic-Inorganic Halide Perovskite Photovoltaics* 255–284 (Springer International Publishing, 2016). doi:10.1007/978-3-319-35114-8\_10.
  16. Calabrò, E. *et al.* Easy Strategy to Enhance Thermal Stability of Planar PSCs by Perovskite Defect Passivation and Low-Temperature Carbon-Based Electrode. *ACS Appl. Mater. Interfaces* **12**, 32536–32547 (2020).
  17. Ceratti, D. R. *et al.* Self-Healing Inside APbBr<sub>3</sub> Halide Perovskite Crystals. *Adv. Mater.* **30**, 1–7 (2018).
  18. Osadchii, D. Y., Olivos-Suarez, A. I., Bavykina, A. V. & Gascon, J. Revisiting Nitrogen Species in Covalent Triazine Frameworks. *Langmuir* **33**, 14278–14285 (2017).
  19. Thampy, S., Zhang, B., Park, J. G., Hong, K. H. & Hsu, J. W. P. Bulk and interfacial decomposition of formamidinium iodide (HC(NH<sub>2</sub>)<sub>2</sub>I) in contact with metal oxide. *Mater. Adv.* **1**, 3349–3357 (2020).
  20. Meier, T. *et al.* Impact of excess PbI<sub>2</sub> on the structure and the temperature dependent optical properties of methylammonium lead iodide perovskites. *J. Mater. Chem. C* **6**, 7512–7519 (2018).

## Chapter 4: Development and tests of synthesized amino carboxylic acids: an approach at the bottom interface

This chapter describes the collaborative work undertaken with ITODYS (Team Organisation Moléculaire Nano2D – MONa2D) in the frame of this thesis research work. The study focuses on grafting self-assembled monolayers SAM based on amino carboxylic acids, which is one of the fields of expertise that NoNa2D team developed on metallic oxide and metal substrates for application in optoelectronics. In the final device, the SAM layer is located at the interface between the perovskite layer and the ETL (rear interface), as shown on the schematic Figure 4.1. Using the SAMs, our objective is to improve the interaction between the ETL and the HaP by reducing the charge recombination.

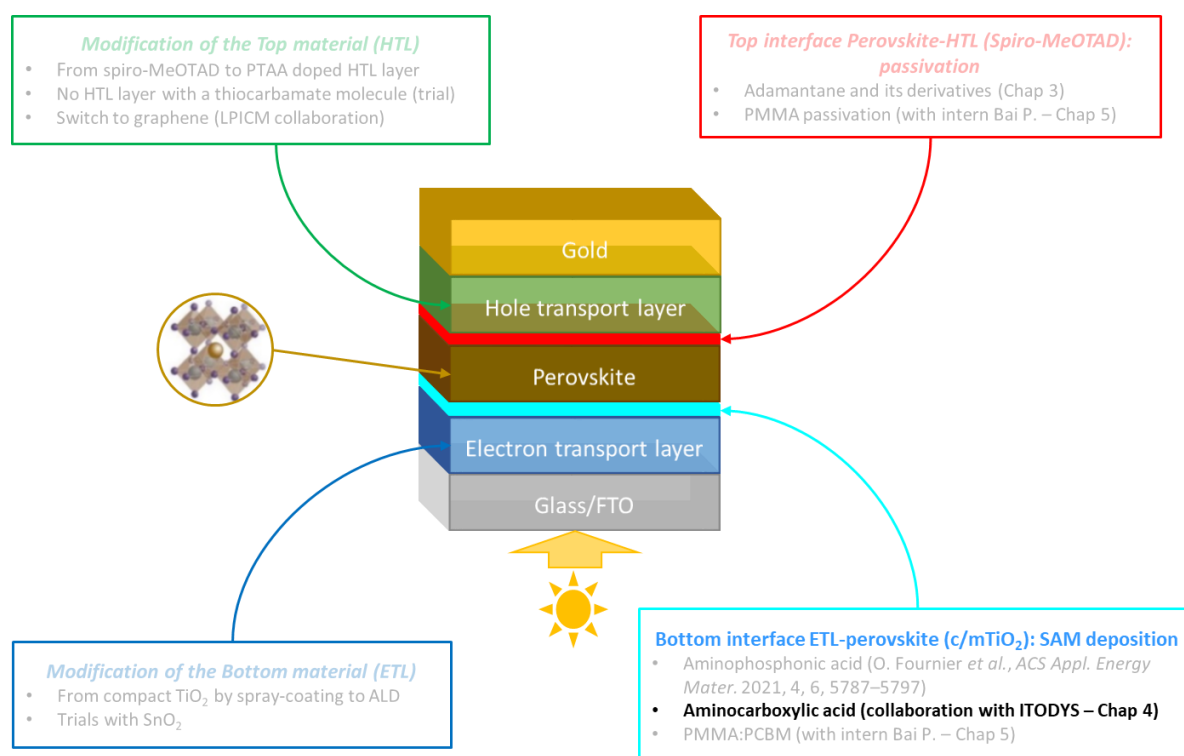


Figure 4.1: Schematic of the working steps through this thesis on NIP configuration perovskite solar cells. Highlight on the bottom interface with Chapter 4

## Table of Contents

4.1	Aminocarboxylic acid as passivation layer at the perovskite / ETL rear interface.....	128
4.2	Deposition process of the SAMs layers on mesoporous TiO <sub>2</sub> .....	129
4.3	Characterization of the mesoporous TiO <sub>2</sub> layer after SAM grafting.....	131
4.4	Integration of the SAMs interlayer in the device.....	132
4.4.1	Influence of surface preparation of the metal oxide layer on the device properties 132	
4.4.2	Integration of the amino and amino-methyl based SAMs (SAM1-4) in the perovskite solar cell structure .....	136
4.4.3	Integration of the amidino-based SAMs (SAM 5-6) in the perovskite solar cell structure 142	
4.4.4	Integration of the amidino-based biphenyl SAM (SAM 7) in the perovskite solar cell structure 147	
4.5	Discussion.....	150
4.6	References.....	152
4.7	Annexes.....	153
4.7.1	ATR-FITR spectra of the SAM-deposited sample in mesoporous TiO <sub>2</sub> compared to a KBr pellet with SAM molecule incorporated .....	153

## 4.1 Aminocarboxylic acid as passivation layer at the perovskite / ETL rear interface

The objective of this study is to use aminocarboxylic acids molecules to form a self-assembled monolayer (SAM) film on top of the ETL layer in the PSC, which in our case is the  $\text{TiO}_2$  film in this project. Generally, the SAMs comprise an anchoring, spacer, and functionalized group as described in Chapter 1: Context and Stat of the art. First, the anchoring group interacts with the metal oxide and attaches the molecule to the underlying layer. Of note, the deposition of the SAM will also modify the modified surface's wettability and might affect the subsequent deposition of the perovskite layer on top. The SAM-forming molecules exhibit a carboxylic acid group as a head group to graft on the metal oxide ETL surface through interaction with either the metal ( $\text{M}^{2+}$ ) or the oxygen ( $\text{O}^{2-}$ )<sup>1,2</sup>. Several possibilities of bond mechanism for carboxylic acids exist from electrostatic attraction to bidentate chelating, as in Figure 4.1.

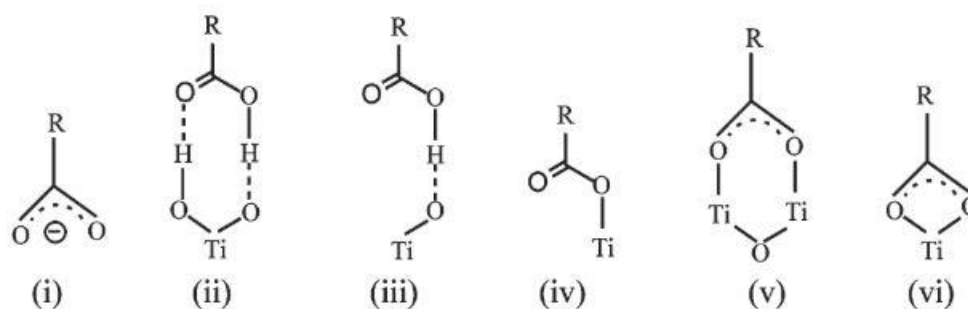


Figure 4.2: Possible binding modes of carboxylic acid group on  $\text{TiO}_2$  nanoparticcles: (i) Electrostatic attraction, (ii, iii) H-bonding, (iv) monodentate (ester-like linkage), (v) bidentate bridging, and (vi) bidentate chelating. Taken from Qu et al<sup>3</sup>

Through Infrared measurements, it is possible to determine the type of bond of the carboxylic acid group. The spacer is a hydrocarbon chain, which should be short enough for the charge carriers to pass and reach the ETL; if composed of conjugated  $\pi$ -electron bonds, carrier transport through the chain is enhanced<sup>4</sup>. In the case of the SAMs used here, the spacers are phenyl or biphenyl groups. To finish, the functional group is composed of an amino site. This group can interact with the perovskite layer, composed of  $\text{MA}^+$  and  $\text{FA}^+$ , on the A-site crystalline structure. With respect to the perovskite structure and likely defects described in Chapter 1, the perovskite layer is likely to be deficient in the A-site cations which are (in part) occupied by volatile organic species.. The

aminocarboxylic acid can interact with the defect site, help stabilize the perovskite layer, and improve the solar cell parameters and the stability of the devices.<sup>2,5,6</sup>

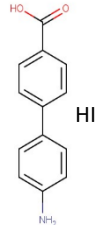
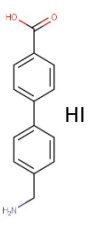
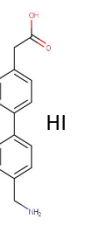
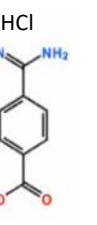
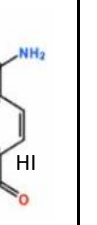
	SAM 1	SAM 2	SAM 3	SAM 4	SAM 5	SAM 6	SAM 7
Molecular structure							
Name	4'-amino-[1,1'-biphenyl]-4-carboxylic acid	4'-amino-[1,1'-biphenyl]-4-carboxylic acid hydroiodide	4'-(aminomethyl)-[1,1'-biphenyl]-4-carboxylic acid hydroiodide	2-[4'-(aminomethyl)-[1,1'-biphenyl]-4-yl]acetic acid hydroiodide	4-amidino-benzoic acid hydrochloride	4-amidino-benzoic acid hydroiodide	4'-amidino-[1,1'-biphenyl]-4-carboxylic acid hydroiodide
Formula	C <sub>13</sub> H <sub>11</sub> NO <sub>2</sub>	C <sub>13</sub> H <sub>12</sub> INO <sub>2</sub>	C <sub>14</sub> H <sub>14</sub> INO <sub>2</sub>	C <sub>15</sub> H <sub>16</sub> INO <sub>2</sub>	C <sub>8</sub> H <sub>8</sub> N <sub>2</sub> O <sub>2</sub> , HCl	C <sub>8</sub> H <sub>8</sub> N <sub>2</sub> O <sub>2</sub> , HI	C <sub>14</sub> H <sub>12</sub> N <sub>2</sub> O <sub>2</sub> , HI
CAS number	5730-78-9	/	/	/	/	/	/
Molecular weight	213.2	341.14	355.17	369.2	200.45	291.9	367.9

Table 4.1: Self-assembled molecules synthesized by ITODYS and used for the collaboration with IPVF and incorporated in NIP configuration

## 4.2 Deposition process of the SAMs layers on mesoporous TiO<sub>2</sub>

The deposition process of the SAM is explained in the Chapter 2.1.6 of this thesis. Except for the SAM 1, which is a commercial product, the SAMs are synthesized in ITODYS from scratch, and the synthesis steps were presented above with the example of the SAM 7. The fabrication process is similar for the other SAM with a difference depending on what we want to produce. NMR analyzes each finalized product to verify by comparison with theoretical spectra if the reaction pathway of the synthesis succeeded (number of cycles and principal hydrogenated functions). For SAM 7 (Reaction 2.3), the protons at  $\delta$ 9.44ppm, 9.13ppm, 7.92ppm, 7.96ppm, 8.02ppm, 8.07ppm et

13.10ppm corresponded respectively to  $\text{CNH}_2^+$ ,  $\text{CNH}_2$ ,  $\text{H}_1$ ,  $\text{H}_2$ ,  $\text{H}_3$ ,  $\text{H}_4$  and  $\text{COOH}$ , in agreement with the expect molecule.

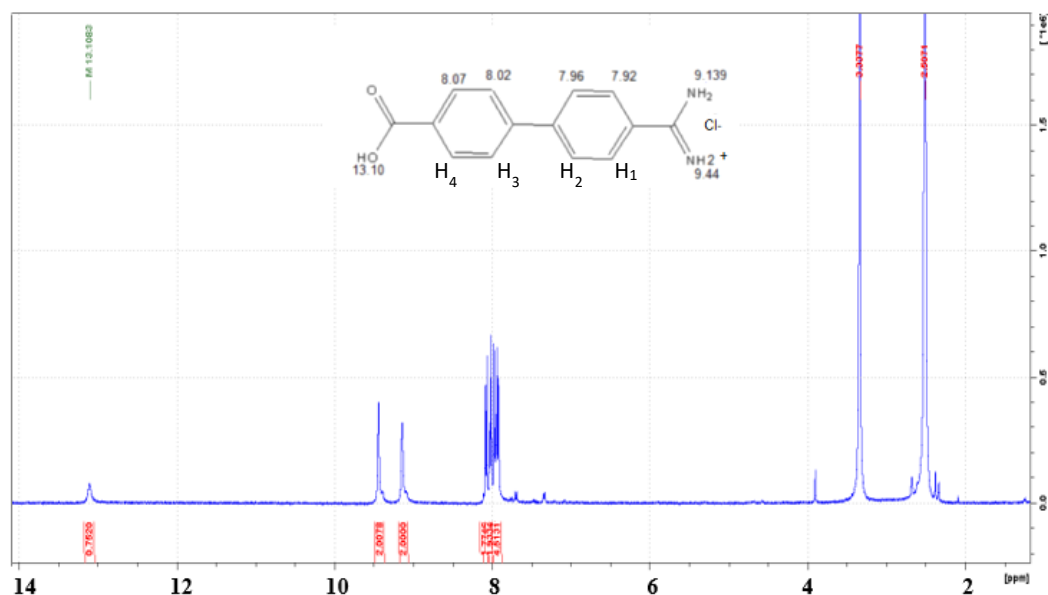


Figure 4.3:RMN experimental spectrum of SAM 7

We keep the same fabrication process as the HaPSC baseline and adapt to incorporate the SAM. The cell fabrication switch from IPVF to ITODYS depends on the fabrication step, and a full week is needed to produce a series of samples. The time of the deposition process is referred in Table 2.3.

	Day 1- Monday	Day 2-Tuesday	Day 3- Wednesday	Day 4- Thursday	Day 5-Friday
Localization of the samples	IPVF	IPVF to ITODYS	ITODYS	ITODYS to IPVF	IPVF
Actions taken	<ul style="list-style-type: none"> <li>Cleaning of the samples</li> <li>Compact <math>\text{TiO}_2</math> deposition</li> </ul>	<ul style="list-style-type: none"> <li>Mesoporous <math>\text{TiO}_2</math> deposition</li> <li>Preparation of the samples in a glovebox</li> <li>Samples sent to ITODYS (afternoon)</li> </ul>	Grafting of the molecules for 24h	<ul style="list-style-type: none"> <li>Taking back the samples</li> <li>Perovskite and Spiro-OMeTAD Deposition</li> </ul>	<ul style="list-style-type: none"> <li>Gold deposition</li> <li>JV measurement</li> </ul>

Table 4.2: Weekly schedule for the deposition process of the SAM-perovskite solar device

After the final layer, the cell is ready for characterization and JV measurements.

### 4.3 Characterization of the mesoporous TiO<sub>2</sub> layer after SAM grafting

As mentioned previously, after SAM deposition, characterization was performed to validate the grafting and the chemical nature of the grafted species on the surface of the ETL layer. ATR-FTIR were made in ITODYS. The techniques are explained in Chapter 2. In the case of the SAM, the vibration  $\nu(\text{HOC}=\text{O})$ , around  $1700\text{ cm}^{-1}$ , is present on all of the pellets prepared. Once the molecules are grafted, the band vibrations  $\nu(\text{HOC}=\text{O})$  and  $\nu(\text{C}-\text{OH})$  should be reduced, indicating the SAM absorption on the surface and the molecule's binding, since the bands are linked to the carboxylic acid showing the adsorption of the acid group on the metal oxide through hydrogen bond. The descriptions will be done on the SAM 7. The other spectra are present in the 4.7 Annexes.

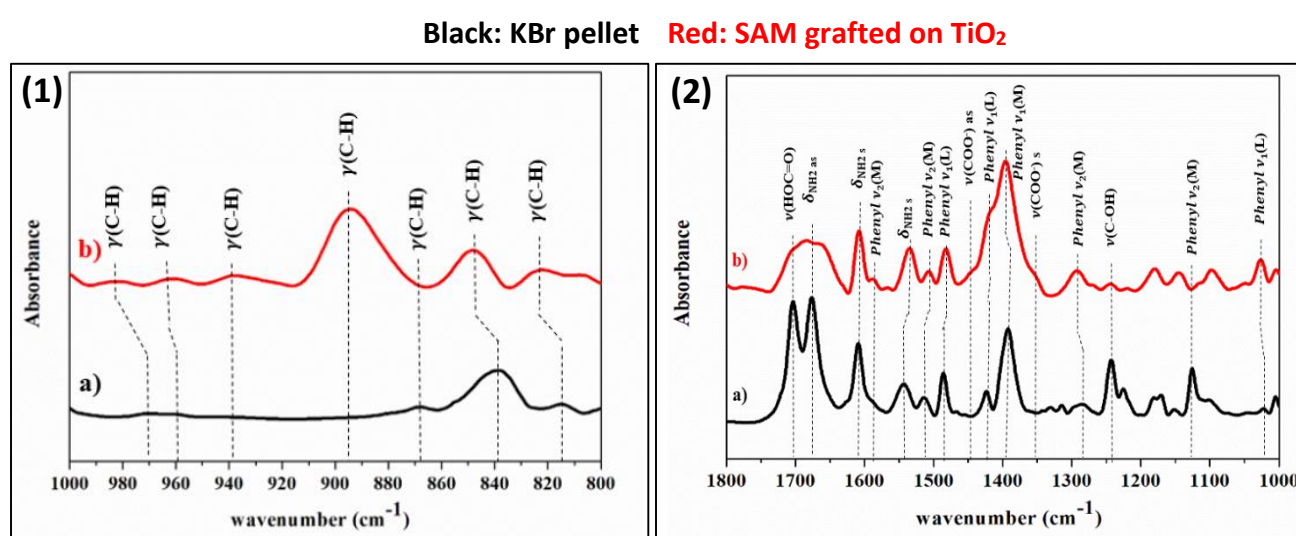


Figure 4.4: FTIR-ATR spectra (1) the region of  $1000 - 800\text{ cm}^{-1}$  and (2) in the region  $1800 - 1000\text{ cm}^{-1}$  of SAM 7 (a) in KBr pellet and (b) grafted on *c-m* TiO<sub>2</sub>

In Figure 4.4, the band vibration  $\nu(\text{HOC}=\text{O})$  at  $1703\text{ cm}^{-1}$  and the band vibration  $\nu(\text{C}-\text{OH})$  at  $1243\text{ cm}^{-1}$  are highly present in the KBr pellet. In the grafted samples, these band vibrations have been reduced partially with  $\nu(\text{HOC}=\text{O})$  at  $1705\text{ cm}^{-1}$  and  $\nu(\text{C}-\text{OH})$  at  $1243\text{ cm}^{-1}$ , indicating a partial grafting of the acid on the surface. The grafting is also defined by this acid function replaced by a carboxylate anion at the  $\text{Ti}^{2+}$  cation following the reaction between the acid group and the TiO<sub>2</sub>, leading to the formation of two new band vibrations, present also on SAM 7: an asymmetrical band  $\nu(\text{COO}^-)_{\text{as}}$  at  $1447\text{ cm}^{-1}$  and a symmetrical band  $\nu(\text{COO}^-)_{\text{s}}$  at  $1353\text{ cm}^{-1}$ .<sup>7</sup> The molecule is grafted partially on the metal oxide layer.

The grafting mode of the carboxylic acid on the metal oxide can be calculated using the difference between the asymmetrical band vibration and the symmetrical band vibration through the equation

$\Delta(\nu \text{COO}^-) = \nu(\text{COO}^-)_{as} - \nu(\text{COO}^-)_s$  for the SAMs. As the difference is inferior to  $150 \text{ cm}^{-1}$ , the grafting can be identified as bidentate—the two atoms of the carboxylic acid bond with one  $\text{Ti}^{2+}$ .<sup>3,8</sup> The grafting mode observed is bidentate for all the SAMs layers grafted (table 4.3).

SAM	$\Delta(\nu \text{COO}^-)$	Grafting mode
SAM 1	140	Bidentate bridging
SAM 2	145	Bidentate bridging
SAM 3	142	Bidentate bridging
SAM 4	143	Bidentate bridging
SAM 5	99	Bidentate chelating
SAM 7	94	Bidentate chelating

*Table 4.3: Shift of  $\text{COO}^-$  vibration mode ( $\Delta(\nu \text{COO}^-)$ ) between the molecule measured by ATR-FTIR grafted on the  $\text{TiO}_2$  substrate. Grafting mode of the SAMs studied*

We are able to identify the presence of the SAM on the c-m  $\text{TiO}_2$  layer through ATR-FTIR, as well as the binding mode of the bonds. Now, we will try to integrate this new interlayer in the perovskite devices and determine the potential effects of this new interaction.

## 4.4 Integration of the SAMs interlayer in the device

Different series of samples were prepared to optimize the interlayer integration step and identify, from device characterizations: 1) The influence of the fabrication process itself on the interlayer quality and 2) the impact of the incorporation of SAMs incorporation in the device structure.

### 4.4.1 Influence of surface preparation of the metal oxide layer on the device properties

Each step of the fabrication process is verified using devices and labeled according to Table 4.4. The classic baseline process, corresponding to samples being prepared with the standard procedure at IPVF, is identified as condition I0 in the table. In this series, the stack below of solar cell structures is kept to compare between the series of this chapter.

Glass/FTO/c- $\text{TiO}_2$ /m- $\text{TiO}_2$ /SAM X/HaP (triple cation)/Spiro-MeOTAD/Gold

<b>I0</b>	Classic baseline	
<b>I1</b>	m-TiO <sub>2</sub> out kept more than 24 hours in IPVF in ambient conditions	
<b>I1'</b>	m-TiO <sub>2</sub> out kept more than 24 hours in ITODYS in ambient conditions	
<b>I2</b>	Heating at 450 °C for 1 hour	
<b>I3</b>	Heating at 450 °C + treated in H <sub>2</sub> SO <sub>4</sub>	
<b>I4</b>	Heating at 450°C + H <sub>2</sub> SO <sub>4</sub> + CBD in SAM-free <b>MeOH</b> overnight	
<b>I4'</b>	Heating at 450°C+ H <sub>2</sub> SO <sub>4</sub> + CBD in SAM-Free <b>DMF</b> overnight	

*Table 4.4: List of the samples that underwent the surface modification process up to different stages in the fabrication and transfer of the SAM deposition process.*

*I0 = standard reference device fabricated at IPVF*

For I1 and I1', samples are conserved more than 24 hours in IPVF or in ITODYS under an ambient atmosphere. By staying in IPVF (I1), these steps are made to determine the influence of the ambient air on the device. The mesoporous layer possibly adsorbs water being stored in ambient atmosphere. Therefore, it leads to a device with a lower stability due to the degradation of the perovskite layer. The difference with corresponding experiment in ITODYS is the fact that samples were transferred under nitrogen in the transfer box before ageing in air 24 hours (I1'). Additionally, the laboratory atmospheres in the ITODYS and IPVF laboratories are not the same since IPVF experiments took place in a cleanroom with controlled temperature, different humidity rates and illumination. From these experiments we obtain important indications about the reactivity and stability of the modified surfaces before the perovskite layer is deposited..

According to the previously detailed procedure, samples were then annealed at 450°C (I2) for the pretreatment of m-TiO<sub>2</sub> before any use to eliminate the possible water readsorption. Then, the samples were treated under sulfuric acid (I3). This step in particular, is suspected to alter the m-TiO<sub>2</sub> layer as sulfuric acid (H<sub>2</sub>SO<sub>4</sub>) is highly corrosive (and toxic).

In the last step, control samples were left in the SAM-free solvent for the night as the chemical bath is done for 24 hours. The usual solvent used is methanol, an alcohol (I4) with additional trials using dimethylformamide (DMF) (I4') instead, as higher performance were reached.

The j-V characteristics of the champion devices from the finalized are depicted in figure 4.8, which also shows the cells parameters  $V_{oc}$ ,  $J_{sc}$ , FF and PCE for the series of cells prepared with the different surface preparation of the m-TiO<sub>2</sub> layer listed in Table 4.4.

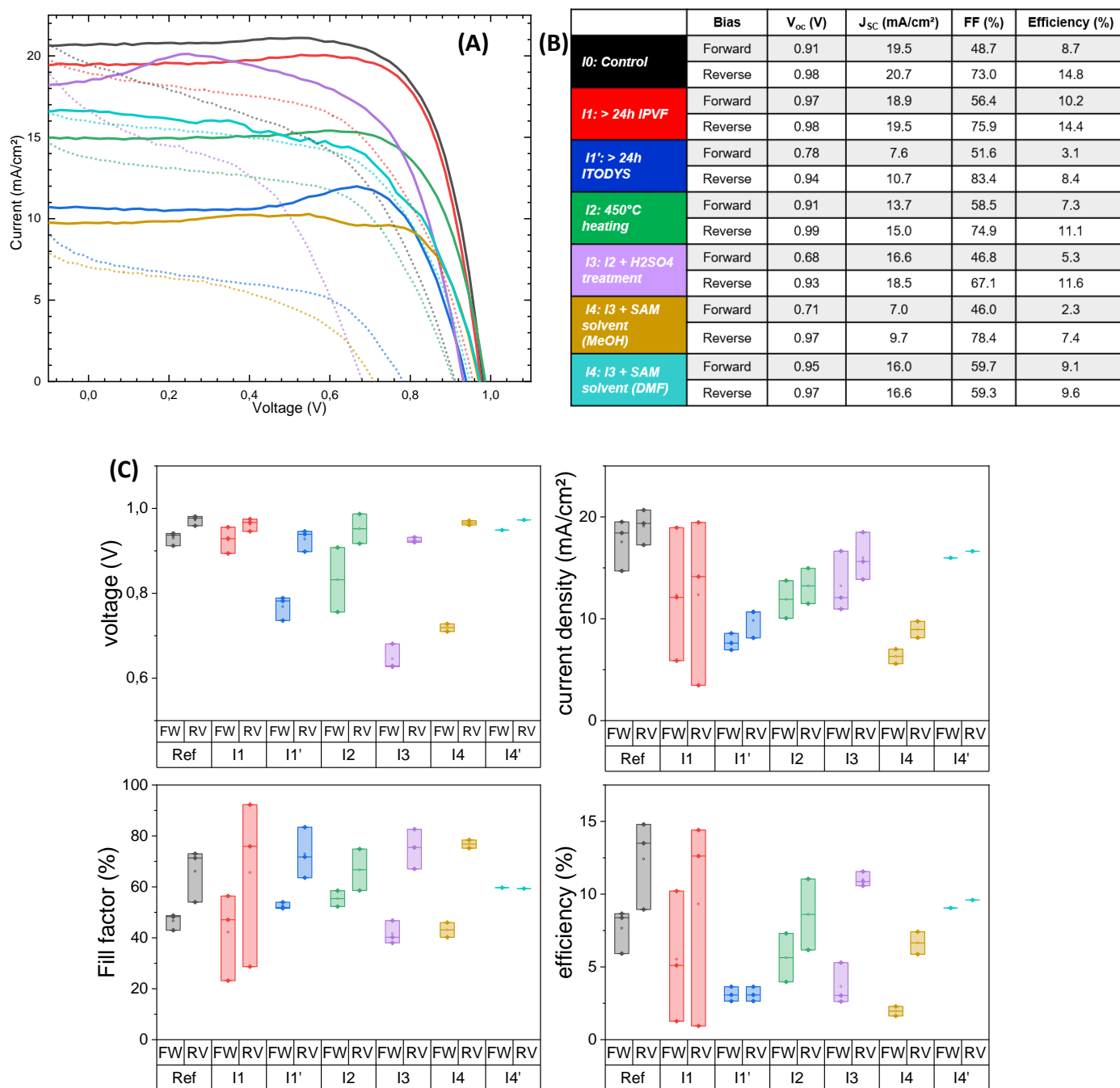


Figure 4.5: Solar cell parameters comparison for the devices fabricated with the  $m\text{-TiO}_2$  prepared layers as detailed in Table 4.4. (A)  $J(V)$  curves of the champion device for each substrate pretreatment condition, (B) table of the solar cell parameters of the best devices, and (C) compilation of the solar cell parameters of the entire series with cell statistics.

Apparent on first sight, the baseline reference samples made and stored entirely at IPVF (I0) exhibit the best performance and notably power conversion efficiencies among the prepared devices. This evidence is mainly shown by the open-circuit voltage with an average at 0.97 V (FW: 0.93 V) and the short-circuit current density at 19.1 mA/cm<sup>2</sup> (FW: 17.5 mA/cm<sup>2</sup>) values. Please note that we find

high hysteresis for the I1 in reverse bias. It is likely coming from the shape of the curve caused by a measurement artifact mirrored in the relatively high hysteresis. The current density is the parameters that change the most with the pretreatment of the metal oxide layer for the chemical bath deposition. This parameter characterizes the crystallization change of the perovskite structure depending on the modified surface of m-TiO<sub>2</sub>. A drop in the current density is noticeable (I1') and mark the environmental differences between the two laboratories, IPVF and particularly at ITODYS, as well as the effects of the transport of the samples from one laboratory to the other. The decrease in device performance could be linked either to a reduction in carrier generation rates, i.e., due to the worst formation of the perovskite layer, or to worse carrier extraction at the interface, e.g., due to contamination layers. The comparably smaller decline in open circuit voltage upon substrate transfer and processing between the laboratories suggests that recombination due to interfacial defects play a minor role. However, the pretreatment of the samples before the chemical bath deposition, annealing and sulfuric acid treatment produce positive effect. We observe an increase in the current density. Finally, the solvent used for the chemical bath plays a role. The dimethylformamide boiling temperature is at 153°C degrees against only 65°C for the methanol. With a less volatile solvent, the concentration stay relatively constant during the chemical bath deposition (24 h duration), explaining why equivalent results are obtained for each deposition in the case of DMF. These results bring important finding to optimize the metal oxide layer surface preparation for SAM grafting.

With this analysis step it is possible to identify several critical points for substrate handling:

- The transport between IPVF and ITODYS of the TiO<sub>2</sub> substrates and storage in ambient conditions is harmful to the device performance. In addition, control over the laboratory atmosphere, as is the case for the samples stored at the IPVF clean room facilities, limits the performance reduction.
- However, the pretreatment of annealing at 450°C and sulfuric acid is useful for regenerating the devices. It hence marks an important intermediate step to operate on high-quality substrates for the SAM formation.
- The solvent used for the SAM preparation plays a significant role in the final devices' performances already at this stage, modifying the ETL substrate layer. The solution is using a less volatile solvent like DMF to secure a constant concentration of the SAMs. With methanol, the ETLs are potentially degraded by the over-concentrated chemical bath for the

SAM solution over time. Hypothetically, since methanol is an alcohol, it possesses a low boiling point at 64.7°C. The methanol can then evaporate, increasing the SAM concentration in the chemical bath overnight. In addition, we find particularly high hysteresis for the methanol solvent (around 40%) coming from the defects made through the fabrication process, characterized by low shunt resistance and low current density sure as pinholes and mesoporous layer degradation.

Following these results, the optimized sample transport and storage conditions were chosen as described in Chapter 2 for the remainder of the experiments of these series to integrate the aminocarboxylic acid SAMs in the PSC device stack.

#### **4.4.2 Integration of the amino and amino-methyl based SAMs (SAM1-4) in the perovskite solar cell structure**

After the substrate handling protocol as well as the effect of the potential treatment steps of the ETL on the device performance have been tested, I targeted the second experimental device series to introduce the SAM layers, that were analyzed in section 4.3, into the device stack starting with SAM 1, SAM 2, SAM 3 and SAM 4.. The device stack was the same as previously, following the baseline IPVF fabrication protocol:

Glass/FTO/c-m TiO<sub>2</sub>/SAM X/HaP (triple cation)/Spiro-MeOTAD/Gold

This time, the m-TiO<sub>2</sub> surface preparation was maintained at the optimized handling protocols (denoted in chapter 2) while the SAM molecule was changed from SAM1, SAM 2, SAM 3 to SAM 4. Thus, by adding a reference device without SAM-forming molecule in the chemical bath to the experimental series a total of five device configurations were analyzed in parallel with three device for each configuration. The J-V characteristics and the summary of the champion cell performances of this series can be found in Figure 4.6.

As a first result, we find that the performance level is overall sub-par compared to other reference runs without any chemical bath treatment of the ETL (referred to as reference in figure 4.9 b). This is likely due to the deviations that occur in the sample handling and laboratory conditions as laid out in section 4.4.1. Nonetheless, we can identify relative differences within this sample batch for the devices that all underwent the same handling conditions. This witness solar cell is subject to the same treatment conditions as the SAM-deposited sample but with no aminocarboxylic acid in the solution to compare the effect of the SAM directly on the performance of the device. In this series, the cells using SAM 1 and SAM 2 present an average power conversion efficiency of respectively

6.79% (FW: 5.34%) and 10.78% (FW: 8.08%). While the witness device without SAM exhibits similar or slightly superior performance levels with a PCE of 8.62% (FW: 5.78%). Generally, SAM 2 led to a smaller statistical spread in the device parameters (see Figure 4.9c) making it a favorable candidate to enhance the reliability of the solar cell fabrication process.

On the contrary, the samples with SAM 3 and SAM 4 reach a performance of 2.25% (FW: 1.45%) and 2.42% (FW: 1.4%). The chemical structure of the molecules can explain this difference in results between the group. In the case of SAM 1 and SAM 2, these two are composed of a biphenyl group directly linked to the amino site and the carboxylic acid group. SAM 3 and SAM 4 have an additional carbon chain (-CH<sub>2</sub>-) in their chemical structure. This leads to a more flexible molecule when grafting onto the metal oxide film. The most significant losses stem from a reduced current density and fill factor which suggests that charge extraction across the SAM covered ETL is detrimentally affected. With current densities averaging at 7.0 mA/cm<sup>2</sup> (FW: 5.8 mA/cm<sup>2</sup>) for SAM 3 and 7.3 mA/cm<sup>2</sup> (FW: 5.6 mA/cm<sup>2</sup>) for SAM 4, carrier extraction (and potentially generation) in these devices is low compared to the control devices (RV: 17.1 mA/cm<sup>2</sup> / FW: 16.3 mA/cm<sup>2</sup>). As represented in Figure 4.6.C, the samples with SAM 3 and SAM 4 also have low fill factor values which are coherent with the perovskite crystallinity issues as the fill factor equation is directly linked to the maximum obtainable power of the device. In the end, the SAM 1 and 2 are promising thanks to their rigid molecular structure and are even comparable to the witness solar cell with an average efficiency of.

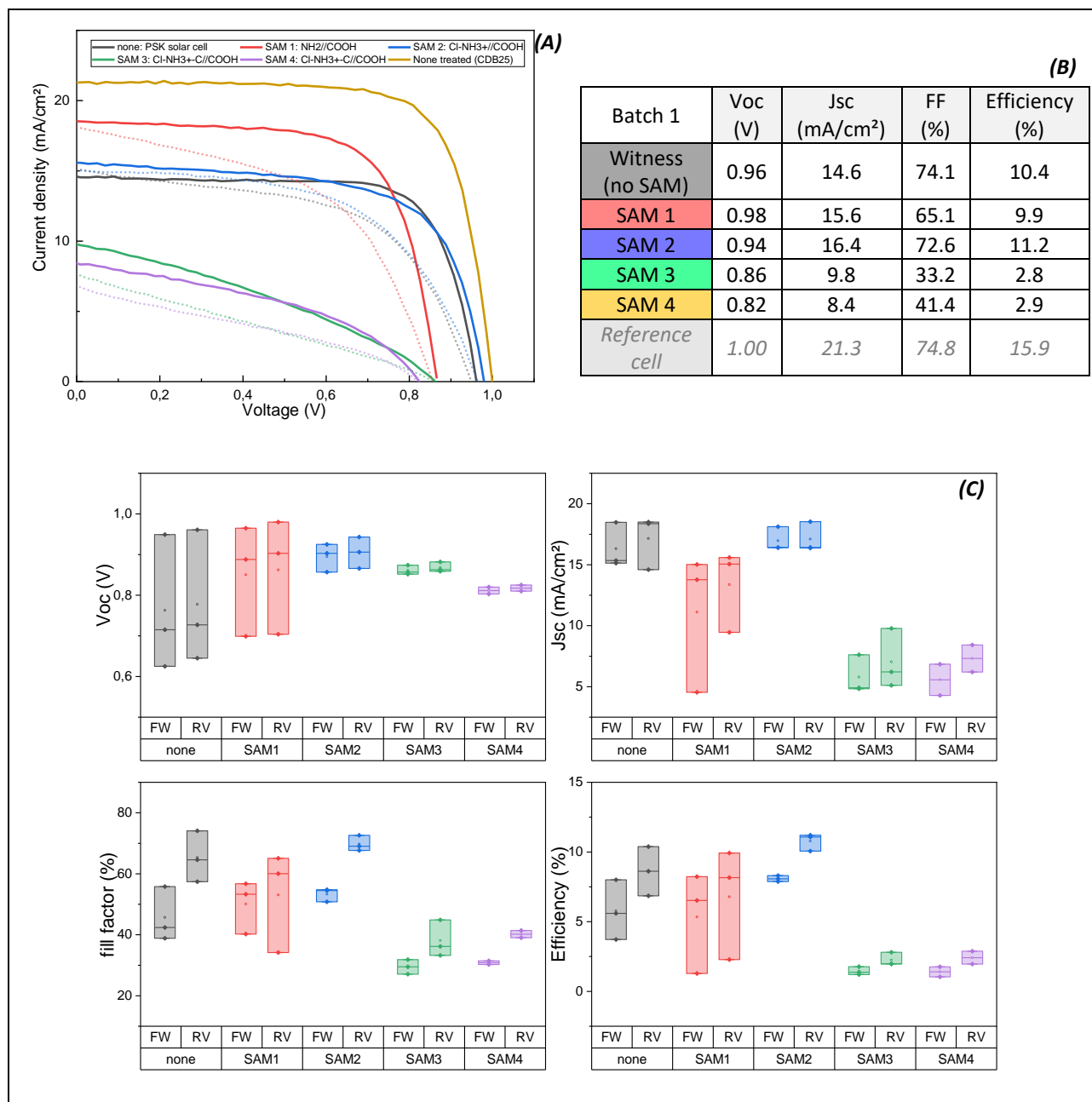


Figure 4.6: (A)  $J(V)$  curve with the best cell results of the samples of the series without/with SAMs compared to a classic sample (REVERSE) (B) coupling with its table (C) Solar parameters values of the first series per SAMs (forward/reverse)

Of note, a possible hypothesis for the general low performances may be related to the annealing of the samples at 180°C for thirty minutes before the perovskite deposition, in the case of m-TiO<sub>2</sub>. As amino biphenylcarboxylic acid molecules, their melting temperatures are lower than 180°C, rather around 120°C to 165°C. The annealing eliminates any trace of water and carbonyl groups trapped in the layer through evaporation before entering the glovebox. By annealing the layer to avoid any water, it improves the device's stability by limiting the degradation of the perovskite solar through

time. However, the beneficial effect becomes detrimental in the case of the SAMs, for which the annealing step, if realized at a temperature higher than the melting point of SAMs, which would lead to the degradation of the molecules. The procedure was then adjusted in follow-up series to improve the device performance such as the current density, especially for the SAM 3 and 4. The devices were also tracked for several weeks to evaluate the evolution of the devices through time, over the course of eight weeks, with a possible maturation and ageing of the devices. During that time, samples were stored in a dessicator in the dark under vacuum. No real improvement was observed between the two series, which means that the influence of the substrate annealing in the first series was insignificant when we compare the measurements at day 0, i.e. on the day the sample production was finalized. We obtain the same trend with the best results for the device using SAM 2, for which the champion sample reaches an efficiency of 12.3% (FW: 10.1%). A loss of current density is observable for the SAM 1 (RV: 7.0%/FW: 6.9%). For the device with SAM3, the one presented is the only one with a tolerable photovoltaic signal, out of 3 samples.

These results show that SAM 3 and SAM 4 do not work well with the triple cation perovskite solar cell, compared to MAPbI<sub>3</sub> absorbers, for which the improved device characteristics were found in a slightly varied device configuration.<sup>8</sup> However, for MAPbI<sub>3</sub>, the average perovskite crystal structure is different from the perovskite used here, which is composed of 78.85% of the FA<sup>+</sup>-based perovskite structure. The compatibility of the SAM is thus likely not the same. This can be explained the interconnection with the chemical architecture depending on the SAMs. Notably, the amino end group might be better suited for the MAPbI<sub>3</sub> growth on top.

This explanation stems from the fact that the A-site of the perovskite, with FA<sup>+</sup> (CH(NH<sub>2</sub>)<sub>2</sub><sup>+</sup>), can be empty due to vacancy defects, which are predominantly located at the surface and interface sites. The SAMs can fill this vacancy. In the case of SAM 1 to SAM 4, by interacting with the A-site using the amino-site, the perovskite layer is more stable with even a decrease of the tolerance factor as the radius of the amino-site is lower than the FA<sup>+</sup>. This reasoning work in the case of SAM 1 and SAM 2. However, in the case of SAM 3 and SAM 4, due to the flexibility of the molecules with the additional methyl group, the crystal structure of the perovskite is less stable, leading to the difficulty of the perovskite crystallization layer.<sup>2</sup>

As indicated above, the devices were measured again after one week, after three weeks and after eight weeks. The results are shown in Figure 4.7. At “day 0”, the samples that were finalized earlier in the day are measured for the first time. The devices featuring the SAM interlayer could preserve

a value around 0.9 V for the open-circuit voltage values. In the case of the reference samples, we even observe an increase of the voltage reaching around 1 V, with respect to the initial measurement. Such an improvement and stabilization of the voltage that we notice for most of the samples indicate an improved or stabilized interface between the perovskite layer and the ETL underneath in the solar cell, respectively. In the case of gradually increasing values for the open-circuit voltage over time, the process can be understood as a maturation during which defects, likely at the interface, are successively reduced.

In the case of the short-circuit current density, as expected, the samples using SAM 3 and SAM 4 retained their low current densities as observed in our previously discussed results or eventually exhibit very low  $J_{sc}$ . However, the  $J_{sc}$  values of the reference devices and the devices using SAM 1 and SAM 2 remained at their initial high levels or even increased a little bit further. In the end, we deem the samples using the SAM 2 as the most promising ones since the performance are slightly better than the reference samples with higher short-circuit current density. Using the SAM 2 at the interface helps improve the net density of photogenerated carriers, while extraction across this interface is enhanced simultaneously.

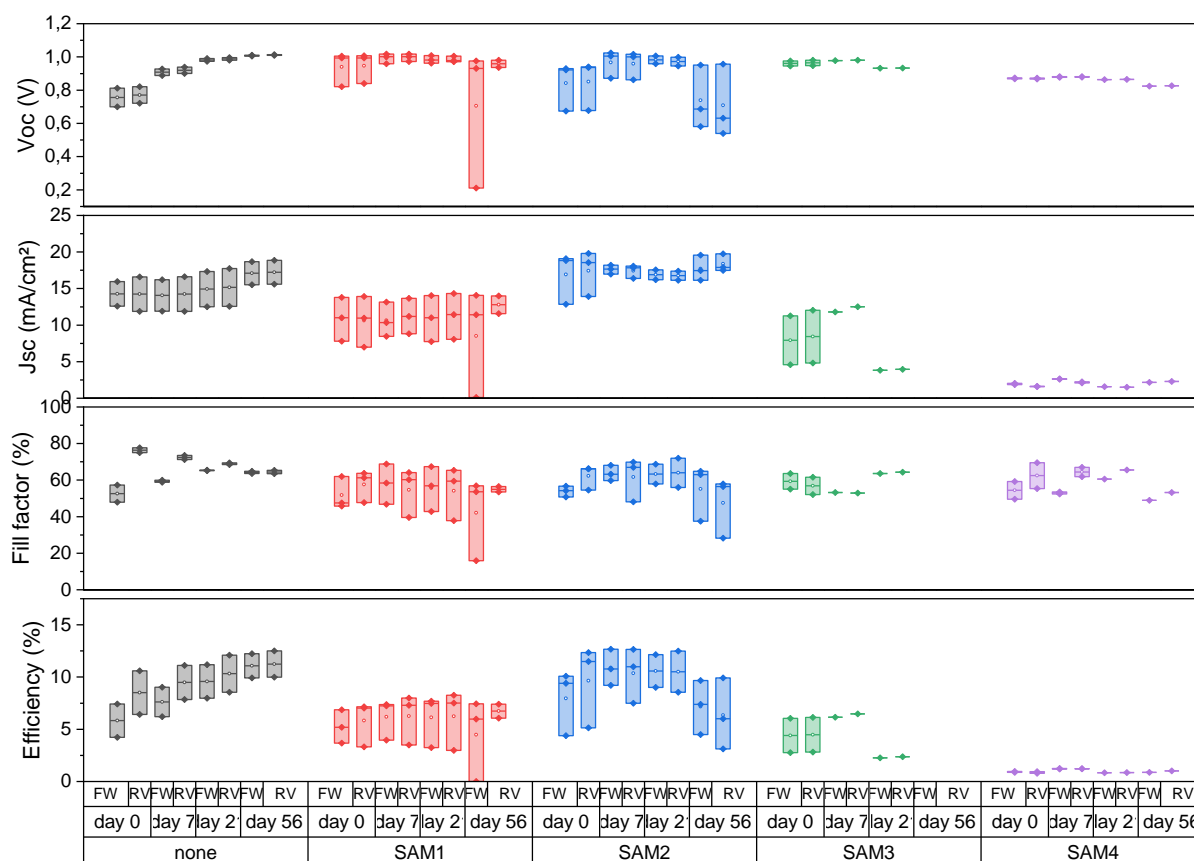


Figure 4.7: Solar cell parameters of the second series of the measurements depending on the molecules deposited on the mesoporous  $TiO_2$  measured at day 0, after one week (day 7), after three weeks (day 21) and after eight weeks (day 56)

In summary, SAM 3 and SAM 4 confirm their incompatibility with the lead halide triple cation perovskite. The focus for the next trials should be directed to the SAM 2 (4'-amino-[1,1'-biphenyl]-4-carboxylic acid hydroiodide) as it presented a slight rise of performance after three weeks of tracking. It is necessary to remember that the current tracking is not performed under “real-life” conditions. However, our assessments already reveals the transient changes in the solar cell and marks a decisive finding for the projection of the cell stability.

Comparing the application of SAMs 1 through 4 as interlayer between the ETL and HaP film, the samples with SAM 2 (4'-amino-[1,1'-biphenyl]-4-carboxylic acid hydroiodide) interlayers presents the best characteristics. However, improvements can be done. Indeed, as the lead halide triple cation perovskite is mostly composed of FA cation in the crystal (78.85%), the next step would be the synthesis of well-fitted molecules that can exactly replace the surface defect from A-site vacancy. In the following steps, our focus now shifts towards the optimization of the SAMs used

with the introduction of newly synthesized molecules: 4-amidino-benzoic (SAM 5) acid and 4-amidino-benzoic acid hydroiodide (SAM 6).

#### 4.4.3 Integration of the amidino-based SAMs (SAM 5-6) in the perovskite solar cell structure

The idea behind the amidino-based molecules, synthesized at ITODYS, for the surface modification SAM 5 and SAM 6, is to achieve a more adapted chemical coupling to the formamidinium-based perovskite (see Figure 4.8). In this case the amidino end group is slated to slot into the A-site vacancies on the perovskite and promote perovskite thin film growth..

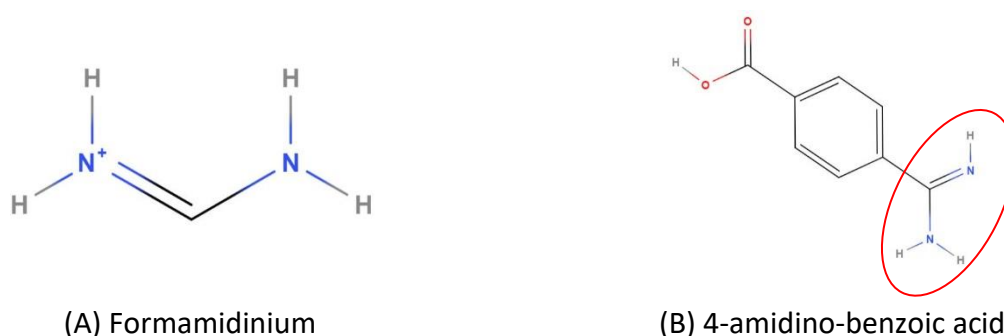


Figure 4.8: Comparison of formadanium ( $FA^+$ ) and 4-amidinobenzoic acid similarity

As mentioned previously, by filling the A-site defects in these molecules, no change will occur theoretically with respect to the Goldschmidt tolerance factor and the crystal structure of the perovskite while the surface is passivated at the same time. Therefore, these SAMs should potentially improve the perovskite solar cell performance better than the previous one. Like the previous series, the J(V) and the EQE were measured for all of the device fresh (day 0) and after day 3 to check for performance improvement. In addition, selected samples were also measured for 100 hours under light and we tracked the power conversion efficiency, current density, and voltage.

By comparing the perovskite solar cell parameters from the control samples made in IPVF and from ITODYS, we observe an overall increase across all device parameters compared to the previous device series, probably due to the improvement of the fabrication process: (a) transport under transfer tube under nitrogen atmosphere, and (b) use of DMF as a SAM solvent. We even retested devices with SAM 3 and SAM 4 and found a considerable enhancement compared to the first series with SAM 3 and SAM 4; from an average of  $12.8 \text{ mA/cm}^2$  (FW:  $12.0 \text{ mA/cm}^2$ ) to  $19.6 \text{ mA/cm}^2$  (FW:  $18.3 \text{ mA/cm}^2$ ) for the SAM 3 and from  $10.7 \text{ mA/cm}^2$  (FW:  $9.5 \text{ mA/cm}^2$ ) to  $17.8 \text{ mA/cm}^2$  (FW:  $16.1 \text{ mA/cm}^2$ ) for the SAM 4. These parameters potentially state that the interface formation has

improved with a lower series resistance and higher current due to better collection. Furthermore, the performances of the devices using the new molecules (SAM 5 and SAM 6) confirm the hypothesis that these layers present themselves as a  $\text{FA}^+$ -friendly substrate (see Figure 4.11). With the presence of the amidino benzoic acid, especially, the hydroiodide version (SAM 6), the cell characteristics rival the one from the reference device while significantly decreasing the observed hysteresis (see table 4.6). The best samples were measured and compared to the reference sample. The SAM 6 samples have an EQE of a maximum of 70.6% and a calculated current density of  $16.5 \text{ mA/cm}^2$ . The results are comparable to the EQE of the reference at a maximum of 72.7% and a current density of  $17.0 \text{ mA/cm}^2$ . Furthermore, this molecule perform the best results compared to the SAM 3 (EQE: 56.8% / $J_{\text{sc}}$ :  $13.3 \text{ mA/cm}^2$ ), SAM 4 (EQE: 49.8% / $J_{\text{sc}}$ :  $11.9 \text{ mA/cm}^2$ ) and SAM 5 (EQE: 61.3% / $J_{\text{sc}}$ :  $14.3 \text{ mA/cm}^2$ ).

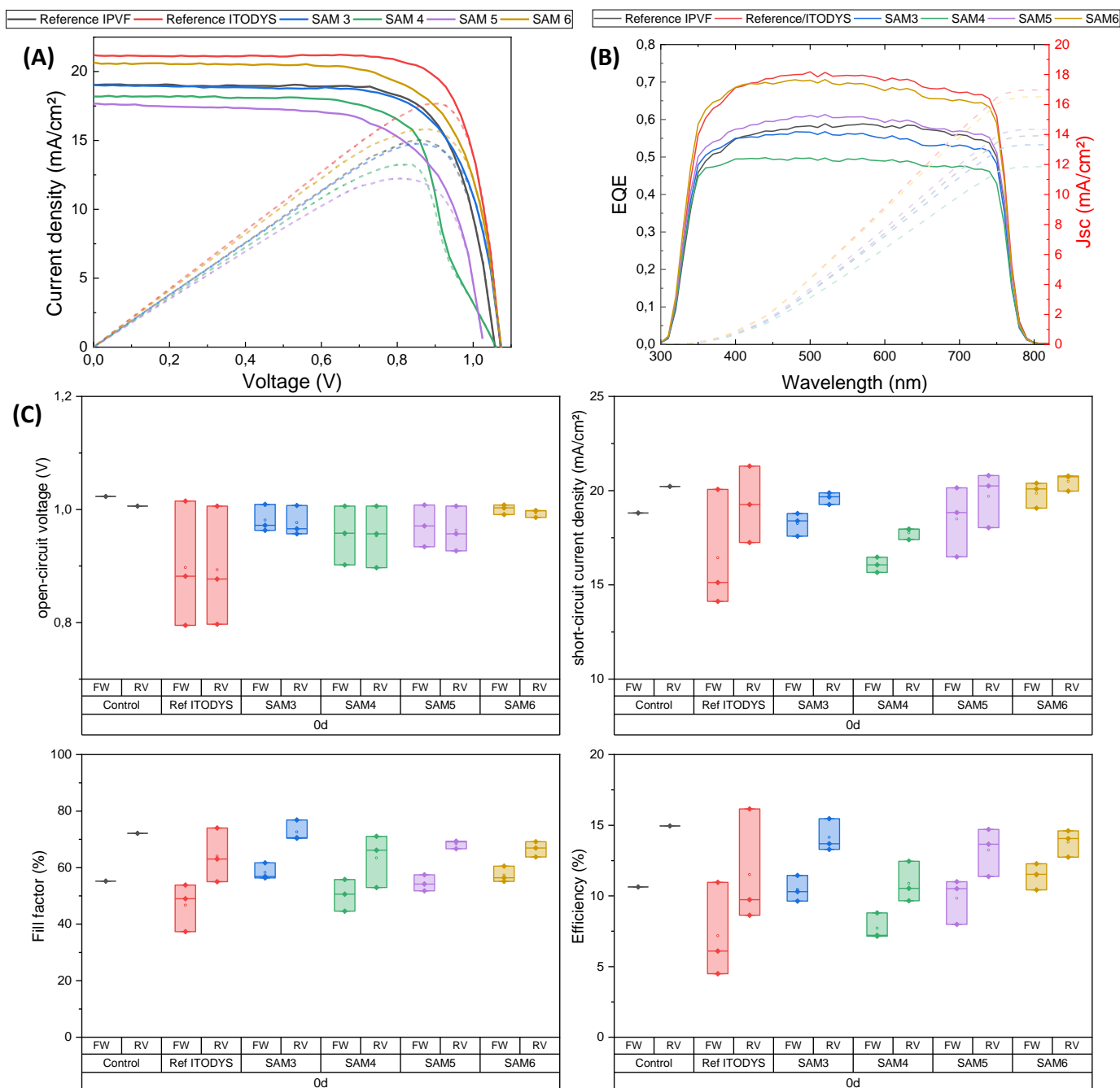


Figure 4.9: Solar cell parameters comparison of the optimized series of the ITODYS-IPVF collaboration (A) JV curves and (B) EQE of the best devices (C) Solar cell parameters of all of the devices at day 0 (0d)

As indicated above, the devices were measured anew three days after fabrication. Again, we observe an increase in the voltage for all samples. We attribute this to the fact that after three days, the spiro-MeOTAD has time to mature due to oxidation thanks to the presence of the dopants and

brief exposure to air.<sup>9</sup> In general, this behavior would help to increase its conductivity and improve the interface contact between the carriers.

At the same time we observe an increase in Voc for all devices. This might be related to as the movement of the carriers is improved into the HTL layer but notably due to reduced recombination at the interface. A slight reduction of the hysteresis is also noticed due to the increase of the fill factor on the forward bias, as indicated in Table 4.5.

Conditions	0d Forward	0d Reverse	Hysteresis	3d Forward	3d Reverse	Hysteresis
Reference IPVF	55.2	72.2	17	65.0	74.6	9.6
Reference ITODYS	46.7	64.0	17.3	62.2	71.4	9.2
SAM3	58.3	72.6	14.3	63.8	68.0	4.2
SAM4	50.4	63.4	13	56.9	65.8	8.9
SAM5	54.5	68.4	13.9	61.1	67.5	6.4
SAM6	57.4	66.6	9.2	65.9	69.9	4

Table 4.5: Fill factors average values of the second series at day 0 (0d) and after 3 three days (3d)

Again, this behavior is linked to the improvement of the carrier transfer between the layers, which is consistent with a possible reduction of the non-radiative recombination on the forward bias.

We used the best-performed devices to perform a light aging and degradation study under one sun illumination. The SAM 4 is not presented as the cell died a few hours after the measurement launch. The power conversion efficiency was tracked for 100 hours under air atmosphere. With the light influence and the atmosphere influence, we were observing if the molecules help to slow down the degradation of the devices through time. Constant decay of the normalized power conversion efficiency is observed over 100 hours of measurements (Figure 4.10). Notably, the 4'-(aminomethyl)-[1,1'-biphenyl]-4-carboxylic acid hydroiodide (SAM 3) exhibits a significantly faster device degradation compared to the other cells tested in the same run. The other molecular modifiers did not perform much worse than the reference samples but also did not improve the degradation dynamics. For the amidino benzoic acid molecules, the power conversion efficiencies of the devices are similar to the reference sample of the series. A drop of the performances is observed after 60 hours under illumination. The reference sample showcased the best result after

100 hours, although its low performance after 100 hours. The voltage of the device stays quite constant after 100 hours of measurement. The power's fast decay comes from the current density decrease through time. Under light and ambient atmosphere, the degradation of the absorber has been accelerated, leading the reduction of the current density values and the power. But eventually, for the devices featuring SAM 5 and SAM 6 the performance dropped to around 10% of the initial performance after the 100h testing duration.

Thus, even as the performance of the devices was slightly improved in this current series, employing SAMs 5 and 6, in the end, the molecules are not a good match for the perovskite solar cell device.

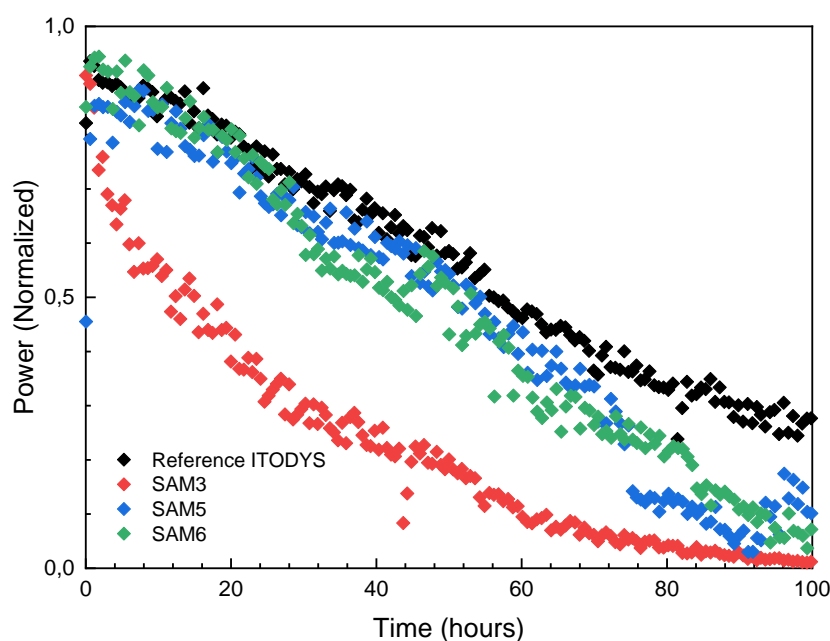


*Figure 4.10: Light ageing degradation tests of non-encapsulated devices under 1 sun for 100 hours*

Finally, the molecules presenting the best results at the end of this series are the amidino benzoic acid hydroiodide (SAM 6). With this FA+ perovskite structure-friendly molecule, the current density was increased. The device was made to challenge the performance of the reference, as it is confirmed with the best device's EQE and the JV curves. Light ageing of the samples was done to confirm the status of these molecules. But the SAM 6 observed a drop in the results after 60 hours of analysis after challenging the reference. The use of SAM 6 is a good sign for us as a room of improvement is noticeable and encouraging. A last series was done with an optimized synthesized molecule : SAM 7, the 4'-amidino -[1,1'-biphenyl]-4-carboxylic acid hydroiodide.

#### 4.4.4 Integration of the amidino-based biphenyl SAM (SAM 7) in the perovskite solar cell structure

We eventually turn to a further optimized molecular structure with the 4'-amidino-[1,1'-biphenyl]-4-carboxylic acid hydroiodide (SAM 7), for which a biphenyl spacer has exchanged the benzoic acid group of SAMs 5 and 6. As the SAM 5 and SAM 6, an amidino site would be adapted for growth of the FA<sup>+</sup>-based perovskite. However, we hypothesize that the reintroduction of the biphenyl group (as in SAMs 1-4) would lead to a more flexible layer, which proved to work well in devices even though all of the SAMs presented the same amino site. SAM 7 is hence poised to combine the two positive effects observed for the previous SAM series.

We applied the same protocol for the device fabrication and characterization. This time, SAM 3 and SAM 5 presented particularly low integrated  $j_{EQE}$  values starting with the EQE. These results were expected for the SAM 3 from the inflexible and MA<sup>+</sup> perovskite-friendly molecules. However, for the SAM 5, I don't have an explanation as the only difference with the SAM 7 is that we pass from a phenyle group to a biphenyle group. This result is not coherent with our previous results above. Then, the results followed with the SAM 4 and finally the SAM 7. Notably, for all samples using the SAMs the results are low compared to the reference. Since no apparent distortion of the EQE spectra is visible, we do not attribute the poor performance of the SAM-modified devices to interfacial effects at the hole collection side, which would be more pronounced in the blue, but rather to worse perovskite film qualities and, connected to this, overall lower carrier generation and higher recombination rate. Further control measurements of the absorption (UV-Vis), recombination (PL), and structure (XRD+SEM) would be required to confirm this statement, but could not be performed in the framework of this screening approach. For JV curve, the same tendencies are observed for the solar cell parameters with the drop of the current densities for all of the devices except the references (RV: 19.9 mA/cm<sup>2</sup>/FW: 20.4 mA/cm<sup>2</sup>). Manufacturing defects seem to also occur in the devices as all of the SAM-deposited samples presented low current densities, between 5 mA/cm<sup>2</sup> and 15 mA/cm<sup>2</sup> in forward scan. The voltages are also slightly lower compared to the references, ranging between 1.05 to 0.95 V, but the values are more acceptable and indicate a decent contact with no substantial interfacial recombination between the layers, further suggesting that the losses in the perovskite bulk are the most prevalent effect.

In the end, in comparison to the reference, the results are quite disappointing. But if we compared all of the SAMs together, the newly synthesized 4'-amidino-[1,1'-biphenyl]-4-carboxylic acid

hydroiodide (SAM 7) showcased the best performances with a low hysteresis (average of 5%) indicating a reduction of the non-radiative recombination compared to the other SAMs. These improvements are noticed as well with the current density and the PCE of the devices with an average of 9.3 % (FW: 10.2%). The same samples were measured again after two weeks yielding the same trends of the device characteristics across the samples. An improvement of the current density is displayed for all of the SAMs probably thanks the structural rearrangement of the perovskite layer.

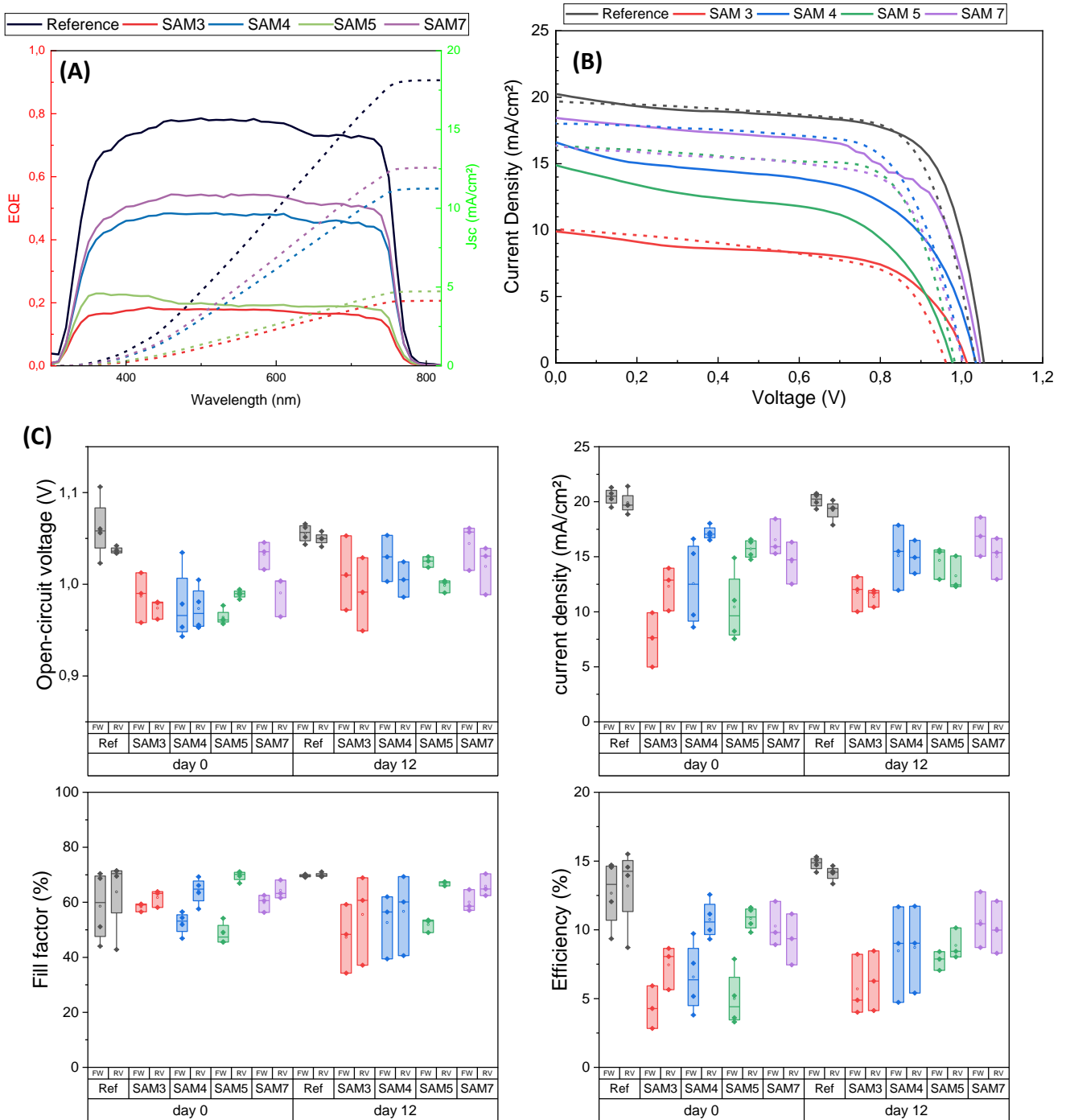


Figure 4.11: Devices with the newly introduced SAM 7 (A) EQE and calculated  $J_{sc}$  and (B) JVs of the best devices in each condition (C) Solar cell parameters of all of the devices at day 0 and after two weeks (day 12)

## 4.5 Discussion

Within this expanded sample series I studied the treatment of the bottom interface in perovskite solar cells by using SAMs based on organic molecules, with the objective to study their suitability in the NIP solar cell architecture. The molecules were synthesized and SAMs were prepared in ITODYS by CBD on a Glass/TiO<sub>2</sub>/m-TiO<sub>2</sub> substrate previously made in IPVF. The grafting of the SAMs was studied via XPS and FTIR, and led to identifying a bidentate grafting mode of all these molecules on the surface.

We followed an empirical approach to screen the molecular layers from there on out by directly integrating them into the full PSC device architecture. Several series of deposition and devices were done with synthesized starting from amino biphenyl carboxylic acids, to amidino phenyl carboxylic acids and to amidino biphenyl carboxylic acids for the last SAMs. We systematically verified the device fabrication process's validity and reproducibility, the pretreatment conditions' impact, and the SAMs' effect and compatibility with the triple cation mixed halide lead perovskite layer. These points were assessed by the measurement of the photovoltaic parameter of specific devices, enabling sequentially studying the impact of the main steps of the cell fabrication. With time, it was possible to evaluate the performances of the SAM-deposited device to reach with the SAM 7 an average of 9.3 % (FW: 10.2%) with the reference at 13.2 % (FW: 12.7 %) in the last series. Compared to the references devices, the performances of the SAM-deposited devices are low, however, a constant improvement of the parameters is noticed with the evolution of the SAM, from a non-flexible molecule that is rather suited for MA<sup>+</sup>-based perovskite layer to a more flexible molecule with an end group that would favor the growth of FA<sup>+</sup>-based perovskites on top. These changes were attributed to the reduction of the non-radiative recombination in the devices, lead to the improvement of the fill factors through the changes, as well with an increase of the current density of the devices which suggests an improvement of the perovskite crystalline quality for the most evolved SAM-modifying samples. However, in the end, we were not able to improve the device's performance past the reference with these SAMs tested here.

One of the reasons for this failure could be attributed to the environmental conditions the samples were subjected to. Even if the sample pretreatment work to regenerate the surface, the performance of the devices showed a large spread in the data. Another indication for the non-ideal performance could be the partial grafting of the SAMs with the presence of remaining band vibrations  $\nu(\text{HOC}=\text{O})$  for some of the SAMs (except for SAM 2 and SAM 5). Such a partial deposition

could lead to the formation of non-equivalent perovskite layer on the mesoporous TiO<sub>2</sub> and create additional defects in the devices. We could consider changing our gold deposition mask to fully utilise our samples. For one sample of 2 x 2 cm<sup>2</sup>, 1 cell of 4 x 4 mm<sup>2</sup> is made. In the future, we anticipate to adapt masks with the possibility of producing four independent cells. It would be able to increase our number of cells and determine the homogeneity of our sample. Another detrimental factor could be the non-annealing of the samples after being brought in IPVF. It is known that humidity is a negative factor for perovskite layer stability. Here, however, we decided not to anneal the samples at 180°C before the perovskite deposition as it could potentially damage the SAMs. The samples are directly placed in the glovebox before the perovskite deposition. This change in the sample handling could lead to incorporate water in the ETL-SAM layer, which accelerates the degradation of the device and the performance drop. Nonetheless, in this case the application of the molecules in the various series showed that the hysteresis could be reduced.

Finally, we would still suggest to perform further in-depth studies using the optimized molecule, 4'-amidino-[1,1'-biphenyl]-4-carboxylic acid hydroiodide (SAM 7). This SAM could form a solid basis to continue this work on the interface modification of the perovskite solar cell. In particular, we suggest to perform detailed studies, beyond the device screening presented here, on the perovskite film formation including an analysis of the crystalline quality and optical properties, i.e. absorption and photoluminescence. At a later stage, molecules can also be developed to apply on the top interface HaP/HTL as was demonstrated in the previous chapter.

## 4.6 References

1. Paniagua, S. A. *et al.* Phosphonic Acids for Interfacial Engineering of Transparent Conductive Oxides. *Chem. Rev.* **116**, 7117–7158 (2016).
2. Fournier, O. *et al.* Chemical Passivation with Phosphonic Acid Derivatives of ZnO Deposited by Atomic Layer Deposition and Its Influence on the Halide Perovskite Interface. *ACS Appl. Energy Mater.* **4**, 5787–5797 (2021).
3. Qu, Q. *et al.* Chemically binding carboxylic acids onto TiO<sub>2</sub> nanoparticles with adjustable coverage by solvothermal strategy. *Langmuir* **26**, 9539–9546 (2010).
4. Terao, J. *et al.* Design principle for increasing charge mobility of  $\pi$ -conjugated polymers using regularly localized molecular orbitals. *Nat. Commun.* **4**, 1–9 (2013).
5. Mangalam, J. *et al.* Modification of NiO x hole transport layers with 4-bromobenzylphosphonic acid and its influence on the performance of lead halide perovskite solar cells. *J. Mater. Sci. Mater. Electron.* **30**, 9602–9611 (2019).
6. Lange, I. *et al.* Tuning the work function of polar zinc oxide surfaces using modified phosphonic acid self-assembled monolayers. *Adv. Funct. Mater.* **24**, 7014–7024 (2014).
7. Torkhani, A. SAM Amine Amino et Amidine Greffées sur c mp TiO<sub>2</sub> IR et XPS. 1–32 (2023).
8. Kouki, H. *et al.* Tailor-Made Amino-Based Self-Assembled Monolayers Grafted on Electron Transport ZnO Layers: Perovskite Solar Cell Performance and Modified Interface Relationship. *ACS Appl. Energy Mater.* **5**, 1635–1645 (2022).
9. Ono, L. K. *et al.* Air-Exposure-Induced Gas-Molecule Incorporation into Spiro- MeOTAD Films. (2014).

## 4.7 Annexes

### 4.7.1 ATR-FITR spectra of the SAM-deposited sample in mesoporous TiO<sub>2</sub> compared to a KBr pellet with SAM molecule incorporated

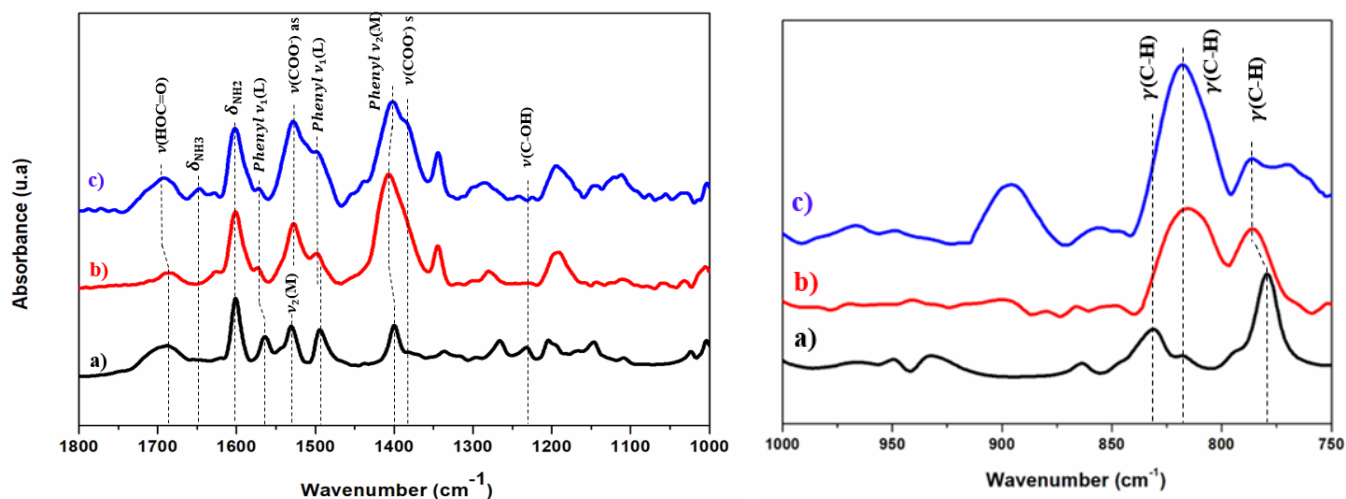


Figure 4.12: FTIR-ATR spectra (left) in the region 1800 – 1000  $\text{cm}^{-1}$  and (right) the region of 1000 – 800  $\text{cm}^{-1}$  of (a) SAM 1 in KBr pellet, (b) SAM 1 and (c) SAM 2 grafted on *m* TiO<sub>2</sub>

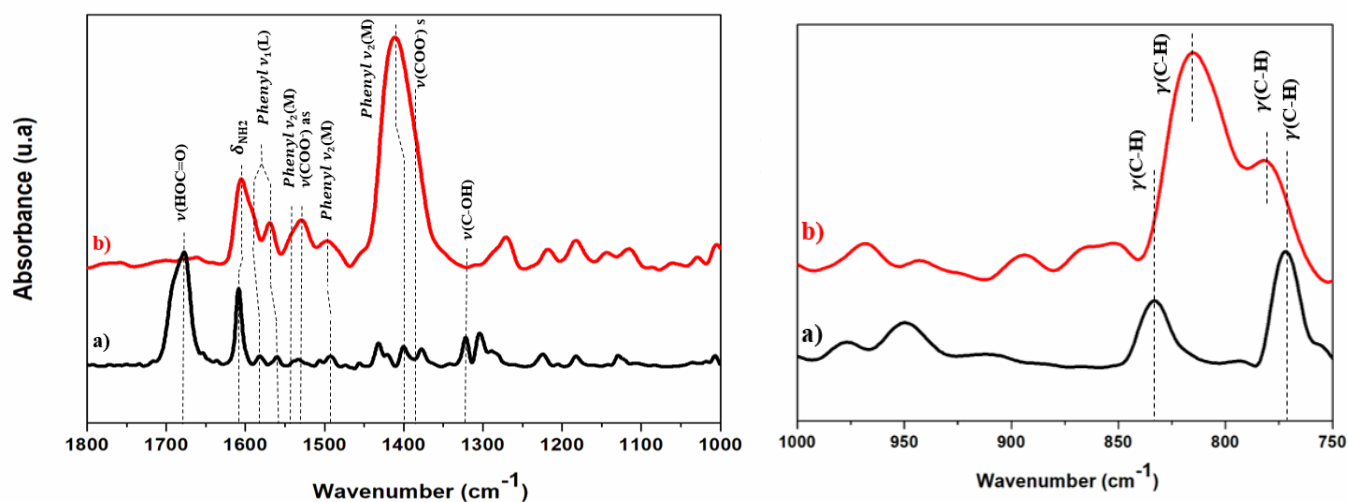


Figure 4.13: FTIR-ATR spectra (left) in the region 1800 – 1000  $\text{cm}^{-1}$  and (right) the region of 1000 – 800  $\text{cm}^{-1}$  of (a) SAM 3 in KBr pellet, (b) SAM 3 grafted on *c-m* TiO<sub>2</sub>

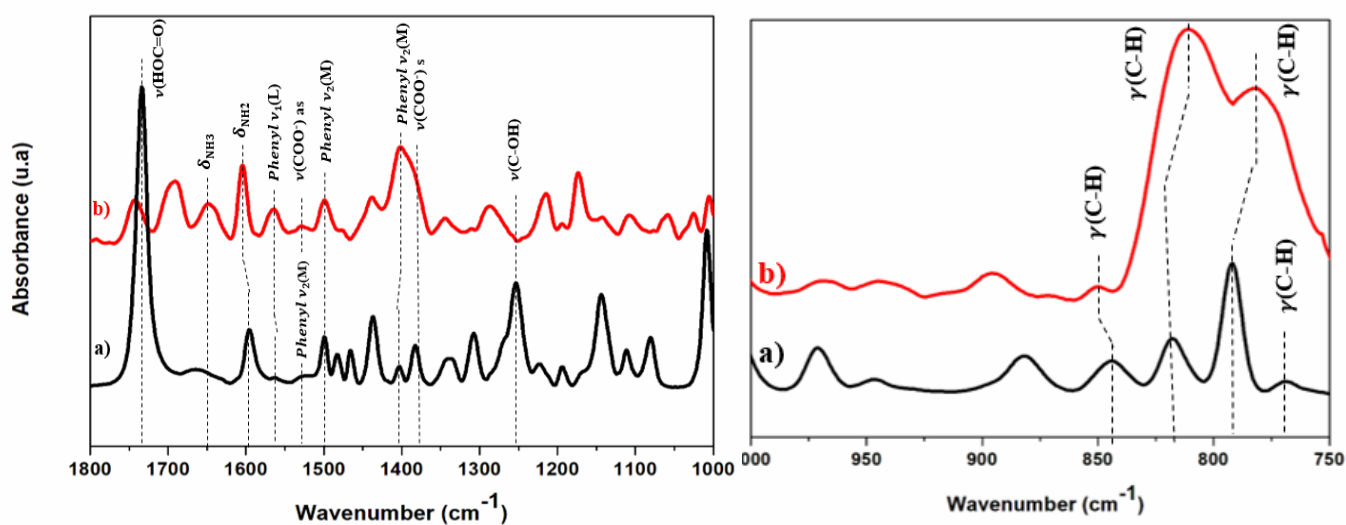


Figure 4.14: FTIR-ATR spectra (left) in the region  $1800 - 1000 \text{ cm}^{-1}$  and (right) the region of  $1000 - 800 \text{ cm}^{-1}$  of (a) SAM 4 in KBr pellet, (b) SAM 4 grafted on *c-m*  $\text{TiO}_2$

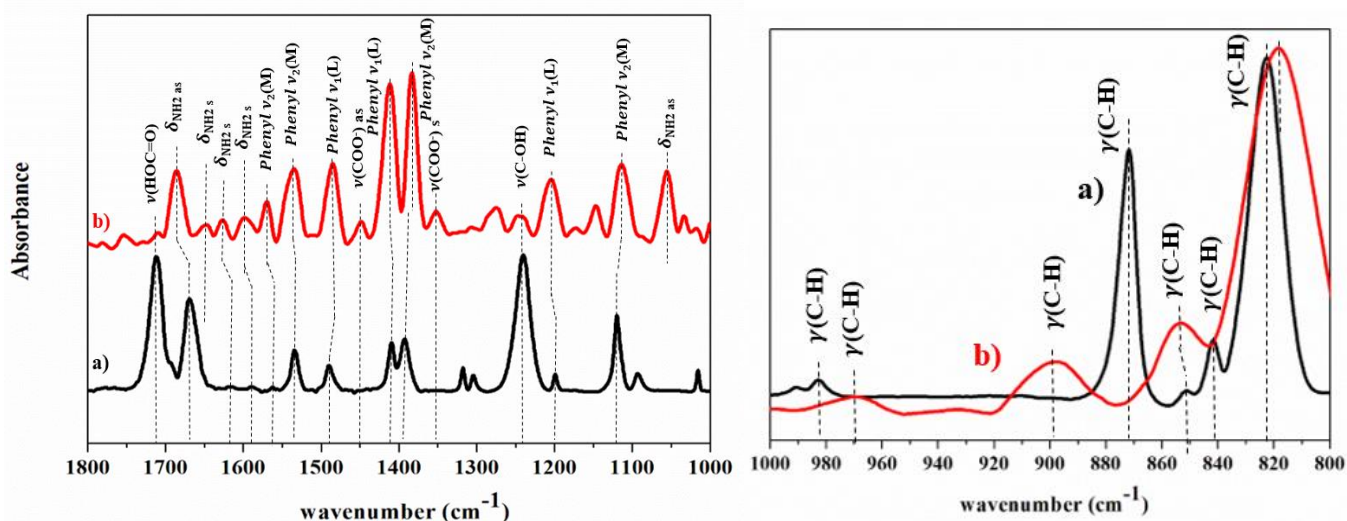


Figure 4.15: FTIR-ATR spectra (left) in the region  $1800 - 1000 \text{ cm}^{-1}$  and (right) the region of  $1000 - 800 \text{ cm}^{-1}$  of (a) SAM 5 in KBr pellet, (b) SAM 4 grafted on *c-m*  $\text{TiO}_2$

## Chapter 5: Another alternative: understanding and application of polymethacrylate PMMA in a device

As the work continued on the interfaces, in Chapter 5, we tested another alternative for the use in perovskite solar cells. Following already good precedent for performance enhancement in several publications, we introduced a thin layer of poly methyl methacrylate (PMMA), first, to compare and understand why our adamantane and its derivatives did not provide as significant an improvement as we expected, and second, to add another possible and optimized interlayer available for the production line at IPVF. This work was pursued with my intern, Peng BAI.

The compound is introduced in two ways in NIP configuration: PMMA on the top interface and in a mixture PMMA:PCBM (phenyl-C61-butyric acid methyl ester) at varied mixing ratios on the bottom interface. Photoelectrical and morphological characterization analyses were made to determine the effect of the interlayers on the device performance and structure. In the end, we single out an optimum concentration of PMMA at 5 mg/mL leading to an improvement of the maximum PCE to up to 19.1 %. A prolonged optimization of PMMA:PCBM deposition is needed to conclude this work with its impact on the device.

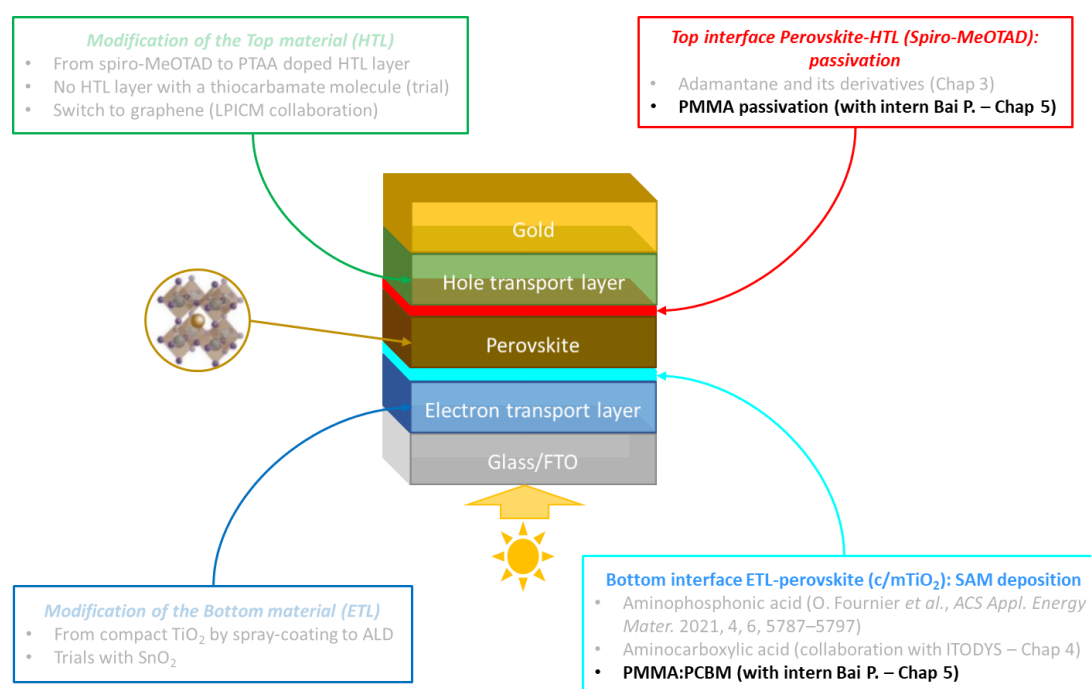


Figure 5.1: Schematic of the working steps through this thesis on NIP configuration perovskite solar cells. Highlight on the bottom and top interface with Chapter 5

## *Table of Contents*

5.1	Introduction.....	157
5.2	Methods .....	158
5.3	Top interface optimization: PMMA.....	158
5.3.1	Low concentration PMMA .....	158
5.3.2	High concentration PMMA – mesoporous TiO <sub>2</sub> ETL .....	162
5.3.3	Low concentration of PMMA – mesoporous TiO <sub>2</sub> .....	167
5.4	Incorporation of the PMMA:PCBM layer .....	172
5.4.1	Material characterization of half-cells .....	172
5.4.2	Electrical performance .....	173
5.5	Conclusion .....	177
5.6	References.....	178

## 5.1 Introduction

As explained throughout this thesis, the interfaces are the key to improve the PSC performance and stability. Different types of interlayers have been used and proposed to this end, with adamantane and its derivatives in Chapter 3 and the aminocarboxylic acids and their derivatives in Chapter 4. The adamantanamine hydrochloride seems to be a new potential family of molecules for surface passivation on the perovskite layer. The amidinocarboxylic acid also presented a good potential for the perovskite solar cell. However, work still needs to be done to optimize these layers. Several of our interface design trials did not demonstrate significant performance improvements in NIP configurations, so we wanted to use and incorporate a stable interlayer in the laboratory. Our choice leaned toward the polymeric organic compound poly(methyl methacrylate) (PMMA) and [6,6]-phenyl-C61-butanoate de méthyle (PCBM). Good precedent for the use of PMMA has been presented in several publications<sup>1-4</sup>, where PMMA is utilized as a barrier on top of the perovskite layer to avoid contact between the two layers and fill voids at grain boundaries. Then, in addition, the PCBM is an organic semiconductor used either in NIP or PIN configuration, as an interlayer or directly as an ETL. Thanks to its passivation, through the grains boundaries and under-coordinated iodine atoms on the surface, the PCBM layer can suppress the hysteresis effect of the perovskite solar cell<sup>5-7</sup>. Here, we intend to achieve a sandwiched passivation of the perovskite layer. In a first step, we exclusively use PMMA to accomplish this effect in part. Then, the final idea is toward a bilayer passivation of the device with a PMMA layer on the top interface and PMMA:PCBM on the bottom interface<sup>4,8</sup> in IPVF to improve the performance and stability of the perovskite solar cell. I employed the various characterization methods at my disposal to determine the cells' efficiency, understand the origin of possible performance enhancement, and establish a comparison of this approach with the previous experiments that brought only moderate improvements.

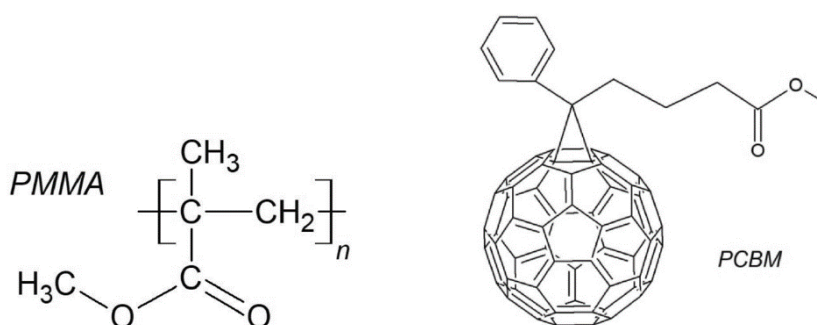


Figure 5.2: Chemical structure of (left) poly methyl methacrylate (PMMA) and (right) [6,6]-phenyl-C61-butanoic acid methyl ester (PCBM)

## 5.2 Methods

The device is fabricated similarly to the baseline configuration, as explained in Chapter 2: I explore several concentration optimization routes to determine the concentration yielding devices with the highest efficiency. For the solution, a quantity of PMMA in chlorobenzene is dissolved within a range from 0 to 20 mg/mL. Chlorobenzene is chosen as it does not dissolve nor affects the crystallinity of the perovskite layer after the annealing as we know from our use of chlorobenzene as an antisolvent<sup>9</sup>. 50 $\mu$ L of a solution is deposited by spin-coating in the glovebox on top of the HTL at 4000 rpm with a ramp of 1000 rpm/s within 24 seconds. For the PMMA:PCBM, two solutions of 5mg/mL each of PMMA and PCBM in chlorobenzene are prepared. Then, the mixed solution is prepared depending on the wanted solution ratio. We worked with ratio PMMA:PCBM of 1:1, 1:3, 1:5. 60 $\mu$ L of the mixed solution is spin-coated on the surface of the ETL at 6000 rpm with a ramp of 2000 rpm/s for 30 seconds.

The layers have been in NIP configuration with two different ETL, mesoporous TiO<sub>2</sub> and SnO<sub>2</sub>, as will be delineated in the individual sections and subsections accordingly.

## 5.3 Top interface optimization: PMMA

The first step of this work is to optimize the PMMA layer. The objective is to deposit a protective layer on the perovskite from the HTL and the ambient conditions. The conditions were trying on two types of perovskite solar cell's stack: Glass/FTO/c-m TiO<sub>2</sub>/HaP/Spiro-MeOTAD/Gold and Glass/FTO/SnO<sub>2</sub>/HaP/Spiro-MeOTAD/Gold. At first, we start with a small concentration of PMMA to obtain a thin layer to follow the guidelines from the perspective of Peng J. et al<sup>4</sup> and to avoid a reduction of J<sub>sc</sub>, i.e., due to a potentially too thick layer. For the very initial test, I varied the concentration from 0 to 1 mg/mL of PMMA.

### 5.3.1 Low concentration PMMA

#### 5.3.1.1 Optoelectrical characterization

After the deposition on top of the perovskite layer, the first analysis comprises whether the process or additional layer changed the properties of the perovskite underneath. In Figure 5.3, three conditions were tested at first: 1 mg/mL of PMMA, 0.5 mg/mL of PMMA and the control sample in comparison. The samples here are prepared in a Glass/FTO/ETL/HaP/PMMA stack for both ETLs, c-

m TiO<sub>2</sub> and SnO<sub>2</sub>. The XRD patterns acquired from these samples reveal no modifications of the perovskite crystal, neither from the samples with TiO<sub>2</sub> as an ETL Figure 5.3(a) and SnO<sub>2</sub> for Figure 5.3(b). Notably, it is within the expectation to not observe any signal from the PMMA layer itself since PMMA is an amorphous polymer.

In the XRD (a), a high peak is observed at 12.5°, which characterizes the PbI<sub>2</sub> contribution, coming from the yellow ( $\delta$ ) phase of the HaP from the FA<sup>+</sup>,<sup>10</sup> which can be taken as an indication for the degradation of the triple cation HaP. In comparison, the sample with PMMA layer presents a smaller peak in this range, suggesting possible protection of the PMMA from the ambient atmosphere. However, the fast degradation seen for the unprotected sample is still quite abnormal for our process and, in this case, could come from the storage in air of the samples after three days between the samples finalization and the XRD measurements. Unfortunately, we could not fully track this phenomenon as we did not observe any issue in our storage conditions later. Nonetheless, this finding aided us in focusing again on the sample fabrication process and analysis of the samples, which includes avoiding prolonged exposure to ambient conditions.

Along these lines, in the XRD pattern of Figure 5.3(b), we do not observe this fast degradation of the control sample on top of SnO<sub>2</sub>, and hence no perovskite modifications are found that could be attributed to the deposition of the PMMA layer. This phenomenon is confirmed by the transmission in Figure 5.3(c); no structural change occurs on the perovskite bulk in the presence of the PMMA. These positive results reassure us in the processing procedure without causing major damage to the perovskite layer in our fabrication process.

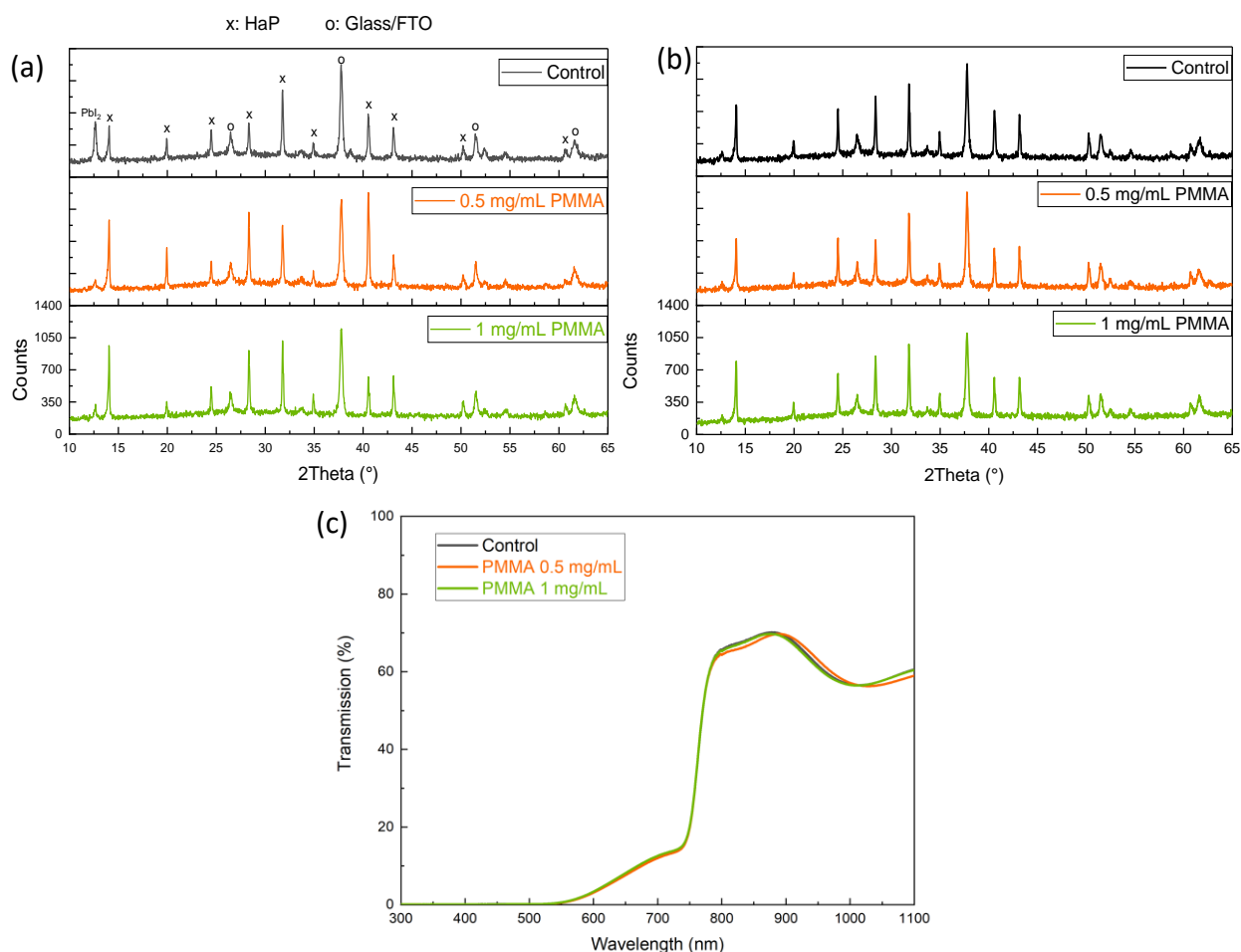


*Figure 5.3: Structural and optical characterization of initial sample runs: (a) XRD of glass/FTO/TiO<sub>2</sub>/Perovskite/PMMA; (b) XRD and (c) Transmission of glass/FTO/SnO<sub>2</sub>/Perovskite/PMMA samples in three conditions: ● Control, ● PMMA 0.5 mg/mL and ● PMMA 1.0 mg/mL*

### 5.3.1.2 Solar cell performances in devices with SnO<sub>2</sub> ETL

With this baseline information about the structure of the perovskite film, we can now determine the influence of the layer on the device performance. In Figure 5.4 we see the results from the first device series incorporating the PMMA layers from the low-concentration solutions on top of the perovskite film, that were employed in the half-cells presented in the previous section, with a total of three devices per conditions for the statistical analysis. The device stack used here of the device is glass/FTO/SnO<sub>2</sub>/HaP/Spiro-MeOTAD/Gold.

Using exclusively SnO<sub>2</sub> in this experimental series, we observed a reduction of the hysteresis compared to devices with TiO<sub>2</sub>, which is likely related to an improvement of the recombination at Institut Polytechnique de Paris

91120 Palaiseau, France

the interface ETL/HaP. The control samples, corresponding to samples without PMMA, exhibit an average PCE of 15.46%. On the otherhand, the samples "0.5 mg/mL of PMMA" reached an average PCE of 17.11% and the samples "1 mg/mL of PMMA are at 17.16%. The  $J_{sc}$  is equivalent for all the conditions confirming that the ultra thin layer does not affect the current density from the device. In Figure 5.4(b) and (c), we notice an increase of the average of  $V_{oc}$  from 1.02 V for the control samples to 1.08 V for the "PMMA 0.5 mg/mL" samples and 1.09 V for the "PMMA 1.0 mg/mL" condition. This is coupled with an increase of the devices' fill factors with the PMMA-deposited cells, in line with previously published data.<sup>4</sup> Thanks to the ultra-thin PMMA layer, the photogenerated holes can pass to the HTL via tunneling effect<sup>3</sup> and reduce the possibility of the short-circuit between the perovskite and the gold by covering the structural pinholes in the perovskite<sup>11</sup>. We attribute this enhancement of the  $V_{oc}$  to a reduction of charge recombination at the interface thanks to the polymeric layer of PMMA.

Notably, the short-circuit current remains the same across the sample set regardless of the implementation of the PMMA layer, but at the same time we observe an improvement in the EQE in Figure 5.4(d), which could potentially be attributed to a higher shunt resistance at the interface HaP/Spiro-MeOTAD. In summary, using the PMMA interlayer improves device stack performance using the  $\text{SnO}_2$  ETL. The improvement is the most pronounced for the highest PMMA concentration (1 mg/mL) and hence the thickness of the resulting layer in this experiment. Thus, We are incentivized to increase the layer thickness to find even better-adapted process conditions. At the same time, we need to ensure that the process can be transferred to the device stack using the c-m  $\text{TiO}_2$  ETL, for which the PMMA layer has already demonstrated a beneficial effect on perovskite film protection.

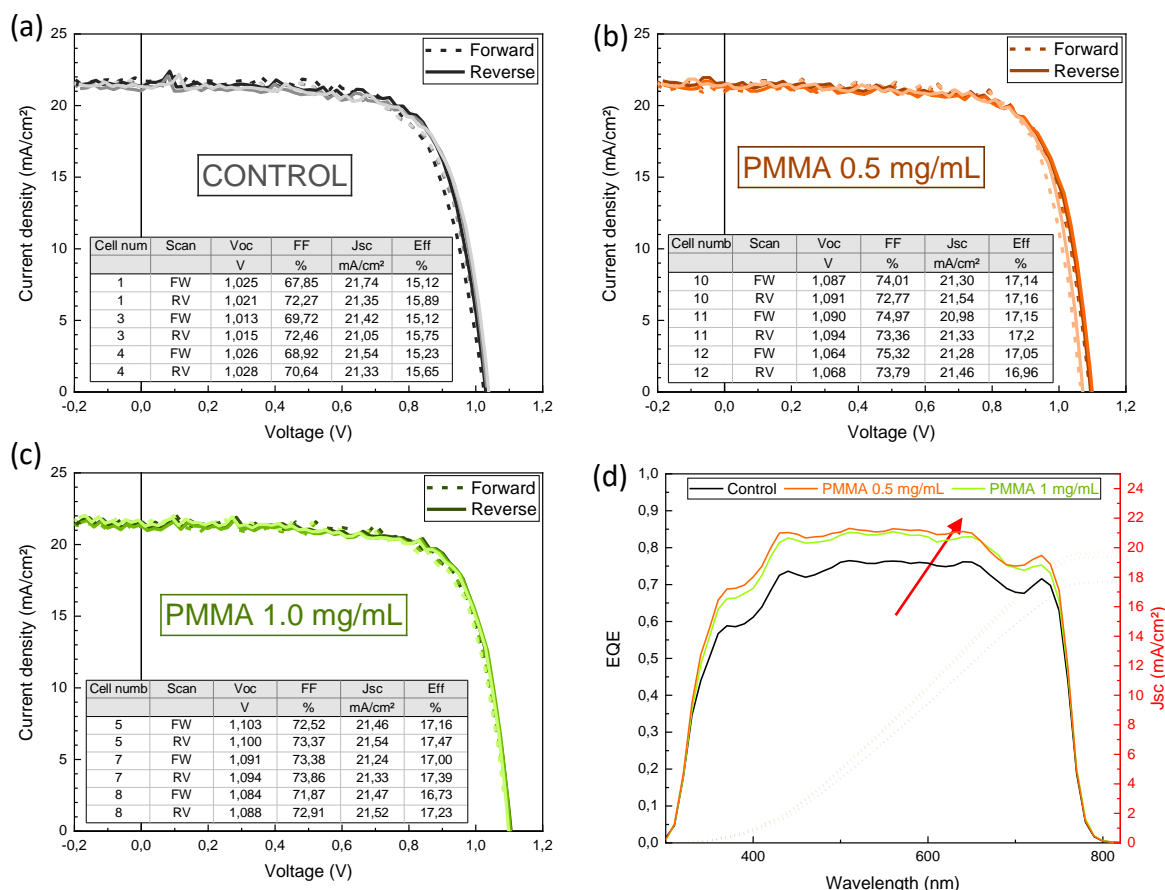


Figure 5.4: Solar cell parameters of glass/FTO/SnO<sub>2</sub>/HaP/PMMA/Spiro-MeOTAD/Gold in three conditions: (a) Control samples, (b) PMMA 0.5 mg/mL and (c) PMMA 1.0 mg/mL. (d) EQE of the best cell in this corresponding batch

## 5.3.2 High concentration PMMA – mesoporous TiO<sub>2</sub> ETL

### 5.3.2.1 Optoelectrical characterization

In the next step, we investigate the effect of an increase of the PMMA solution's concentration with another series of samples in the glass/FTO/c-m TiO<sub>2</sub>/HaP/PMMA stack configuration to test on another ETL. This change was due to a more reliable ETL layer through the different changes in the laboratory. For the concentration, we now expanded the range from 0 to 20 mg/mL. The corresponding characterization of the layers is presented in Figure 5.5 following the publication of Wang et al<sup>12</sup>. The samples are sorted in Figure 5.5(a) depending on the deposited PMMA solution's concentration. The same deposition method is applied with the only difference being the concentration of the PMMA solution and hence the thickness of the PMMA layer. With the increase

of the concentration, we directly observe a visual change of the sample color of the devices from green, corresponding to the color of the classic device for this standard stack, to violet, with the highest concentration of PMMA at 20 mg/mL.

These visual differences indicate a change in the absorption of the light in the device. The optical UV-Vis measurements presented in Figure 5.5 (b) suggest that no significant change occurs to the bulk of the perovskite as observed on the transmittance and absorption in Figure 5.5 (b). However, we find a rise of the absorbed photons with increasing PMMA concentration in the wavelength range from 350 nm to 760 nm. In addition, a higher transmittance with increasing PMMA concentration is observed in the wavelength range from 790 nm to 1100 nm. At the same time, we see a slight change in the interference fringes in this high wavelength regime with a shift of the peak to higher wavelength. The only change between the different samples is the concentration of the PMMA solution. Other methods could have been used to solidify our hypothesis as the profilometer measurement or the infrared measurement to measure the thickness and correlate to the evolution of the concentration.

Figure 5.5 (c) presents the normalized PL peaks of the perovskite samples for the different concentrations of the PMMA solution. The reference peak is centered at 780 nm, and we see a red shift for increasing the concentration of the PMMA solution. This shift cannot be attributed to a change in the perovskite band gap, as the position of the absorption edge has not changed. We instead assign this change to differences in defect passivation and hence recombination dynamics. Furthermore, this shift is in the same direction as for the transmittance which could potentially indicate a link with the concentration of the solution of PMMA and the thickness of the materials. An unidentified pump is presented at around 710 nm for the samples with PMMA, we could not determine the cause of the phenomenon.

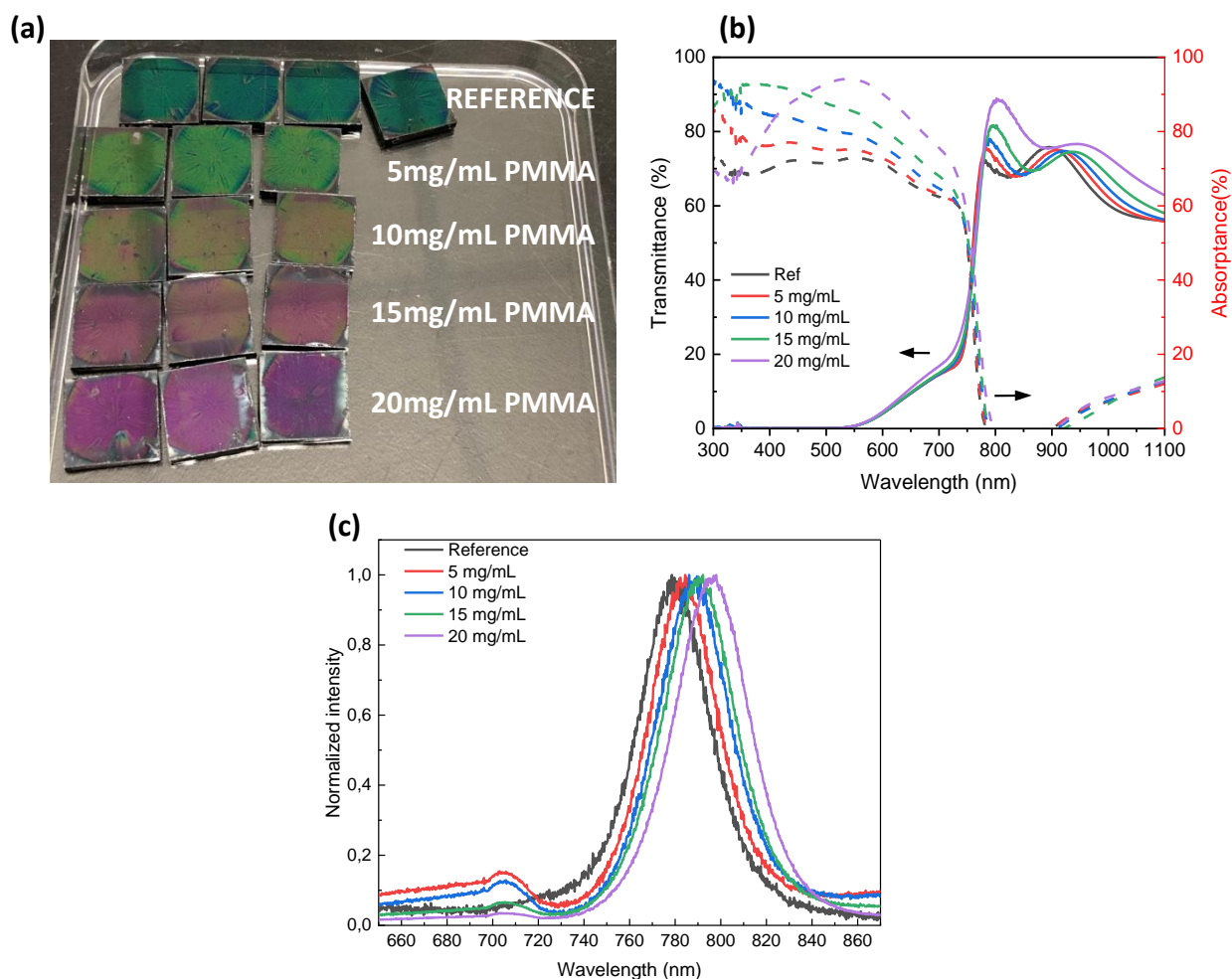


Figure 5.5: Samples of glass/FTO/TiO<sub>2</sub>/HaP/PMMA/Spiro-MeOTAD with varied PMMA solution concentrations (5, 10, 15, 20 mg/mL) compared to the reference sample: (a) Photograph of the devices before the gold deposition; (b) UV-Vis optical transmittance and absorption of the samples glass/FTO/TiO<sub>2</sub>/HaP/PMMA; (c) Photoluminescence of glass/FTO/TiO<sub>2</sub>/HaP/PMMA

### 5.3.2.2 Solar cell performances

Photoelectrical measurements have been acquired for full devices to determine the effect of the PMMA concentration on the device characteristics. The best reference device yielded a PCE of 18.4% from a reverse scan, with a Voc of 1.10 V and a Jsc of 21.9 mA/cm<sup>2</sup> in Figure 5.6.(a). After inserting the PMMA interlayer, the JV curves first got better than the reference group at 5 mg/mL of PMMA. Then, we got a champion cell increase of PCE of 19.1%, a Voc of 1.13 V and a Jsc of 22.3 mA/cm<sup>2</sup>. This increase is also observed in the average results with lower statistical spread and, as a result, a better reproducibility of the devices. However, as we continuously increase the PMMA concentration, the cell performance declines with a clear drop in the current and the fill factor. The curve is approaching a linear shape, indicating that the cells with higher concentrations of Institut Polytechnique de Paris

91120 Palaiseau, France

PMMA behave more like a resistor than a diode. As the concentration of the PMMA rises, the PMMA gets thicker, and it starts to block the carrier transport between the HTL and the perovskite as the holes cannot pass through the PMMA, augmenting the series resistance.

The EQE of Figure 5.6(b) indicated the same tendencies of the JV curves with an augmentation of the EQE at 5 mg/mL of PMMA and then a diminution as the concentration of PMMA is further increased. The amount of incident and absorbed photons is similar for all samples or even increased in case of the higher concentration of PMMA (see Figure 5.4(b)). This means that the number of collected carriers is decreasing with increasing PMMA thickness, which confirms the hypothesis that the thicker PMMA layer impedes hole transfer to the HTL.

More precisely, compared to the reference sample, at 5 mg/mL and 10 mg/mL, we collected a higher number of photons, which is observable on the  $J_{sc}$ . Then, a drop in the overall EQE is noticed at 15 mg/mL and 20 mg/mL. The phenomenon is the same across all wavelengths but is slightly more pronounced in the red than in the blue. This complementary information confirmed that the thickness of PMMA directly affects the number of collected photons. In the same way as the publication of Wang et al<sup>12</sup>, the increase of the PMMA concentration affects the current density, as well as the shunt resistance and the series resistance in the device, which determine the fill factor. An optimum has been found at 5 mg/mL of PMMA for the high concentration of PMMA for the stack glass/FTO/c-m TiO<sub>2</sub>/HaP/Spiro-MeOTAD/Gold.

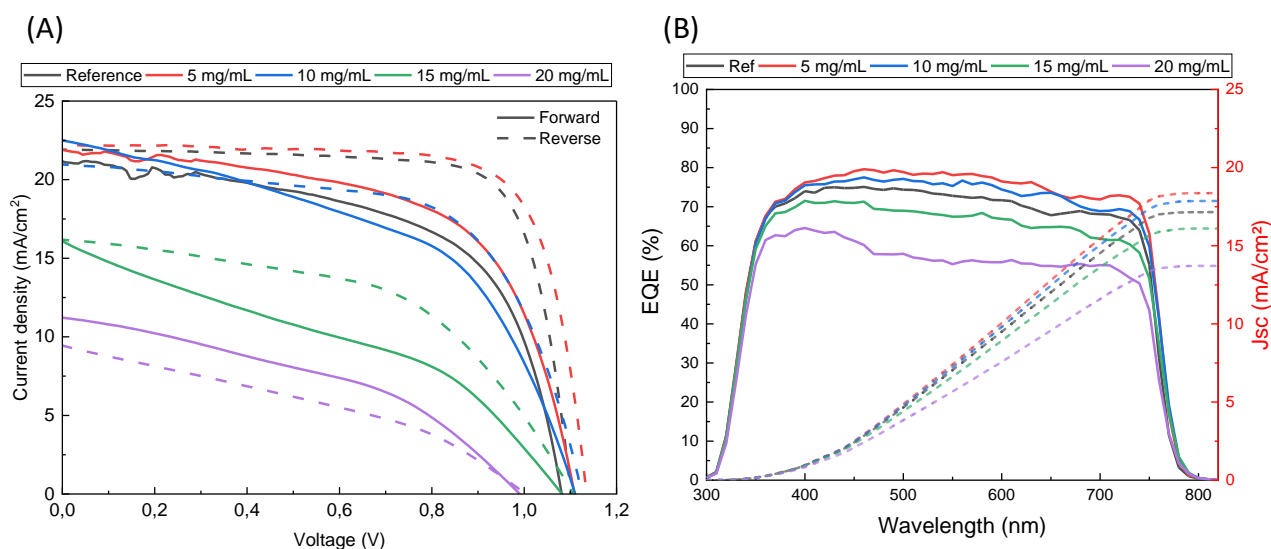


Figure 5.6: Photoelectrical performance of devices glass/FTO/c-m TiO<sub>2</sub>/HaP/PMMA/Spiro-MeOTAD/Gold. (a) JV curve and (b) QE measurements with five conditions: 5 mg/mL, 10 mg/mL, 15 mg/mL and 20 mg/mL of PMMA compared to reference samples

$C_{\text{PMMA}}$ (mg/mL)	$J_{\text{sc}}$ (mA/cm <sup>2</sup> )	$V_{\text{oc}}$ (V)	FF (%)	PCE (%)
Reference	21.9 (22.0)	1.07 (1.10)	64.6 (76.5)	14.5 (18.4)
5	22.2 (22.4)	1.13 (1.14)	74.6 (75.5)	18.8 (19.1)
10	20.8 (21.2)	1.12 (1.13)	63.6 (64.1)	14.9 (15.2)
15	16.4 (17.7)	1.10 (1.10)	49.3 (51.7)	8.91 (9.75)
20	5.05 (9.45)	0.94 (1.00)	36.6 (37.7)	1.79 (3.36)

Table 5.1: Average values of the photovoltaic parameters out of 3 devices for the PMMA deposited samples and 4 devices for the reference samples extracted from J-V curves of perovskite solar cells of the series with different PMMA concentrations, the value in parenthesis is the best value of the group

If we compile our electrical performances and our optical results in high concentrations of PMMA, the PMMA assists in the reduction of shunt resistance by filling the gap from the traps and holes of the perovskite layer and improving the surface of the perovskite, as represented in Figure 5.7. Hypothetically, the carriers pass through the PMMA by tunneling effects as the molecule in a polymer. However, as the concentration of the PMMA increases, the layer acts as a blocking layer, and the carriers cannot pass through, as indicated by the JV curve evolution and the partially blocked blue light in the absorption spectrum.

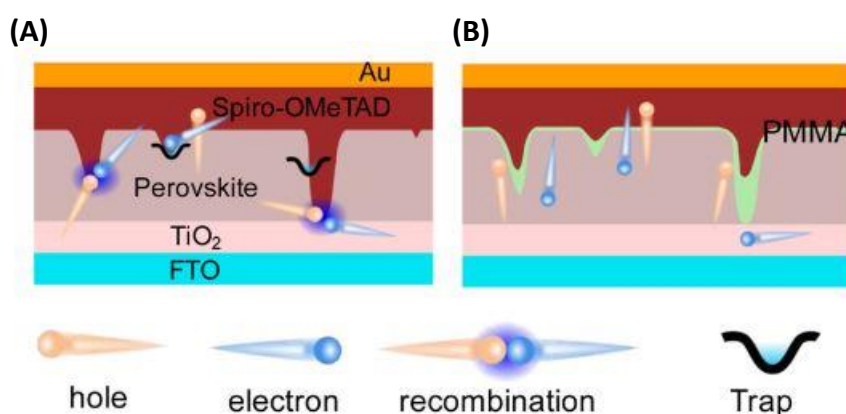


Figure 5.7: Schematics of the carrier dynamics model in perovskite solar cells (a) without and (b) with a PMMA layer. Taken from the publication of Wang et al.<sup>12</sup>

For the TiO<sub>2</sub> ETL, we optimize at 5 mg/mL of PMMA. However, we need to check the device evolution between 0 to 5 mg/mL as what if the best concentration is lower than 5 mg/mL. Consequently,

we divide the conditions with 0, 1.5, 3, and 5 mg/mL of PMMA to uncover the variation rule of cell performance at low PMMA concentrations. As a result, JV curves are made, and performance changes are tracked under the operation of the best devices for 90 hours.

### **5.3.3 Low concentration of PMMA – mesoporous TiO<sub>2</sub>**

#### **5.3.3.1 Solar cell properties**

With the previous results indicating that little to no changes to the perovskite structural and optoelectronic properties are expected for low concentration of the applied PMMA solution, we immediately turn towards the device fabrication and characterization. The JV curve of Figure 5.8(a) presented the data of the champion devices. This time we find a prominent hysteresis effect for all of the devices with TiO<sub>2</sub> as an ETL and Spiro-MeOTAD as HTL. The hysteresis is inherent with this ETL and shows that the fabrication process of the device and the properties of the different layer plays an equally important role<sup>13</sup>. There is not much change in the device performance with similar data acquired with the increase of the PMMA. Table 5.2 confirms these concentrations' low influence on the device performances. At 1.5 mg/mL, the average fill factor decreased, conveying problems with the device fabrication. One possibility could come from the ultra-thin PMMA at 1.5 mg/mL, which could lead to partial covering of the perovskite and, as a result, to holes, traps and a non-uniform layer of spiro-MeOTAD. In Figure 5.8.(b), the EQE indicates that the highest amount of photons is collected for the samples fabricated with PMMA at 5 mg/mL concentration. At lower concentrations, a slight drop of the collected photons is observed for 1.5 mg/mL and 3 mg/mL with a significant decrease in the wavelength range between 700 nm to 780 nm.

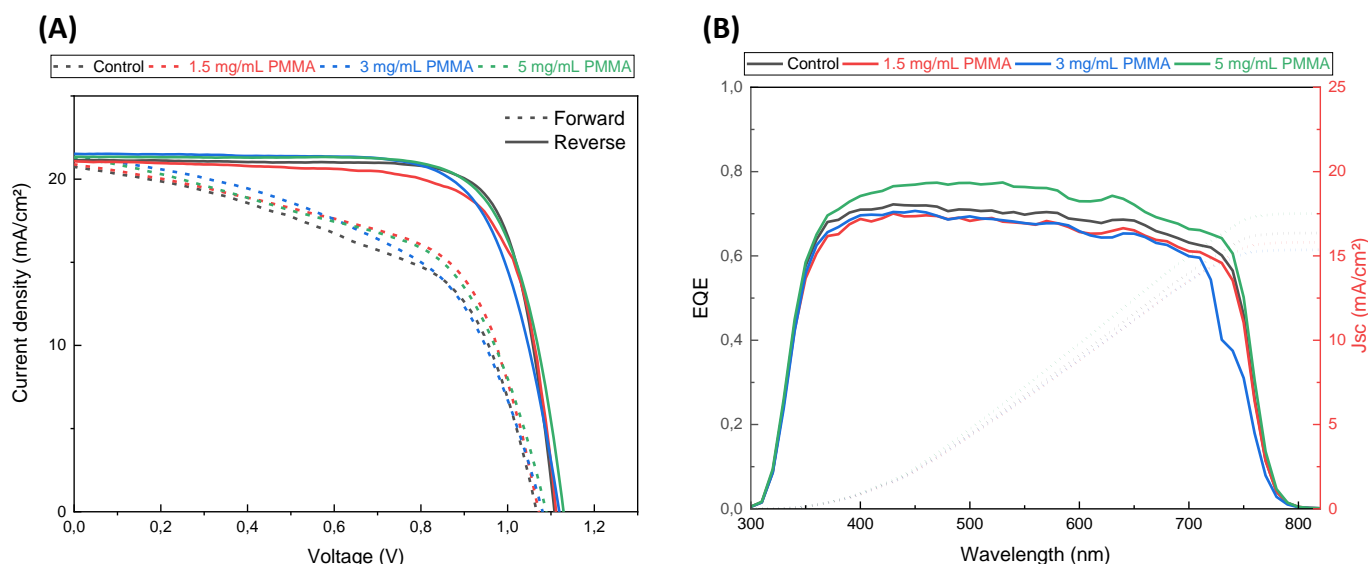


Figure 5.8: Photoelectrical measurements of glass/FTO/c-m TiO<sub>2</sub>/HaP/PMMA/Spiro-MeOTAD devices at low concentrations of PMMA (1.5 mg/mL, 3 mg/mL and 5 mg/mL compared to the reference device): (a) JV curves and (b) QE of the best devices in each condition

C <sub>PMMA</sub> (mg/mL)	Voc (V)	Jsc (mA/cm <sup>2</sup> )	FF (%)	PCE (%)
Reference	1.09	21.5	75.2	17.6
	(1.11)	(21.1)	(77.6)	(18.2)
1.5	1.10	21.2	68.2	15.6
	(1.10)	(21.1)	(73.5)	(17.2)
3	1.12	21.4	73.2	(17.5)
	(1.12)	(21.5)	(72.4)	(17.4)
5	1.13	21.1	73.8	17.7
	(1.13)	(21.3)	(74.7)	(18.0)

Table 5.2: Average values of the photovoltaic parameters in reverse bias out of 3 devices for each condition. The value in parenthesis is the best value of the group

The devices are measured one day after the deposition and, here, again seven days later to verify the evolution of the devices and then a potential effect of PMMA in Figure 5.9. After one day, we could observe that an increase in the Voc is mostly impacted for the PMMA passivation for 3 mg/mL and 5 mg/mL. This confirms an improvement of the surface recombination at the interface HaP/HTL. We also notice a reduction of spread in the characteristics for these concentrations of the PMMA solution, showing that these modifications have a higher potential for making more reproducible devices. The average Voc of the control cells is 1.09 V, this increases to 1.10 V with 1.5 mg/mL, 1.12 V with 3 mg/mL, and 1.13 V with 5 mg/mL. This result is coherent with our previous results and the effect of the PMMA concentration on the devices' performances. However, this time the Jsc

slightly decreases with PMMA concentration, even for these relatively thinner PMMA films. The FF and PCE of the cells decreased compared with the control group. However, they improve with rising PMMA concentrations, and significantly the average PCE increased from 15.6 % at 1.5 mg/mL to 17.7 % at 5 mg/mL thanks to a better device reproducibility. After seven days, all parameters vary as the trend as the first time but with a lower value. This overall decrease across the devices parameters likely stems from the degradation during the measurements. But due to the limited number of samples, confirmation of this hypothesis would require larger statistics and supplementary measurements.

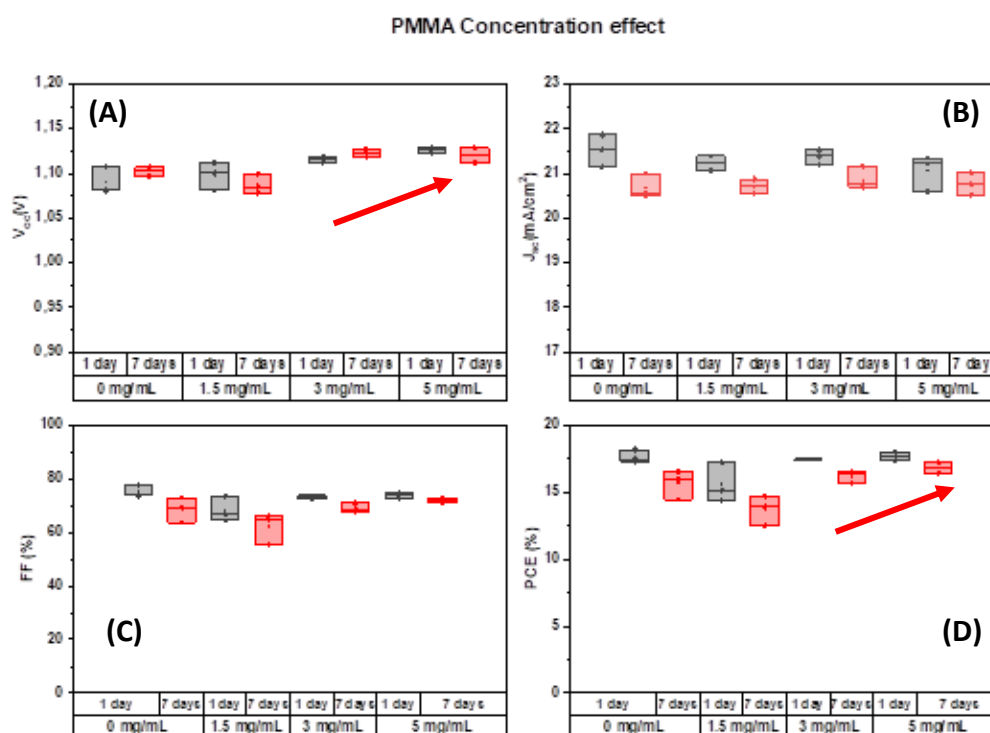
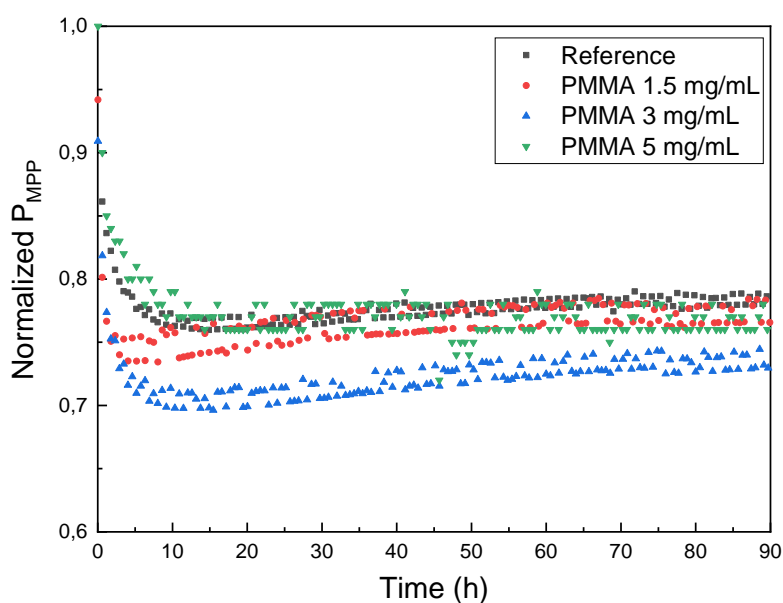


Figure 5.9: Distribution of the solar cell parameters for control and different PMMA passivated cell concentrations. (a) Voc. (b) Jsc. (c) FF. (d) PCE

As we increase the concentration, reproducibility improves with a minimum spread in the recorded device parameters for an optimum concentration of 5 mg/mL of PMMA. At 1.5 mg/mL, the PMMA is hypothetically not well coated on the perovskite, leading to the remaining presence of traps and pinholes and a non-uniform layer of HTL on the perovskite and eventually a large spread in the device parameters. In this case, the traps and pinholes play a major role for losses in the Voc and Jsc.

We also wanted to determine the long-term stability of the device as we know the exposure to the light accelerated the degradation of the perovskite. Therefore, a dedicated aging test is carried out, to track and plot the power at the maximum power point for 90 hours as presented in Figure 5.10.



*Figure 5.10: Aging test results of champion cells at each condition: Normalized power in maximum power point ( $P_{MPP}$ ) tracking*

In summary, the degradation process follows very similar trends for all cells, irrespective of the used PMMA interlayer. However, after 90h of continuous operation, the cell with a concentration of 5 mg/mL of PMMA retains 78 % of initial power, the same as the 1.5 mg/mL and reference devices, whereas the sample with the 3 mg/mL concentration trails. In addition, the 5 mg/mL PMMA solution gives the best long-term stability performance in Voc, PCE, and  $P_{MPP}$  compared with the control group.

### 5.3.3.2 Photoluminescence characterization

After studying the electrical properties of the devices, we conducted photoluminescence measurements of the samples in half-device configuration (glass/FTO/c-m TiO<sub>2</sub>/HaP/PMMA) to evaluate further the potential changes to the carrier dynamics and recombination inferred to by the full device results. The corresponding results are summarized in the following Figure 5.11. The PL spectra, shown in Figure 5.10(a), of the control sample are the same as for the sample with a concentration of 1.5 mg/mL of PMMA, confirming the hypothesis that partial and in-complete coverage of the PMMA, does not eliminate the most prominent recombination and shunt pathways.

Then, at higher PMMA concentrations we again find that the PL peak slightly shifts to the red, which corresponds with the previous result for high concentration in section 5.3.2.1.

The Time-Resolved Photoluminescence (TRPL) is made on the same half cells to assess if the PMMA layer could affect the charge carrier extraction. At 1.5 mg/mL of PMMA, the sample shows an average carrier lifetime of around 97.2 ns, similar to the reference group (96.7 ns), while at 3 mg/mL of PMMA 37.3 ns and 5 mg/mL of PMMA 64.1 ns. The PMMA at 1.5 mg/mL presents the longest carrier lifetime among all groups. However, the carrier lifetime is extended as we increase the concentration from 3 to 5 mg/mL. The carrier lifetime corresponds to when a carrier can reside and move in the film without interaction before recombination. Faster PL decays can hence be related to improved carrier extraction or additional unwanted interfacial recombination. Therefore, this result remains inconclusive, as one would expect an increase in lifetime if surface defects are passivated and thus recombination reduced, which we intend to achieve with the PMMA interlayer. Another hypothesis is the accumulation of the carriers in the layer as they can pass through, leading to the formation of a blocking layer. Further dedicated experimental series of PL experiments and quantitative modeling would be required better to assess this behavior and dynamics of the photogenerated carriers.

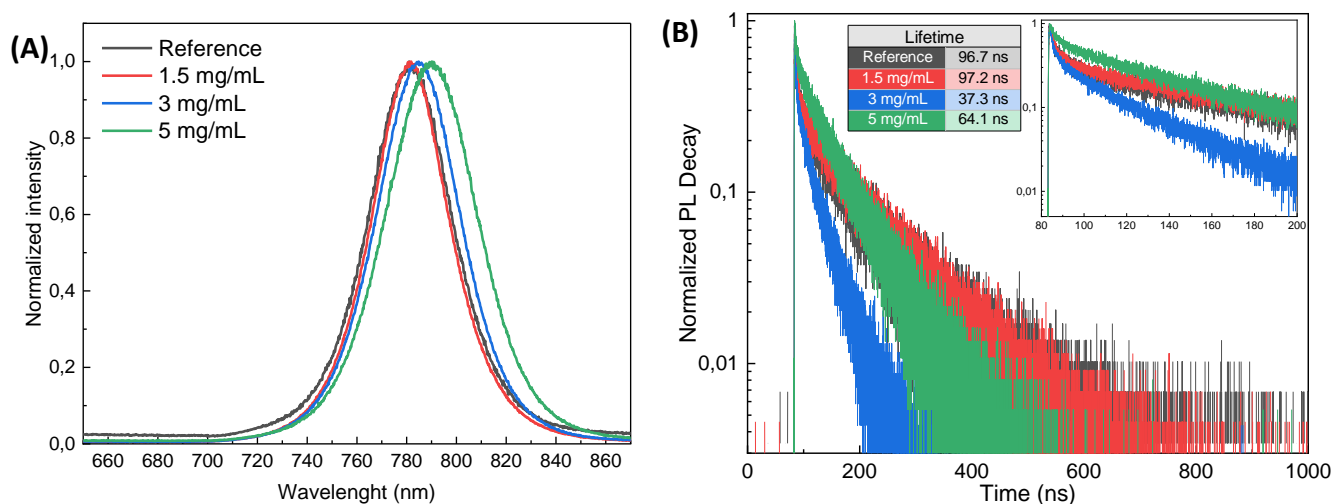


*Figure 5.11: Sample of glass/FTO/c-m TiO<sub>2</sub>/HaP/PMMA: (a) Normalized PL measurements for various conditions of PMMA; (b) TRPL measurements on perovskite layer with and without PMMA interlayer passivation. The laser intensity is  $8 \times 10^{17}$  photon/(cm<sup>2</sup>·s). The inset table displays the average carrier lifetime of each measured sample from different groups calculated from the ExponentialDecay function fitting. The inset figure zooms on the curves between 80 ns to 200 ns to show the decay rate after the injection.*

In conclusion of this experimental series, which was performed in the framework of the internship of Peng Bai, who I supervised, we determined an optimized concentration at 5 mg/mL for the ETL of mesoporous TiO<sub>2</sub>. This value presents the best solar performances compared to the other concentrations. If the concentration is too low, it affects the Voc and the reproducibility of the device. However, if the concentration is too high, we produce a blocking layer indicated by a drop in the current and the collected photons in the device. After optimizing the top interface, we focus on the bottom interface ETL/PMMA.

## 5.4 Incorporation of the PMMA:PCBM layer

With this optimized PMMA top layer configuration, we now turn to the final objective: to produce a bilayer passivation of the perovskite solar cell using PMMA and PMMA:PCBM. Hence, we tried different concentration ratios of PMMA and PCBM mixture layer: 1:1, 1:3, and 1:5, at the bottom interface to examine the effect of these materials and what is the best-performing deposition condition in our structure. The concentration of PMMA:PCBM followed the ratio 1:X as for 1 mg/mL of PMMA we have X mg/mL of PCBM<sup>4,8</sup>. This ultra-thin layer deposited on the mesoporous layer has the same role as on top interface: to fill the hole of the mesoporous layer. Furthermore, PCBM is added and assured in the layer to improve electron charge transport from the HaP to the ETL.

### 5.4.1 Material characterization of half-cells

The sample's PL measurements of the half-device sample stack (glass/FTO/c-m TiO<sub>2</sub>/PMMA:PCBM/HaP) are presented in Figure 5.12.(a). As in the top interface deposition, we notice a red shift for the deposited samples. However, there was no shift increase depending on the concentration of PCBM. This shift could hence be primarily attributed to the formation and presence of the PMMA layer. Figure 5.12.(b) exhibits the X-ray diffraction results of different ratio groups to check the crystalline structure. Similarly to the top interface deposition, there is also no noticeable change in the HaP structure. The bottom interface PMMA:PCBM seems to exert no influence on the crystal structure of the HaP layer.

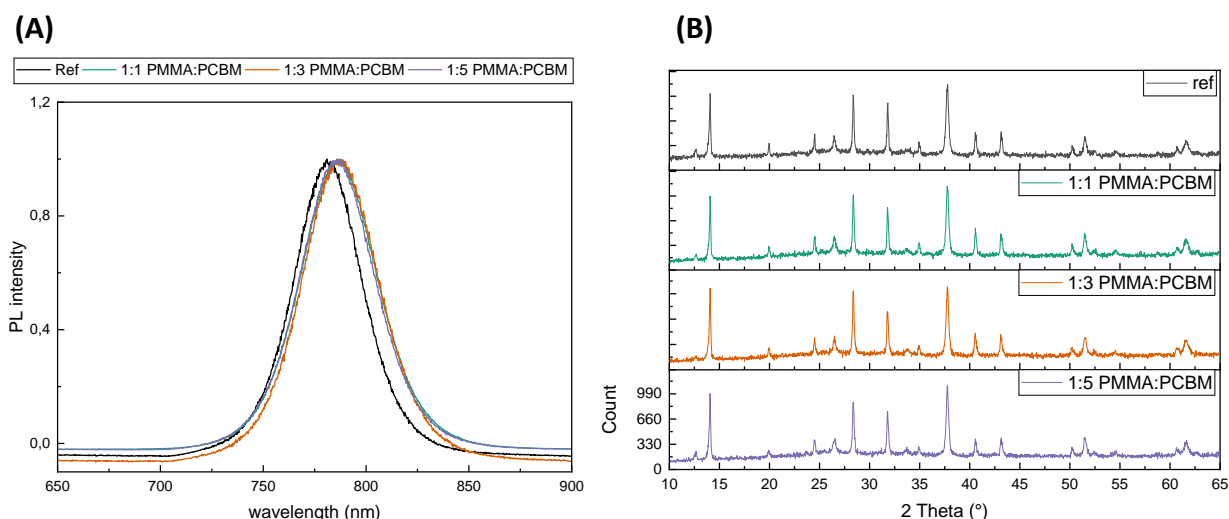


Figure 5.12: Sample of glass/FTO/c-m TiO<sub>2</sub>/PMMA:PCBM/HP with several ratios of PMMA:PCBM (1:1, 1:3 and 1:5): (a) Normalized photoluminescence measurements (b) the X-ray diffraction

## 5.4.2 Electrical performance

With the absence of any significant changes to the perovskite bulk and a minimal influence on the PL signal, we now evaluate the effect of the bilayer system on the characteristics of completed devices. Figure 5.12.(a) shows the JV curves of the best devices in each condition. Of note, all the JV curves exhibit a strong hysteresis. The reverse bias performs better than forward bias under the same illumination. We noticed a decrease of Jsc from the reference sample (around 21.5 mA/cm<sup>2</sup>) to all PMMA:PCBM mixture (1:1, 1:3 and 1:5 ratios got around 17, 8.7 and 11.5 mA/cm<sup>2</sup> of Jsc, respectively). In Figure 5.13.(b), EQE measurements of the control and PMMA:PCBM-passivated sample also show significant variation in the EQE response. As the ratio of PCBM increases, the EQE of the sample decreases. For the 1:5 group, the EQE curve reaches the lowest values, with the peak efficiency around 35 % at 350 nm. This decrease in the device performance and beginning build-up of an S-shape characteristic of the JV curve shape with an increasing PMMA:PCBM concentration ratio suggests that the layer exhibits inferior electron transfer properties and could even constitute a barrier for electron extraction.

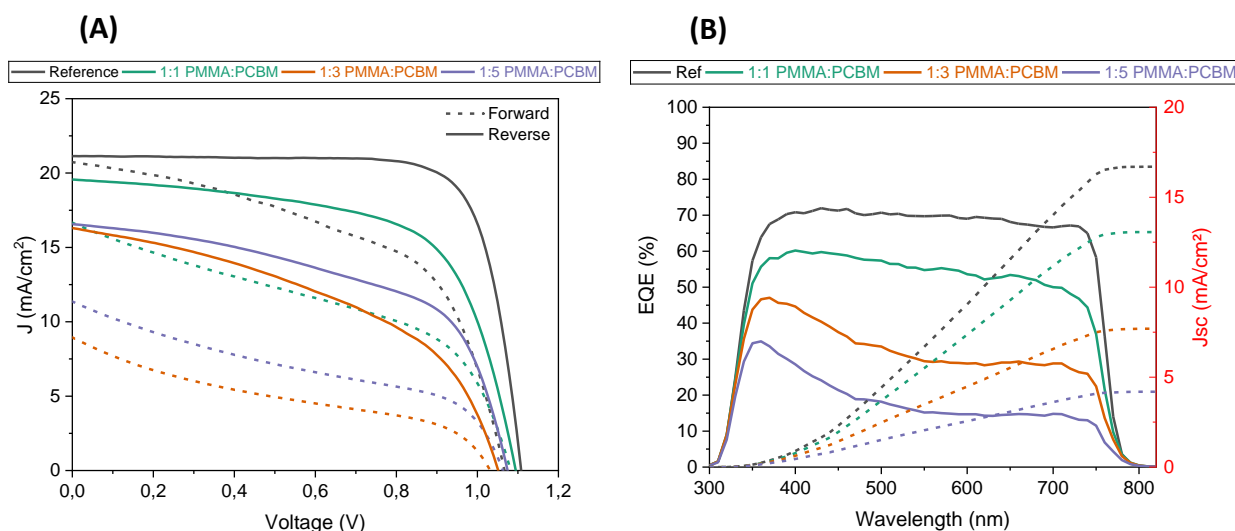


Figure 5.13: Sample of glass/FTO/c-m TiO<sub>2</sub>/PMMA:PCBM/HA/P/Spiro-MeOTAD with several ratios of PMMA:PCBM (1:1, 1:3 and 1:5): (a) JV curves (b) EQE spectra

Ratio PMMA:PCBM	Jsc (mA/cm <sup>2</sup> )		Voc (V)		Fill factor (%)		PCE (%)	
	Forward	Reverse	Forward	Reverse	Forward	Reverse	Forward	Reverse
Reference	21.10 (20.73)	21.51 (21.14)	1.04 (1.07)	1.09 (1.11)	48.71 (53.84)	75.20 (77.58)	10.66 (11.90)	17.63 (18.17)
1:1 PMMA:PCBM	17.21 16.86)	19.44 (19.52)	0.91 (1.08)	0.85 (1.10)	44.32 (47.56)	48.06 (66.12)	7.03 (8.66)	8.74 (14.15)
1:3 PMMA:PCBM	11.26 (8.96)	16.86 (16.31)	0.96 (1.03)	0.83 (1.05)	29.76 (32.17)	40.34 (45.25)	3.18 (2.97)	5.62 (7.75)
1:5 PMMA:PCBM	10.87 (11.37)	15.45 (16.57)	1.05 (1.06)	1.07 (1.07)	36.63 (37.98)	53.66 (55.29)	4.17 (4.59)	8.87 (9.84)

Table 5.3: Average values of the photovoltaic parameters out of 3 devices for the samples extracted from J-V curves of perovskite solar cells of the series with different PMMA:PCBM ratios, the value in parenthesis is the best value of the group

With this layer, an essential loss of collected photons is observed. Instead of improving the device, it seems that we are creating a blocking layer. The results contradict the findings in the publication of Peng J. et al<sup>8</sup>. This issue is potentially linked to the device fabrication. We did not adopt the same ramp speed as their device with our process at 6000 rpm, 2000 rpm/s for 30s without further annealing while in their method, they use 5000 rpm, 5000 rpm/s for 30s with annealing at 100°C.

The annealing seems to play a big part in the layer fabrication, probably evaporating remaining solvents and adjusting the morphology of the layer.

The hypothesis of the blocking layer is also confirmed with the aging test and the TRPL measurements. An aging test has been done for 90 hours in Figure 5.14.(a). The normalized Voc curve showcased a stable Voc for the reference sample. As the concentration of PCBM in the ratio increase, the Voc decreases to 80% of the initial value for 1:1 PMMA:PCBM ratio, and to 30 % of the initial value for 1:3 PMMA:PCBM ratio. Then, at 1:5 PMMA:PCBM, the Voc reaches 85 % of its initial value. As shown in Figure 5.14.(a), the reference cell performs 75 % of the initial value after 90 hours of exposure for the normalized efficiency. While for the PMMA:PCBM deposited devices keep 40% of their initial value for 1:1 and 1:5 PMMA:PCBM after 90 hours and 10% of its initial value for 1:3 PMMA/PCBM. Thus, all cells employing the PMMA:PCBM layer yield a worse stability than the reference device. In comparison, we measured the TRPL on half-cell glass/FTO/c-m TiO<sub>2</sub>/PMMA:PCBM/HaP in Figure 5.14.(b) and calculated the carrier lifetime. The reference cell has a carrier lifetime around 96.7 ns, and three PMMA:PCBM passivated samples exhibit a lifetime of more than 200 ns. Theoretically, the longer the lifetime, the longer a carrier can spend in an excited state after electron-hole generation in the absorber before recombining. This gives carriers a higher probability of being transported to the adjacent transport layers, thus usually increasing the cell's Jsc and efficiency of the cell<sup>14</sup>. This contrasts our results from the JV measurements and further confirms our hypothesis that the PMMA:PCBM layer creates a barrier at the ETL/HaP interface, which blocks the electrons. As a result, the carriers accumulate in the absorber before recombination since they cannot migrate and enhance their lifetime.

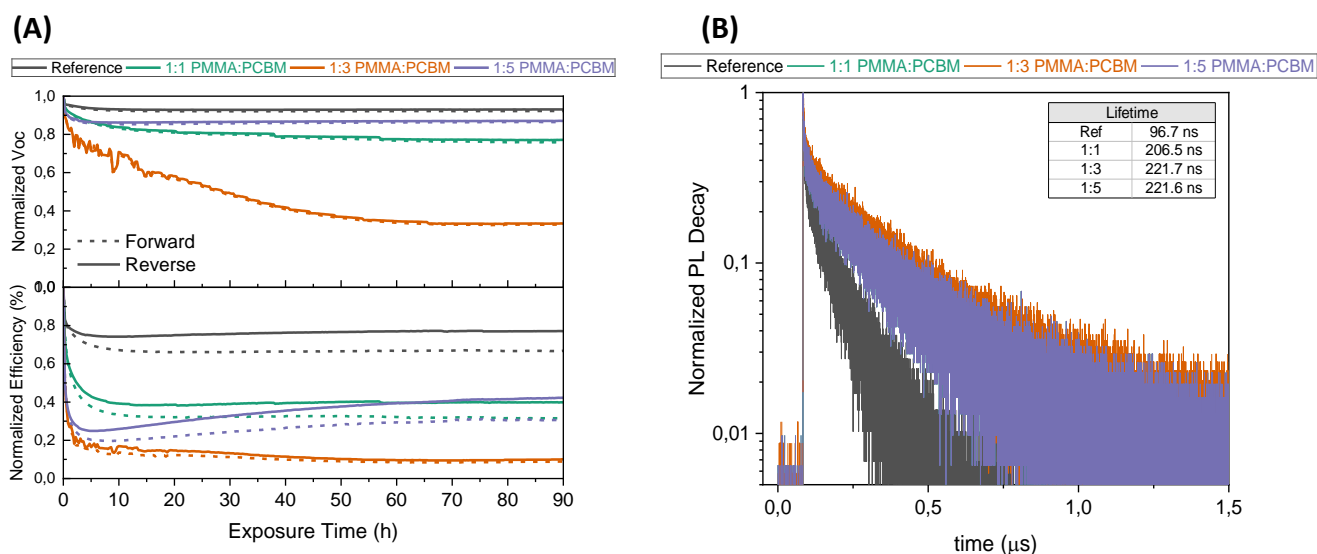


Figure 5.14: (a) Aging test results of champion cells for each condition: (top) Tracking of the normalized Voc; (bottom) Tracking of the normalized efficiency. (b) TRPL measurements on perovskite layer with and without PMMA:PCBM interlayer passivation. The inset table displays the average carrier lifetime of each measured sample for the samples with different PMMA:PCBM ratios from a fit by a single exponential decay function

## 5.5 Conclusion

The objective of this project was the elaboration of a double passivation layer for the interface to an HaP absorber film to improve their stability against the influence of ambient atmosphere and reduce surface charge defects, for which we used an approach incorporating PMMA and PMMA:PCBM for the NIP PSC device configuration to implement this possible deposition process at IPVF. The PMMA layer is deposited at the top interface HaP/HTL, while The PMMA:PCBM layer is deposited at the bottom interface ETL/HaP. For the top interface, we successfully optimize the PMMA layer with a 5 mg/mL solution concentration. It enables average open circuit voltage up to 1.13 V (best cell: 1.14 V). We report an average PCE of 18.8% (best cell: 19.1%) for the 5 mg/mL PMMA passivation in the glass/FTO/c-m TiO<sub>2</sub>/HaP/PMMA/Spiro-MeOTAD device stack. A lower concentration of 1 mg/mL of the PMMA solution was selected for the samples with SnO<sub>2</sub> as ETL. However, further work would still be required with testing higher concentrations to validate this choice.

Using the right concentration, the PMMA layer improves the perovskite layer's morphology by filling in the perovskite pinholes and traps, reducing surface defects. PMMA:PCBM is initially intended to suppress the perovskite solar cell's hysteresis and enhance the electrons extraction from the HaP layer to the mesoporous layer. We tried using different concentration ratios to optimize the layer (PMMA:PCBM: 1:1, 1:3 and 1:5 with 1mg/mL of PMMA). However, a significant decrease of the photon collection and current generation was observed for all of the samples with this additional interlayer with respect to the reference device, meaning that we created a blocking layer at the interface

In the end, we did not finish implementing the double-side passivation of the perovskite film due to the low performance of the bottom interface modification with the PMMA:PCBM layer. At that project stage, the most pressing question remained: how can we improve the PMMA:PCBM deposition to enhance the perovskite surface and, eventually the device? Could the double passivation even introduce new defects into the device? These are some questions that we can discuss about in the perspectives of my thesis and to determine the possible evolution of my projects for IPVF and future works.

## 5.6 References

1. Zhang, S. *et al.* Barrier Designs in Perovskite Solar Cells for Long-Term Stability. *Adv. Energy Mater.* **10**, 1–49 (2020).
2. Turren-Cruz, S. H., Hagfeldt, A. & Saliba, M. Methylammonium-free, high-performance, and stable perovskite solar cells on a planar architecture. *Science (80-. )*. **362**, 449–453 (2018).
3. Aydin, E., De Bastiani, M. & De Wolf, S. Defect and Contact Passivation for Perovskite Solar Cells. *Adv. Mater.* **31**, 1–20 (2019).
4. Peng, J. *et al.* A Universal Double-Side Passivation for High Open-Circuit Voltage in Perovskite Solar Cells: Role of Carbonyl Groups in Poly(methyl methacrylate). *Adv. Energy Mater.* **8**, 1–9 (2018).
5. Kegelmann, L. *et al.* It Takes Two to Tango - Double-Layer Selective Contacts in Perovskite Solar Cells for Improved Device Performance and Reduced Hysteresis. *ACS Appl. Mater. Interfaces* **9**, 17245–17255 (2017).
6. Niu, T., Xue, Q. & Yip, H. L. Molecularly Engineered Interfaces in Metal Halide Perovskite Solar Cells. *J. Phys. Chem. Lett.* **12**, 4882–4901 (2021).
7. Nouri, E., Mohammadi, M. R. & Lianos, P. Improving the stability of inverted perovskite solar cells under ambient conditions with graphene-based inorganic charge transporting layers. *Carbon N. Y.* **126**, 208–214 (2018).
8. Peng, J. *et al.* Interface passivation using ultrathin polymer-fullerene films for high-efficiency perovskite solar cells with negligible hysteresis. *Energy Environ. Sci.* **10**, 1792–1800 (2017).
9. Taylor, A. D. *et al.* A general approach to high-efficiency perovskite solar cells by any antisolvent. *Nat. Commun.* **12**, 1–11 (2021).
10. Frost, J. M. & Walsh, A. Molecular Motion and Dynamic Crystal Structures of Hybrid Halide Perovskites. in *Organic-Inorganic Halide Perovskite Photovoltaics* 1–17 (Springer International Publishing, 2016). doi:10.1007/978-3-319-35114-8\_1.
11. Peng, J. *et al.* Nanoscale localized contacts for high fill factors in polymer-passivated perovskite solar cells. *Science (80-. )*. **371**, 390–395 (2021).
12. Wang, F. *et al.* Highly efficient and stable perovskite solar cells by interfacial engineering using solution-processed polymer layer. *J. Phys. Chem. C* **121**, 1562–1568 (2017).
13. Jena, A. K. & Miyasaka, T. Hysteresis Characteristics and Device Stability. in *Organic-Inorganic Halide Perovskite Photovoltaics* 255–284 (Springer International Publishing, 2016).

doi:10.1007/978-3-319-35114-8\_10.

14. Jiang, J. *et al.* Carrier lifetime enhancement in halide perovskite via remote epitaxy. *Nat. Commun.* **10**, 1–12 (2019).

## Chapter 6: Summary and Perspectives

---

### 6.1 Summary of thesis objectives, key results and suggestions for follow-up studies

To conclude this thesis, we close the loop on the summary objective of my PhD project, which is designing and analyzing interfaces in lead halide perovskite (HaP) solar cells (PSCs). Tailoring the interfaces in a PSC is the key to developing a stable device with higher power conversion efficiency (PCE). This approach can be executed at the various junctions in the device, explored in a large body of work in literature, from direct material engineering, e.g. through compositional control and additives to dedicated interface passivation strategies through the targeted deposition of interlayers. In summary, in this manuscript I described the work on three projects with focus on (i) interface modification between the perovskite film and HTL on top, (ii) modification of the buried interfaces between the ETL on bottom and the perovskites, and (iii) double layer passivation strategy.

In Chapter 3, I presented my work on the HaP/HTL interface using adamantane (AD) and its derivatives, 1-adamantanamine (1ADA) and 1-adamantanamine hydrochloride (1ADAHCl), deposited as an interlayer on top of the perovskite film before the deposition of the HTL in NIP device configuration. The molecules were selected because of their hydrophobicity, which makes them good candidates for protection of the sensitive HaP layer underneath against the humidity and hence long-term improvement of the device stability. First off, producing solar cells based on a triple cation mixed halide perovskite absorber ( $\text{Cs}_{0.05}(\text{MA}_{0.17}, \text{FA}_{0.83})_{0.95}\text{Pb}(\text{Br}_{0.17}, \text{I}_{0.83})_3$ ) with the interlayers, we were able to only achieve a minor improvement of the device performance in the stack glass/FTO/c-m  $\text{TiO}_2$ /HaP/AD-interlayer/Spiro-MeOTAD compared to the reference stack without AD-based interlayer. Champion devices in these series reached up to 17.5% power conversion efficiency over a power conversion efficiency of 16.5% for the reference devices. In particular, we do not find any significant increase of  $V_{\text{OC}}$ , which would have indicated better passivating properties, i.e., mitigation of interface defects, compared to the direct HaP/HTL interface. In the next step, using periodic XPS measurements, the samples were tracked after storage under an ambient atmosphere over the course of several months to compare the evolution of the perovskite layer in the molecule's presence. 1ADAHCl gives us the most promising results as

Institut Polytechnique de Paris

91120 Palaiseau, France



good preservation of the perovskite layer over a moderate time span of roughly two weeks out of the other surface modifiers. However, after more than 45 days of storage, the molecules were no longer detectable; thus, the interlayer can still not be used for long-term stability. Nonetheless, this family of molecules represented a good opportunity for the synthesis of a new generation and can be interested in other configurations. For example, in one last result obtained within the device stack consisting of glass/FTO/SnO<sub>2</sub>/HaP/AD-interlayer/Spiro-MeOTAD compared to devices with TiO<sub>2</sub>, an improvement of the V<sub>oc</sub> is observed when switching the ETL from TiO<sub>2</sub> to SnO<sub>2</sub> (see Figure 6.1). This result is likely connected to the incorporation of defects at the bottom interface in our TiO<sub>2</sub> fabrication, which can then dominate the loss effects. Improving the HTL interface, i.e. via the application of the adamantane-based interlayer on the other side can be beneficial for the carrier dynamics across the device stack and also influence carrier extraction and back-recombination at the other side, as has been shown for carbon nanotube interlayers for example.<sup>1</sup> Indeed, with 1ADAHCl, an increase of the Voc is noticed, showing a more pronounced passivation of surface defects. Adamantane and its derivatives remain an interesting option for the passivation of interfaces and could further be explored, e.g., in the pre-baseline process at IPVF, to confirm the results and how switching ETL affects the properties this way.

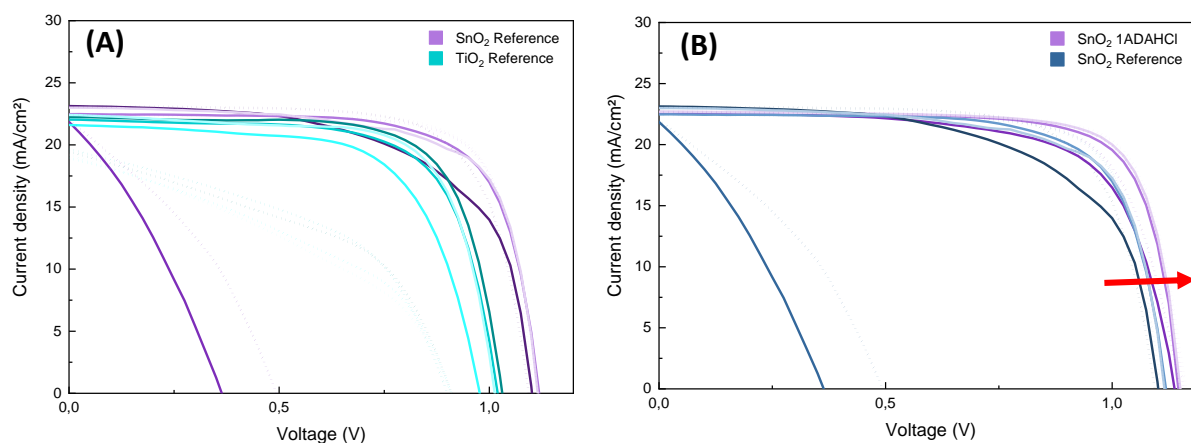


*Figure 6.1: JV curve of glass/FTO/ETL/HaP/modifiers/Spiro-MeOTAD (a) ETL comparison of references devices without Adamantane-based interlayer with c-m TiO<sub>2</sub> and SnO<sub>2</sub> (b) Comparison of the devices with 1ADAHCl and the reference devices*

	TiO <sub>2</sub> Ref	TiO <sub>2</sub> Ref	SnO <sub>2</sub> Ref	SnO <sub>2</sub> Ref	SnO <sub>2</sub> HCl	SnO <sub>2</sub> HCl
<b>Bias</b>	Reverse	Forward	Reverse	Forward	Reverse	Forward
<b>J<sub>sc</sub> (mA/cm<sup>2</sup>)</b>	22.2	19.5	22.5	22.4	22.7	22.7
<b>V<sub>oc</sub> (V)</b>	1.03	0.91	1.12	1.12	1.15	1.16
<b>Fill factor (%)</b>	71.7	45.9	72.1	75.3	77.0	77.4
<b>PCE (%)</b>	16.4	8.1	18.2	18.9	20.1	20.4

*Table 6.1: JV parameters of the best devices for each condition: TiO<sub>2</sub> reference, SnO<sub>2</sub> reference, SnO<sub>2</sub> hydrochloride*

In Chapter 4, I worked on the ETL/HaP interface in NIP device configuration in collaboration with ITODYS to look for alternative molecules of surface modifiers. As alternative molecules, I looked into self-assembled monolayers (SAMs) of carboxylic acid terminated molecules. In contrast to the preceding study on the adamantane interlayer at the opposite side, this work followed an empirical method screening larger device sets for which we modified the ETL with the SAM. Then, depending on our device results, the surface modification was adapted in an iterative fashion introducing better-suited molecules successively. This work was then separated into two parts. First, we needed to understand the effects of the sample handling during the various processing steps as the devices from the experimental series were transferred between laboratories for the SAM deposition and the perovskite cell fabrication. We noticed that this affected the device performance, and this issue was one of the keys to control the fabrication process. The second part was then focused on the choice and testing of the SAM molecules. For the initial device runs, the performances of the devices with the SAM-treated ETLs remained low compared to the reference devices. However, we achieved a continuous improvement of the device parameters with the evolution of the SAM from one iteration to the next, through the choice of the molecular interlayer, for which we went from a non-flexible molecule that would promote the growth of MA<sup>+</sup>-based perovskites (SAM1) to a flexible molecule that is better adapted for the growth of FA<sup>+</sup>-based perovskite films with 4'-amidino-[1,1'-biphenyl]-4-carboxylic acid hydroiodide (SAM 7). As the triple cation mixed halide perovskite used in this study is a triple cation composed of 83% of FA<sup>+</sup>, SAM 7 was adapted best to the HaP's crystal structure and eventually yielded the most promising results.

Further improvements could be achieved by (i) relocating all fabrication steps to one single laboratory space, thereby reducing exposure times which can lead to the incorporation of impurities, and by (ii) post-annealing of the films and devices. The latter step could be decisive as

with  $\text{TiO}_2$ , there is a high chance of incorporating water in the mesoporous layer which can already affect the SAM's formation process. As laid out in Chapter 1, this could further lead to rapid degradation of the perovskite layer and hence inferior performance levels.

Finally, in Chapter 5, I elaborated a double passivation strategy of the HaP layers to improve their stability against the ambient atmosphere and reduce the density of surface defects. We employed PMMA at the HaP/HTL top interface and PMMA:PCBM at the ETL/HaP bottom interface. We successfully optimized the top interface with a PMMA concentration of 5 mg/mL in chlorobenzene for a stack with  $\text{TiO}_2$ . As a result, we improve the Voc up to 1.13 V and the best cell, reaching a PCE of 19.1%. This result indicated that we could improve the perovskite layer by passivating traps and pinholes in the absorber layer. However, the additional PMMA:PCBM at the bottom interface did not further enhance these performance gains. While we expected to enhance the performance by suppressing the hysteresis in the mesoporous ETL, we only observed a drop of the photocurrent for all deposited samples, indicating a blocking layer formation at the bottom interface. This result was confirmed with TRPL measurements pointing to this accumulation of carriers in the sample.

Further optimization of the bottom interface can be envisioned by an additional annealing step after the deposition of the PCBM:PMMA. Further prospective exploration could be pursued to understand the effect of this interfacial layer on the perovskite film and the device. We expanded the optoelectronic characterization with preliminary modulated photoluminescence (MPL) experiments. Generally, the MPL yields information about the detectable defects within the structure by injecting photons and modulating the laser beam at a fixed power level at a frequency range that spans five orders of magnitude. Suppose at least one defect is either in the bulk or at the absorber surface. In that case, it will alter the recombination pathway and the lifetime of the charge carriers, which will then show as a drop in the MPL signature at a characteristic frequency. This work and the complex data evaluation is still in an early stage but could eventually lead to a profound understanding of the defect passivation on both sides of the perovskite absorber layer.

## 6.2 Outlook beyond the design of interfaces

Aside from the dedicated interface design that I pursued in my thesis and which are summarized in the previous section, I was also targeting potential modification of the perovskite layer itself which would then eventually act as a new test platform for interface modifications. This step has been identified as a critically important approach for research on HaP-based devices, since small changes in the composition, e.g., through precursor engineering or additives (see Chapter 3), can already lead to significant alteration of the surface and hence interface. Consequently, this can result in stringent requirements to change and adapt the interface passivation strategy to match the perovskite composition (see Chapter 4).

One particularly promising approach to enhance the reliability of the perovskite deposition is the substitution of the individual precursors by a fully synthesized perovskite powder precursor. Typically, the perovskite layer is produced from several precursors and dissolved prior to the HaP deposition in the glovebox. This requires careful handling of the solution, as exposure to humidity and other traces of impurities can lead to degradation and strongly varying results. However, another alternative is the fabrication of single powder perovskite. This work was done in collaboration with the University of Bayreuth, following a previous ongoing partnership on the use of perovskite powder precursors described by N. Leupold et al.<sup>2</sup>: The initial precursors are mixed in a milling jar and form the perovskite powder through mechanochemical synthesis. Here, we were able, to successfully produce single and double-cation HaP powder precursors for the formation of full films and devices at IPVF. Our preliminary UV-Vis absorption measurements indicate a sharp absorption edge and similar performances for the two fabrication routes via individual precursors and the complete powder precursor. These promising results are obtained in NIP or PIN configuration devices, indicating the method's versatility. Whether the interface optimization routes would be the same given potential differences in the film formation as a function of the precursor chemistry remains an open question.

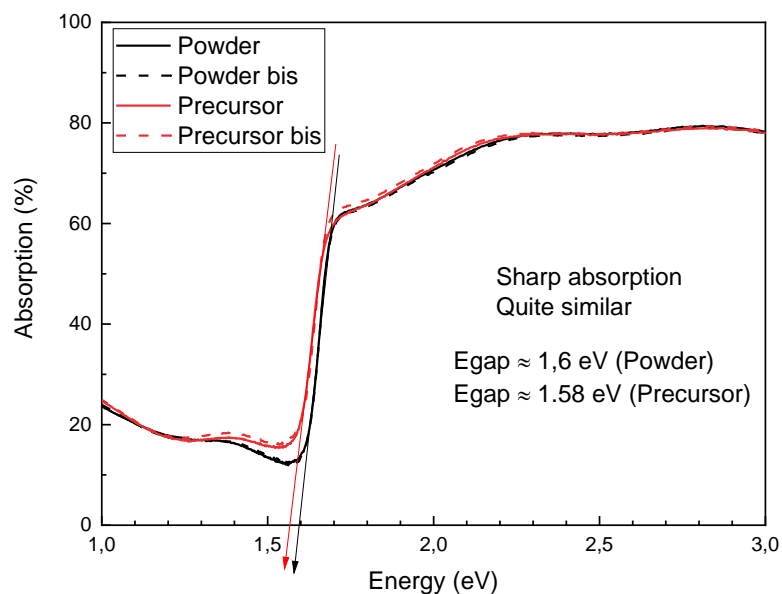


*Figure 6.2: Absorption spectrum of the perovskite layer (red) "precursor" sample made for the classic HaP IPVF's recipe (black) "powder" made from the ball-milling fabrication process*

Hence, after this thesis, several aspects of my various projects can be expanded on further to improve the perovskite solar cell performance and stability. The individual projects I have been working on are small yet decisive pieces to develop an ensemble that is the stepwise optimization of the interfaces adapted to the specific perovskite layer composition.

## Chapter 7: Résumé en français

### *Traitement et design des interfaces au sein des cellules solaires à base de pérovskite*

#### **Introduction**

Une source d'énergie abondante existe et alimente la terre toute l'année : le soleil. Plusieurs moyens sont disponibles pour récolter cette énergie, le plus prometteur étant le dispositif photovoltaïque, c'est-à-dire la cellule ou le panneau solaire. Plusieurs générations de technologies de cellules solaires existent passant de cellules à base de silicium à des cellules organiques. Un nouveau matériau a fait son apparition pour la première fois dans la communauté photovoltaïque en 2009: la pérovskite aux halogénures métalliques (HaPSC). Elles sont apparues dans la publication de Kojima et al. en étant incorporé dans des cellules solaires à pigment photosensible (DSSC), atteignant une efficacité de 3.5 %. En une dizaine d'années, l'efficacité des cellules solaires à base de pérovskite ont subi une fulgurante augmentation atteignant une efficacité de 25.8 % en 2023 et 33.2 % dans une configuration en tandem avec une sous-cellule à base de silicium, apportant une révolution dans le domaine photovoltaïque. Ce matériau, utilisé au sein des cellules pérovskites en tant qu'absorbeur, est convoité grâce à ces propriétés optoélectroniques et sa rentabilité, a comme composition  $ABX_3$  avec un centre métallique de plomb (Figure 7.1).

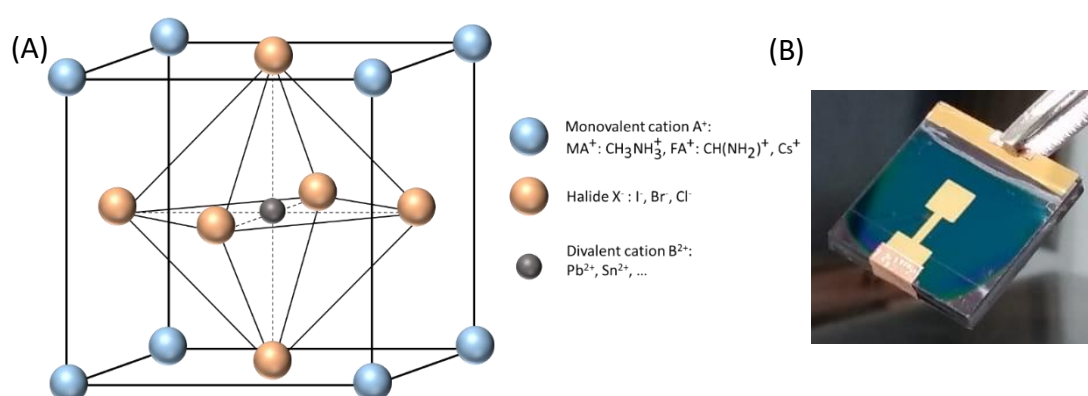


Figure 7.1: (a) Structure cristalline de la pérovskite aux halogénures métalliques (b) Photographie d'une cellule pérovskite

Cependant, les PSC souffrent considérablement de leur instabilité causée principalement par l'inadéquation de l'interface, car le dispositif est une cellule solaire à hétérojonction couplée à une migration ionique et soumise à des facteurs extrinsèques tels que l'humidité ou la température. Nous décrivons les techniques de dépôts utilisés et développés au cours de la thèse dans la fabrication des cellules pérovskites ainsi que les analyses de caractérisation qui m'ont accompagné pendant trois et demi dans mon manuscrit et les principaux résultats sont décrits dans ce résumé. Grâce au savoir-faire de l'IPVF sur la technologie de la pérovskite, mon projet a commencé avec la cellule de référence de l'IPVF verre/FTO/compact TiO<sub>2</sub>/mésoporeux TiO<sub>2</sub>/HaP/Spiro-MeOTAD/Or.

L'objectif principal de ma thèse était la conception d'interface pour la PSC par passivation d'interface. Mon travail se résume autour de la configuration NIP. Durant mon stage déjà, j'avais travaillé sur l'interface couche de transport d'électrons (ETL)/pérovskite (HaP) avec une monocouche auto-assemblée (SAM) pour améliorer le transport de charge entre le TiO<sub>2</sub> ou ZnO déposés par ALD et la pérovskite, en me concentrant sur le dépôt méthode des SAMs. Ce stage a conduit à un article sur le greffage des acides aminophosphoniques publié dans notre manuscrit par O. Fournier et al. Dans la même continuité, l'objectif principal de ma thèse de doctorat est devenu d'améliorer la stabilité des PSC en protégeant les couches sensibles du dispositif contre l'humidité, et d'augmenter l'efficacité des cellules en réduisant la recombinaison de charge aux interfaces. Cette thèse s'est séparée en trois principaux projets distincts.

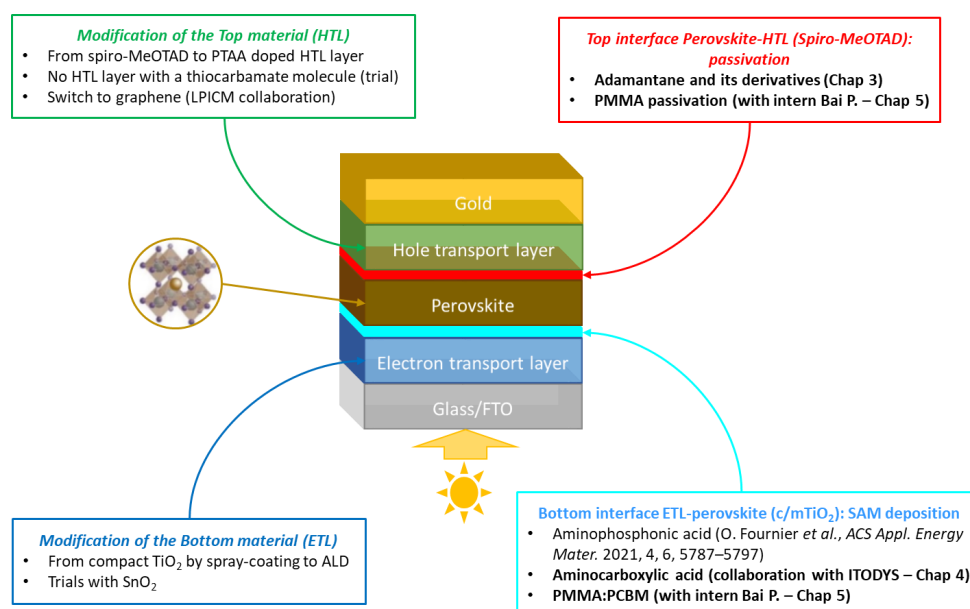
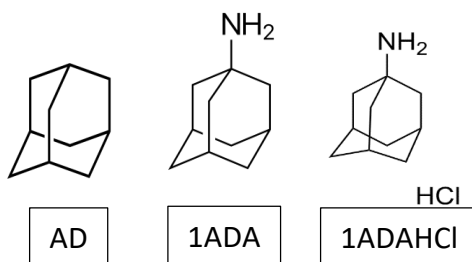


Figure 7.2 : Récapitulatif de mes travaux au cours de mon doctorat

## ***Une nouvelle potentielle famille de molécules pour les pérovskites : Adamantane et ces dérivés***

Ce chapitre 1 décrit notre travail avec l'adamantane (AD) et ses dérivés, la 1-adamantanamine (1ADA) et le chlorhydrate de 1-adamantanamine (1ADAHCl). Ces molécules sont de petites molécules hydrophobes (Figure 3.1). Une couche de protection est déposée à l'interface HaP/couche de transport de trous (HTL) et on espère une préservation la couche de pérovskite pendant une courte période.



*Figure 7.3 : Adamantane (AD) et ces dérivés: 1-adamantanamine (1ADA) and 1-adamantanamine hydrochloride (1ADAHCl)*

Une couche de protection est déposée à l'interface HaP/couche de transport de trous (HTL) et préserve la couche de pérovskite pendant une courte période. Les échantillons sont stockés à l'air ambiant pendant cinq semaines. Le dispositif de référence est complètement dégradé après 5 semaines de stockage alors qu'avec l'adamantane et ses dérivés, la couche de pérovskite est partiellement préservée et montre l'efficacité partiel de notre interface (Figure 7.4).

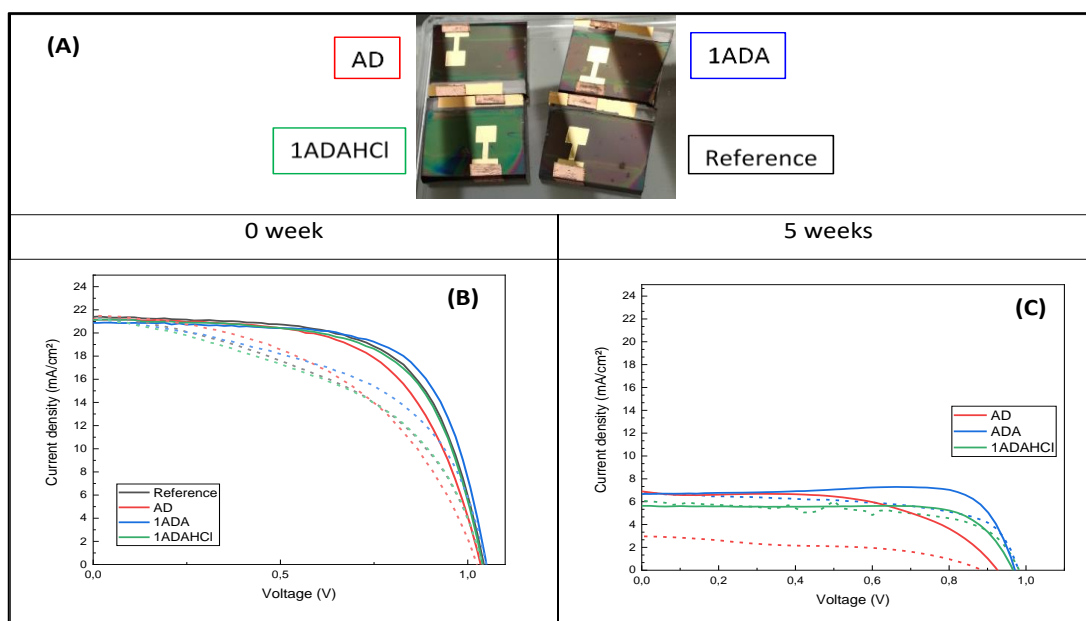


Figure 7.4 : Cellule pérovskite de verre/FTO/c-m TiO<sub>2</sub>/HaP/Spiro-MeOTAD/Or stocké sous air ambient (a) Photographie des cellules après 5 semaines (b) courbe JV avant le stockage des échantillons (c) JV après 5 semaines

De plus, il s'agit encore d'une résultat préliminaire mais nous observons en outre une amélioration des performances avec la réduction de la recombinaison de charge pour 1ADAHCl lors de l'utilisation de SnO<sub>2</sub> comme ETL au lieu de TiO<sub>2</sub>, comme présenté sur la figure 2, indiquant que TiO<sub>2</sub> conduit à des défauts dans la couche de pérovskite. Ces changements ont entraîné un PCE maximum de 20,4 % (20,1 % de polarisation directe) avec un Voc de 1,16 V (1,14 V) par rapport au TiO<sub>2</sub> protégé de cette série à 14,6 % (8,2 %) avec un Voc de 1,02 V (0,92 V). LA continuation de ce projet serait potentiellement avec une ETL SnO<sub>2</sub> afin d'observer, dans un premier temps, la réduction de l'hystérésis avec le changement de l'ETL, et dans un second temps, une amélioration du Voc avec la présence de 1ADAHCl.

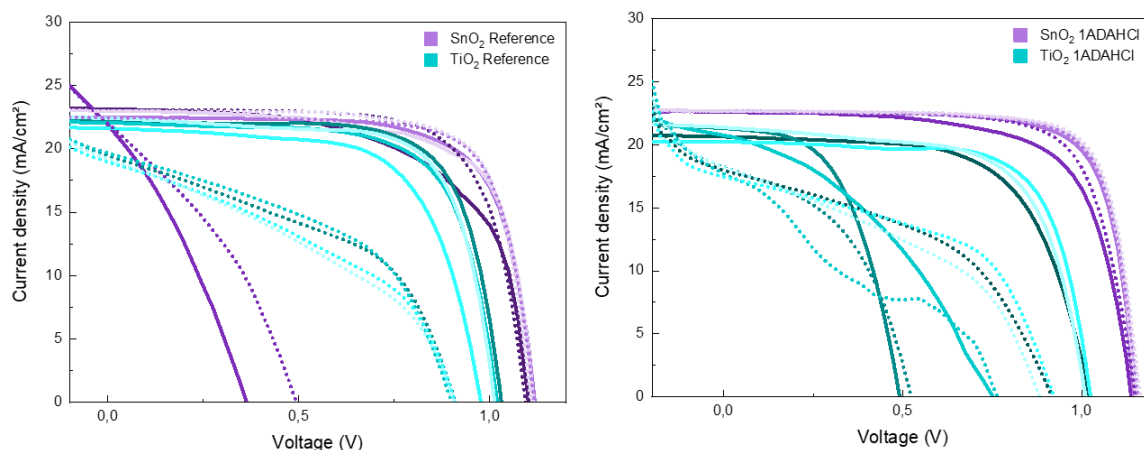


Figure 7.5 : Cellule pérovskite avec une ETL de TiO<sub>2</sub> vs SnO<sub>2</sub> (verre/FTO/c-m TiO<sub>2</sub>/HaP/X/Spiro-MeOTAD/Or) (a) Cellule de référence (b) traité à l'1ADAHCl (=X)

## **Développement et test d'une couche de SAMs synthétisé : Approche de l'interface ETL/HaP**

Mon chapitre 2 montre mon travail en collaboration avec ITODYS, un laboratoire en France, avec le développement d'acides aminocarboxyliques et d'acides amidinocarboxyliques comme SAMs à l'interface ETL/HaP. Cette collaboration devait combiner l'expertise d'IPVF du procédé solaire pérovskite et le savoir-faire d'ITODYS pour la synthèse SAM spécialisée. Une cellule complète avec les SAMs se finalisent en une semaine entre le premier dépôt et la première analyse de caractérisation. Ce projet a suivi une approche empirique avec l'utilisation des SAM proposés sur les appareils, suivie d'une compréhension de l'effet sur les paramètres de nos appareils PSC. Plusieurs parties ont été déterminées dans ce projet : les effets des SAM sur l'appareil, les effets de transport sur les échantillons et les effets de processus. Au final, nous terminons en incorporant un groupe de SAM adapté à la structure de notre HaP : l'iodhydrate d'acide 4'-amidino-[1,1'-biphényl]-4-carboxylique. Notre pérovskite est composée en majorité de formadinium sur le site A, ce qui permet à des groupes d'amarrage spécifiques de favoriser le dépôt de film de pérovskite.

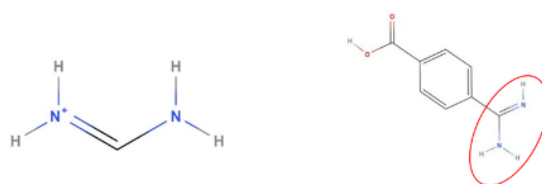
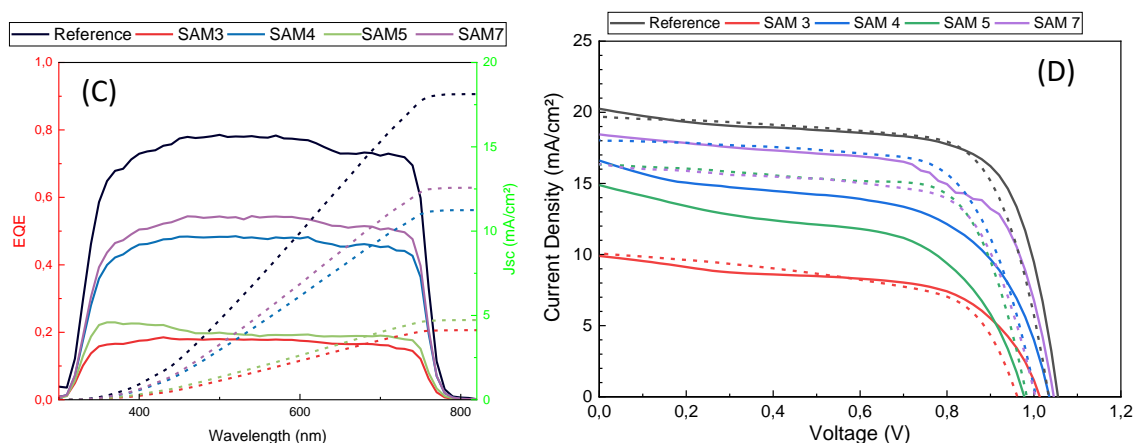
(A) Formamidinium (FA<sup>+</sup>) (B) 4-amidino-benzoic acid

Figure 7.6 : Comparison des similarités entre (a) formadinium (FA<sup>+</sup>) et (b) 4-amidinobenzoic acid  
(c) Courbes JV et (d) EQE des meilleurs cellules pour la série finale avec SAM 3, 4, 5 et 7

Ce SAM a présenté les performances les plus élevées par rapport aux autres molécules car il peut combler le défaut du cation A et stabiliser la structure cristalline de la pérovskite (Figure 7.6). Elle ne présente pas encore des résultats rivalisant avec notre référence mais je pense qu'il s'agit d'une bonne base pour la continuation de ce projet.

## Une alternative : compréhension et application de polyméthacrylate dans une cellule

Ce dernier chapitre 3 a été mon projet avec un stagiaire, que j'ai encadré, avec comme objectif le dépôt d'une double couche de passivation en sandwich autour de la pérovskite en utilisant les couches moléculaires organiques PMMA et PCBM. Le PMMA est un polymère qui peut combler les trous dans la couche de pérovskite, réduisant ainsi la quantité de trous d'épingle et augmentant la résistance du shunt, tandis que le PCBM peut favoriser l'extraction d'électrons à l'interface avec l'ETL. La solution PMMA uniquement est optimisée à 5 mg/mL à l'interface HaP/HTL, alors que PMMA:PCBM a été utilisé à l'interface ETL/HaP avec une amélioration de la moyenne du Voc à 1,13 V à 5 mg/mL contre 1,09 V pour la référence. Une amélioration aussi observée pour l'EQE pour 5 mg/mL().

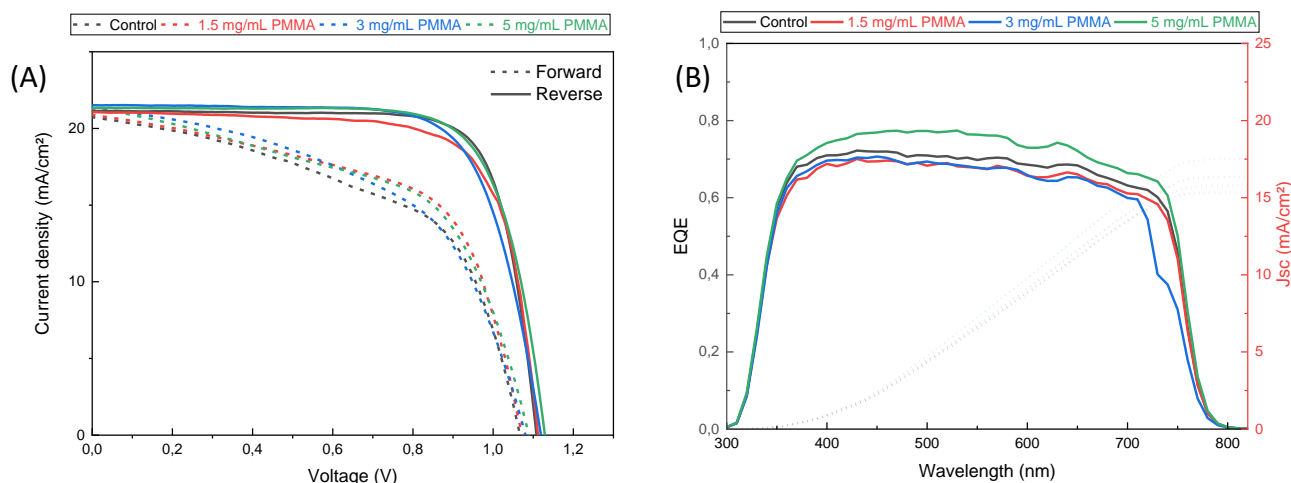


Figure 7.7 : Mesures photoélectriques de cellules verre/FTO/c-m TiO<sub>2</sub>/HaP/PMMA/Spiro-MeOTAD traité par PMMA (1.5 mg/mL, 3 mg/mL and 5 mg/mL comparé à la cellule de référence):  
(a) Courbe JV et (b) EQE

En fin de compte, nous constatons que, de manière surprenante, le PMMA:PCBM n'a pas joué un rôle favorable dans notre configuration car il agissait comme une couche de blocage entre la couche mésoporeuse et la pérovskite démontrée par une augmentation de la durée de vie du porteur à l'interface avec quasiment le double de temps de vie pour les échantillons avec PMMA:PCBM (Figure 7.8).

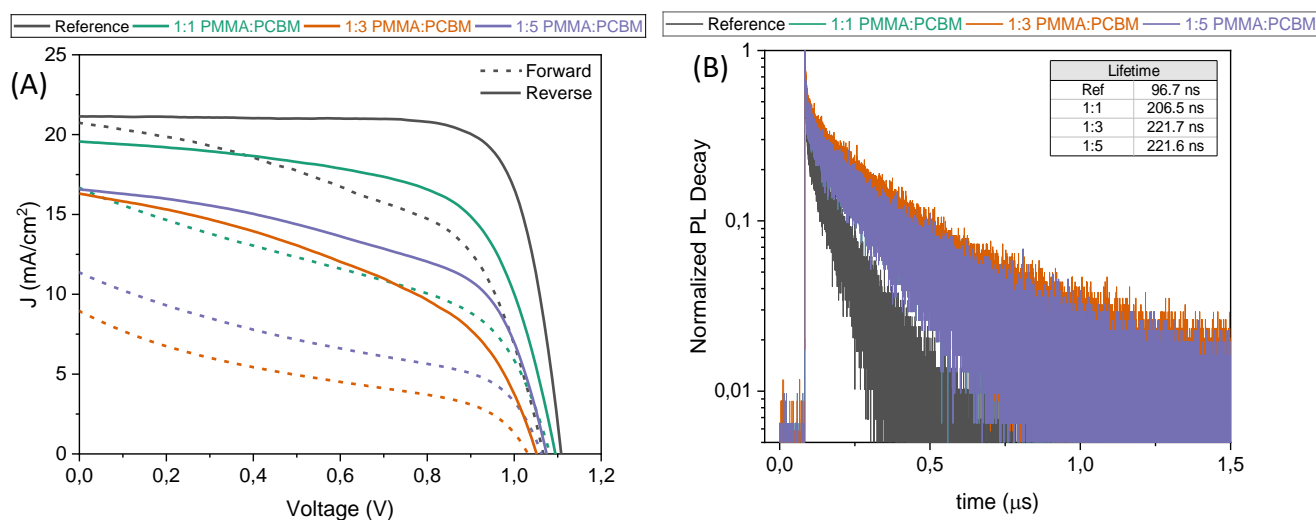


Figure 7.8 : (a) Courbe JV de cellule verre/FTO/c-m TiO<sub>2</sub>/PMMA:PCBM/HaP/Spiro-MeOTAD/Or avec différents ratio PMMA:PCBM (b) Mesure TRPL de couches pérovskite avec ces couches de PMMA:PCBM en interface (insert table avec les temps de vie des charges dans chaque condition)

**Titre :** Traitement et design des interfaces au sein des cellules solaires à base de pérovskite

**Mots clés :** photovoltaïque, cellule solaire à base de pérovskite, passivation, interface, XPS

**Résumé :** Les cellules solaires à pérovskite (HaPSC) sont l'une des technologies émergentes de la dernière décennie grâce à leurs propriétés optoélectriques opportunes, leurs matériaux à faible coût et une large gamme d'applications, atteignant 25,8% en 2023. Cependant, les PSC souffrent considérablement de leur instabilité dû à des facteurs externes, comme l'humidité ou la température, et internes, comme les défauts d'interface conséquence du dispositif en hétérojonction. L'objectif principal de ma thèse était d'améliorer la stabilité des PSC en protégeant les couches sensibles du dispositif contre l'humidité, et d'augmenter les performances en réduisant la recombinaison de charge aux interfaces. J'ai abordé cet objectif sous plusieurs angles au cours de ma thèse, de la fabrication des dispositifs à leur caractérisation complète. Dans mon premier projet, j'ai travaillé avec l'adamantane et ses dérivés, la 1-adamantanamine et l'1-adamantanamine hydrochlorure. Ces molécules étant hydrophobes, je voulais réaliser une couche protectrice contre l'humidité et éventuellement passivante, déposée à

l'interface pérovskite (HaP)/HTL.

Une préservation de la HaP est obtenue pendant une courte période avec 1ADAHCl. Nous n'avons pas observé d'amélioration des performances avec comme TiO<sub>2</sub> un ETL. Mon deuxième projet était en collaboration avec ITODYS sur le développement d'acides aminocarboxyliques et d'acides amidocarboxyliques comme couche de molécules auto-assemblées (SAM), afin d'améliorer l'interface ETL/HaP. Au final, sur 7 SAMs, l'iodhydrate d'acide 4'-amidino-[1,1'-biphényl]-4-carboxylique a présenté les performances les plus élevées grâce à ses groupes d'amarrage spécifiques favorisant le dépôt du film de pérovskite. J'ai poursuivi mon troisième projet avec mon stagiaire, avec l'introduction de la passivation en sandwich en utilisant du PMMA et PCBM. La solution PMMA est optimisée à 5 mg/mL à l'interface HaP/HTL, alors que PMMA:PCBM a été utilisé à l'interface ETL/HaP. Au final, nous constatons qu'étonnamment le PMMA:PCBM n'a pas joué un rôle favorable dans notre configuration car il agissait comme une couche bloquante à l'interface.

**Titre :** Interface design of halide perovskite solar cells

**Keywords :** photovoltaic, perovskite solar cell, passivation, interface, XPS

**Abstract:** Perovskite (HaP) solar cells are one of the emerging technologies of the last decade thanks to their expedient optoelectrical properties, low-cost materials, and a large range of applications, reaching 25.8% of PCE in 2023. However, PSCs suffer significantly from their instability caused mainly by the interface mismatch as the device is a heterojunction solar cell coupled with ion migration and subject to extrinsic factors like humidity or temperature. The main focus of my thesis was the interface design of the halide perovskite solar cell in NIP configuration through interface passivation. The main objective of my PhD thesis follows my work during my internship, which was to improve the stability of PSCs by protecting the sensitive layers in the device against humidity, and to increase the performance by reducing charge recombination at the interfaces. I attacked this objective from several angles during my thesis, from device fabrication to their full characterization. In my first project, we worked with adamantane and its derivatives, 1-adamantanamine and 1-adamantanamine hydrochloride. These molecules are hydrophobic.

We wanted to produce a protective layer against humidity and possible favorable passivation. We successfully deposit a protective layer at the interface HaP/HTL, preserving HaP for a short-term period with 1ADAHCl. We did not observe an improvement in performance with as TiO<sub>2</sub> an ETL. My second project was pursued in collaboration with ITODYS to develop aminocarboxylic acids and amidocarboxylic acids as SAMs to improve the interface ETL/HaP. In the end, the SAM 4'-amidino-[1,1'-biphenyl]-4-carboxylic acid hydroiodide presented the highest performances compared to the other molecules as its specific docking groups help to promote perovskite film deposition. I pursued my third project with an intern, that I supervised, with the introduction of bilayer passivation of PSCs using the organic molecular layers PMMA and PCBM. The PMMA-only solution is optimized at 5 mg/mL at the interface HaP/HTL, whereas PMMA:PCBM was used at the interface ETL/HaP. In the end, surprisingly, the PMMA:PCBM did not play a favorable role in our configuration as it acted as a blocking layer.